Utrecht University

Determination of lithological interfaces above the Groningen gas field using RZ-decon of borehole SDM-01 check shot data and synthetics

Abstract

The extraction of gas from the Groningen gas field has led to subsidence and induced seismicity in the area, resulting in both damage to buildings and concern among the inhabitants of Groningen. Detailed information about the lithology and geological structure of the subsurface in this area is therefore needed. In this study, check shot data from borehole SDM-01 is used for testing a new method to determine the depths of lithological interfaces above the reservoir rock. This method is based on the deconvolution between the radial and vertical components of the geophones on a string, called RZ-decon. This method is applied to both real data and synthetic data. The real data is retrieved from check shots around borehole SDM-01, measured by 10 geophones on a string inside the borehole at depths between 2700 and 300 m, inside the Rotliegend reservoir sandstones. The synthetic data is produced using Specfem2D with an input velocity and density model provided by NAM. When comparing the real data with the synthetics, it can be concluded that the RZ-decon method is a useful tool for determining interfaces with velocity contrasts and that the model used in Specfem2D to approximate the reality is quite accurate. When the velocity structure is unknown, this method can be used to estimate the depths of velocity contrasts due to lithological interfaces beneath a set of geophones, using a source from below, such as earthquakes, but the uncertainty in this estimation increases with depth.

E. Arwert
4015096

Master thesis *Earth Structure and Dynamics*
Department of Earth Sciences
Utrecht University

Date: October 3, 2019
First supervisor: dr. H. Paulssen
Second supervisor: W. Zhou MSc

Contents

List of figures

List of tables

Introduction

The Groningen gas field in the Netherlands is the 7th largest gas field of the world and has been producing since 1963 (Van Thienen-Visser & Breunese, 2015). The extraction of gas has led to subsidence and induced seismicity in the area, resulting in both damage to buildings and concern among the inhabitants of Groningen. Detailed information about the lithology and structure of the subsurface in the area is needed, for example to be able to calculate the exact location of earthquakes.

In 2013, when the induced seismicity reached its highest level so far, two geophone strings were placed in two boreholes that were originally used as production wells. A string of 10 geophones was positioned in borehole SDM-01 in order to monitor seismicity in the reservoir (Nederlandse Aardolie Maatschappij, 2016). The locations of these two boreholes are shown in Figure 1a.

In this study, check shot data from borehole SDM-01 is used for testing a new method to determine the depths of lithological interfaces above the reservoir rock. This method is based on the deconvolution between the radial and vertical components of the geophones on the string.

The main question of this study is: Does this method work and how accurate is it? Another objective of this study is to compare this radial to vertical deconvolution of the real check shot data to that of synthetic data retrieved using Specfem2D, in order to interpret the quality of the input P- and S-wave velocity and density model provided by NAM.

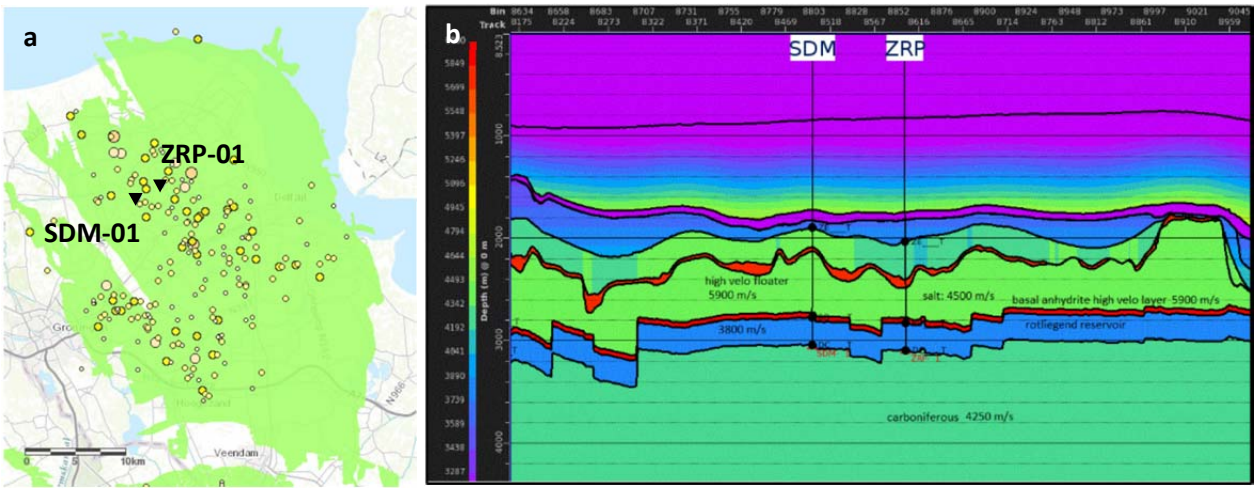

Figure 1: After (Zhou & Paulssen, 2017): a) Groningen gas field (green) with locations SDM-01 and ZRP-01 (triangles) b) Cross section (length ~20 km, depth 4.4 km) through a P-wave velocity model provided by NAM with boreholes SDM-01 and ZRP-01 (scale: 3287-6000 m/s).

Geological setting

The Groningen gas field is located in the northeast of the Netherlands, on the Groningen High between the Ems Graben and the Lauwerszee Trough. The formation of the structure occurred during the late Kimmerian extensional phase. The reservoir depth is 2600 to 3200 m, which consists mostly of Permian sandstones of the Rotliegend Group. The seal is formed by the salt and evaporites of the Zechstein Group, with varying thickness from tens of meters to over 1 km (Van Thienen-Visser & Breunese, 2015).

The stratigraphic setting is explained below, from the surface down to the Carboniferous underburden below the reservoir. The stratigraphic units are based on DGM-deep v4.0 (TNO, 2014), at the location of the borehole SDM-01. The units that are present at this location are visualized in a lithostratigraphic column in Figure 2. The depths of the interfaces between these units are observed in the borehole log and are listed in Table 1.

The top layer is the North Sea Group of which the thickness varies between 600 and 1000 m in the Groningen area. It is subdivided into an upper and combined middle and lower part. The transition from Upper North Sea Group (NU) to Middle and Lower North Sea Groups (NM + NL) is at approximately 400 m depth. In most places, the Upper North Sea Group unconformably overlies the Middle North Sea Group. The sequence consists of clays and fine-grained to coarse sands. The Upper North Sea Group is of Neogene age (Van Adrichem Boogaert & Kouwe, Upper North Sea Group, 1993-1997). The Middle and Lower North Sea Groups consist of predominantly marine sands, clays and silts of Paleogene age (Van Adrichem Boogaert & Kouwe, Middle North Sea Group, 1993-1997), (Van Adrichem Boogaert & Kouwe, Lower North Sea Group, 1993-1997).

The next layer is the Chalk Group (CK) which consists of mainly marine limestones of late Cretaceous age. The thickness of the Chalk Group in the Groningen area is between 500 and 800 m (Van Adrichem Boogaert & Kouwe, Chalk Group, 1993-1997).

A sequence of three thinner sedimentary layers is found below the Chalk Group. These layers are the Rijnland Group (KN), the Altena Group (AL) and the combined Upper and Lower Germanic Trias Groups (RB + RN). The Rijnland Group consists of formations of (sometimes marly) clays, which may contain beds of sandstone, from the early Cretaceous (Van Adrichem Boogaert & Kouwe, Rijnland Group, 1993-1997). The Altena Group contains mainly clayey deposits of Jurassic age, with some calcareous and clastic alternations (Van Adrichem Boogaert & Kouwe, Altena Group, 1993-1997). At the borehole location, the Altena Group is absent. The Upper and Lower Germanic Trias Groups consist of silty claystones, evaporites, carbonates, siltstones and sandstones from the Triassic and are separated by an unconformity (Van Adrichem Boogaert & Kouwe, Upper and Lower Germanic Trias Groups, 1993-1997).

The Zechstein Group (ZE) is a layer of rock salt evaporites of late Permian age. In general, the Zechstein Group is referred to as the impermeable salt layer above the gas reservoir, acting as the reservoir seal. The Zechstein Group is thickest in the central area of the gas field near Loppersum and tends to get thinner at the north, south and east flanks of Groningen (Van Adrichem Boogaert & Kouwe, Zechstein Group, 1993-1997). Note the lateral variations in the Zechstein Group with horst and graben structures in Figure 1b.

Two thin layers of anhydrite are present within the Zechstein Group; one anhydrite layer floats in the upper part of the Zechstein Group (ANH1) and the other is located right above the gas reservoir (ANH2) (Van Gent, Urai, & De Keijzer, 2011). These brittle layers inside the soft salt formation cause strong reflections and refractions of passing seismic waves. The depths of these anhydrite layers, as stated in Table 1, are interpreted from the P-wave velocity model provided by NAM, for they are recognizable by their high acoustic velocities, see Figure 1b.

The reservoir is composed of porous Permian sandstone in the Upper Rotliegend Group (RO). The depth of the gas reservoir is on average 3 km, but varies laterally over Groningen (Van Adrichem Boogaert & Kouwe, Upper Rotliegend Group, 1993-1997).

The sedimentary layer below the Rotliegend Group is part of the Limburg Group (DC) of late Carboniferous age. The Limburg Group forms a thick succession of fine-grained siliciclastic sediments, generally with intercalated coal seams in the upper and middle parts (Van Adrichem Boogaert & Kouwe, Limburg Group, 1993-1997).

The carbon-rich sediments of the Limburg Group form the source rock for the gas that has been pushed upwards into the sandstones of the Upper Rotliegend Group and is prevented from migrating further upward by the impermeable salt of the Zechstein Group.

Faults are mainly present in the sandstones of the Rotliegend Group and are caused by extensional stress. They do not extend vertically into the Zechstein Group due to the ductile behavior of rock salt under high pressure, see Figure 1b. The faults are oriented in general in NW-SE direction (Kraaijpoel & Dost, 2013). Several faults have been reactivated during the gas production in Groningen (Spetzler & Dost, 2017).

Table 1: Depths of lithological units from well log data of SDM-01 (source: NAM).

Name of unit	Abbreviation	Depth top (m-NAP)	Depth bottom (m-NAP)
Upper North Sea Group	NU	0	343.28
Middle and Lower North Sea Groups	NM + NL	343.28	843.26
Chalk Group	CK	843.26	1727.23
Rijnland Group	KN	1727.23	1828.20
Upper and Lower Germanic Trias Groups	RB + RN	1828.20	1871.16
Zechstein Group	ZE	1871.16	2768.88
Upper Rotliegend Group	RO	2768.88	3040.38
Limburg Group	DC	3040.38	3071.28
Upper Anhydrite Layer	ANH1	2100	2145
Lower Anhydrite Layer	ANH2	2720	2768.88

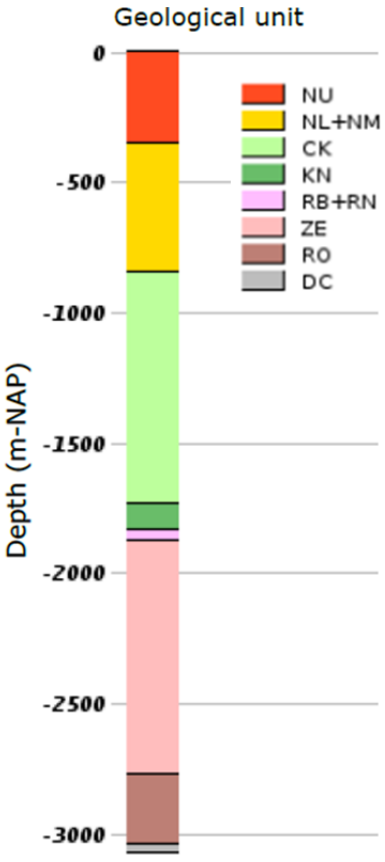

Figure 2: Lithostratigraphic column from well log data of SDM-01, retrieved from Dinoloket (TNO, 2017).

Method

In this study, a new method is tested for determining the depths of lithological interfaces. This method is based on the deconvolution between the radial and vertical components of the geophones, in this study called “RZ-decon”. This RZ-decon is done for both real data and synthetic data. The real data is retrieved from check shots that are fired around borehole SDM-01 and measured by 10 geophones on a string inside the borehole at depths between 2700 and 300 m. The synthetic data is produced using Specfem2D, which computes synthetic seismograms with an input P- and S-wave velocity and density model, a synthetic source and synthetic receiver strings.

Preparation of the check shot data

Before the aforementioned deconvolution can be applied between the radial and vertical components of the geophones, the current orientations of the components of the geophones need to be calculated. While the geophones were placed at approximately 3 km depth, they were able to rotate on the string before attaching to the borehole walls, so that the orientations of the horizontal components of the different geophones are not known and randomly distributed with depth. Also the vertical components of the geophones are not exactly vertically oriented at depth, because of the inclination of the borehole itself, which also changes with depth. To be able to apply a deconvolution between the vertical and radial component per geophone, the orientations of the components of the different geophones should be exactly the same, therefore the raw data (see Appendix 1) recorded on the three components of the geophones needs to be rotated in such a way that they are all in the exact same orientation.

Calculation of the orientations of the geophones

The data recorded by the geophones is in a left-handed coordinate system: (C1, C2, C3) = (X, Y, Z), with Y = X + 90 (as seen from above) and Z = up, see Figure 3. The orientation of Z is left out of consideration for the calculation of the orientations of X and Y and is assumed to be perfectly vertical (although it is not), and therefore the angle between the azimuth of X and Y is assumed to be exactly 90 degrees. For the calculation of the orientations of the X and Y components, check shot data from four different directions is used. Check shots are artificial sources that are generated by a shallow explosion. Since they are explosions, they will generate mainly P-waves with a first motion outwards and away from the check shot location.

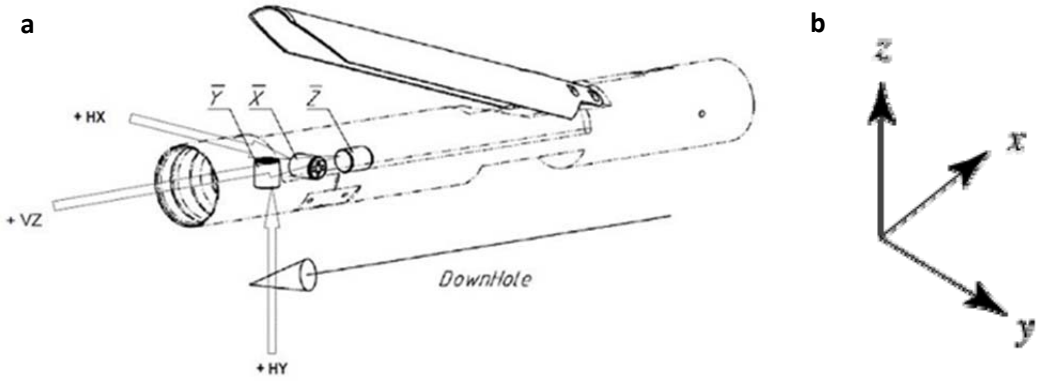

Figure 3: a) Geophone arrangement, arrows indicate the direction of the positive X, Y and Z axes, from (Sercel seismic tools specifications, 2014). b) Left-handed coordinate system with Y = X + 90 (as seen from above) and Z = up.

First, the expected orientations of the R-axis and T-axis (radial axis and transversal axis) are calculated for the four different check shot locations. The R-axis is always oriented in the opposite direction of the check shot location, so on the R-axis the recorded energy of P- and SV-waves is maximum. The T-axis is always oriented perpendicular to the R-axis, so on the T-axis the recorded energy is minimum. For consistency the coordinate system of the R- and T-axes is also chosen as a left-handed system: (C1, C2, C3) = (R, T, Z), with T = R + 90, where the azimuth is relative to North over East, and Z = up. For the four different check shot locations, the expected orientations of the R- and T-axes are shown in Figure 4.

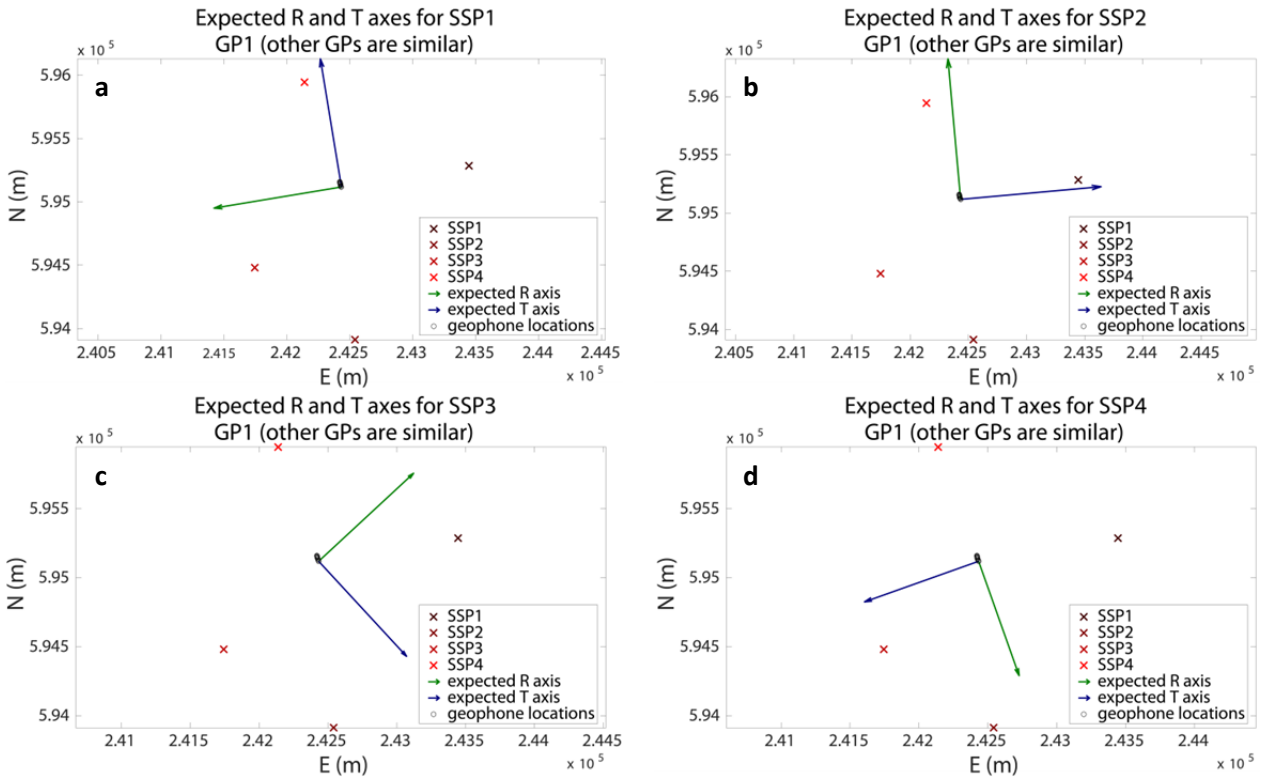

Figure 4: Expected R-axis (green) and T-axis (blue) for four different check shot locations a) SSP1 b) SSP2 c) SSP3 d) SSP4.

Second, the angle ϕ between the X- and Y-axes of the raw data and the expected R- and T-axes, respectively, is calculated. For each recording of X and Y, the peak of the first arriving wave, either positive or negative, is picked and then the absolute value of the area under the peak is calculated by integrating over a time window of -0.001 to +0.001 seconds (5 samples) around the maximum or minimum of the peak. This is done while increasing the angle ϕ clockwise by one degree each time and rotating the raw data clockwise by applying the following equations:

$$X' = X \cos\varphi + Y \sin\varphi$$

$$Y' = Y \cos\varphi - X \sin\varphi$$

X' and Y' are the recordings on the new set of axes after rotation, X and Y are the recordings on the initial set of axes of the raw data, and ϕ is the rotation angle. The starting situation for ϕ = 0 is X' = X and Y' = Y, see Figure 5a. The integral under the peaks of X and Y will be different after rotating by different values

for ϕ. As soon as the raw data is rotated by ϕ degrees in such a way that X' is aligned with the actual orientation of the R-axis for that particular check shot location and Y' is aligned with the actual orientation of the corresponding T-axis, the true value of the integral under the peak for the X'-component will be maximum and the absolute value of the integral under the peak for the Y'-component will be minimum. This is under the assumption that there is a 1-D horizontally layered structure, so that the P-wave is assumed to travel exactly in the direction of the R-axis.

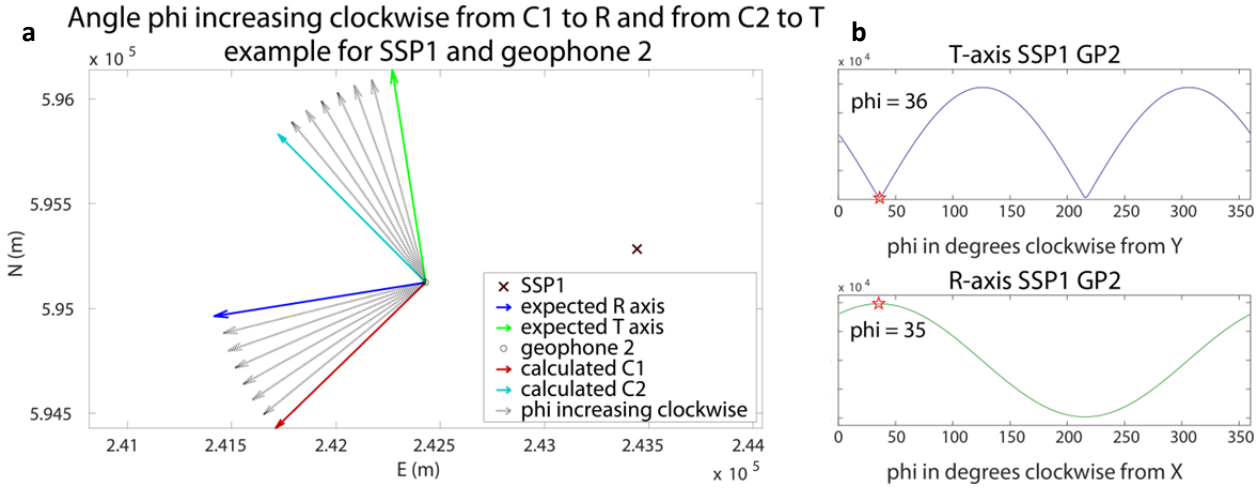

Figure 5: a) Angle phi increasing clockwise, example for SSP1 geophone 2. b) Calculated phi between the X-axis and R-axis and between the Y-axis and T-axis, red stars indicate the angle phi for which the energy on X is maximum and the energy on Y is closest to zero, example for SSP1 geophone 2.

The angle ϕ for which the integral of X' is maximum is the angle between the orientation of X and the R-axis, and the angle ϕ for which the absolute integral of Y' is minimum is the angle between the orientation of Y and the T-axis. In Figure 5b the integrals under the peaks as a function of the rotation angle ϕ is shown for one check shot and one geophone, for all results see Appendix 2. The maximum true value for the integral of X' and the minimum absolute value for the integral of Y' are indicated by a red star. Since R and T are 90 degrees apart, the two obtained values for ϕ should be nearly the same. The orientation of X and Y can then be calculated from the orientations of the expected R-axis and T-axis using the equations:

$$X = R - \varphi$$

$$Y = T - \varphi$$

This way, X and Y are calculated independent from each other. Y can also be calculated from X or the other way around, since they are in principal 90 degrees apart, such that:

$$X = Y - 90 \quad or \quad Y = X + 90$$

This results in eight independent calculations of X and eight independent calculations of Y. From these eight values of both X and Y, the average value and the standard deviation are calculated. This is shown in Figure 6 and in Table 2 and Table 3. The calculated average orientations of X and Y for all geophones are shown with their average and standard deviation in Figure 6.

Table 2: Azimuth of X, calculated from R and from Y, average and standard deviation.

GP	Azimuth of X calculated from R				Azimuth of X calculated from Y				Av.	Std.
	SSP1	SSP2	SSP3	SSP4	SSP1	SSP2	SSP3	SSP4		
1	298	278	261	287	297	278	265	287	281	18
2	226	199	191	209	225	200	189	209	206	19
3	347	322	300	332	347	318	303	332	325	23
4	324	297	276	305	325	295	276	305	300	24
5	316	287	269	299	316	287	271	298	293	24
6	338	319	291	321	338	319	300	319	318	24
7	222	203	186	200	221	203	185	200	203	18
8	335	323	298	318	336	323	303	317	319	19
9	344	339	286	322	344	337	314	322	326	29
10	72	64	49	57	71	65	50	58	61	11

Table 3: Azimuth of Y, calculated from T and from X, average and standard deviation.

GP	Azimuth of Y calculated from T				Azimuth of Y calculated from X				Av.	Std.
	SSP1	SSP2	SSP3	SSP4	SSP1	SSP2	SSP3	SSP4		
1	27	8	355	17	28	8	351	17	11	18
2	315	290	279	299	316	289	281	299	296	19
3	77	48	33	62	77	52	30	62	55	23
4	55	25	6	35	54	27	6	35	30	24
5	46	17	1	28	46	17	359	29	23	24
6	68	49	30	49	68	49	21	51	48	24
7	311	293	275	290	312	293	276	290	293	18
8	66	53	33	47	65	53	28	48	49	19
9	74	67	44	52	74	69	16	52	56	29
10	161	155	140	148	162	154	139	147	151	11

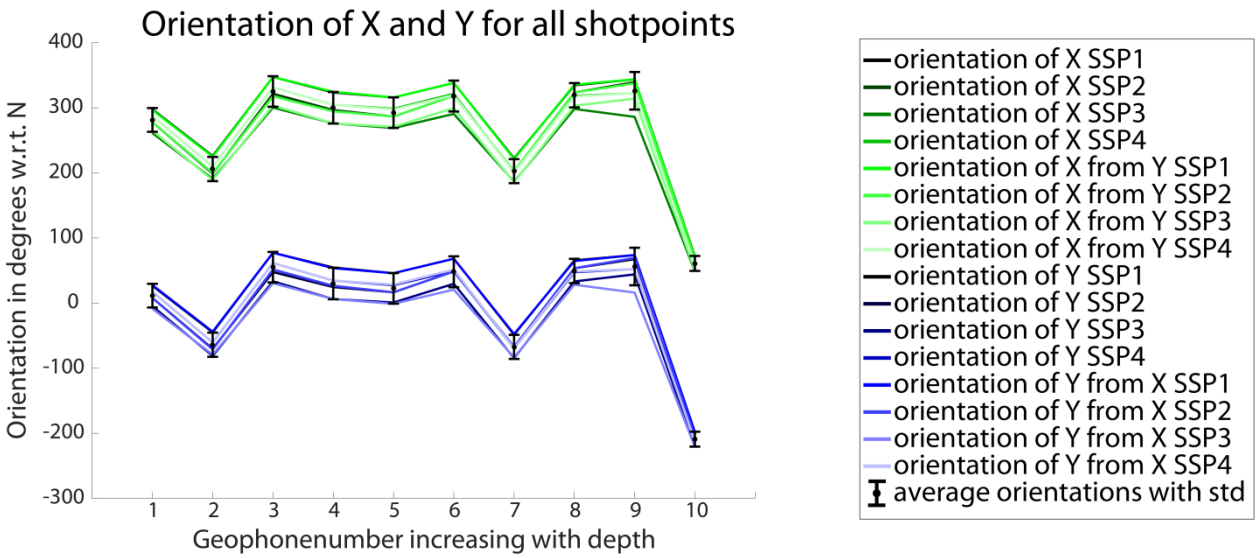

Figure 6: Azimuth of X and Y, calculated from R and T, respectively, and from Y and X, respectively, average orientations are indicated with black dots and the standard deviation with error bars.

Although the assumption is made that the geophones have no inclination in order to make calculation of the azimuth of X and Y easier, in reality the geophones do have an inclination. The inclination and azimuth of the vertical Z-axes of the geophones depends on the local inclination of the borehole itself and is calculated using the locations of the geophones. The geophones are connected by the borehole and the orientation of the vertical component of the geophones can be assumed to be parallel to the tangent to the curve of the borehole at the location of the geophones.

This can be approximated in the following way, see Figure 7. If one geophone is located in the origin of the coordinate system and the geophone above is located at (x,y,z), where x is the horizontal distance in the x-direction, for example North, between the two geophones, y is the horizontal distance in the y-direction, for example East between the two geophones, z is the vertical distance between the two geophones, and r is the distance between the two geophones, then the angle θ will be the inclination of the geophone at the origin and the angle ϕ can be used to determine the azimuth of the geophone at the origin. The equations used for this calculation are:

$$r = \sqrt{(x)^2 + (y)^2 + (z)^2}$$

$$x = r \sin\theta \sin\varphi$$

$$y = r \sin\theta \cos\varphi$$

$$z = r \cos\theta$$

This method allows calculating the inclinations and azimuths of the lower 9 geophones, the upper one has to be estimated by extrapolation of the inclination, and by assuming the azimuth is equal to the one of the first geophone below it. The calculated inclinations and azimuths of the vertical Z-axes are shown in Table 4. For each geophone only one calculation of the inclination and azimuth is done, so there is no average or standard deviation. To satisfy the fact that a left-handed coordinate system is used, the Z-components should be positive up. The inclination is therefore calculated on a scale from 0 to 180 degrees, with 0 degrees representing an inclination vertically up and 180 degrees representing an inclination vertically down.

Table 4: Azimuth and inclination of Z.

GP	Calculated inclination (θ)	Calculated azimuth (ϕ)
1	15.6	114.4
2	14.0	114.4
3	12.4	117.8
4	10.5	104.8
5	9.2	105.8
6	8.5	96.5
7	7.7	103.0
8	6.9	104.4
9	6.4	105.7
10	5.8	105.4

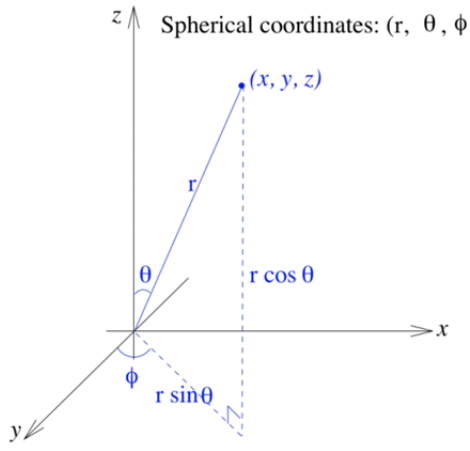

Figure 7: Calculating the inclination and azimuth of geophones in spherical coordinates (r, u, f) from the horizontal and vertical distances between the geophones (x,y,z).

Evaluation of the calculated orientations

When relating the calculated orientations to the raw data (see Appendix 1), it can be concluded that the calculated orientations are probably correct. This conclusion follows from the expected form of the first arriving peaks (positive/negative, large/small) and comparing this with the observed first peaks in the raw data, taking into account that the first arriving peak is always a P-wave with first motion away from the source. The first peaks of the raw data are enlarged in Appendix 3. In the case that one of the horizontal components of a geophone points exactly in the opposite direction of one of the check shot locations, so aligned with the R-axis, we expect to see a large positive peak in the raw data on that component of the geophone for that particular check shot. In the case that one of the horizontal axes of a geophone points exactly towards one of the check shot locations, so in opposite direction of the R-axis, we expect to see a large negative peak in the raw data on that component of the geophone for that particular check shot. The larger the angle between the horizontal component of a geophone with the R-axis or negative R-axis, the smaller the amplitude of the first arrival is expected to be, and in the case that one of the horizontal components of a geophone is aligned with a T-axis or negative T-axis of one of the check shot locations, there is expected to be no peak in the raw data on that component for that particular check shot. On horizontal components that are oriented between the positive R-axis and either the positive or the negative T-axis of one of the check shot locations, we expect to see a positive first arrival in the raw data for that particular check shot, and on horizontal components that are oriented between the negative R-axis and either the positive or the negative T-axis of one of the check shot locations, we expect to see a negative first arrival in the raw data for that particular check shot.

All forms of the peaks (positive/negative, large/small) of the first arrivals of the raw data on the horizontal components meet the expectations based on the calculated orientations of the X- and Y-components. Concerning the vertical orientations, we see a negative first arrival on all vertical components of the raw data, which agrees with a positive upwards Z-component. The calculated inclinations of the Z-axes are decreasing with depth, which indicates that the borehole gets more vertical with depth. The calculated azimuths of the Z-axes are around ~110 degrees, so to the ESE. Since it is known that the geophones have horizontal coordinates more towards the WNW with depth, this ESE azimuth also agrees with a positive up Z-axis.

The NAM has also calculated the orientations of the three components of the geophones in a slightly different way. Instead of only the first peak of the arriving waves they used the direction of the particle motion of the first arriving waves both away from the source and back to the starting position and then towards the source and back to the starting position again, so at least one full wave or more. This measurement is over a larger time window, which makes it probably less accurate, because the particle motion directly after the first onset can already be disturbed by P-S converted waves or scattered waves, which can influence the measurements. Therefore the standard deviation of the NAM results will be larger than the standard deviation of our calculations.

The NAM results are shown in Table 5 together with our calculated results. The check shots that were used for our calculations were fired on 27-11-2013, so the results should be compared to the results of NAM from MAG140435 that are valid for the operational period from 12-10-2013 to 23-12-2013.

As can be seen in Table 5, the calculated results for the X-components of the geophones are very similar to the results from the NAM. The absolute difference is smaller than the standard deviation of the calculated results for all geophones, except for geophone 1, where the absolute difference is only two degrees larger than the standard deviation, indicated with a red cell color in Table 5.

For the Y-components of the geophones, there is an absolute difference between ~160 and ~200 degrees. This means that the orientations calculated by the NAM are more or less in the opposite direction, because they switched to a right-handed coordinate system by changing the sign of the Y-component. However, as stated before, the calculated results of this study are probably correct, based on the comparison between the expected and observed waveforms. A switch of 180 degrees in the Y orientation will cause expected waveforms that are positive instead of negative or vice versa on (at least one of) the components. Therefore the results of NAM for the Y components are incorrect if not corrected for a switch of the Y-component. For the next part of this research, the calculated results of this study will be used.

Table 5: Calculated azimuth of the X-components and Y-components for all geophones compared to the azimuth of the X-components and Y-components calculated by NAM, with absolute difference and standard deviation.

GP	Calc. X	Std.	NAM X	Abs. diff.	Calc. Y	Std.	NAM Y	Abs. diff.
1	281	18	301	20	11	18	210	199
2	206	19	222	16	296	19	133	163
3	325	23	344	19	55	23	252	197
4	300	24	318	18	30	24	227	197
5	293	24	309	16	23	24	219	196
6	318	24	332	14	48	24	242	194
7	203	18	216	13	293	18	126	166
8	319	19	334	15	49	19	244	195
9	326	29	342	16	56	29	252	196
10	61	11	70	9	151	11	341	190

Table 6: Calculated azimuth and inclination of the Z-components for all geophones compared to the azimuth and inclination of the Z-components calculated by NAM, with absolute difference.

GP	Azimuth			Inclination		
	Calc. Z-azi	NAM Z-azi	Abs. diff.	Calc. Z-incl	NAM Z-incl	Abs. diff.
1	114.4	295.5	181.1/1.1	15.6	15.7	0.1
2	114.4	294.8	180.4/0.4	14.0	13.8	0.2
3	117.8	294.8	177.0/3.0	12.4	12.0	0.4
4	104.8	286.5	181.7/1.7	10.5	10.7	0.2
5	105.8	285.5	179.7/0.3	9.2	9.0	0.2
6	96.5	276.9	180.4/0.4	8.5	8.4	0.1
7	103.0	282.4	179.4/0.6	7.7	7.6	0.1
8	104.4	285.0	180.6/0.6	6.9	6.8	0.1
9	105.7	285.5	179.8/0.2	6.4	6.4	0
10	105.4	285.5	180.1/0.1	5.8	5.7	0.1

Concerning the vertical orientations, the calculated results are also in the opposite direction of the orientations calculated by NAM, see Table 6. This is caused by their switch to a right-handed coordinate system, resulting in a 180 degrees difference in both their calculation of the Y-components and their calculation of the Z-components. When changing the NAM results into a positive up orientation, the calculated results don't differ much from the results calculated by the NAM. For the rotation of the data, the vertical orientations are ignored.

Rotating the data

Now that the orientations of the geophone components are known, the check shot data can be rotated to the orientations of the radial and vertical axes of the corresponding check shot locations. With this rotation it is assumed that the X- and Y-components are perfectly horizontal, otherwise the calculation will become very complex. The radial axis is ϕ degrees clockwise from X and the transversal axis is ϕ degrees clockwise from Y. The angle ϕ is calculated as the difference between the calculated orientation of X and the orientation of the R-axis, and as the difference between the calculated orientation of Y and the orientation of the T-axis, which gives the same result, see Table 7. When rotating the raw data to the radial and transversal axes, the recordings on the R-axis are calculated by rotating the raw data on the X-component by ϕ degrees, and the recordings on the T-axis are calculated by rotating the raw data on the Y-component by the same angle ϕ, so that the orientation of the T-axis is exactly 90 degrees clockwise from the R-axis, using the following equations:

$$R = X \cos\varphi + Y \sin\varphi$$

$$T = Y \cos\varphi - X \sin\varphi$$

Table 7: Angle ϕ between the orientation of the R-axis and the orientation of the X-component of the geophones for each check shot and all geophones.

GP	Calc. X	Calc. Y	SSP1			SSP2			SSP3			SSP4		
			R	T	ϕ	R	T	ϕ	R	T	ϕ	R	T	ϕ
1	281	11	261	351	340	355	85	74	47	137	126	160	250	239
2	206	296	261	351	55	355	85	149	47	137	201	160	250	314
3	325	55	261	351	296	355	85	30	46	136	81	161	251	196
4	300	30	262	352	322	355	85	55	46	136	106	161	251	221
5	293	23	262	352	329	355	85	62	46	136	113	161	251	228
6	318	48	262	352	304	355	85	37	46	136	88	160	250	202
7	203	293	262	352	59	355	85	152	45	135	202	160	250	317
8	319	49	263	353	304	354	84	35	45	135	86	160	250	201
9	326	56	263	353	297	354	84	28	45	135	79	160	250	194
10	61	151	263	353	202	354	84	293	45	135	344	160	250	99

This is done for each geophone and for each check shot. The vertical components do not need to be rotated. Now that the raw data is rotated, all recordings of all geophones are aligned perfectly above each other, the orientation of which depending on the check shot location. This rotated data can now be used for the analysis of the RZ-decon of the data, as explained in the section RZ-decon.

Preparation of the synthetic data

For creating the synthetic data the method "Specfem2D" is used, to simulate the check shots and produce synthetic seismograms at the same distance and depths between the real check shot locations and the borehole SDM-1. The input models are the P-wave and S-wave velocity model and density model from well log data provided by NAM. This velocity model has to be smoothed before it can be used in the Specfem2D model.

Specfem2D

Specfem2D (Komatitsch & Tromp, 1999) is a numerical method to calculate wave propagation and synthetic seismograms in 2 dimensions, making use of the spectral-element method. The spectral-element method is explained in more detail in Appendix 4, following the steps from Computational Seismology (Igel, Computational Seismology: A practical introduction, 2016).

The spectral-element method is a method to create a numerical solution for partial differential equations. The solution is obtained by a series expansion, where the continuous solution field is replaced by a finite sum over basis functions. To make computation possible, the continuous solution has to be broken up into a finite number of elements with a finite size and in each element the exact solution is approximated by a finite number of basis functions. For this approximation, the weak form of the elastic wave equation is used, in 1D:

$$\int_D v\rho \frac{\partial^2 u}{\partial t^2} dx + \int_D \mu \frac{\partial v}{\partial x}\frac{\partial u}{\partial x} dx = \int_D v f dx$$

u = displacement, depends on x and t

f = external force, depends on x and t

ρ = mass density, depends on x

μ = shear modulus, depends on x

v = time-independent test function

D = domain going from x = 0 to x = L

For the time-independent test functions a series of Lagrange polynomials, with mutual orthogonality, is chosen for the approximation of the exact solution. The solution equation for the spectral-element system at the element level is obtained, in matrix notation:

$$\sum_{i=1}^{N+1} M_{ji}^e \frac{\partial^2 u_i^e(t)}{\partial t^2} + \sum_{i=1}^{N+1} K_{ji}^e u_i^e(t) = f_j^e(t), \quad e = 1, \dots, n_e$$

u^e = coefficients of the unknown displacement inside the element

M^e = elemental mass matrix

K^e = elemental stiffness matrix

f^e = elemental vector containing the volumetric forces

n^e = number of elements

The global matrices and vectors, indicated with a subscript g, are obtained by combining the elemental matrices, which are overlapping and summed at the element boundaries. The time-dependent coefficients of the displacement in the global system u_g are extrapolated with a simple centred finite-difference scheme to the next time step $t + dt$:

$$u_g(t + dt) = dt^2\left[M_g^{-1}(f_g(t) - K_g u_g(t))\right] + 2u_g(t) - u_g(t - dt)$$

This way, the global displacement field is calculated for each time step. In Specfem2D, also the velocity field or the acceleration field can be chosen to calculate. These are simply obtained by the derivative and second derivative of the displacement field. For this study, the velocity field is calculated by Specfem2D, because the data of the geophones is also a measurement of the velocity. Specfem2D calculates the displacement field in 2D, making use of the 2D elastic wave equation. This causes u and f in de wave equation to become vectors, rather than scalars.

Input velocity and density model

The input of Specfem2D consists of the following components: a file describing the source, a file describing the velocity and density model, a file describing the regions of the velocity and density model, a file describing the interfaces between the regions of the velocity and density model, and a parameter file where everything comes together and where the receiver(s) and other parameters are defined. In Appendix 5 all the input parameters in these files for the simulation of the check shot data for this study are described and defined.

The P-wave velocity (V_p) model is obtained from well log data provided by NAM (Romijn, 2017), see Figure 8. The S-wave velocity (V_s) model and density (ρ) model are obtained from formulas that describe the ratio between P- and S-wave velocities and the relations between P-wave velocity, density and depth, also provided by NAM (Romijn, 2017). For each lithological layer, these formulas are given below. For some formulas the slowness in µs/ft is used, which is defined by:

$$slowness\ [s/m] = \frac{1}{V_p\ [ft/\mu s]/3.2808399 \cdot 10^{-6}}$$

where $3.2808399 \cdot 10^{-6}$ = conversion factor from in m/s to µs/ft

0 - 30 m:

The P-wave velocity is measured from a depth of 30.0083 meters downward, so the upper 30 meters are assumed to have a constant P-wave velocity that is equal to the first measurement at 30.0083 m depth.

$$V_s = \frac{V_p}{4.782 - 0.0047 \cdot depth}$$

$\rho = 2.04\ g/cm^3$

North Sea Up (30 - 343.28 m):

$$V_s = \frac{V_p}{4.782 - 0.0047 \cdot depth}$$

$\rho = 2.04\ g/cm^3$

North Sea Down (343.28 - 843.26 m):

$V_s = \frac{V_p}{\lambda}, \quad \lambda = 3.02$

$\rho = 2.04\ g/cm^3$

Chalk Formation (843.26 - 1727.23 m):

$V_s = 0.6045 \cdot V_p - 415.6$

$\rho = -0.01076 \cdot slowness + 3.305$

Rijnland/Jurassic/Triassic (1727.23 - 1871.16 m):

$V_s = 0.7423 \cdot V_p - 745.003$

$\rho = -0.01 \cdot slowness + 3.3$

Zechstein (1871.16 - 2768.88 m):

$V_s = 0.50092 \cdot V_p + 282.23$

$\rho = -0.04068 \cdot slowness + 4.912, \quad for\ V_p < 5000\ m/s$ (rocksalt)

$\rho = 2.81\ g/cm^3, \quad for\ V_p > 5000\ m/s$ (anhydrite)

Reservoir clay/sand (2768.88 - 3040.38 m):

$V_s = 0.5364 \cdot V_p + 193.96$

$\rho = -0.01109 \cdot slowness + 3.324$

Carboniferous underburden (3040.38 - 6065 m):

$V_p = 0.514 \cdot depth + 2572.3$

$V_s = 0.927 \cdot V_p - 1547.313$

$\rho = 2.61\ g/cm^3$

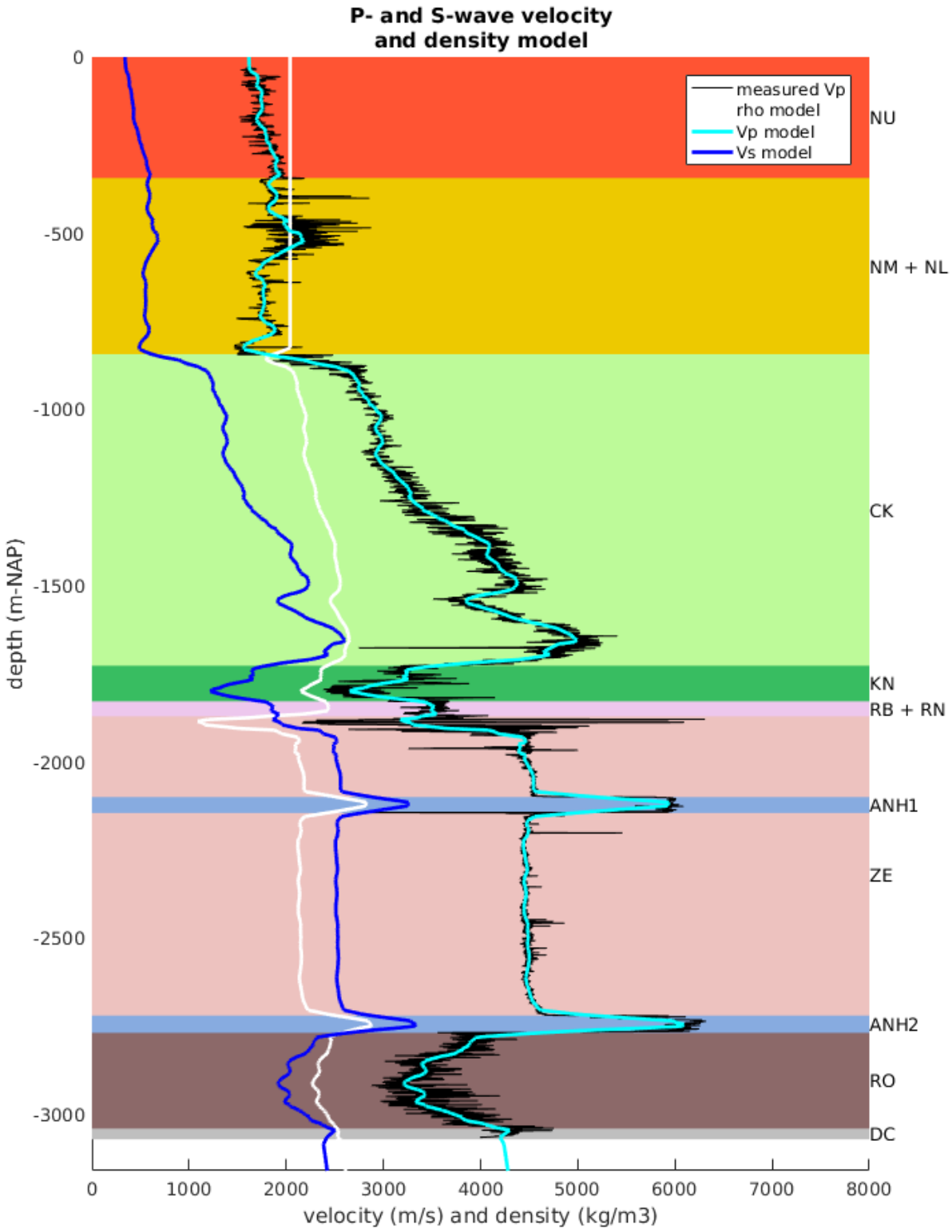

Figure 8: Smoothed P- and S-wave velocity and density model (cyan, blue and white lines, respectively), calculated from well log data for Vp (black line), plotted on top of the lithostratigraphic column retrieved from Dinoloket (TNO, 2017).

Additional homogeneous layer for PML absorbing (6065 - 6210 m):

V_p, V_s and ρ are equal to the last value of the Carboniferous underburden, throughout the PML (Perfectly Matching Layer).

The P-wave and S-wave velocity models and density model are smoothed with moving harmonic averaging. The blocks of the model are 5 meters wide and 5 meters thick for a depth of 0 to 2775 m, 2.5 meters for a depth of 2775 to 3040 m, and 20 meters for a depth of 3045 to 6205 m. This amount of smoothing is still accurate enough, based on the guideline that the blocks of the model should be maximum one quarter of the wavelength of the wave traveling through the model.

The dominant frequency (f_0) of the source is set to 15.0 Hz, which is similar to the frequency content of the real data of the check shots. The dominant period (T_0) of the source is then:

$$T_0 = \frac{1}{f_0} = \frac{1}{15.0\ Hz} = 0.0667\ s$$

The wavelength of the wave depends on the period and the propagation velocity, which varies with depth. The wave will have the smallest wavelength where the velocity is minimum, so at the top of the model. The lowest S-wave velocity in the model is equal to 338.1 m/s.

$$\lambda = V_{s,min} \cdot T_0 = 338.1\ m/s\ \cdot 0.0667\ s = 22.5\ m$$

The blocks of the model should therefore be maximum one quarter of this wavelength, so 5.64 meters thick. Both 5.0 m and 2.5 m thickness of the blocks of the model are fine.

For the lower part of the model, the minimum S-wave velocity is at a depth of 3085 m equal to 2383 m/s. Below this depth, the wavelength of the wave traveling through the model is minimum:

$$\lambda = V_{s,min} \cdot T_0 = 2383\ m/s\ \cdot 0.0667\ s = 159\ m$$

The blocks of the model should therefore be maximum one quarter of this wavelength, so 39.7 meters thick. So a thickness of 20.0 meters for the model below this depth is fine.

Output of Specfem2D

The output of Specfem2d consists of the following components: snapshots of the wave propagation through the model, a file containing the recordings in the radial (x) direction for all receivers on all receiver strings, a file containing the recordings in the vertical (z) direction for all receivers on all receiver strings, a plot of the source time function and a histogram of the points per wavelength.

In the snapshots of the model, see Figure 9, the velocity model is shown in shades of grey, where higher velocities are darker and lower velocities are lighter. The source is located just beneath the surface and the receiver strings are the green vertical bars. The propagation of the energy from the source is shown as the red area that gets bigger with time and the front moves further away from the source with time. The synthetic seismograms are included in Appendix 6.

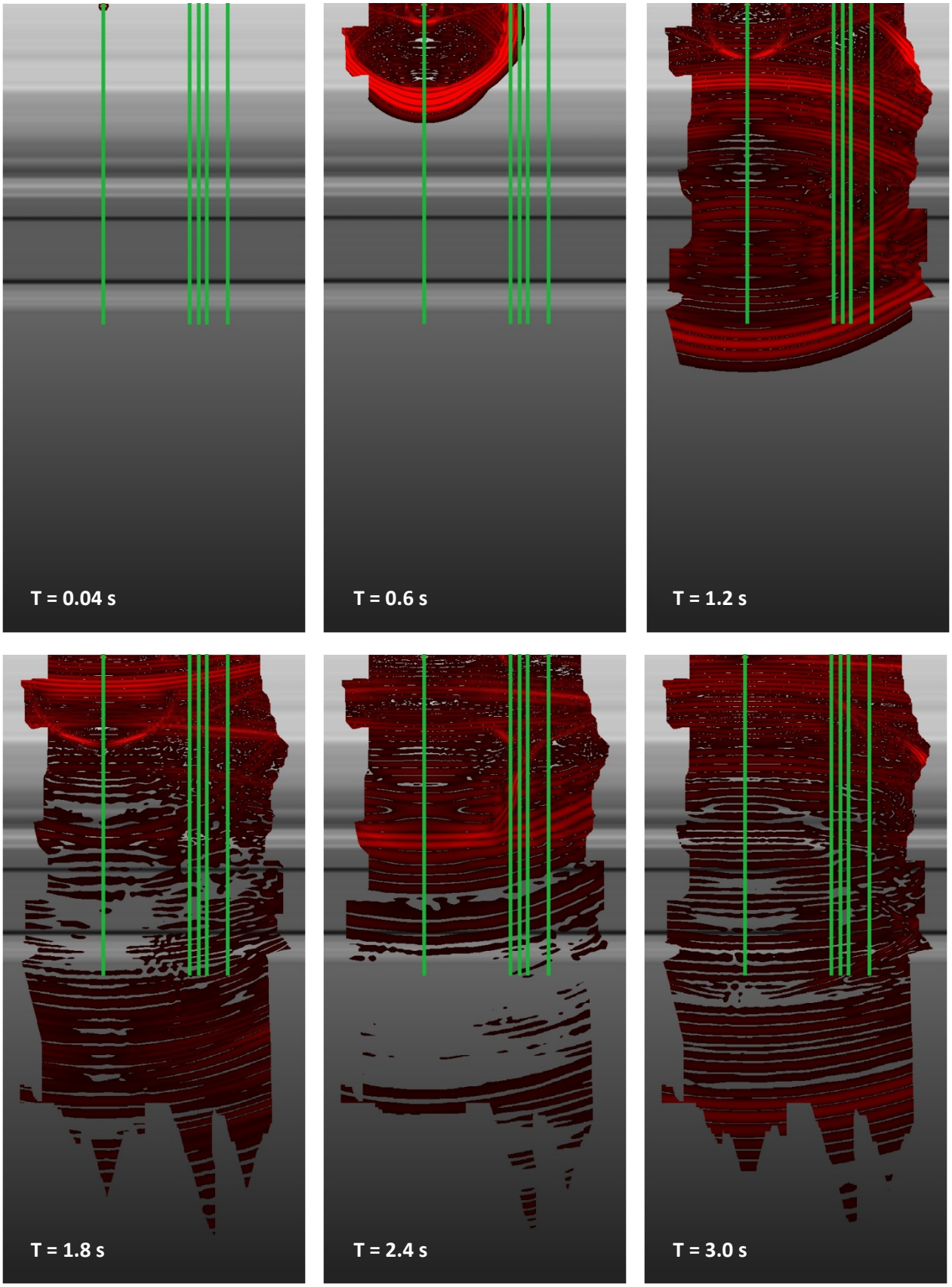

Figure 9: Snapshots of wave propagation (red) through the model (grey shades), green lines are receiver strings.

RZ-decon

Now that the recorded data on the three components of all 10 geophones are rotated in such a way that they are all aligned per check shot, and synthetic data is generated with Specfem2D, both the real data and the synthetic data can be analyzed with the radial to vertical deconvolution method, used in this study. This method is similar to the calculation of receiver functions (Owens, Zandt, & Taylor, 1981) or H/V (horizontal to vertical spectral ratios) (Theodulidis, Bard, Archuleta, & Bouchon, 1996).

Receiver functions are time series, computed from three-component seismograms, which show the relative response of Earth structure near the receiver. A direct P-wave (P) is recorded at the receiver at time t_P. At a certain interface at depth d, a P-wave can be converted into an S-wave (Ps), which is recorded at the receiver later than the direct P-wave at time t_{Ps}, since it traveled part of the path (through medium 2) with a lower velocity, see Figure 10. The time difference between these two arrivals depends on the P- and S-wave velocity structure (V_P and V_S) and the depth of the interface (d). For semi-vertical incidence, such as this case, this can be approached by the simple equation for the time difference for vertical incidence:

$$t_{Ps} - t_P = d\left(\frac{1}{V_S} - \frac{1}{V_P}\right)$$

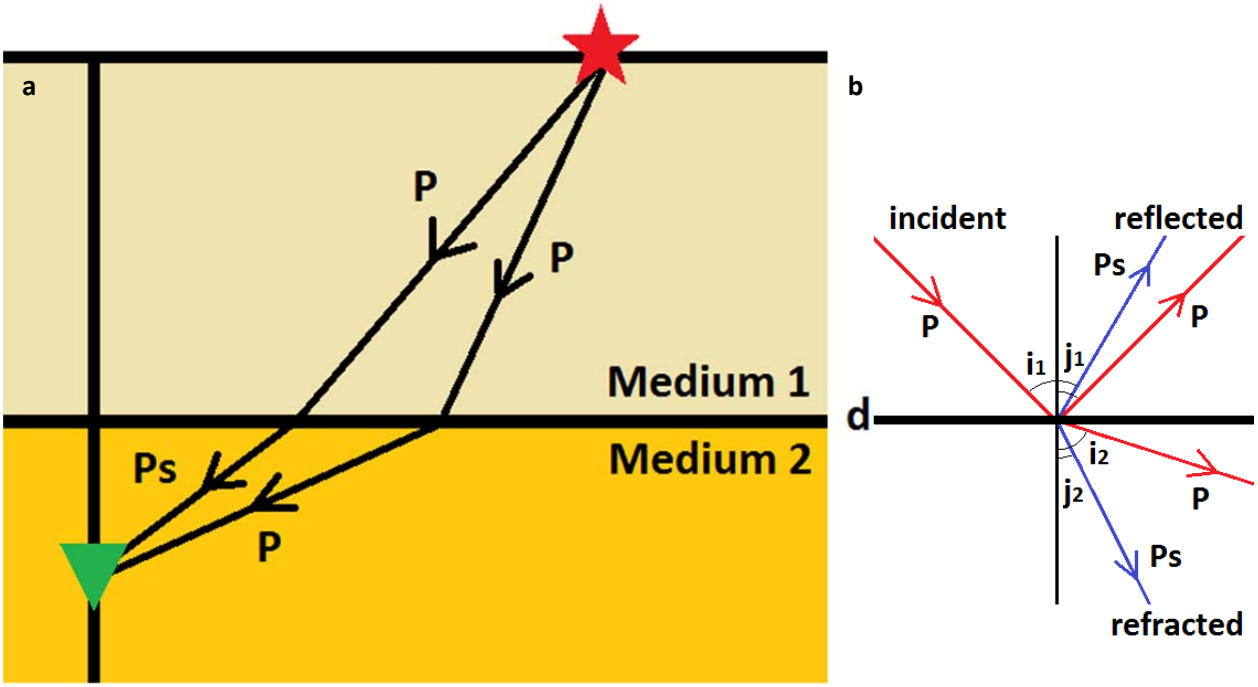

Figure 10: a) Refraction of a P-wave and conversion of a P-wave to an S-wave at an interface at depth d, with higher velocities in medium 2 than in medium 1 in this case. The red star is the source and the green inverted triangle is a receiver on a string. b) Angles of incidence, reflection and refraction of P to S conversion.

The time difference between the direct P-wave and the P to S converted wave can be obtained from the receiver function and knowing the V_P and V_S, the depth d of the interface can be calculated. In this study the name receiver function is not very accurate, because we are not looking at the Earth structure close to the receiver, but at the Earth structure up to 3 km above the receivers (since the receivers are placed

inside the gas reservoir). Therefore, instead of the word receiver function the word RZ-decon (Radial component over Vertical component deconvolution) is used to describe it.

The measured data on the vertical component ($Z(t)$) and on the radial component ($R(t)$) at the geophones is influenced by the source time function ($S(t)$) and the effect of Earth structure ($E(t)$), which is an impulse response from source to receiver. This is in the time domain described by:

$$Z(t) = S(t) * E_Z(t)$$

$$R(t) = S(t) * E_R(t)$$

$$* means\ convolution$$

After a Fourier transform, this becomes in the frequency domain:

$$Z(\omega) = S(\omega)E_Z(\omega)$$

$$R(\omega) = S(\omega)E_R(\omega)$$

The RZ-decon in the frequency domain is then obtained by:

$$RZ(\omega) = \frac{R(\omega)}{Z(\omega)} = \frac{S(\omega)E_R(\omega)}{S(\omega)E_Z(\omega)} = \frac{E_R(\omega)}{E_Z(\omega)}$$

This eliminates the effect of the source time function, so it makes no difference in the calculation of the RZ-decon if we use the check shot data or data from different sources, such as train noise. If the value for $Z(\omega)$ at a certain frequency is close to zero, the deconvolution will become unstable and will give very wiggly RZ-decon. Therefore a "water level" (WL) is set at a certain percentage of the maximum autocorrelation $Z(\omega)Z^*(\omega)$, where $Z^*(\omega)$ is the complex conjugate of $Z(\omega)$:

$$RZ(\omega) = \frac{R(\omega)Z^*(\omega)}{Z(\omega)Z^*(\omega)} \approx \frac{R(\omega)Z^*(\omega)}{max\ of\ \left[Z(\omega)Z^*(\omega) or\ WL \cdot \max\left(Z(\omega)Z^*(\omega)\right)\right]}$$

Applying an inverse Fourier transform to $RZ(\omega)$ gives the RZ-decon in the time domain $RZ(t)$. Because the P-waves generated by the check shots are measured mainly on the vertical component and the P to Sv converted waves are measured mainly on the radial component with a delay time due to the difference in propagation velocity, the RZ-decon in the time domain will show the P to S conversions clearly in the form of peaks at these delay times.

For the synthetic data a water level of 0.5% (0.005) is used, but due to differences in data quality from the real check shot data, different water levels are chosen for the different check shots. For the data from check shots SSP2 and SSP3 a water level of 0.5% is also sufficient, but for SSP1 and SSP4 a higher water level of 5% and 10%, respectively, had to be used.

Results and interpretation

The RZ-decon of the synthetic data for four check shots and all synthetic geophones are included in Appendix 7. The RZ-decon of the synthetic data for four check shots but only the synthetic geophones that are located at the depths of the real geophones in borehole SDM-01 are included in Appendix 8, both for a time window of 1 second and for a time window of 2 seconds. The RZ-decon of the real data for four check shots are included in Appendix 9, both for a time window of 1 second and for a time window of 2 seconds.

Meaning of peaks and lines in the RZ-decon

A peak in the RZ-decon means there has been a P-SV conversion at an interface at a certain distance above the receiver. The x-axis shows the time difference between arrival of the P-wave and arrival of the converted SV-wave. The longer the time difference is, the further away the interface is located above the receiver. A certain interface above geophone 1 will become visible on all 10 geophones, but at a little longer time difference for the deeper geophones, for the P and converted P-SV waves have traveled a little further from interface to receiver. These peaks can be connected by a slightly sloping line, representing this interface.

The steepness of these lines depends on the difference between P-wave velocity and S-wave velocity and the magnitude of both velocities. A smaller velocity difference results in a steeper line, but also higher velocities result in a steeper line. Whenever the velocities are more or less constant within a lithological layer, the line will be straight, but with increasing or decreasing velocities, the line will be curved. This follows from the equation for the delay time, which can be rewritten as:

$$t_{Ps} - t_P = d\left(\frac{1}{V_S} - \frac{1}{V_P}\right) = d\left(\frac{V_P - V_S}{V_P V_S}\right)$$

The first motion of the downwards traveling direct P-waves generated by the check shots arriving at the geophones is always downward and away from the source. Because of the left handed system (R,T,Z) with Z positive up, this results in a negative peak on the Z-axis, and a positive peak on the R-axis. Therefore the deconvolution gives a negative first peak on all geophones, which is visible in the RZ-decon figures in Appendix 7, 8 and 9 as a red peak at a delay time of zero seconds. The other peaks in the RZ-decon might be either positive (black) or negative (red), depending on the velocity and density contrast at the interfaces causing the peaks.

Conversion coefficient

Whether a peak in the RZ-decon is positive or negative depends on the conversion coefficient at the interface that gives rise to that specific peak in the RZ-decon. The conversion coefficient depends on the product of the density and velocity for each medium, a quantity called the acoustic impedance (Stein & Wysession, 2003). Usually the strongest reflections and therefore also conversions occur where the acoustic impedance changes significantly, and an increase of this property usually results in a negative conversion coefficient and a decrease in a positive conversion coefficient. The equations to calculate the coefficient for P down to SV down conversions ($\grave{P}\grave{S}$) are very complex and are obtained from Quantitative Seismology (Aki & Richards, 2002):

$$\dot{P}\dot{S} = 2\rho_1 \frac{\cos i_1}{\alpha_1} \frac{Hp\alpha_1}{\beta_2 D}$$

$$D = EF + GHp^2$$

$$E = b\frac{\cos i_1}{\alpha_1} + c\frac{\cos i_2}{\alpha_2}$$

$$F = b\frac{\cos j_1}{\beta_1} + c\frac{\cos j_2}{\beta_2}$$

$$G = a - d\frac{\cos i_1}{\alpha_1}\frac{\cos j_2}{\beta_2}$$

$$H = a - d\frac{\cos i_2}{\alpha_2}\frac{\cos j_1}{\beta_1}$$

$$a = \rho_2(1 - 2\beta_2^2 p^2) - \rho_1(1 - 2\beta_1^2 p^2)$$

$$b = \rho_2(1 - 2\beta_2^2 p^2) + 2\rho_1\beta_1^2 p^2$$

$$c = \rho_1(1 - 2\beta_1^2 p^2) + 2\rho_2\beta_2^2 p^2$$

$$d = 2(\rho_2\beta_2^2 - \rho_1\beta_1^2)$$

$$\cos i_1 = \sqrt{1 - \alpha_1^2 p^2}$$

$$\cos i_2 = \sqrt{1 - \alpha_2^2 p^2}$$

$$\cos j_1 = \sqrt{1 - \beta_1^2 p^2}$$

$$\cos j_2 = \sqrt{1 - \beta_2^2 p^2}$$

$$p = slowness = \frac{\sin i_1}{\alpha_1} = \frac{\sin i_2}{\alpha_2} = constant$$

α_1 = P-wave velocity of upper layer

α_2 = P-wave velocity of lower layer

β_1 = S-wave velocity of upper layer

β_2 = S-wave velocity of lower layer

ρ_1 = density of upper layer

ρ_2 = density of lower layer

i_1 = angle of incidence of P-wave

i_2 = angle of refraction of P-wave

j_1 = angle of reflection of S-wave

j_2 = angle of refraction of S-wave

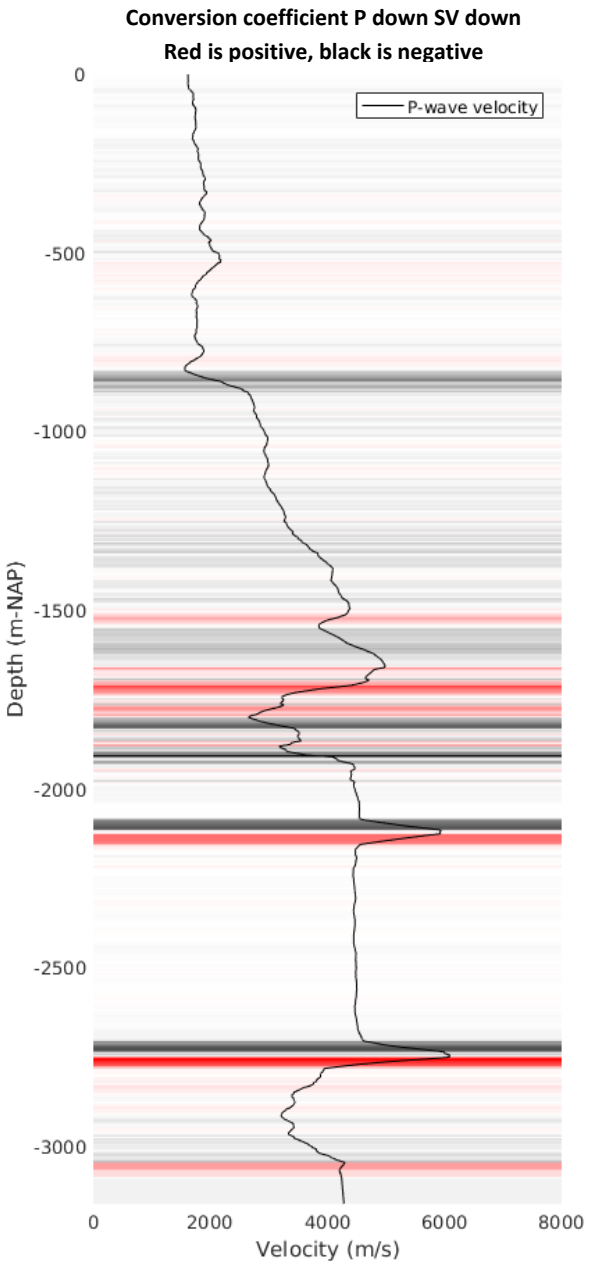

Figure 11: Calculated conversion coefficient as a function of depth, red is positive, black is negative, and the brightness of the color indicates how strong the conversion coefficient is.

The waves travel more horizontally, so with a larger angle of incidence, through layers with higher velocities, and more vertically, so with a smaller angle of incidence, through layers with lower velocities. The waves will have the largest angle of incidence where the P-wave velocity is maximum. If the angle of incidence is 0°, the slowness is equal to zero and therefore no conversion from P to SV waves occurs. If the angle of incidence is 90°, the wave will keep travelling horizontally and will not go down to reach the lower receivers. This means that the angle of incidence should always be larger than 0° and smaller than 90°. This is achieved by taking a value for the slowness p that is somewhere between 0 and the sine of the maximum angle i_{max} (90°) divided by the maximum P-wave velocity $V_{p,max}$ (~7000 m/s). For larger values of p, the conversion coefficient will have a complex component.

$$\sin i_{max} = \sin 90° = 1$$

$$V_{P,max} = 6091\ m/s$$

$$0 < p < \frac{\sin i_{max}}{V_{P,max}} = \frac{1}{6091}\ s/m$$

For the calculation of the $\grave{P}\grave{S}$ conversion coefficient, the slowness should be between 0 and 1/6091 s/m, so a value of 1/7000 s/m is used. At each interface of the velocity model that is used in Specfem2D, the $\grave{P}\grave{S}$ conversion coefficient is calculated using the above equations. The conversion coefficient as a function of depth is visualized in Figure 11, where shades of red indicate a positive conversion coefficient and shades of black indicate a negative conversion coefficient. The brightness of the color indicates how strong the conversion coefficient is. What stands out is that the conversion coefficient is strongest at sharp velocity changes and that the conversion coefficient is positive for a velocity decrease and negative for a velocity increase.

The sign of the conversion coefficient at an interface determines the sign of a peak in the RZ-decon caused by this interface. Whenever the down going P-wave gives a positive peak on the vertical component of the geophones and the conversion coefficient of an interface is negative, the converted SV-wave will give a negative peak on the horizontal component of the geophones. Since the down going P-wave in this case always gives a negative peak on the vertical component of the geophones, an interface with a positive conversion coefficient always gives rise to a negative peak in the RZ-decon and an interface with a negative conversion coefficient always gives rise to a positive peak in the RZ-decon.

For the interpretation of the RZ-decon of the full synthetic data set, the conversion coefficient as a function of depth, together with the velocity and density model, and lithostratigraphy, is plotted next to the RZ-decon, see Figure 12. The colors of the conversion coefficient (red positive, black negative) correspond to the colors of the peaks in the RZ-decon (red negative, black positive).

Some of the clear lines connecting the peaks are labeled with letters and/or colors which are referred to in the text. These lines in the RZ-decon can be traced upward to see at what depth the peak has 0 seconds delay time. This depth is the depth of the interface that causes the P-SV conversion. The same labels are added to the synthetic RZ-decon for only the 10 geophones at the depths of the real geophones, see Figure 13. In the next section, these labeled peaks in both figures will be interpreted.

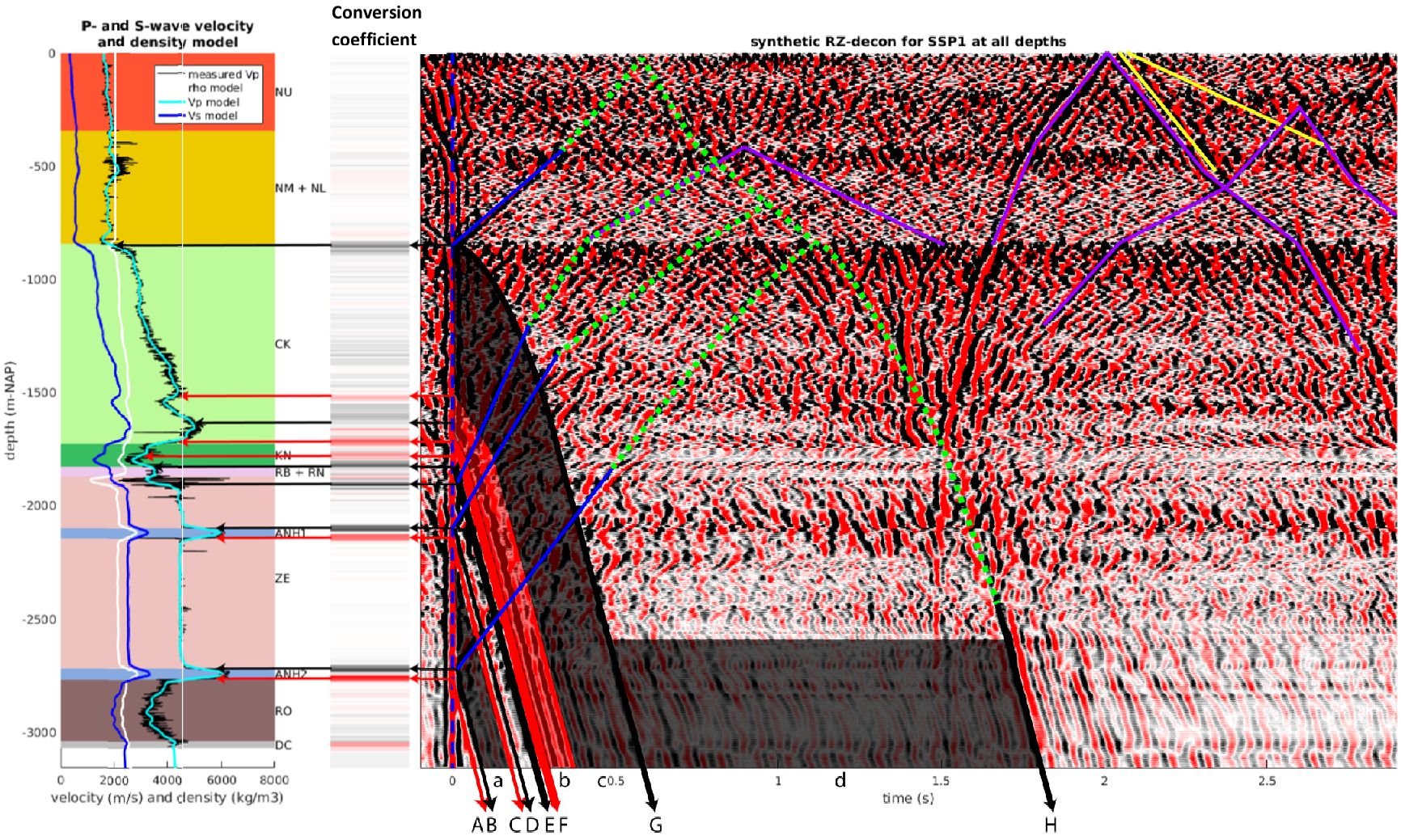

Figure 12: RZ-decon of synthetic data for all geophones, together with lithostratigraphic column, velocity and density models and conversion coefficient. Black and red arrows indicate prominent P to SV conversions labeled with letters.

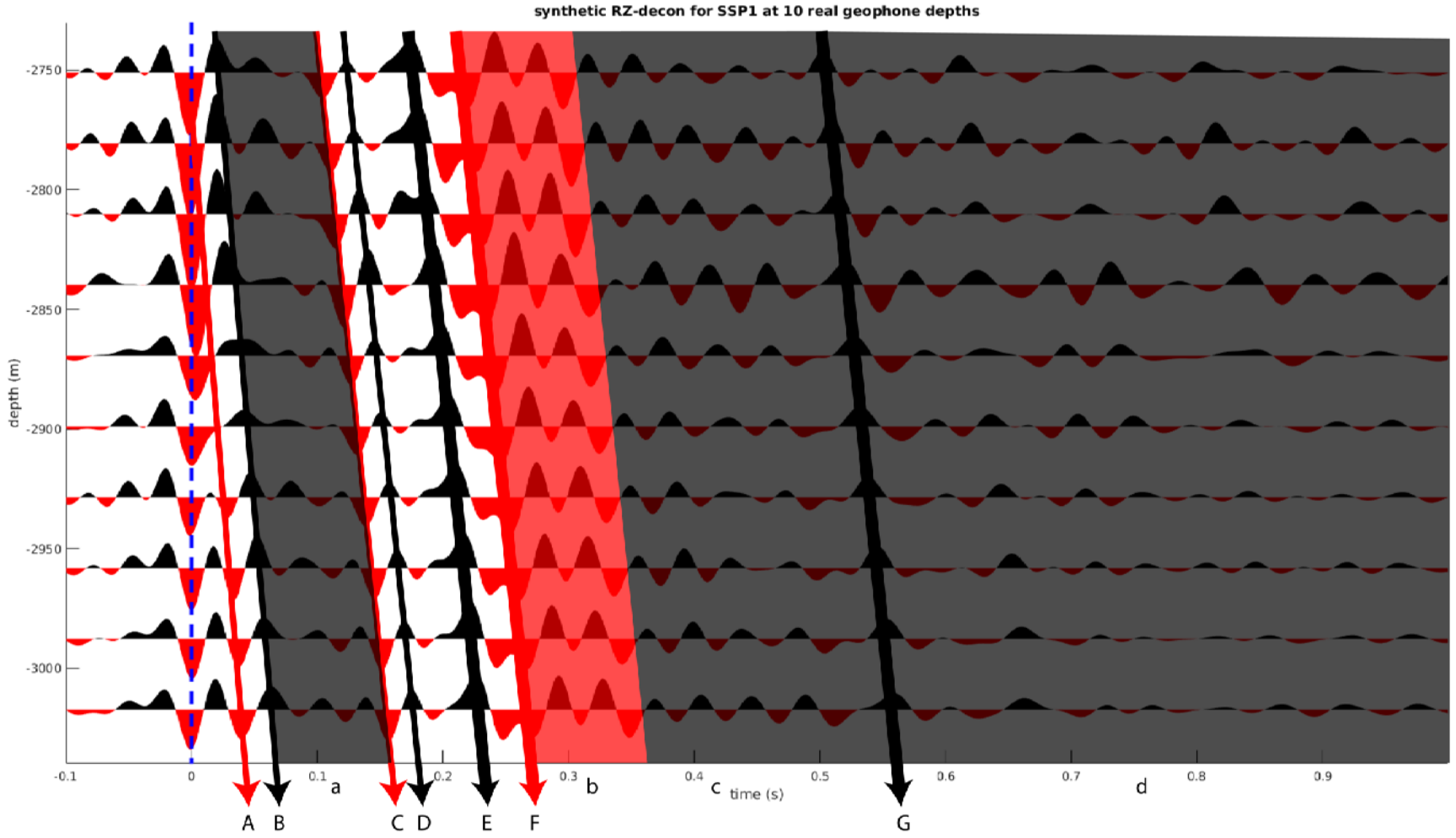

Figure 13: RZ-decon of synthetic data for 10 geophones at real geophone depths, for check shot SSP1. Black and red arrows indicate prominent P to SV conversions labeled with letters.

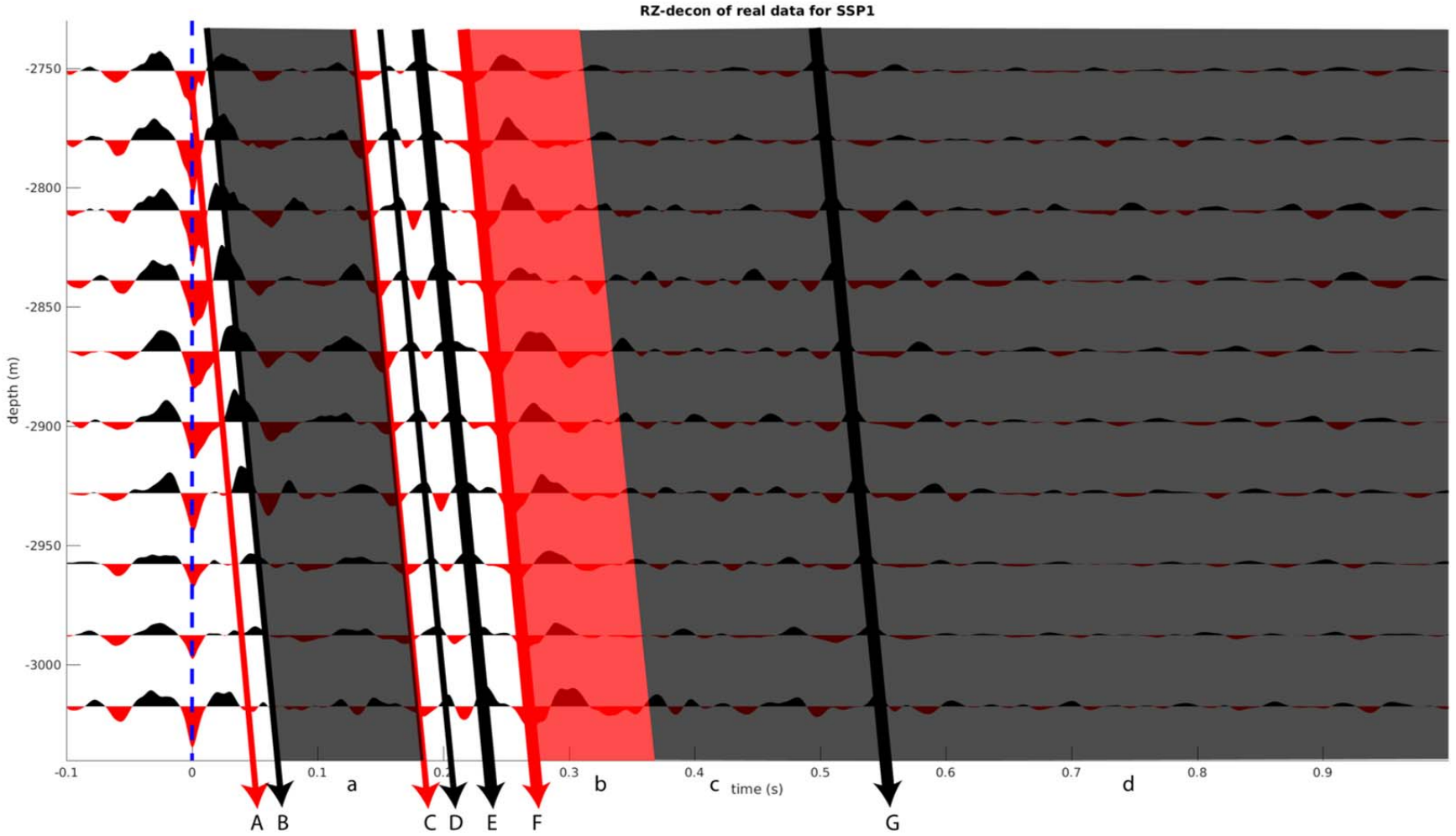

Figure 14: RZ-decon of real data of 10 geophones for check shot SSP1. Black and red arrows indicate prominent P to SV conversions labeled with letters.

Interpretation of the RZ-decon

The negative peak labeled with “A” (red) can be connected to the abrupt velocity decrease at the interface between the second anhydrite layer (ANH2) and the Rotliegend reservoir sandstone (RO). This peak is closely followed by the positive peak labeled with “B” (black), which can be connected to the abrupt velocity increase at the top of the second anhydrite layer in the Zechstein Group (ZE). In the grey shaded area labeled with “a”, no clear peaks are visible, which can be explained by the very homogeneous velocity profile inside the Zechstein Group between the two anhydrite layers. The peaks labeled with “C” (red) and “D” (black) can be connected to the bottom and top, respectively, of the first anhydrite layer (ANH1) inside the Zechstein Group.

The peaks labeled with “E” (black) and “F” (red) are both very wide, maybe even double, peaks. The first can be interpreted as the stepwise velocity increase from the bottom part of the Rijnland Group (KN) to the Zechstein Group, through the Upper and Lower Germanic Trias Groups (RB + RN). The second can be interpreted as the stepwise velocity increase from the bottom part of the Chalk Group (CK) to the bottom part of the Rijnland Group. These two peaks are followed by a red shaded area labeled with “b”, which consists of an alternation of some positive and negative peaks that cannot be clearly linked to boundaries between lithological formations. This alternation of peaks is probably caused by the irregular velocity profile in the lower part of the Chalk Group.

After another grey shaded area labeled with “c”, where no clear peaks can be distinguished due to the very gradual velocity increase within the Chalk Group, another clear positive peak is visible, labeled with “G” (black). This peak can be traced all the way up to the velocity increase between the North Sea Group and the Chalk Group. What stands out is that the slope of the line decreases when going up through the Chalk Group in Figure 12. This can be explained by the gradual change in velocity within this formation.

Also some reflections can be distinguished in the RZ-decon. Clear direct reflections are visible at the top of the Chalk Group, top of the Zechstein Group, top of the first anhydrite layer and top of the second anhydrite layer, indicated with blue lines. Also some reflections at the free surface and some multiples, especially within the North Sea Group, are visible, indicated with purple lines.

The lines in the RZ-decon are usually steeper in the lower part of the stratigraphy and shallower in the upper part, which is associated with an increasing P- and S-wave velocity with depth. Not only P to SV conversions are visible in the RZ-decon, but also reflections of P-waves, reflections of S-waves and SV to P conversions. This follows from the slope of the lines, because P-waves always have a higher velocity than S-waves, the lines in the RZ-decon caused by P-waves (either reflected or converted) are steeper than the lines caused by S-waves (either reflected or converted). Therefore it is possible that inside one lithological layer lines with 2 different slopes are visible. One clear example inside the Upper North Sea Group is indicated with yellow lines.

After another grey shaded area of more than 1 second wide, labeled with “d”, another clear peak appears in the RZ-decon of the synthetic data inside the Rotliegend reservoir, labeled with “H” (black) at almost 2 seconds delay time. Some possible interpretations of this peak are indicated by green dotted lines in Figure 12. This peak might be originating from a reflection at the top of the Chalk Group, the top

of the Zechstein Group, the top of the first anhydrite layer or the top of the second anhydrite layer, going upwards and reflecting again at the free surface, somewhere within the North Sea Group, or at the top of the Chalk Group, and then going downwards all the way to the Rotliegend reservoir. Some P to SV conversions or the other way around should have occurred along the way to satisfy the differences in the slope along the lines.

When comparing the RZ-decon of the synthetic data with the RZ-decon of the real data, it is useful to look at only the 10 synthetic geophones at the depths of the real geophones, see Figure 13, and compare this to the RZ-decon of the 10 real geophones, see Figure 14. In the real data only significant peaks are visible in the first second, so only the first second is plotted for both the real data and the synthetic data for comparison. From these figures it is clear that peaks A-G and areas a-d are all visible in both the synthetic data and the real data, at more or less the same delay times.

From the above analysis can be concluded that the RZ-decon method is a useful tool for determining interfaces with velocity contrasts and that the model used in Specfem2D to approximate the reality is quite accurate.

Discussion

Specfem2D is a 2D method, which assumes a flat layered earth structure. It is known that this is not the case in reality. Some layers might be dipping, and especially the Zechstein salt might have strange shapes, for example salt domes or diapirs, etc. Since the RZ-decon of the real data is computed for four different directions, this should be visible in the results.

When looking closely at the synthetic RZ-decon for the four different check shots, it is clear that the peaks are not exactly at the same delay time for all check shots, but slightly shifted with respect to each other. The peaks in the RZ-decon are at larger delay times for the check shots that are further away from the receivers in the order of increasing delay times: SSP4, SSP3, SSP1, SSP2. This corresponds to an increasing horizontal distance from source to receiver, as expected.

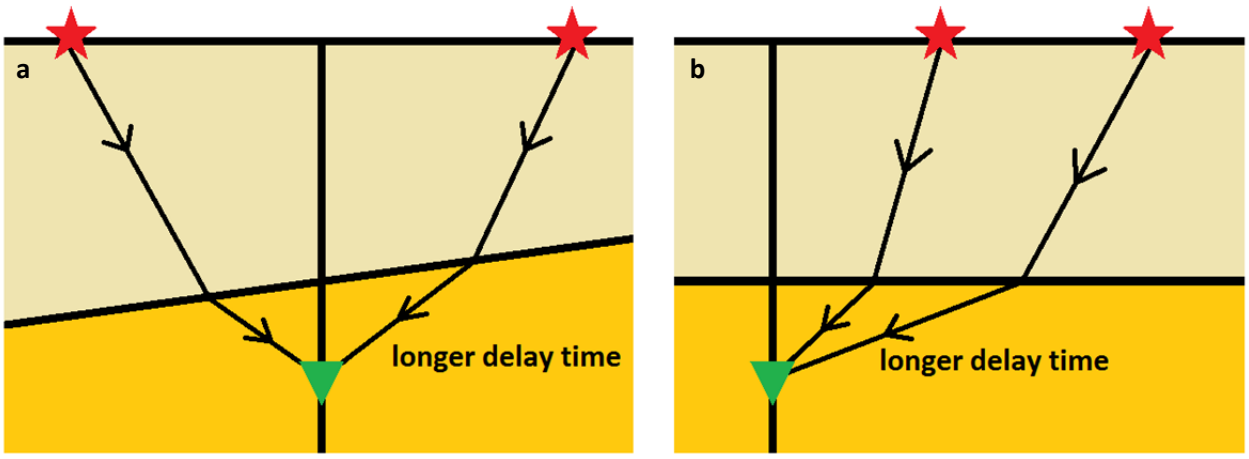

Figure 15: The effect of a) dipping interfaces and b) distance from source to receiver, on the delay time in the RZ-decon for different check shots. The red stars indicate the locations of the source; the green inverted triangle indicates the receiver.

When looking closely at the real RZ-decon for the four different check shots, however, the peaks are also shifted to smaller or larger delay times with respect to each other, but not in the same order as that of the synthetic data. That means that this shift in delay time cannot (only) be explained by the difference in horizontal distance from source to receiver. Another explanation for differences in delay time for the different check shots is a dipping interface causing the conversion. In Figure 15 the effect of both differences in horizontal distance and dipping interfaces is shown.

For most of the peaks, the shift in delay time is not easily distinguished, but for peak “G”, caused by the interface between North Sea Group and Chalk Group, the order of increasing delay times is clear: SSP4, SSP3, SSP2, SSP1. In this case the delay time for SSP2 is larger than that of SSP1, whereas the horizontal distance between source and receiver is larger for SSP1 than for SSP2. This could be explained by a dipping interface that dips more towards SSP2 than towards SSP1, so that the waves traveling from SSP2 have traveled a shorter distance at a lower velocity through the medium below the interface, after conversion to an S-wave than the waves traveling from SSP1.

When comparing the real data with the synthetic data more thoroughly, for each check shot separately, some small shifts between the peaks in the real RZ-decon and the peaks in the synthetic RZ-decon are visible. For SSP1, the peaks are more or less at the same delay times, but peak “A” is not clearly visible in the real data. For SSP2, peaks “E”, “F” and “G” all have a slightly smaller delay time in the real data with respect to the synthetic data. For SSP3, peaks “E” and “F” have a slightly larger delay time in the real data with respect to the synthetic data, and peak “G” has a slightly smaller delay time in the real data with respect to the synthetic data. For SSP4, peaks “E” and “F” have a slightly larger delay time in the real data with respect to the synthetic data, and peak “G” has a slightly smaller delay time in the real data with respect to the synthetic data.

Peaks “E” and “F” are in check shot SSP2 at a smaller delay time and in check shot SSP3 and SSP4 at a larger delay time in the real data with respect to the synthetic data. This might mean that the velocity fluctuations between the lower part of the Chalk Group and the upper part of the Zechstein Group, causing these conversions, occur in reality at a smaller depth than the model suggests in the direction of SSP3 and 4 and at a larger depth than the model suggests in the direction of SSP2, so that these layers are dipping towards the West.

Peak “G” is in 3 out of 4 check shots in the real data at a smaller delay time with respect to the synthetic data, which means that probably the interface causing this conversion (North Sea Group to Chalk Group) is in reality a bit deeper than the model suggests, or the interface is dipping in the direction of SSP2, SSP3 and SSP4, so more or less a dome in 3 directions.

Peak “H”, defined in the RZ-decon of the synthetic data at almost 2 seconds delay time at depths in the Rotliegend reservoir, is not visible in the real data, compare Figure 16a and b. As mentioned before, this peak probably originates from a multiple reflection between a deeper interface and a shallower interface or even the free surface. The fact that this peak is not visible in the real data might be explained by the fact that with Specfem2D, the effect of damping is ignored. The values for the quality factors $Q\mu$ and $Q\kappa$ are set to 9999, see Appendix 5. This allows waves to be reflected up and down between the free surface and deeper interfaces without being attenuated, whereas in reality, the upper part of the subsurface is

very unconsolidated and therefore has a very low quality factor, causing much damping. This is probably why in the real data waves that are reflected at deeper interfaces and then reflected again from a shallower interface or the free surface will not appear a second time in the data, for they are already attenuated in the upper part of the subsurface before arriving at the receivers at depth. To test this, Specfem2D can be used to compute synthetic seismograms, which in turn can be used to calculate the RZ-decon, but this time with realistic values for the quality factor.

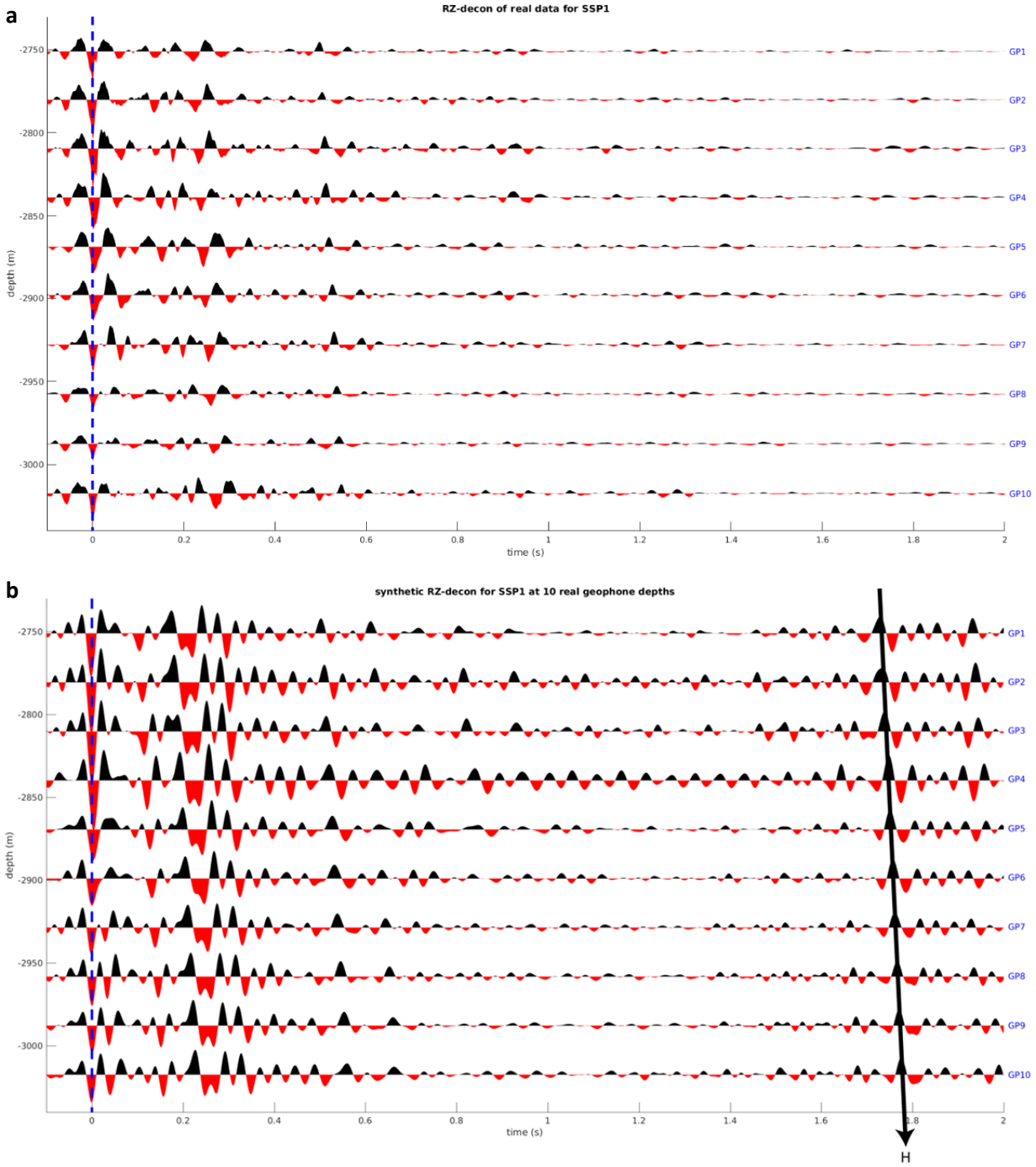

Figure 16: RZ-decon of a) the real data and b) the synthetic data, for check shot SSP1, for 2 seconds delay time.

In this study, the peaks in the RZ-decon are interpreted based on a known velocity structure above the set of geophones in the reservoir, using check shots from above. It would be very useful if it is also possible to interpret an unknown velocity structure beneath a set of geophones from the peaks in the RZ-decon, so the other way around, using a source from below, for example earthquakes.

Whenever the line through the peaks in the RZ-decon intersects with the z-axis (where the delay time is equal to zero), within the limits of the geophone depths, this depth is with certainty the depth of a velocity contrast that causes this P to SV conversion. If this is not the case, the line through the peaks has to be extrapolated downwards until it intersects with the z-axis. The problem here is that the slope of this line depends on the P- and S-wave velocities in the layers above the interface causing the P to SV conversion, which are unknown. Therefore the uncertainty of this method to determine the depth of interfaces increases more and more with depth.

With the RZ-decon method it is also possible to say something about the shape of the velocity structure within the limits of the geophone depths. The slope of the lines connecting the peaks depends on both the difference between P- and S-wave velocity and the magnitude of the velocities. A steeper line can be caused by either higher velocities or a smaller difference between P- and S-wave velocity, or both. If the line is straight, it means that the velocity structure is more or less constant. If it is curved, it means that the velocity increases with depth and/or the P- and S-wave velocities converge, for lines getting steeper with depth, or the velocity decreases with depth and/or the P- and S-wave velocities diverge, for lines getting shallower with depth.

Intersections with the z-axis say something about the depths of strong contrasts in the velocity structure and the shape of the lines connecting the peaks says something about the shape of the velocity structure, but the magnitude of the velocities remains unknown. With a known interface depth and a known delay time ($t_{Ps} - t_P$) at a certain depth the difference between P- wave and S-wave velocity ($\frac{1}{V_S} - \frac{1}{V_P}$) can be approximated using the aforementioned equation for the delay time for vertical incidence, where d is the distance to the interface:

$$t_{Ps} - t_P = d\left(\frac{1}{V_S} - \frac{1}{V_P}\right)$$

$$\frac{1}{V_S} - \frac{1}{V_P} = \frac{(t_{Ps} - t_P)}{d}$$

This assumes that the P- and S-wave velocities are constant down to the interface and that the incidence angle is (near) vertical. An empirical formula for the ratio between the P- and S-wave velocities can be used to calculate both velocities, but this ratio usually depends on the lithology, which has to be known in order to calculate the velocities accurately. All these factors cause a lot of uncertainty, so the velocity structure can only be estimated.

Conclusion

To conclude this study, the main questions can be answered. The main question was if the RZ-decon method works and how accurate it is. The other objective of this study was to compare the RZ-decon of the real check shot data to that of synthetic data retrieved using Specfem2D, in order to interpret the quality of the input P- and S-wave velocity and density model provided by NAM.

The RZ-decon method has proven to show peaks at delay times that are associated with strong velocity contrasts. This means that this method works and that it is useful for determining interfaces in the subsurface. When the velocity structure is unknown, this method is useful to estimate the depths of velocity contrasts due to lithological interfaces beneath a set of geophones, but the depth at which a line in the RZ-decon intersects with the z-axis depends on the unknown velocity structure, so the uncertainty in this estimation increases with depth.

In general, the RZ-decon of the synthetic data and the RZ-decon of the real data show the same peaks at more or less the same delay times. This means that the model generally agrees with the reality. Some of the peaks are slightly shifted to smaller or larger delay times for one or more of the check shots, which can be explained by the fact that Specfem2D ignores lateral variations in thickness and depth of lithological layers.

Further research is recommended on the effect of a 3D layered structure using Specfem3D on the RZ-decon of synthetic data, to see if it will fit even better to the RZ-decon of the real data. Also the effect of attenuation will have to be investigated, in order to be able to explain the presence or absence of peaks in the RZ-decon at large delay times.

Acknowledgements

I would like to thank the Nederlandse Aardolie Maatschappij (NAM) for providing me with the check shot data, well log data of borehole SDM-01 for the P-wave velocity structure and the ratios between the P- and S-wave velocity, density, slowness and depth, which are used to build the velocity and density model as input for Specfem2D. Also, I would like to thank dr. Hanneke Paulssen and Wen Zhou MSc for their supervision during this study.

Bibliography

Aki, K., & Richards, P. G. (2002). *Quantitative Seismology.* University Science Books.

Igel, H. (2016). *Computational Seismology: A practical introduction.* Oxford University Press.

Igel, H. (2017). *Computational Seismology.*

Komatitsch, D., & Tromp, J. (1999). Introduction to the spectral element method for three-dimensional seismic wave propagation. *Geophysical Journal International, 139*, 806-822.

Kraaijpoel, D., & Dost, B. (2013). Implications of salt-related propagation and mode conversion effects on the analysis of induced seismicity. *Journal of Seismology, 17*, 95-107.

Nederlandse Aardolie Maatschappij. (2016). *Study and data acquisition plan induced seismicity in Groningen - Winningsplan.* NAM report.

Owens, T. J., Zandt, G., & Taylor, S. R. (1981). Seismic evidence for an ancient rift beneath the cumberland plateau: a detailed analysis of broadband teleseismic P waveforms. *Journal of geophysical research, 89*, 7783-7795.

Paulssen, H. (n.d.). *Linear Algebra and Vector Analysis: course notes.*

Romijn, R. (2017). *Groningen Velocity Model 2017 - Groningen full elastic velocity model September 2017.* Nederlandse Aardolie Maatschappij.

Sercel seismic tools specifications. (2014). Retrieved from Sercel: http://www.sercel.com/products/Lists/ProductSpecification/Downhole_Seismic%20tools_specifications_Sercel.pdf

Spetzler, J., & Dost, B. (2017). Hypocenter estimation of induced earthquakes in Groningen. *Geophysical Journal International*.

Stein, S., & Wysession, M. (2003). *An Introduction to Seismology, Earthquakes, and Earth Structure.* Blackwell Publishing.

Theodulidis, N., Bard, P., Archuleta, R., & Bouchon, M. (1996). Horizontal-to-vertical spectral ratio and geological conditions: The case of Garner Valley downhole array in southern California. *Bulletin of the Seismological Society of America, 86*(2), 306-319.

TNO. (2014). *DGM-deep version 4.0.*

TNO. (2017). *Ondergrondmodellen*. Retrieved from Dinoloket: https://www.dinoloket.nl/ondergrondmodellen

Van Adrichem Boogaert, H., & Kouwe, W. (1993-1997). Altena Group. *Stratigraphic Nomenclature of the Netherlands*.

Van Adrichem Boogaert, H., & Kouwe, W. (1993-1997). Chalk Group. *Stratigraphic Nomenclature of the Netherlands*.

Van Adrichem Boogaert, H., & Kouwe, W. (1993-1997). Limburg Group. *Stratigraphic Nomenclature of the Netherlands*.

Van Adrichem Boogaert, H., & Kouwe, W. (1993-1997). Lower North Sea Group. *Stratigraphic Nomenclature of the Netherlands*.

Van Adrichem Boogaert, H., & Kouwe, W. (1993-1997). Middle North Sea Group. *Stratigraphic Nomenclature of the Netherlands*.

Van Adrichem Boogaert, H., & Kouwe, W. (1993-1997). Rijnland Group. *Stratigraphic Nomenclature of the Netherlands*.

Van Adrichem Boogaert, H., & Kouwe, W. (1993-1997). Upper and Lower Germanic Trias Groups. *Stratigraphic Nomenclature of the Netherlands*.

Van Adrichem Boogaert, H., & Kouwe, W. (1993-1997). Upper North Sea Group. *Stratigraphic Nomenclature of the Netherlands*.

Van Adrichem Boogaert, H., & Kouwe, W. (1993-1997). Upper Rotliegend Group. *Stratigraphic Nomenclature of the Netherlands*.

Van Adrichem Boogaert, H., & Kouwe, W. (1993-1997). Zechstein Group. *Stratigraphic Nomenclature of the Netherlands*.

Van Gent, H., Urai, J., & De Keijzer, M. (2011). The internal geometry of salt structures - A first look using 3D seismic data from the Zechstein of the Netherlands. *Journal of Structural Geology, 33*, 292-311.

Van Thienen-Visser, K., & Breunese, J. (2015). Induced seismicity of the Groningen gas field: History and recent developments. *The Leading Edge, 34*, 664-671.

Zhou, W., & Paulssen, H. (2017). P and S velocity structure in the groningen gas reservoir from noise interferometry. *Geophysical Research Letters, 44*, 11785-11791.

Appendices

Appendix 1: Raw data

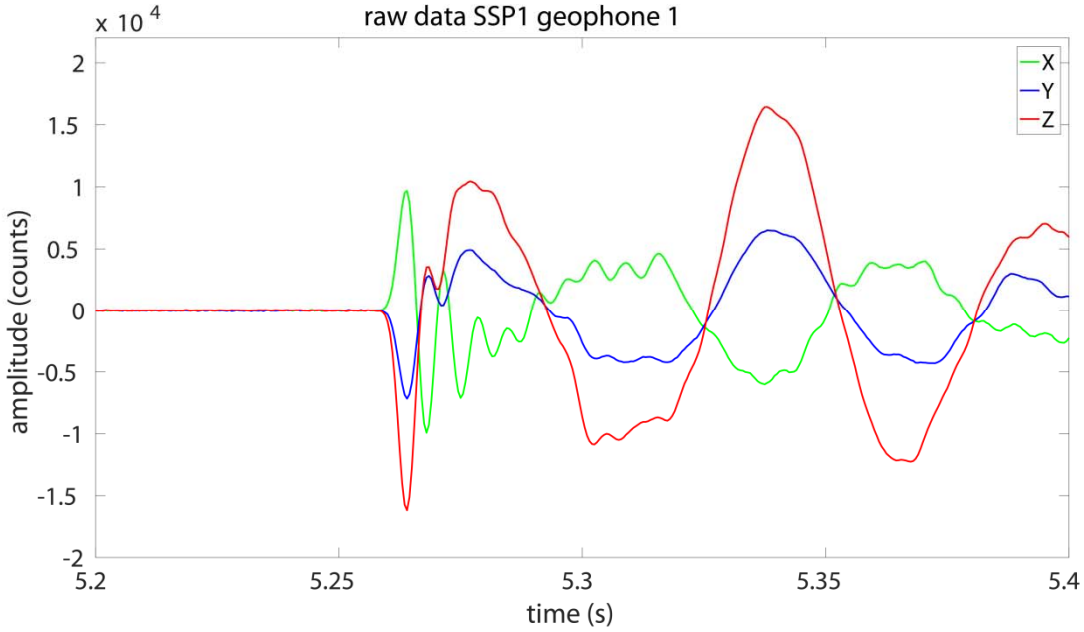
raw data SSP1 geophone 1
x 10 4
amplitude (counts)
time (s)
X
Y
Z
2
1.5
1
0.5
0
-0.5
-1
-1.5
-2
5.2
5.25
5.3
5.35
5.4

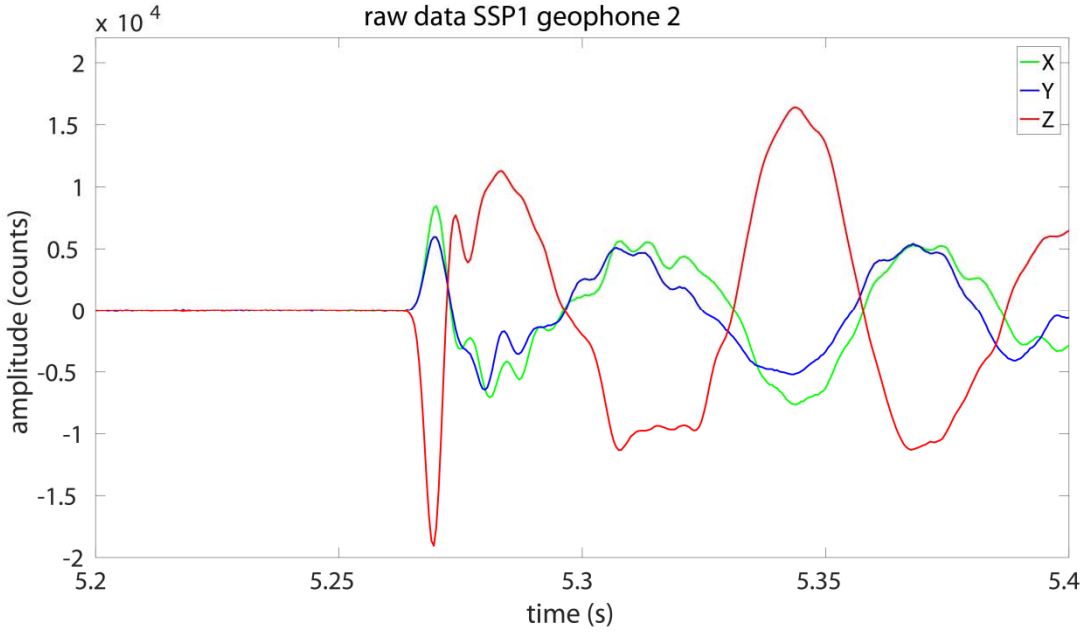
raw data SSP1 geophone 2
x 10 4
amplitude (counts)
time (s)
X
Y
Z
2
1.5
1
0.5
0
-0.5
-1
-1.5
-2
5.2
5.25
5.3
5.35
5.4

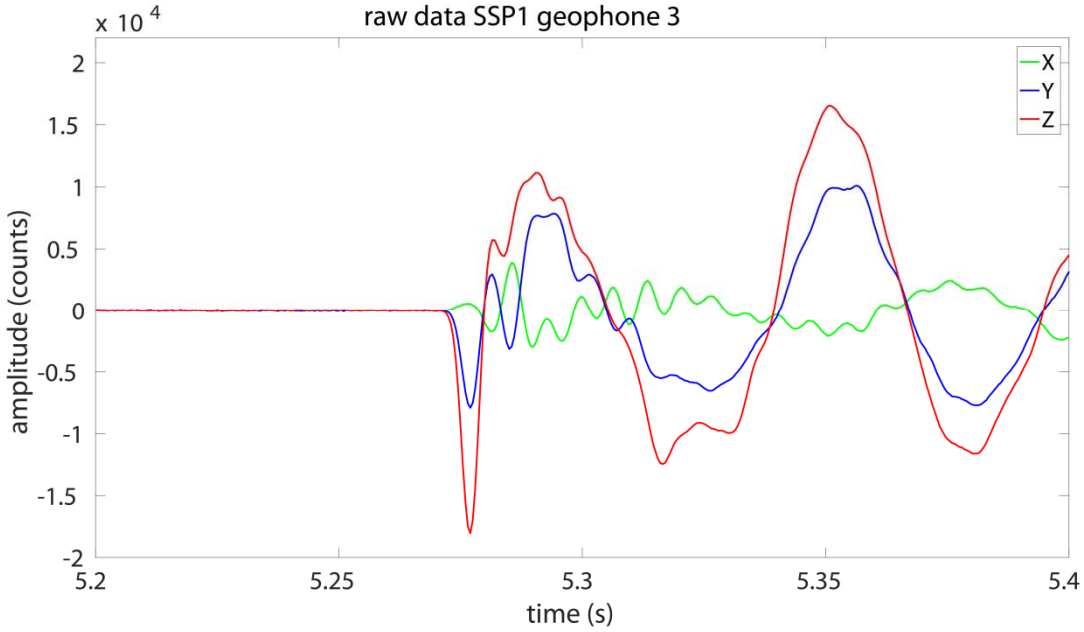
raw data SSP1 geophone 3
x 10 4
amplitude (counts)
time (s)
X
Y
Z
2
1.5
1
0.5
0
-0.5
-1
-1.5
-2
5.2
5.25
5.3
5.35
5.4

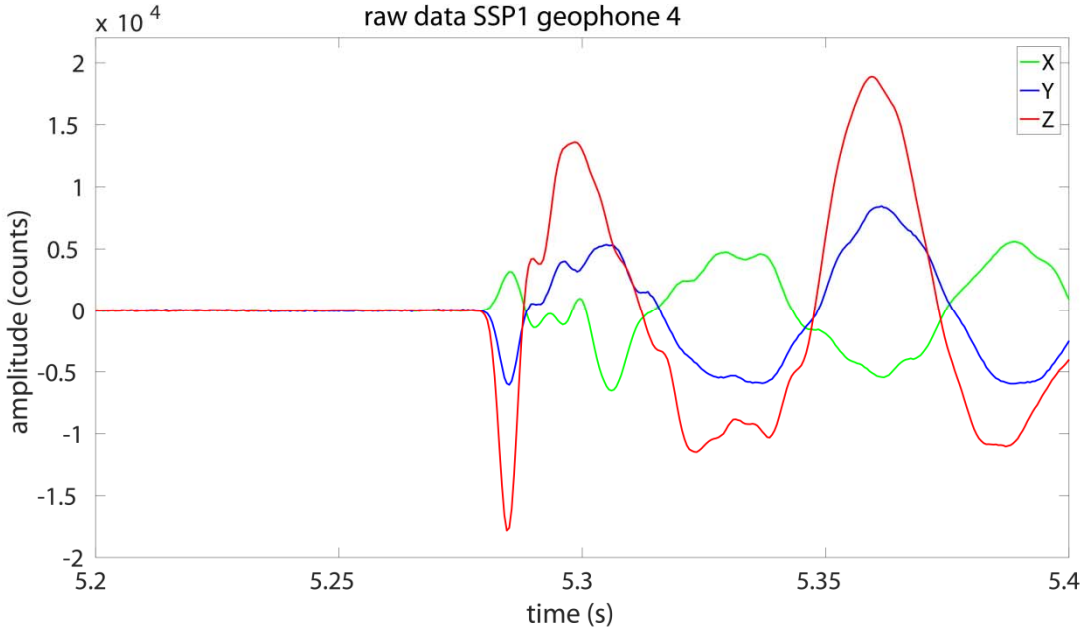
raw data SSP1 geophone 4
x 10 4
amplitude (counts)
time (s)
X
Y
Z
2
1.5
1
0.5
0
-0.5
-1
-1.5
-2
5.2
5.25
5.3
5.35
5.4

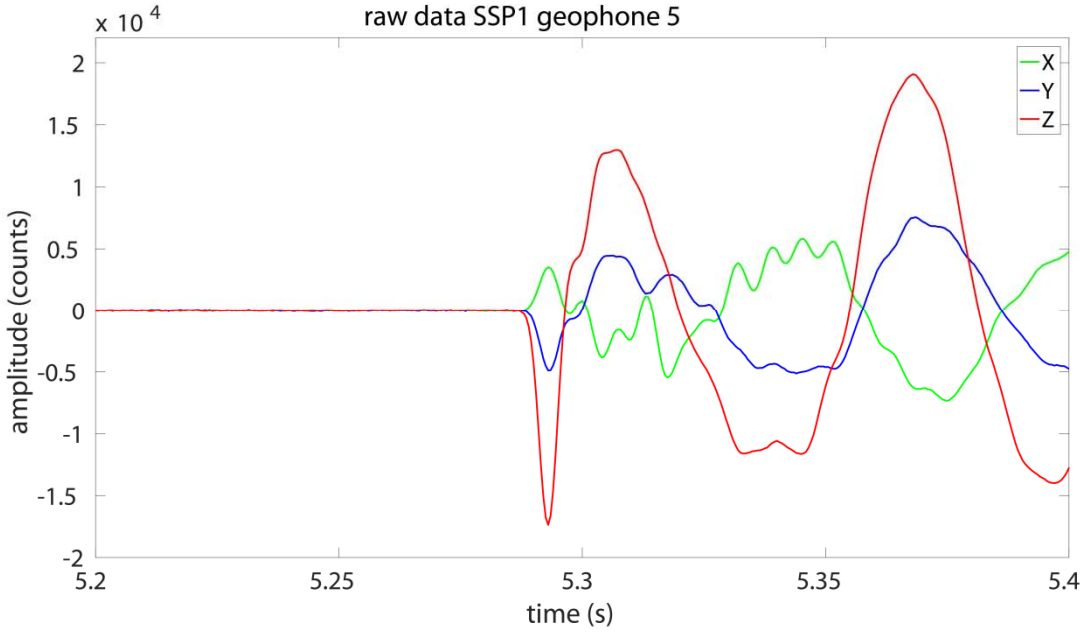
raw data SSP1 geophone 5
x 10 4
amplitude (counts)
time (s)
X
Y
Z
2
1.5
1
0.5
0
-0.5
-1
-1.5
-2
5.2
5.25
5.3
5.35
5.4

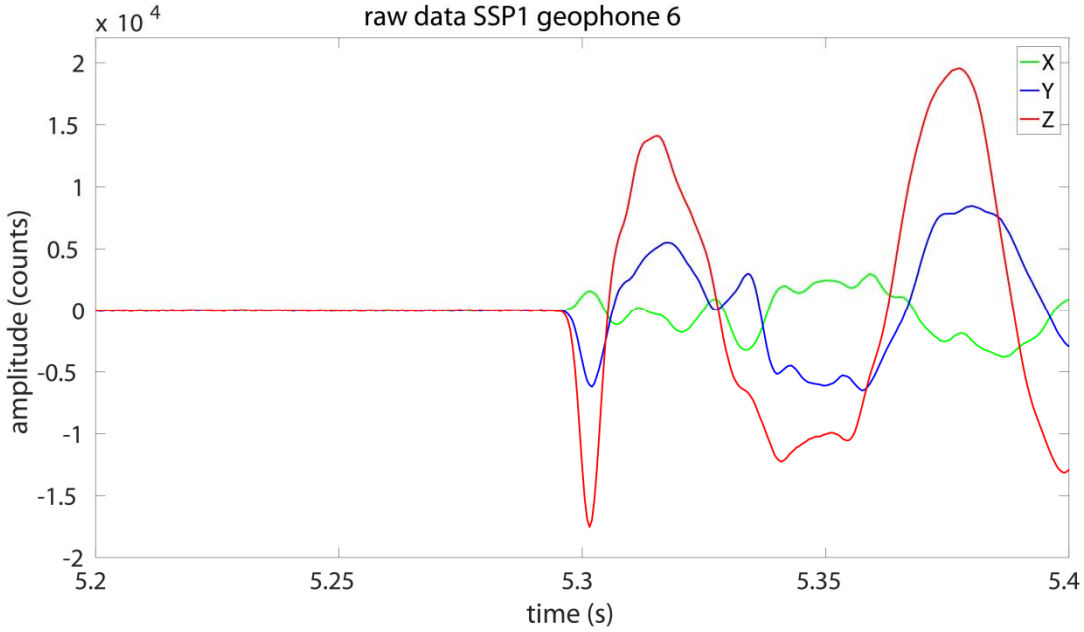
raw data SSP1 geophone 6
x 10 4
amplitude (counts)
time (s)
X
Y
Z
2
1.5
1
0.5
0
-0.5
-1
-1.5
-2
5.2
5.25
5.3
5.35
5.4

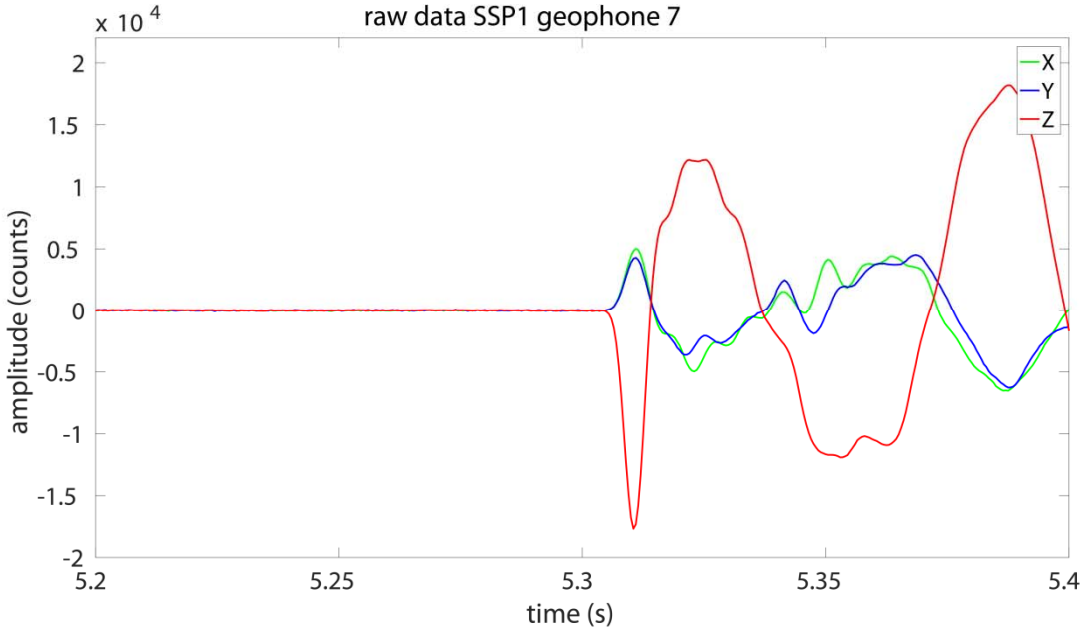
raw data SSP1 geophone 7
x 10 4
amplitude (counts)
time (s)
X
Y
Z
2
1.5
1
0.5
0
-0.5
-1
-1.5
-2
5.2
5.25
5.3
5.35
5.4

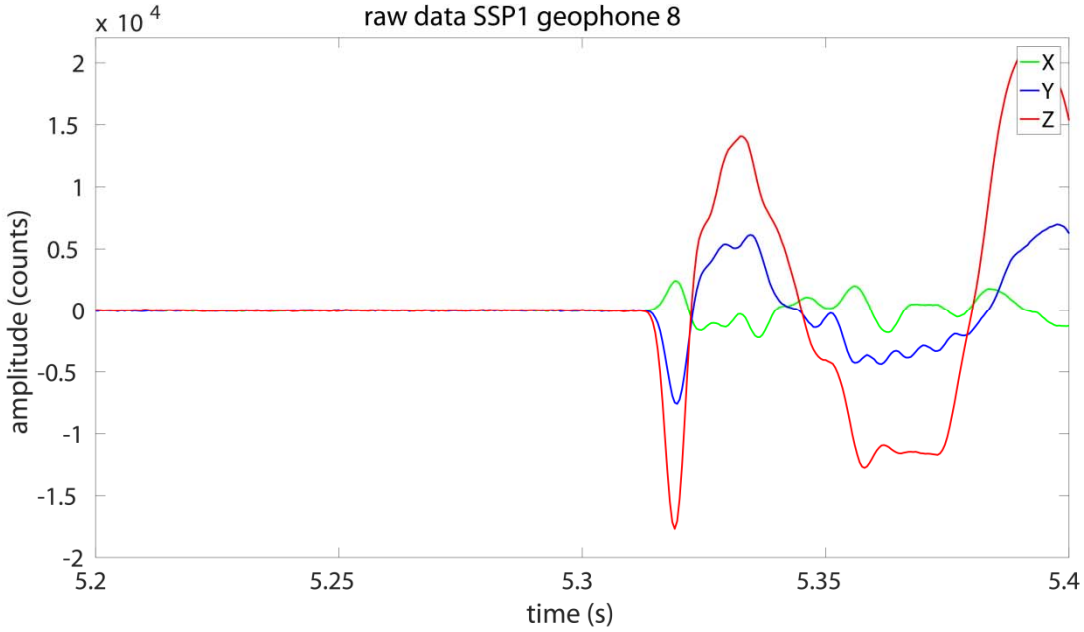
raw data SSP1 geophone 8
x 10 4
amplitude (counts)
time (s)
X
Y
Z
2
1.5
1
0.5
0
-0.5
-1
-1.5
-2
5.2
5.25
5.3
5.35
5.4

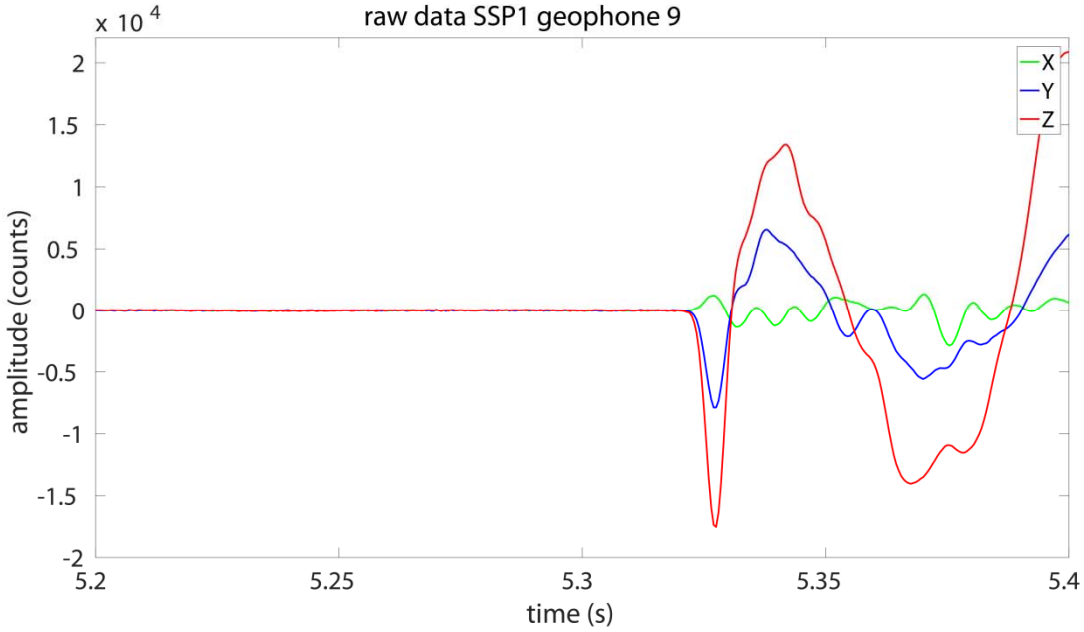
raw data SSP1 geophone 9
x 10 4
amplitude (counts)
time (s)
X
Y
Z
2
1.5
1
0.5
0
-0.5
-1
-1.5
-2
5.2
5.25
5.3
5.35
5.4

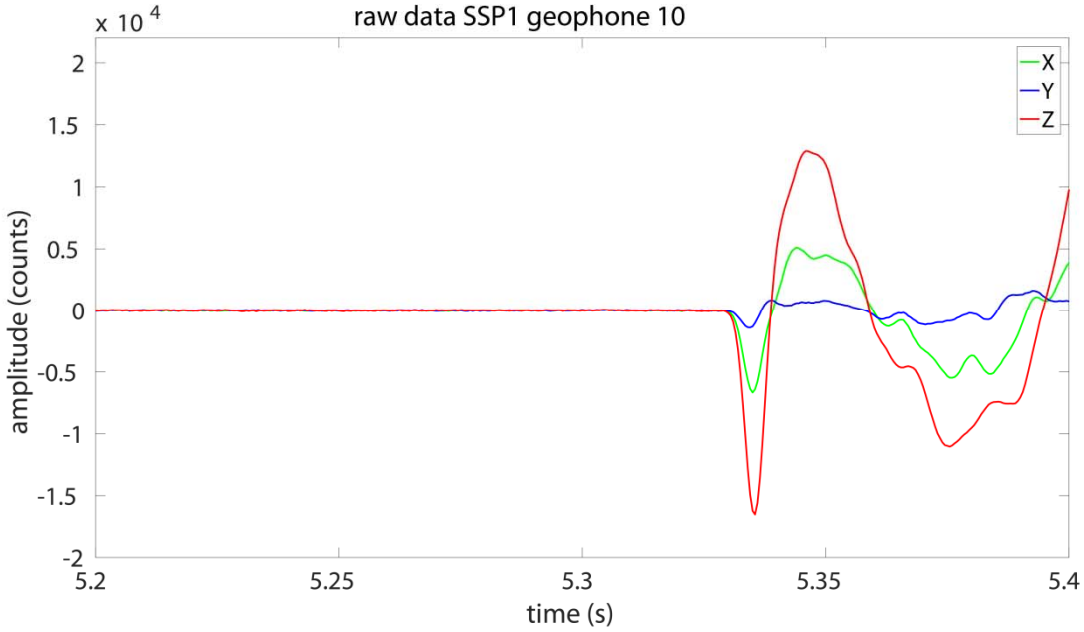
raw data SSP1 geophone 10
x 10 4
amplitude (counts)
time (s)
X
Y
Z
2
1.5
1
0.5
0
-0.5
-1
-1.5
-2
5.2
5.25
5.3
5.35
5.4

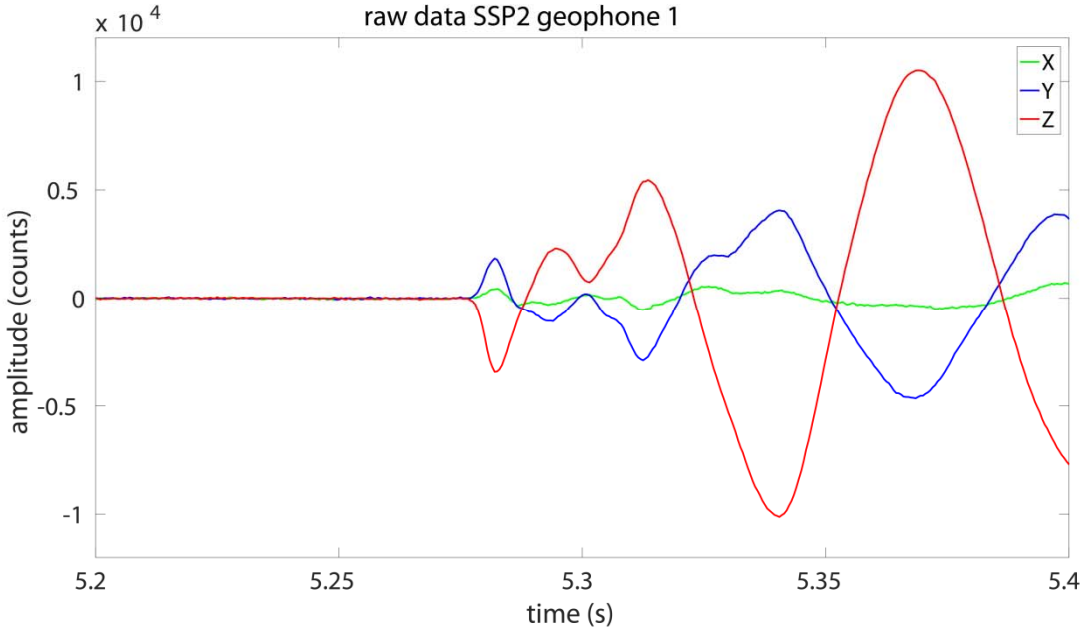
raw data SSP2 geophone 1
x 10 4
amplitude (counts)
time (s)
X
Y
Z
1
0.5
0
-0.5
-1
5.2
5.25
5.3
5.35
5.4

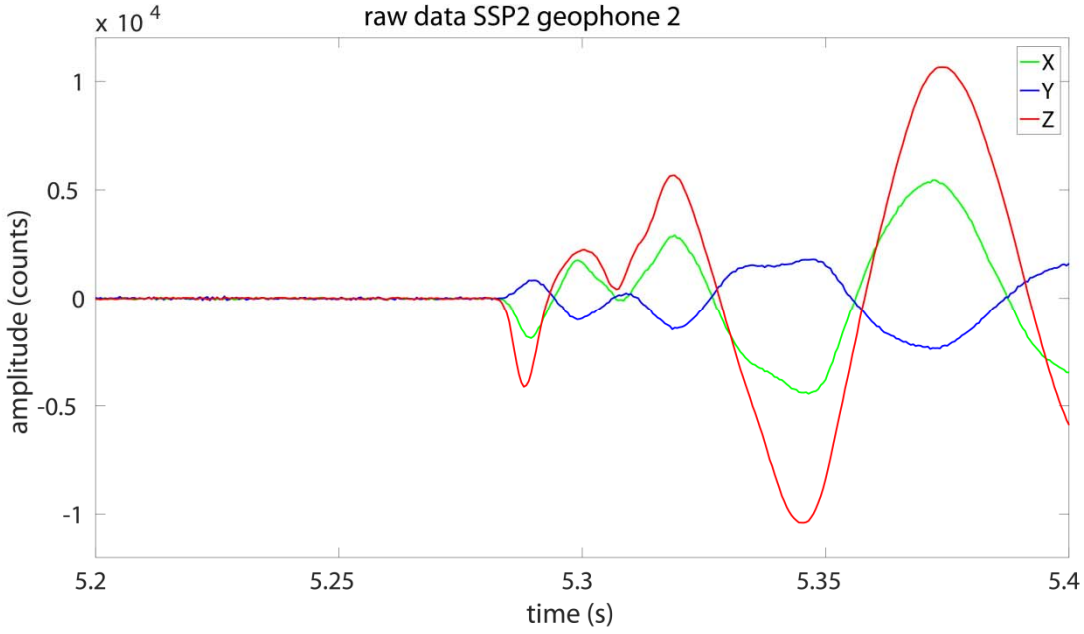
raw data SSP2 geophone 2
x 10 4
amplitude (counts)
time (s)
X
Y
Z
1
0.5
0
-0.5
-1
5.2
5.25
5.3
5.35
5.4

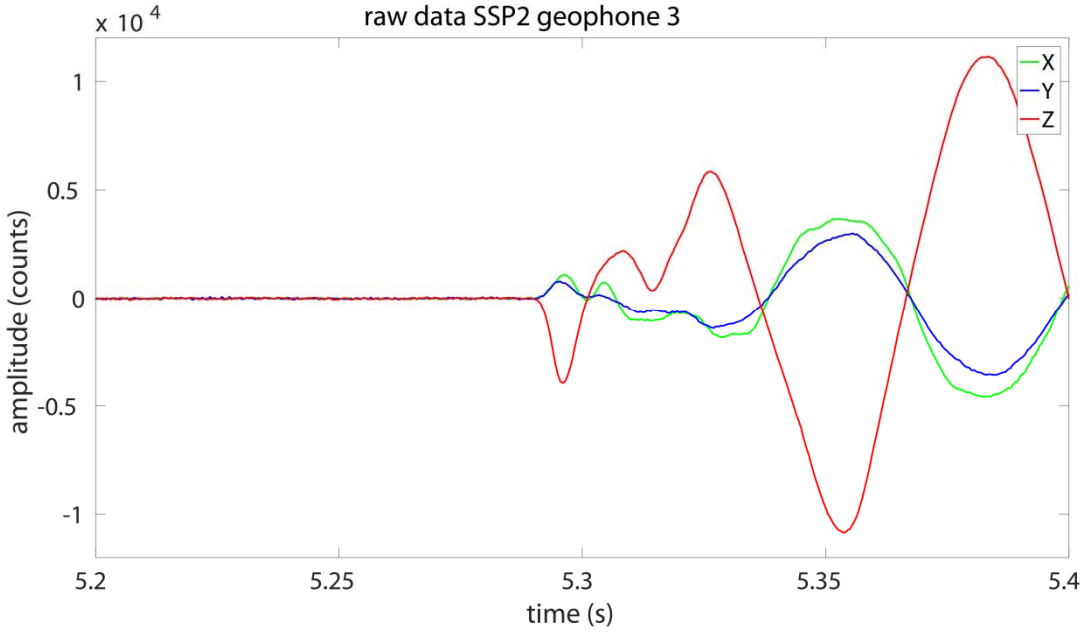
raw data SSP2 geophone 3
x 10 4
amplitude (counts)
time (s)
X
Y
Z
1
0.5
0
-0.5
-1
5.2
5.25
5.3
5.35
5.4

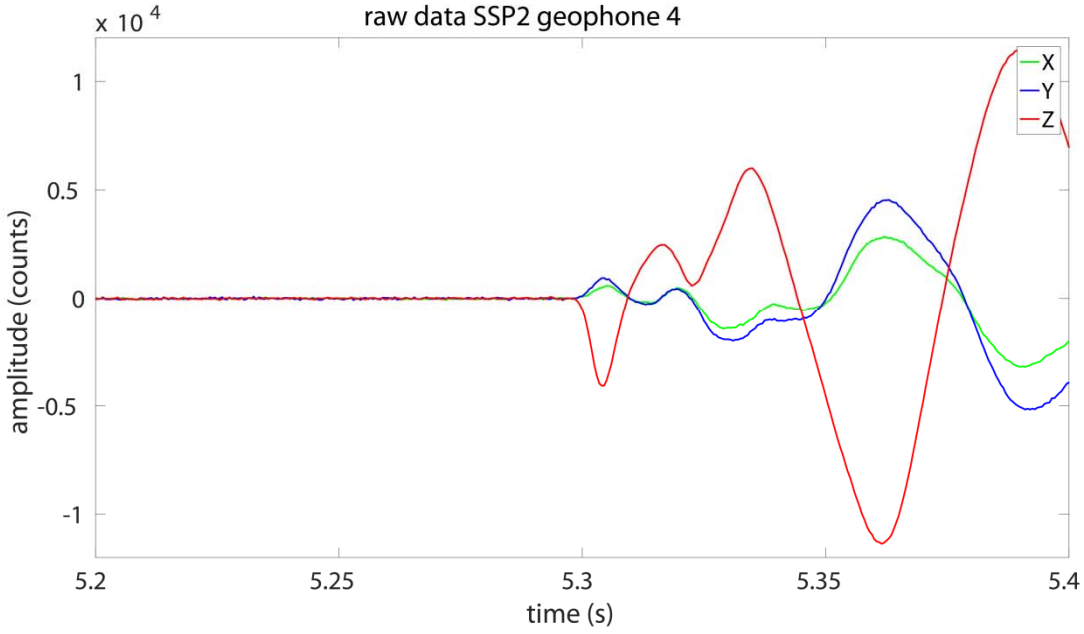
raw data SSP2 geophone 4
x 10 4
amplitude (counts)
time (s)
X
Y
Z
1
0.5
0
-0.5
-1
5.2
5.25
5.3
5.35
5.4

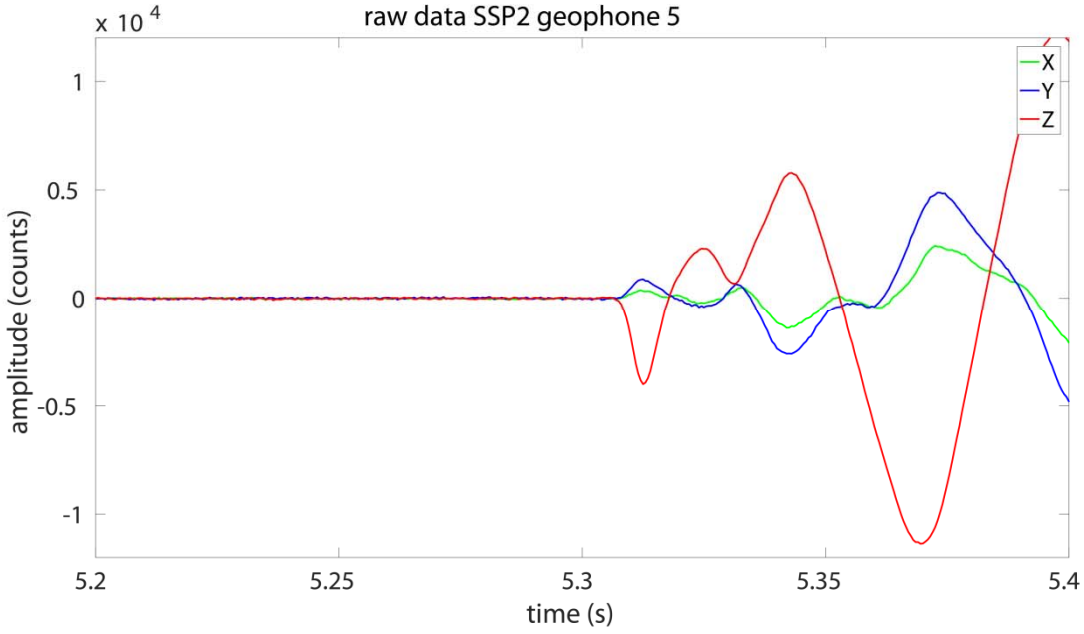
raw data SSP2 geophone 5
x 10 4
1
0.5
0
-0.5
-1
amplitude (counts)
5.2
5.25
5.3
5.35
5.4
time (s)
X
Y
Z

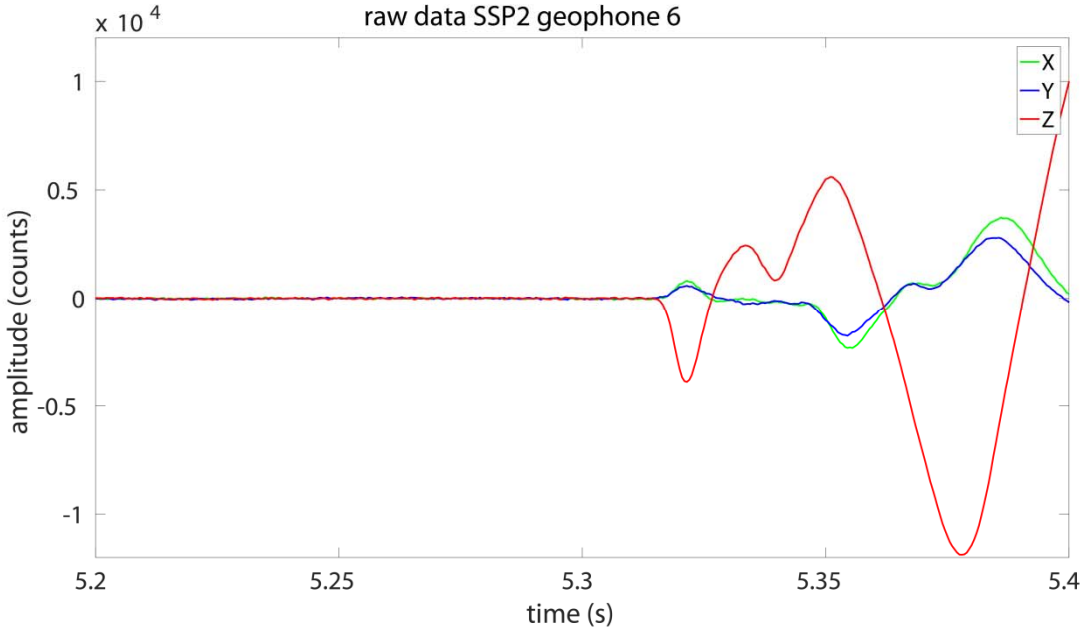
raw data SSP2 geophone 6
x 10 4
1
0.5
0
-0.5
-1
amplitude (counts)
5.2
5.25
5.3
5.35
5.4
time (s)
X
Y
Z

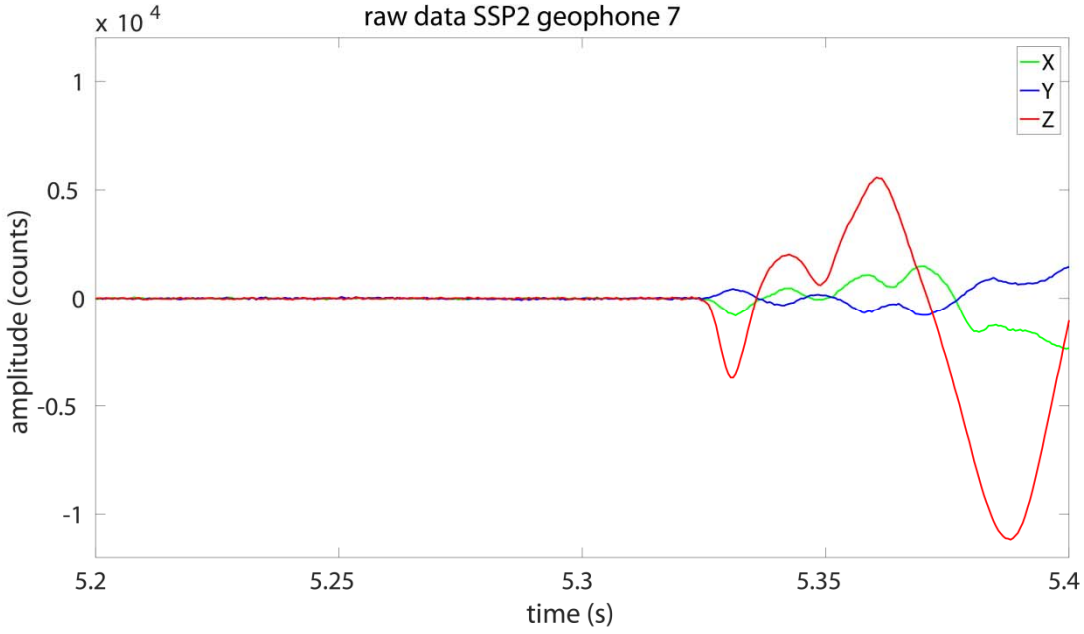
raw data SSP2 geophone 7
x 10 4
amplitude (counts)
time (s)
X
Y
Z
1
0.5
0
-0.5
-1
5.2
5.25
5.3
5.35
5.4

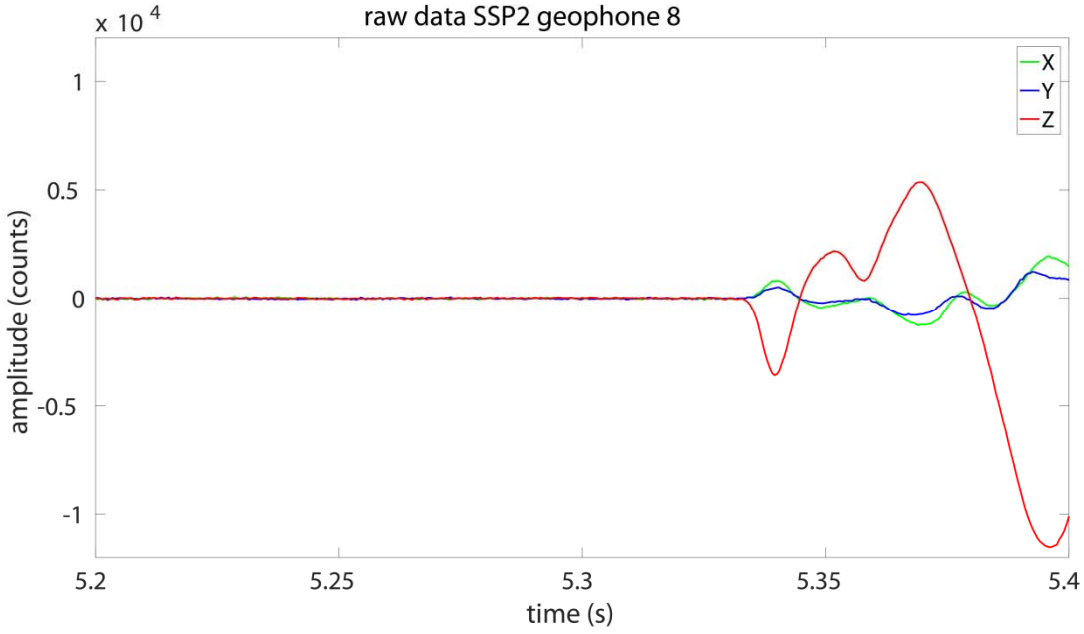
raw data SSP2 geophone 8
x 10 4
amplitude (counts)
time (s)
X
Y
Z
1
0.5
0
-0.5
-1
5.2
5.25
5.3
5.35
5.4

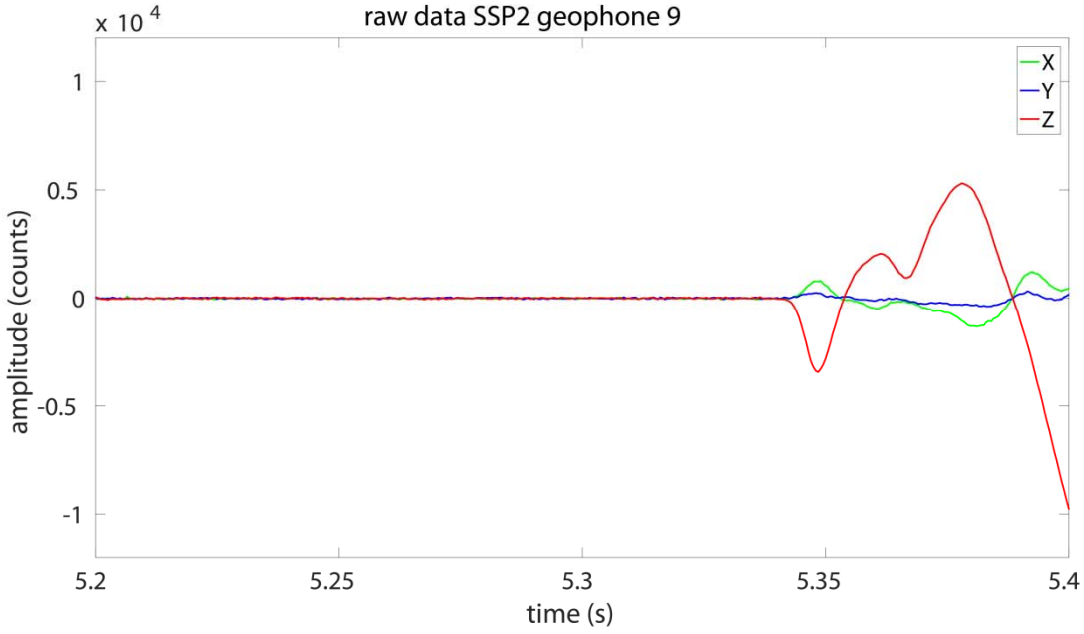
raw data SSP2 geophone 9
x 10 4
1
0.5
0
-0.5
-1
amplitude (counts)
5.2
5.25
5.3
5.35
5.4
time (s)
X
Y
Z

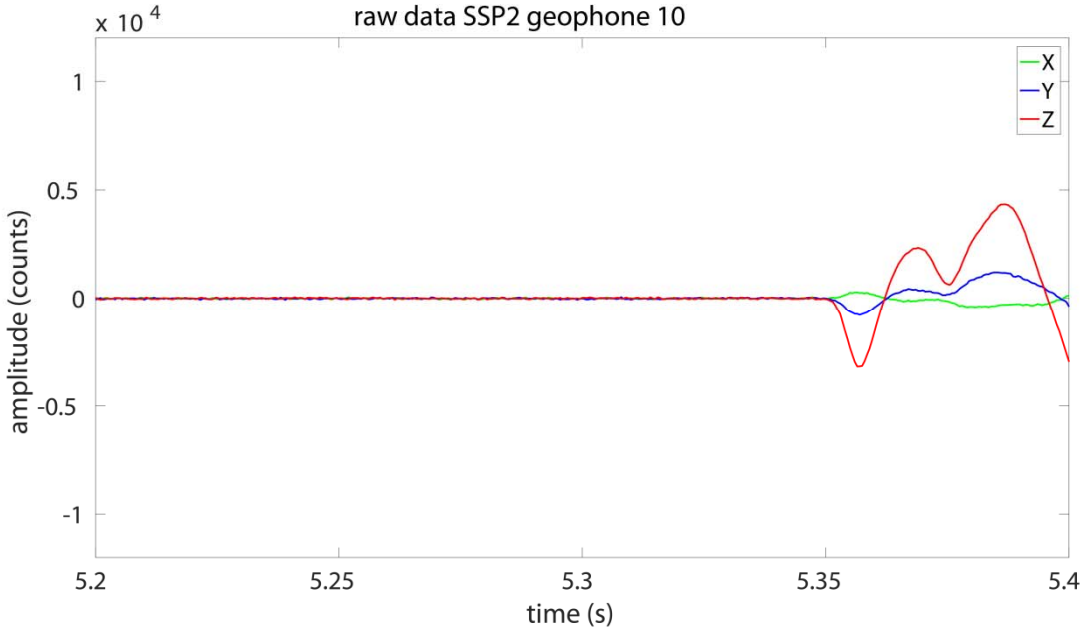
raw data SSP2 geophone 10
x 10 4
1
0.5
0
-0.5
-1
amplitude (counts)
5.2
5.25
5.3
5.35
5.4
time (s)
X
Y
Z

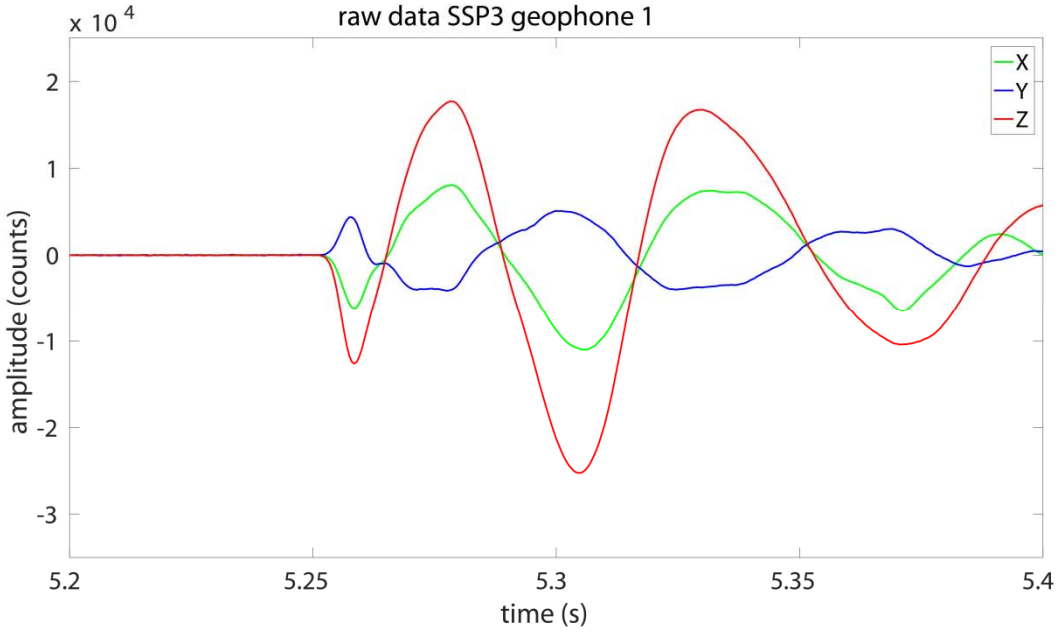
raw data SSP3 geophone 1
x 10 4
amplitude (counts)
time (s)
X
Y
Z
2
1
0
-1
-2
-3
5.2
5.25
5.3
5.35
5.4

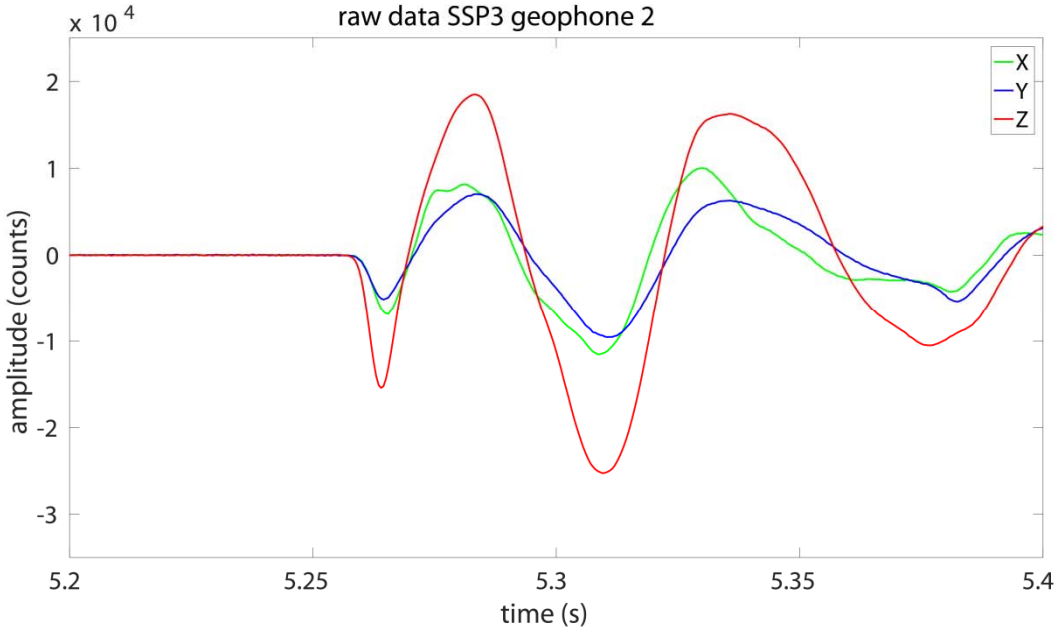
raw data SSP3 geophone 2
x 10 4
amplitude (counts)
time (s)
X
Y
Z
2
1
0
-1
-2
-3
5.2
5.25
5.3
5.35
5.4

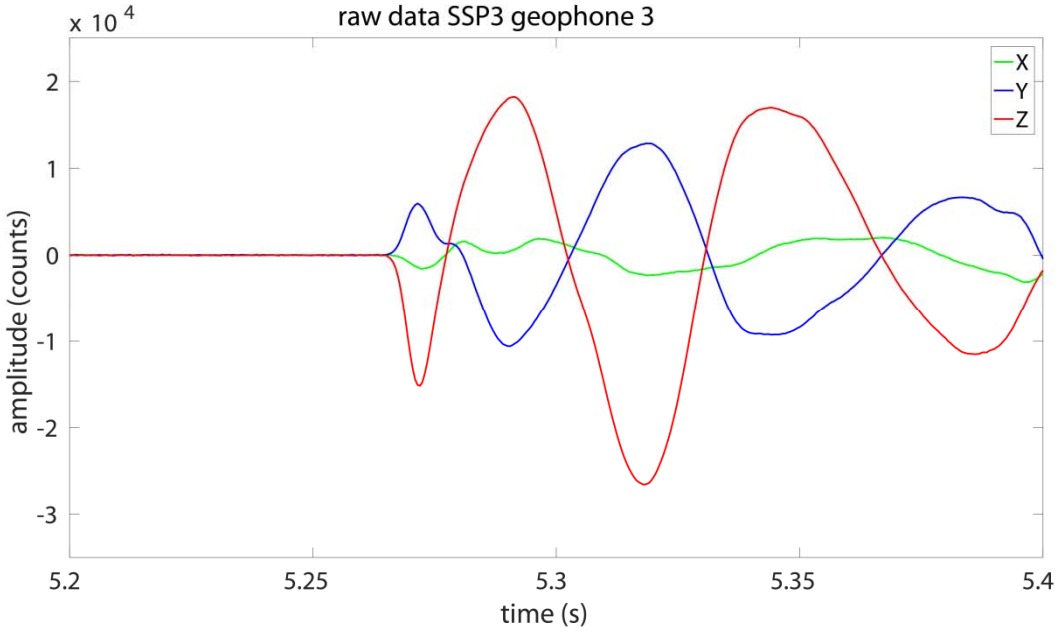
raw data SSP3 geophone 3
x 10 4
amplitude (counts)
time (s)
X
Y
Z
2
1
0
-1
-2
-3
5.2
5.25
5.3
5.35
5.4

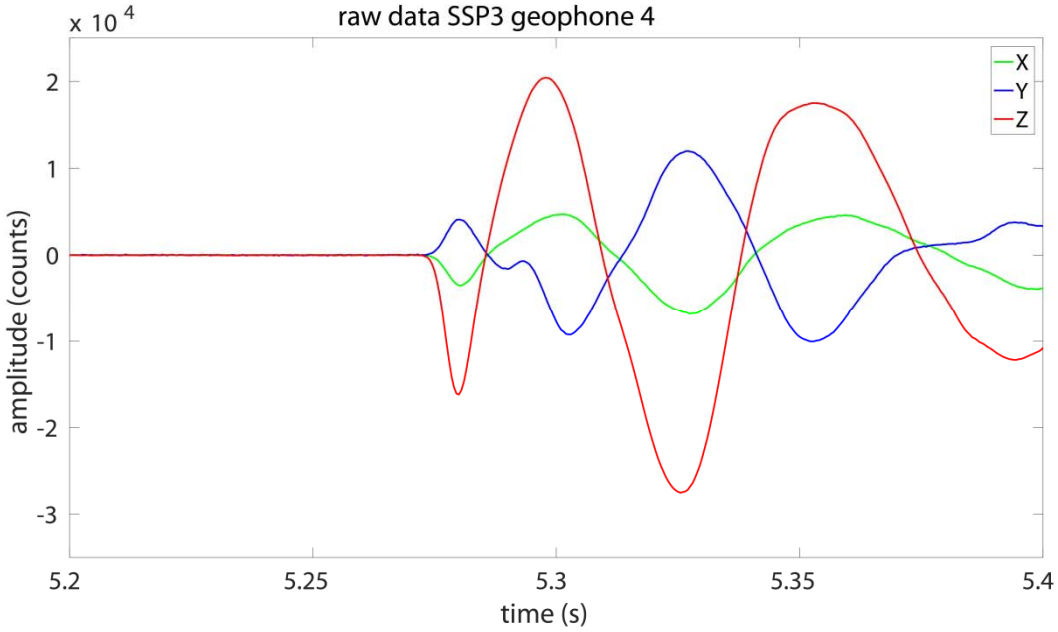
raw data SSP3 geophone 4
x 10 4
amplitude (counts)
time (s)
X
Y
Z
2
1
0
-1
-2
-3
5.2
5.25
5.3
5.35
5.4

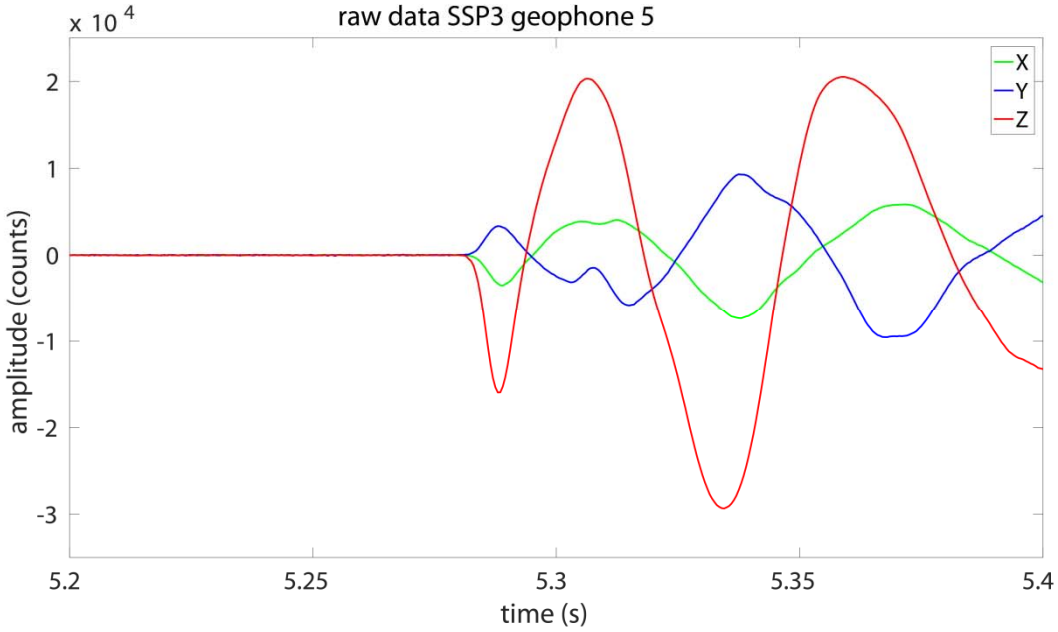
raw data SSP3 geophone 5
x 10 4
amplitude (counts)
time (s)
X
Y
Z
2
1
0
-1
-2
-3
5.2
5.25
5.3
5.35
5.4

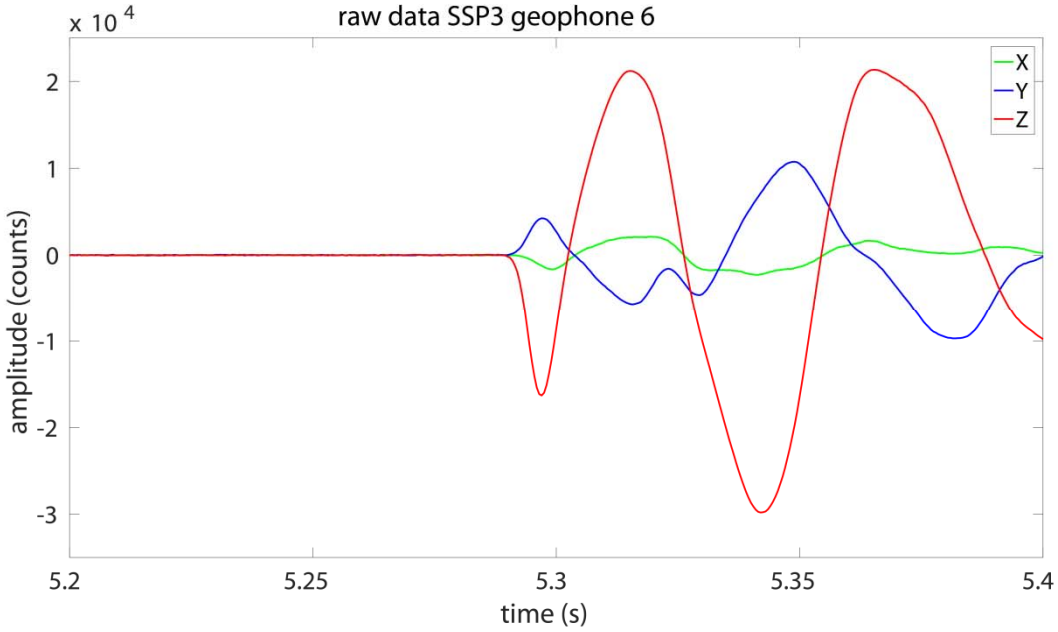
raw data SSP3 geophone 6
x 10 4
amplitude (counts)
time (s)
X
Y
Z
2
1
0
-1
-2
-3
5.2
5.25
5.3
5.35
5.4

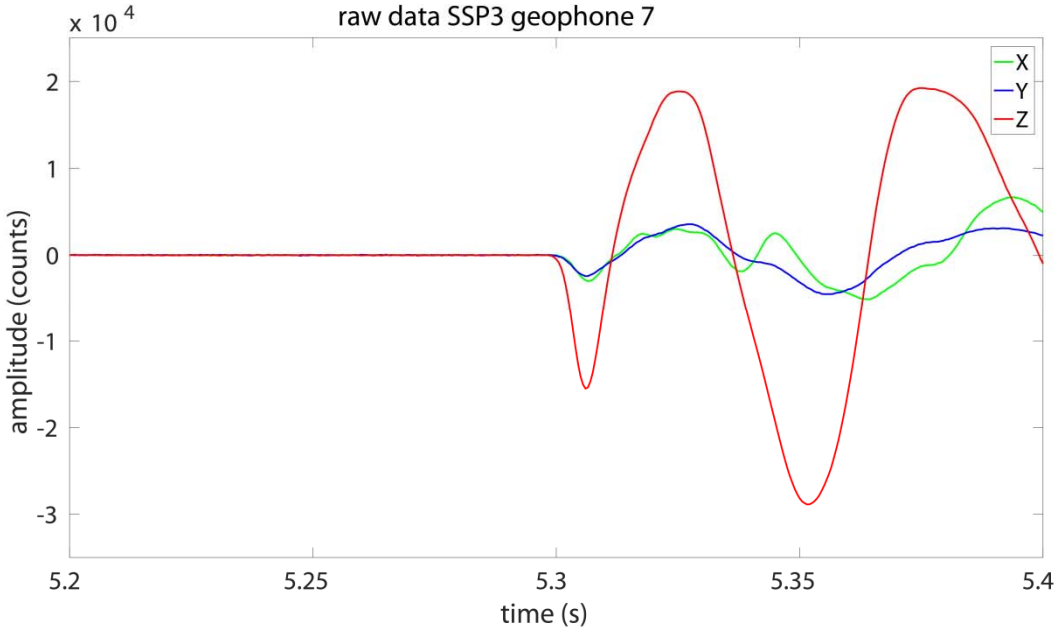
raw data SSP3 geophone 7
x 10 4
amplitude (counts)
time (s)
X
Y
Z
2
1
0
-1
-2
-3
5.2
5.25
5.3
5.35
5.4

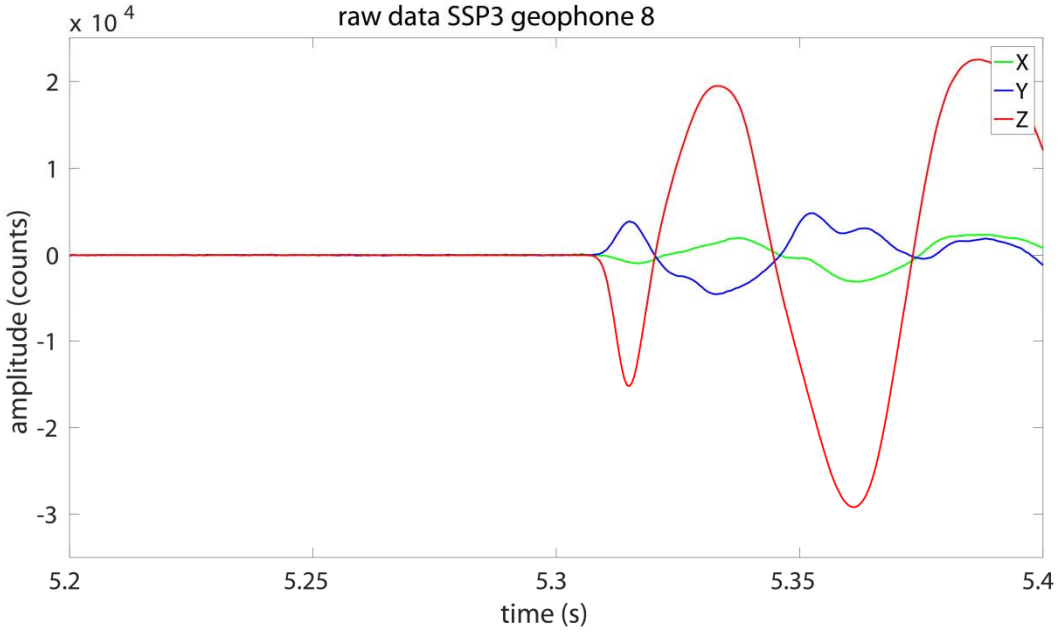
raw data SSP3 geophone 8
x 10 4
amplitude (counts)
time (s)
X
Y
Z
2
1
0
-1
-2
-3
5.2
5.25
5.3
5.35
5.4

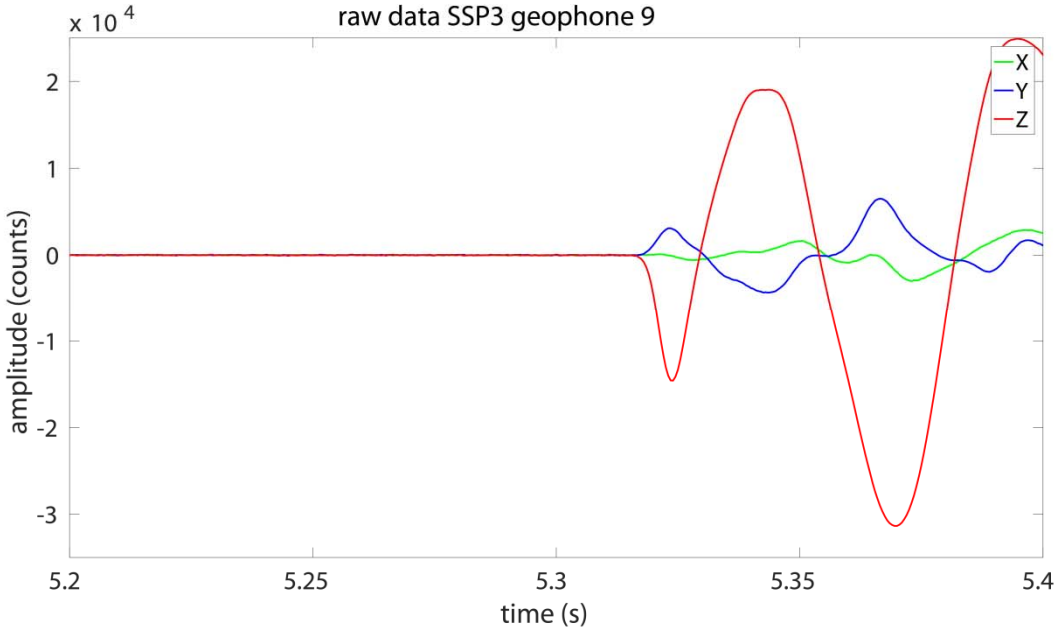
raw data SSP3 geophone 9
x 10 4
amplitude (counts)
time (s)
X
Y
Z
2
1
0
-1
-2
-3
5.2
5.25
5.3
5.35
5.4

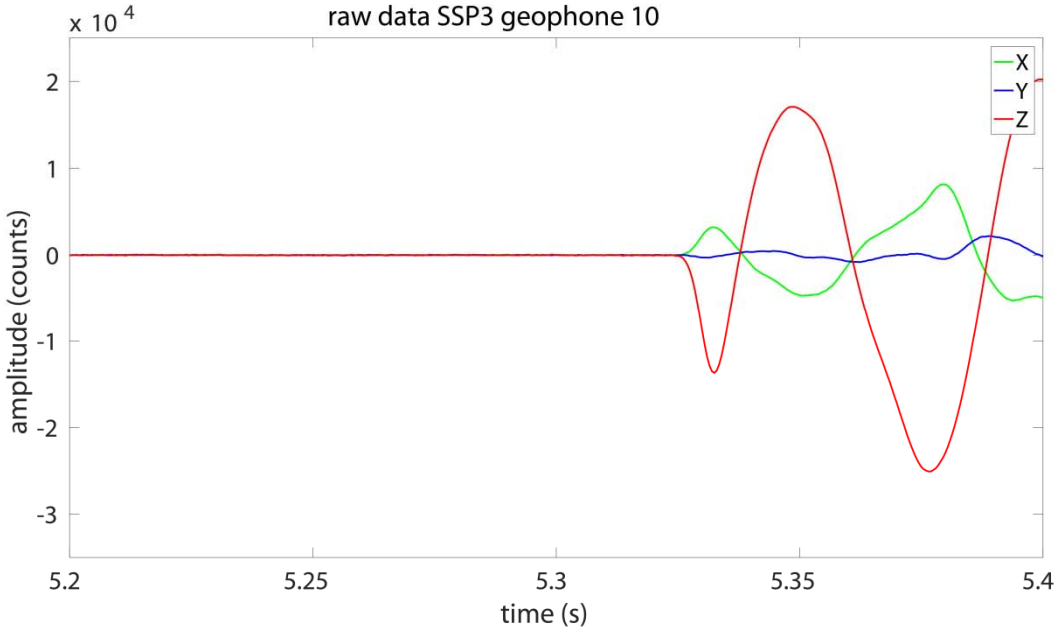
raw data SSP3 geophone 10
x 10 4
amplitude (counts)
time (s)
X
Y
Z
2
1
0
-1
-2
-3
5.2
5.25
5.3
5.35
5.4

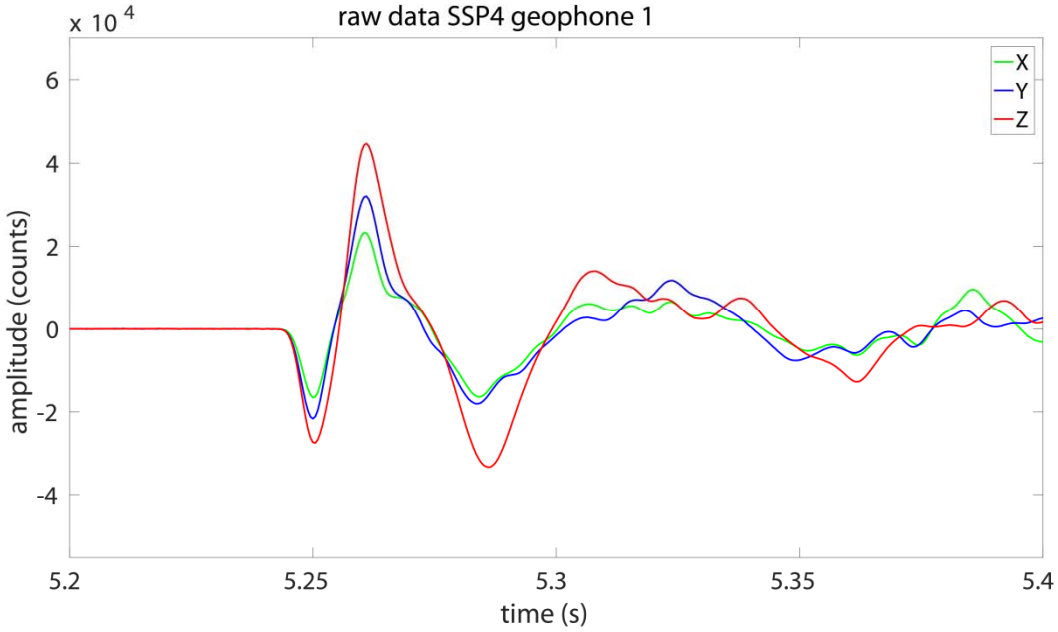
raw data SSP4 geophone 1
x 10 4
amplitude (counts)
time (s)
X
Y
Z
6
4
2
0
-2
-4
5.2
5.25
5.3
5.35
5.4

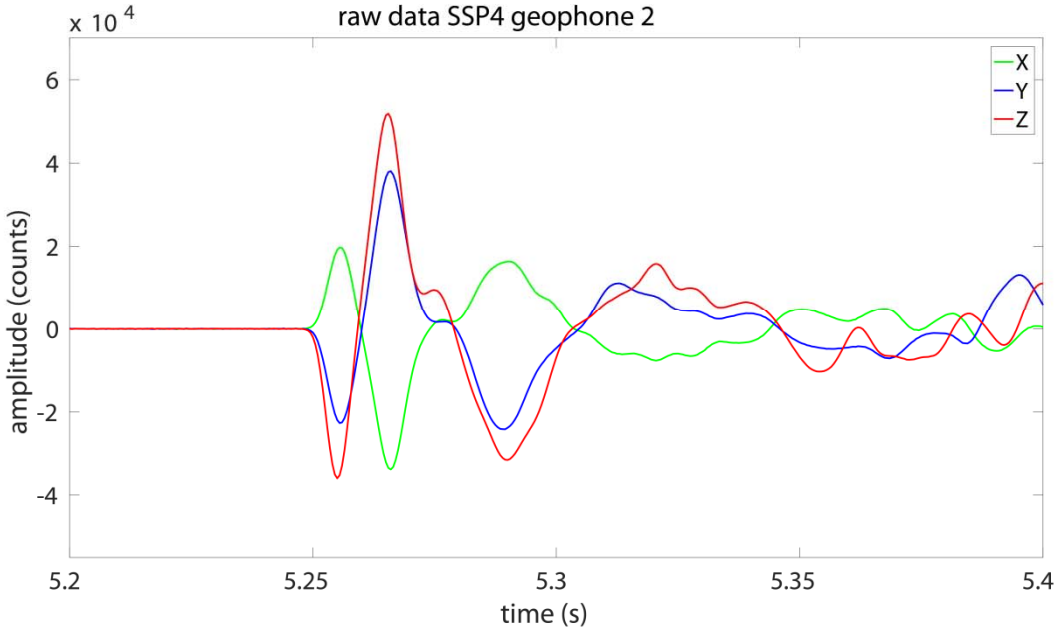
raw data SSP4 geophone 2
x 10 4
amplitude (counts)
time (s)
X
Y
Z
6
4
2
0
-2
-4
5.2
5.25
5.3
5.35
5.4

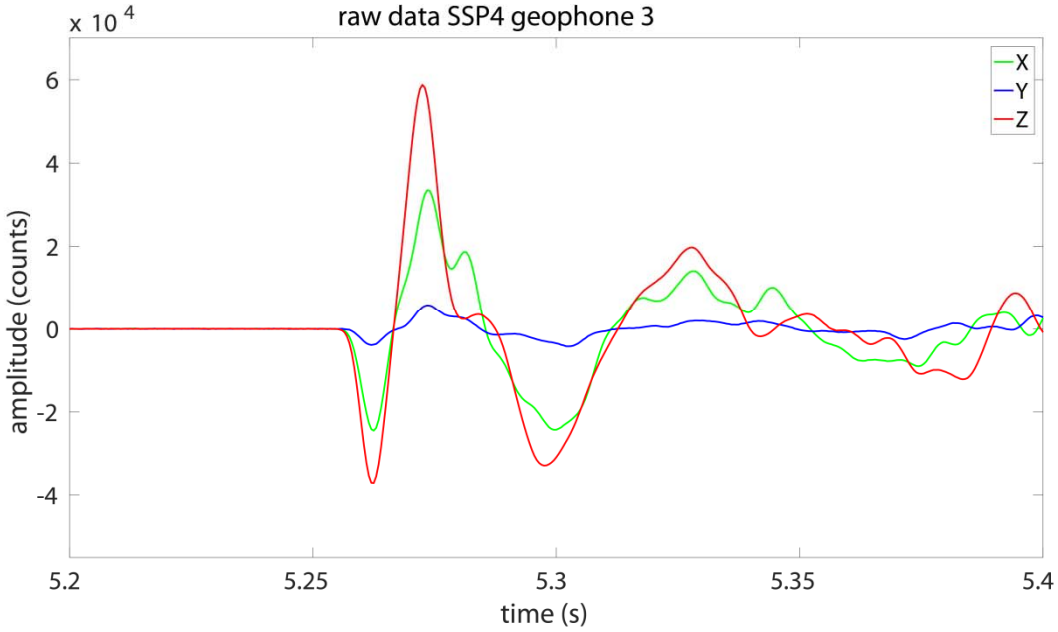
raw data SSP4 geophone 3
x 10 4
6
4
2
0
-2
-4
amplitude (counts)
5.2
5.25
5.3
5.35
5.4
time (s)
X
Y
Z

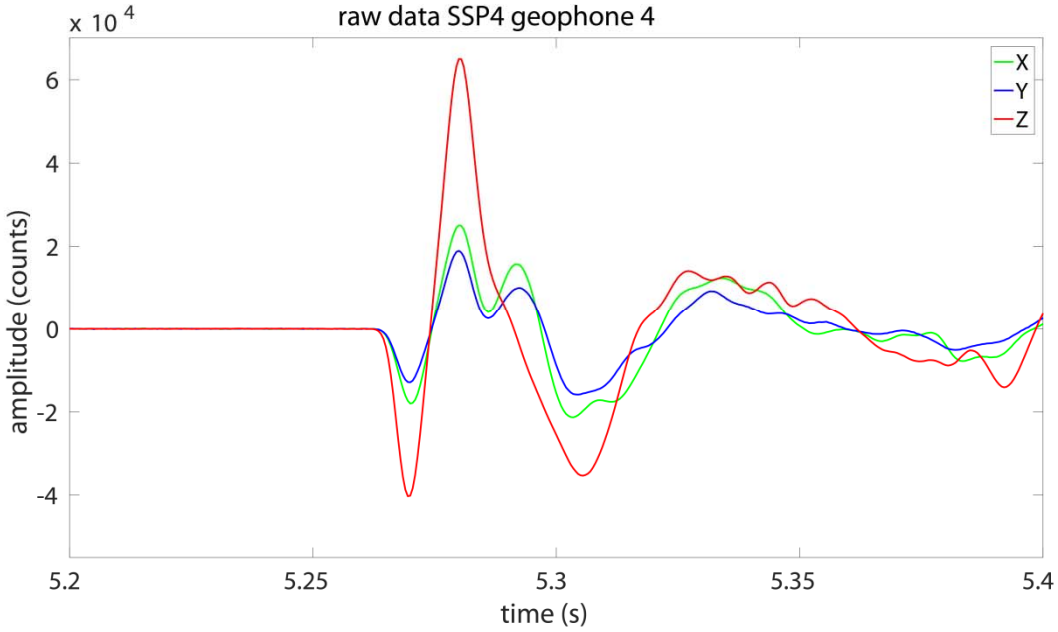
raw data SSP4 geophone 4
x 10 4
6
4
2
0
-2
-4
amplitude (counts)
5.2
5.25
5.3
5.35
5.4
time (s)
X
Y
Z

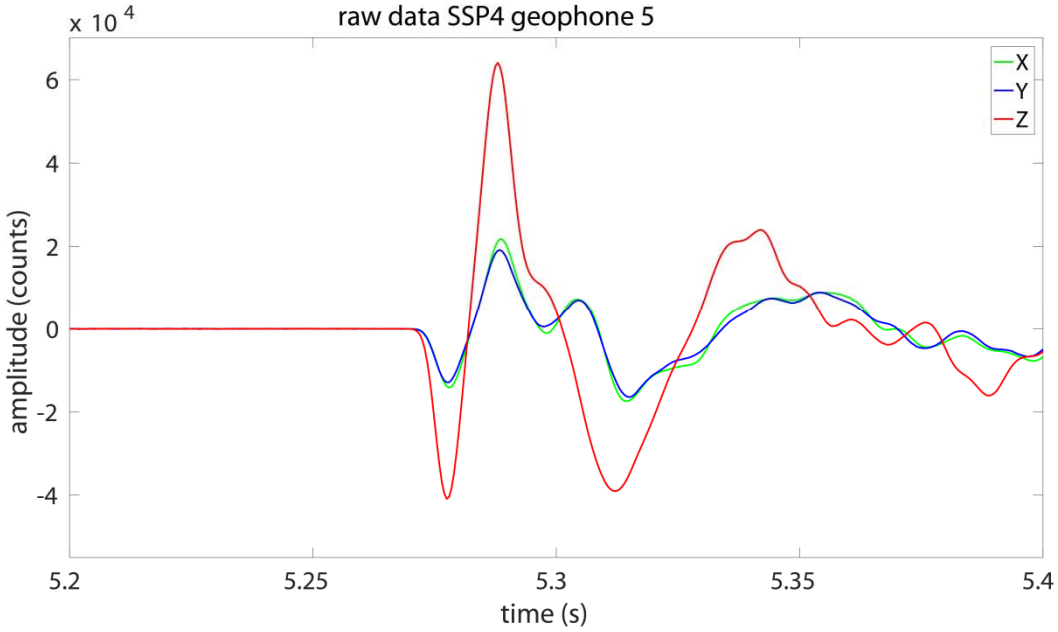
raw data SSP4 geophone 5
x 10 4
6
4
2
0
-2
-4
amplitude (counts)
5.2
5.25
5.3
5.35
5.4
time (s)
X
Y
Z

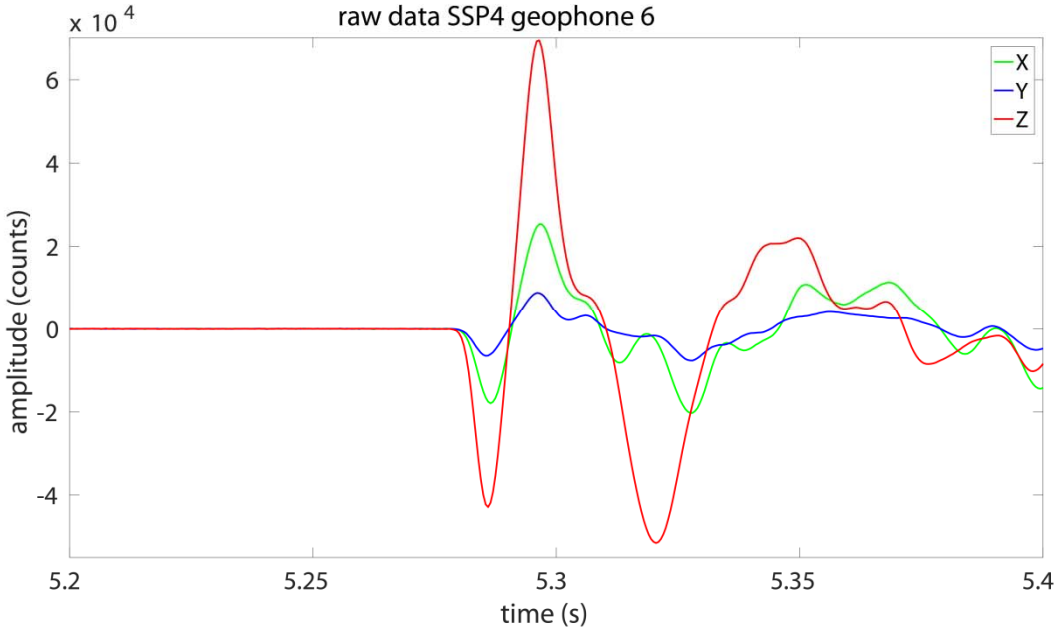
raw data SSP4 geophone 6
x 10 4
6
4
2
0
-2
-4
amplitude (counts)
5.2
5.25
5.3
5.35
5.4
time (s)
X
Y
Z

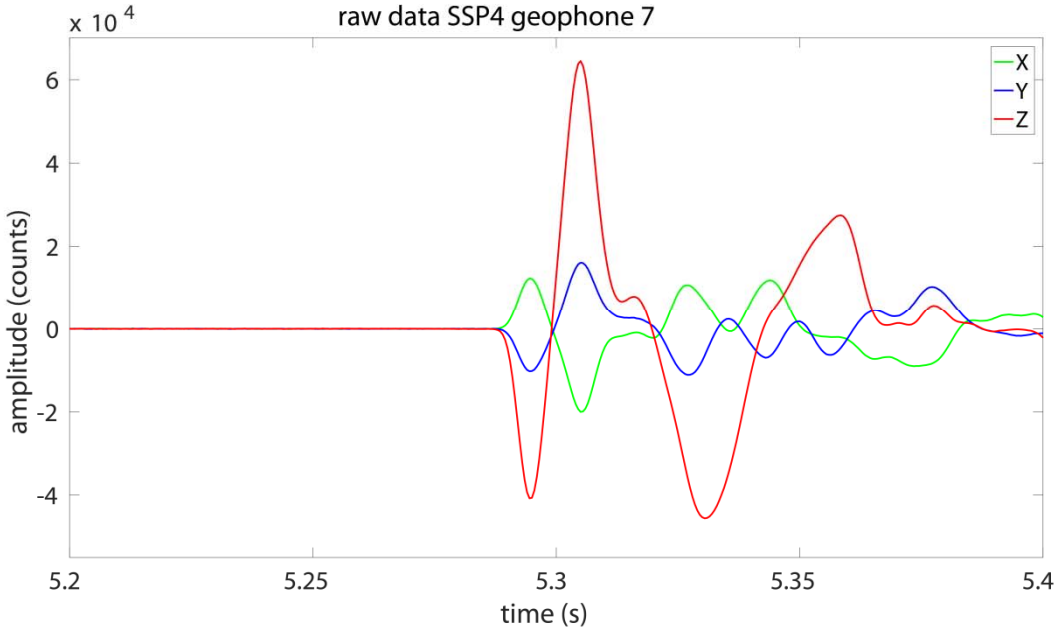
raw data SSP4 geophone 7
x 10 4
amplitude (counts)
time (s)
X
Y
Z
6
4
2
0
-2
-4
5.2
5.25
5.3
5.35
5.4

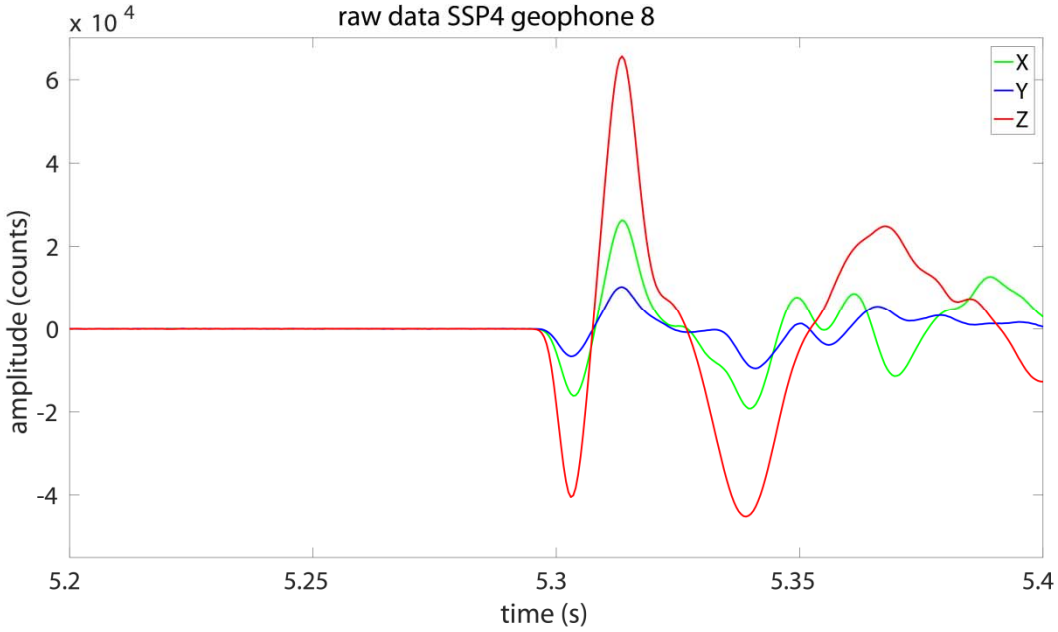
raw data SSP4 geophone 8
x 10 4
amplitude (counts)
time (s)
X
Y
Z
6
4
2
0
-2
-4
5.2
5.25
5.3
5.35
5.4

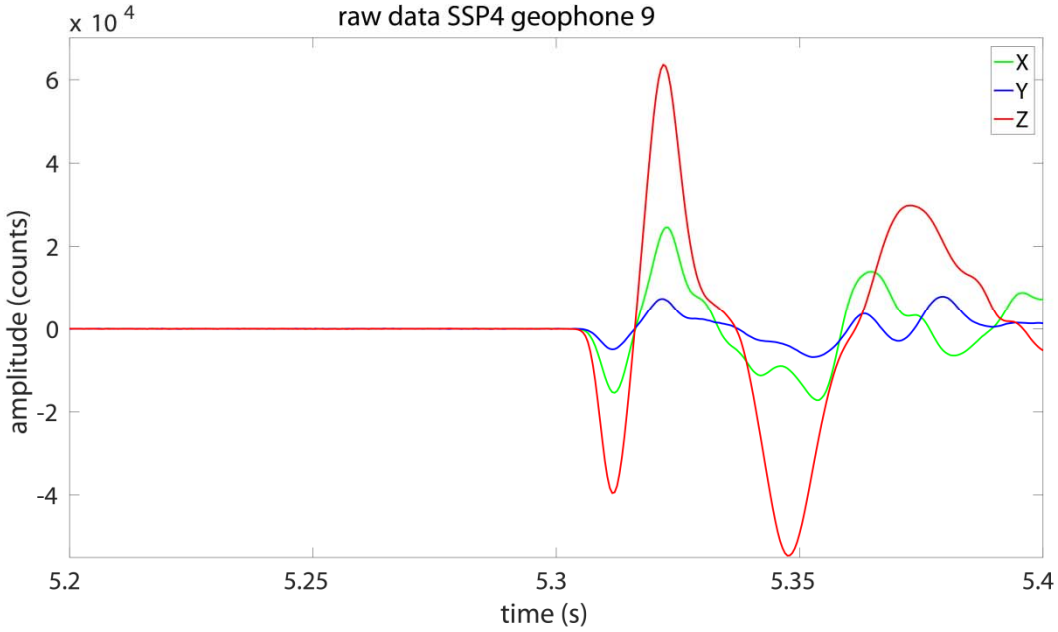
raw data SSP4 geophone 9
x 10 4
amplitude (counts)
time (s)
X
Y
Z
6
4
2
0
-2
-4
5.2
5.25
5.3
5.35
5.4

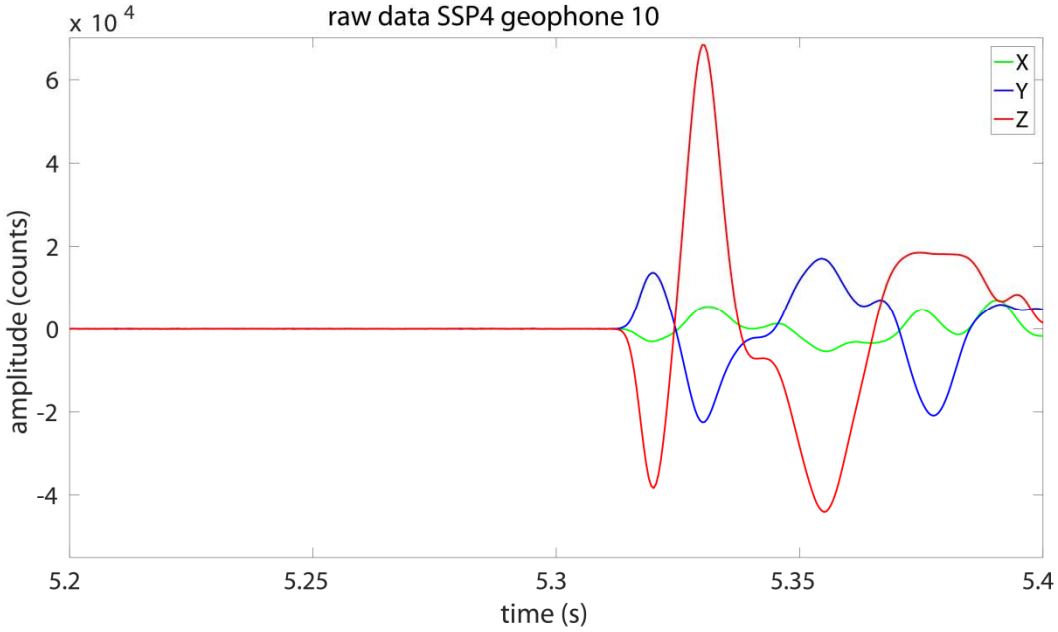
raw data SSP4 geophone 10
x 10 4
amplitude (counts)
time (s)
X
Y
Z
6
4
2
0
-2
-4
5.2
5.25
5.3
5.35
5.4

Appendix 2: Calculated phi

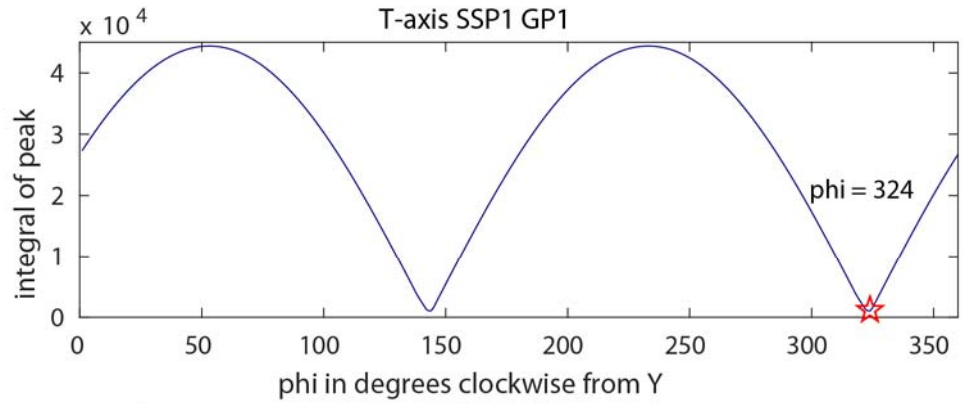
T-axis SSP1 GP1
x 10 4
integral of peak
phi = 324
phi in degrees clockwise from Y

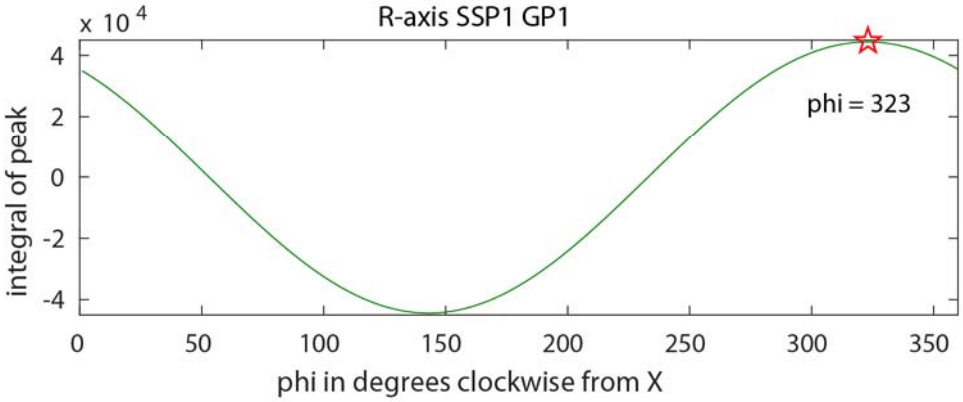
R-axis SSP1 GP1
x 10 4
integral of peak
phi = 323
phi in degrees clockwise from X

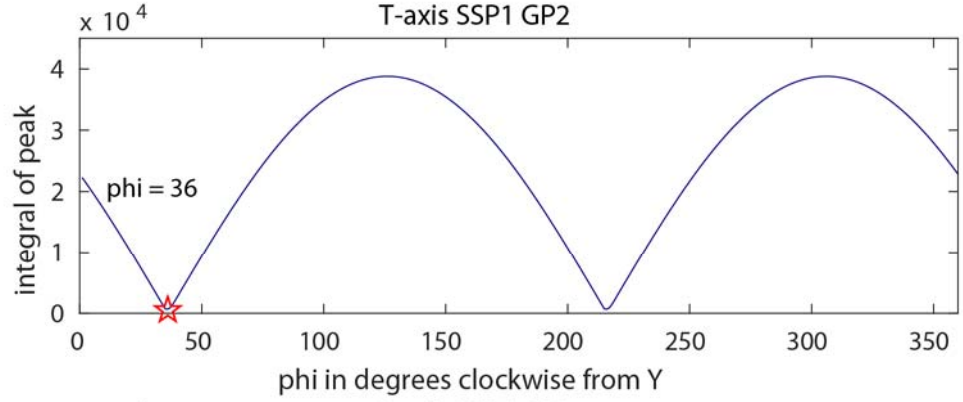
T-axis SSP1 GP2
x 10 4
integral of peak
phi = 36
phi in degrees clockwise from Y

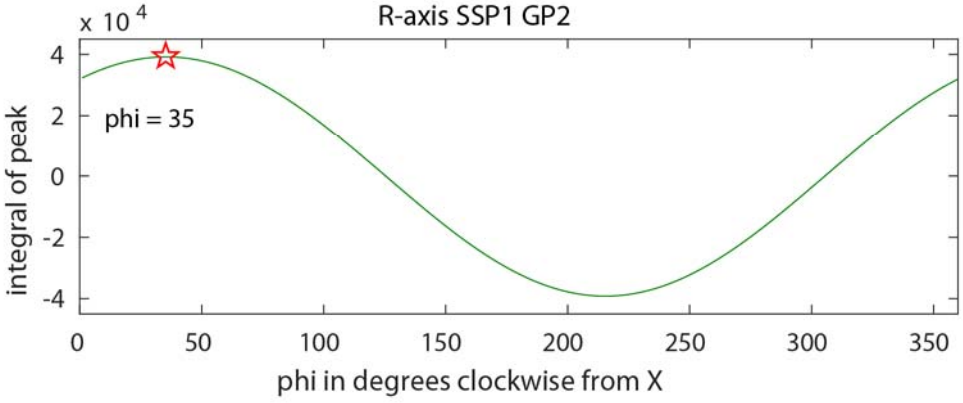
R-axis SSP1 GP2
x 10 4
integral of peak
phi = 35
phi in degrees clockwise from X

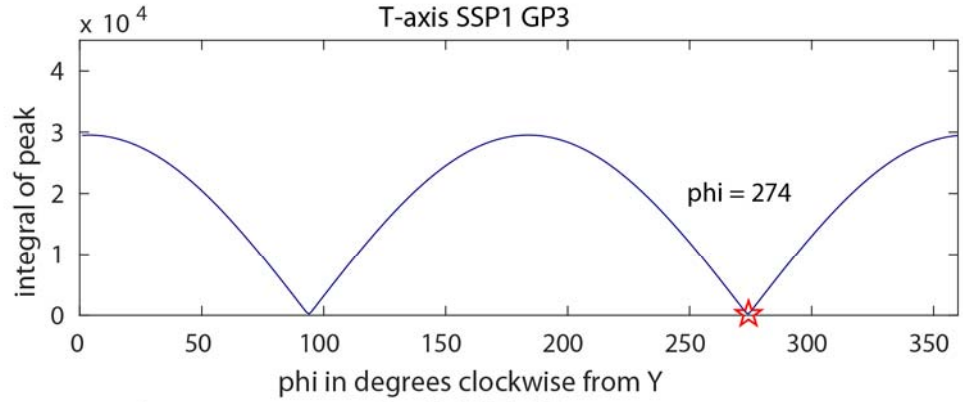
T-axis SSP1 GP3
x 10 4
integral of peak
phi = 274
phi in degrees clockwise from Y

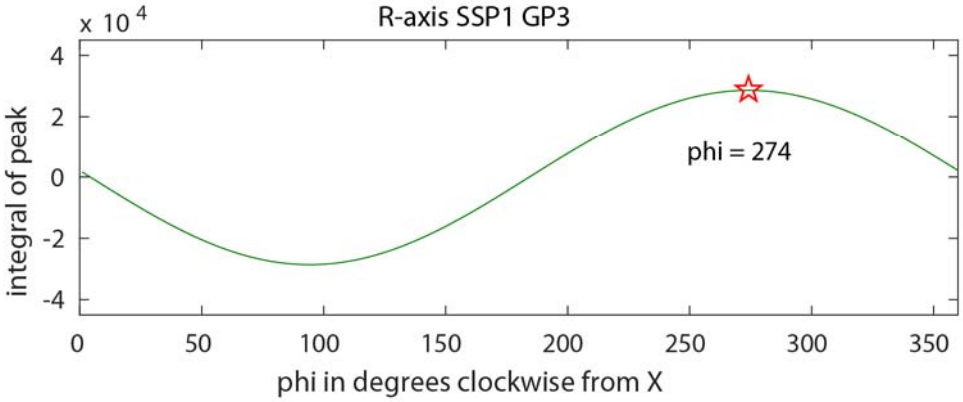
R-axis SSP1 GP3
x 10 4
integral of peak
phi = 274
phi in degrees clockwise from X

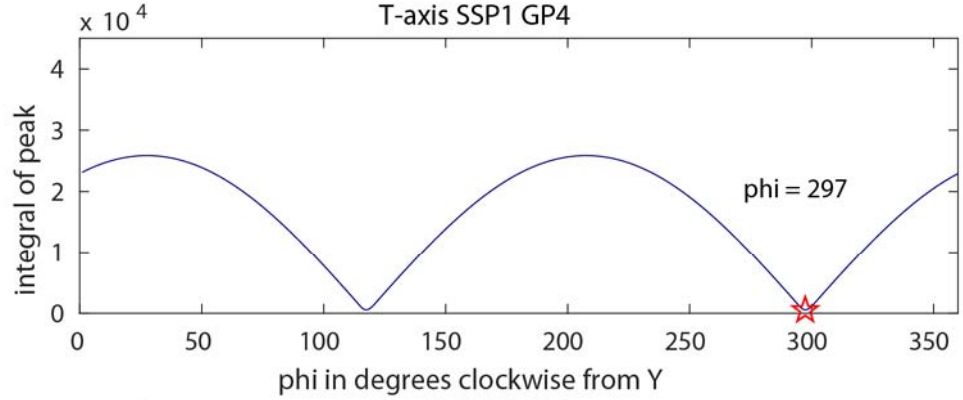
T-axis SSP1 GP4
x 10 4
integral of peak
phi = 297
phi in degrees clockwise from Y

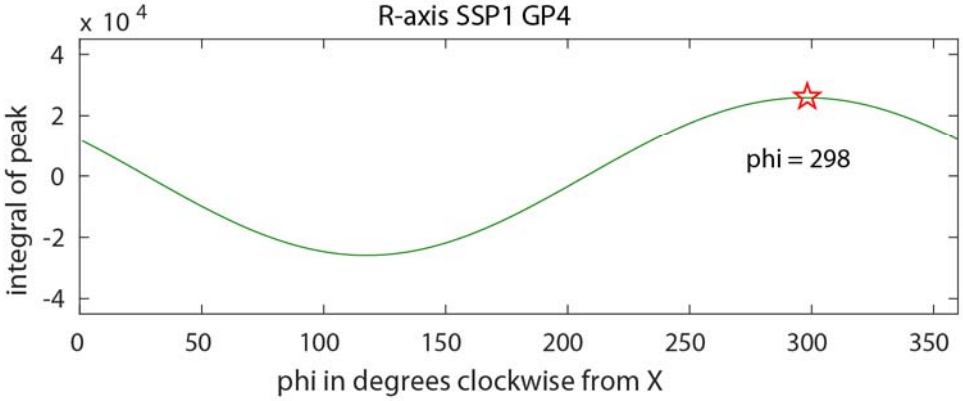
R-axis SSP1 GP4
x 10 4
integral of peak
phi = 298
phi in degrees clockwise from X

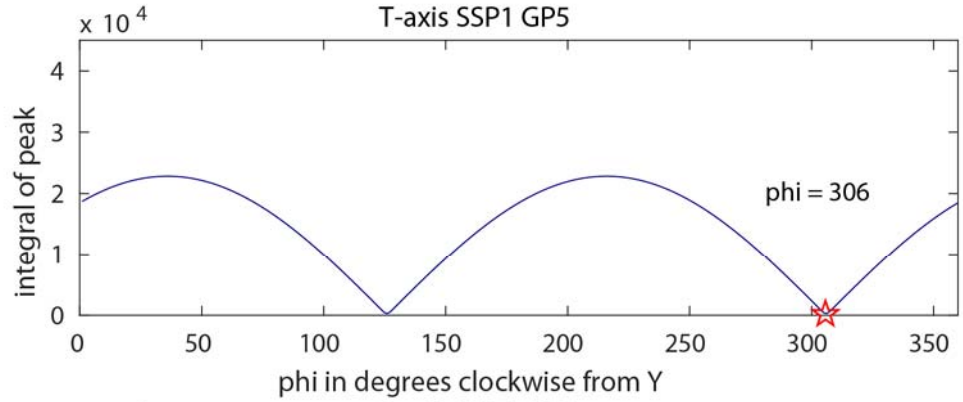
T-axis SSP1 GP5
x 10^4
integral of peak
phi = 306
phi in degrees clockwise from Y

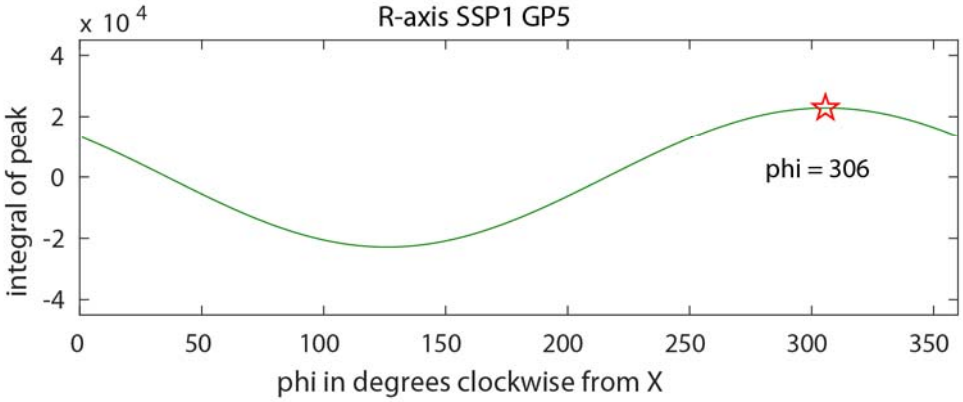
R-axis SSP1 GP5
x 10^4
integral of peak
phi = 306
phi in degrees clockwise from X

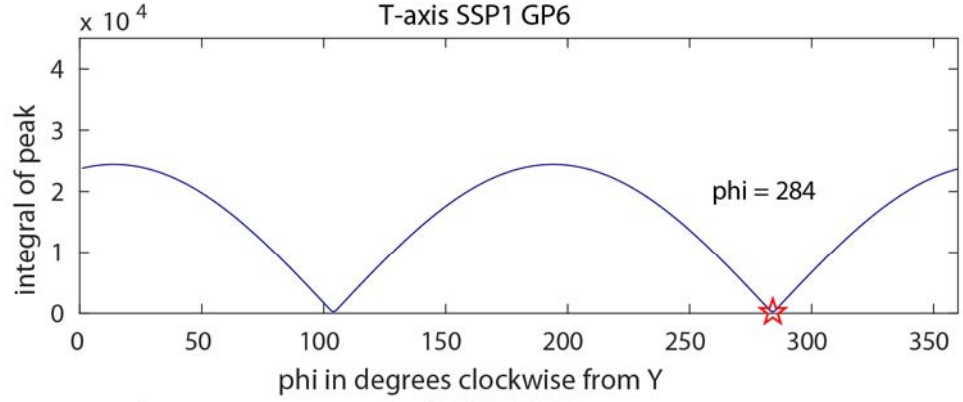
T-axis SSP1 GP6
x 10^4
integral of peak
phi = 284
phi in degrees clockwise from Y

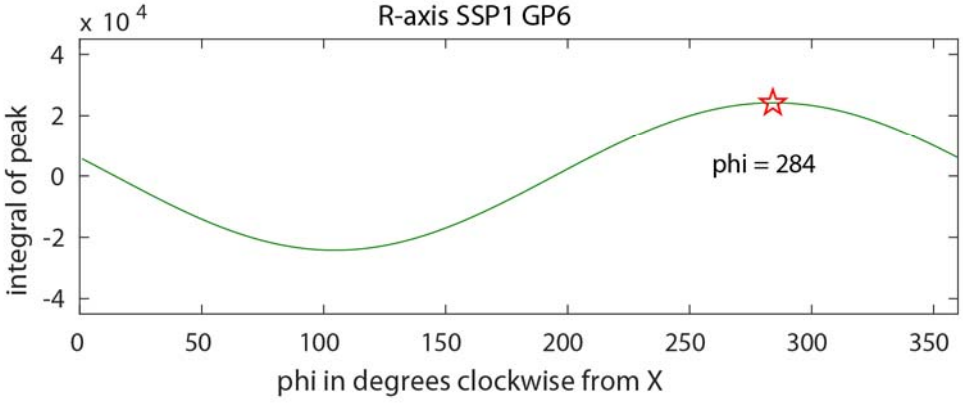
R-axis SSP1 GP6
x 10^4
integral of peak
phi = 284
phi in degrees clockwise from X

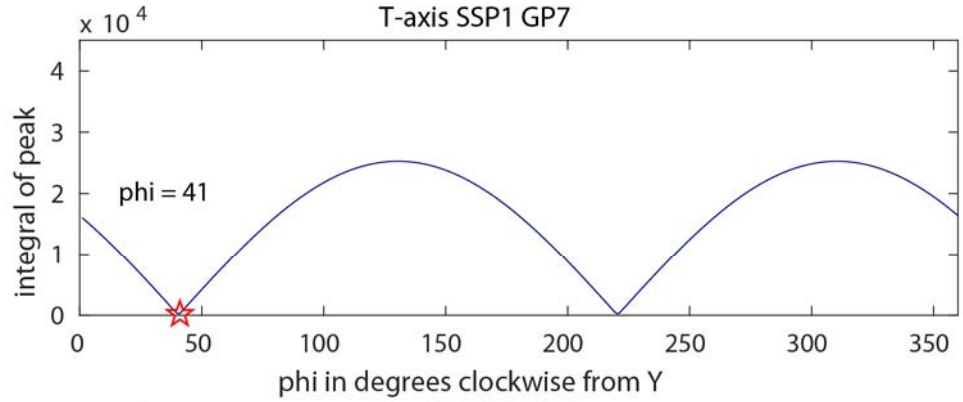
T-axis SSP1 GP7
x 10 4
integral of peak
phi = 41
phi in degrees clockwise from Y

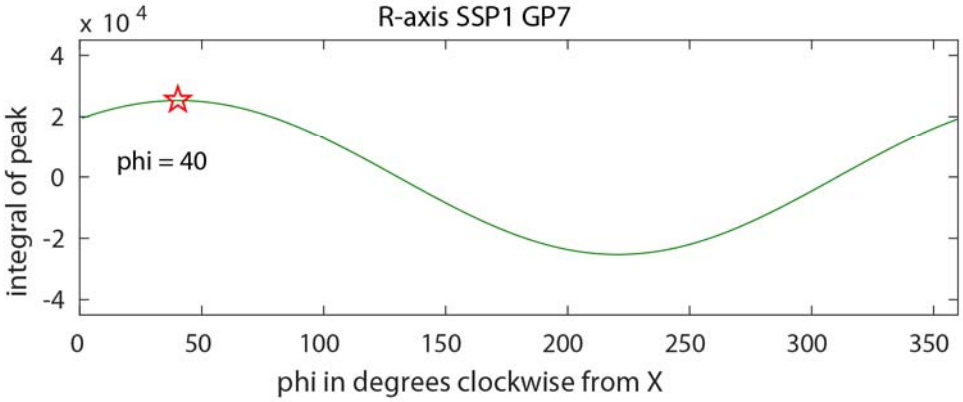
R-axis SSP1 GP7
x 10 4
integral of peak
phi = 40
phi in degrees clockwise from X

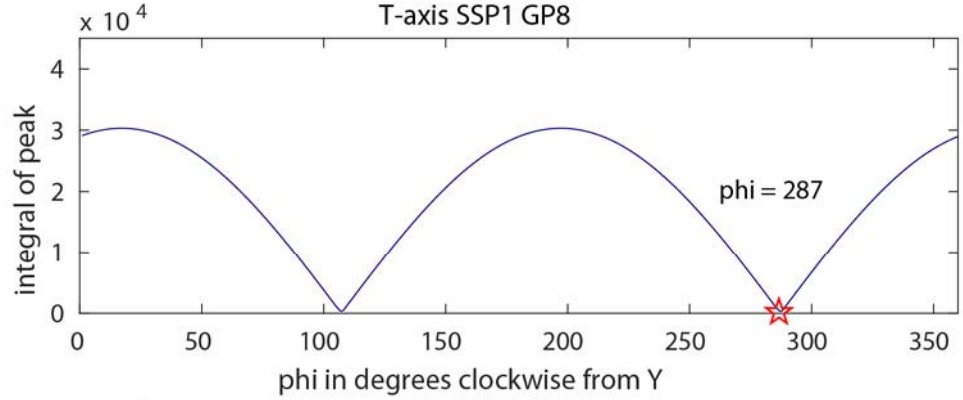
T-axis SSP1 GP8
x 10 4
integral of peak
phi = 287
phi in degrees clockwise from Y

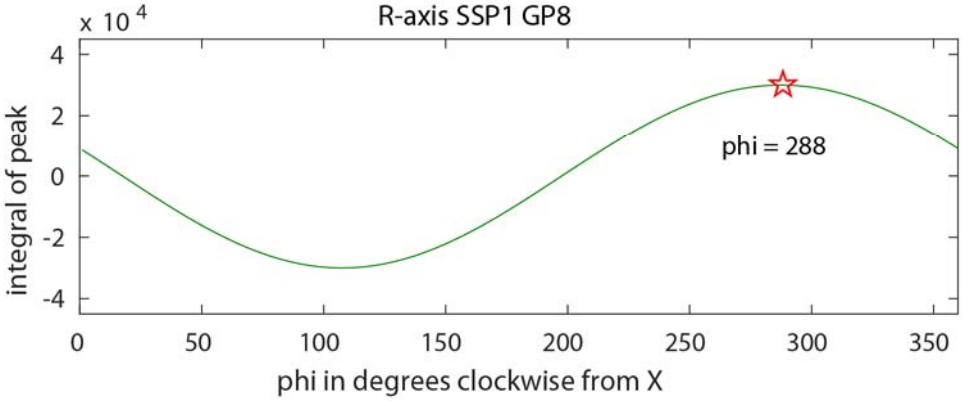
R-axis SSP1 GP8
x 10 4
integral of peak
phi = 288
phi in degrees clockwise from X

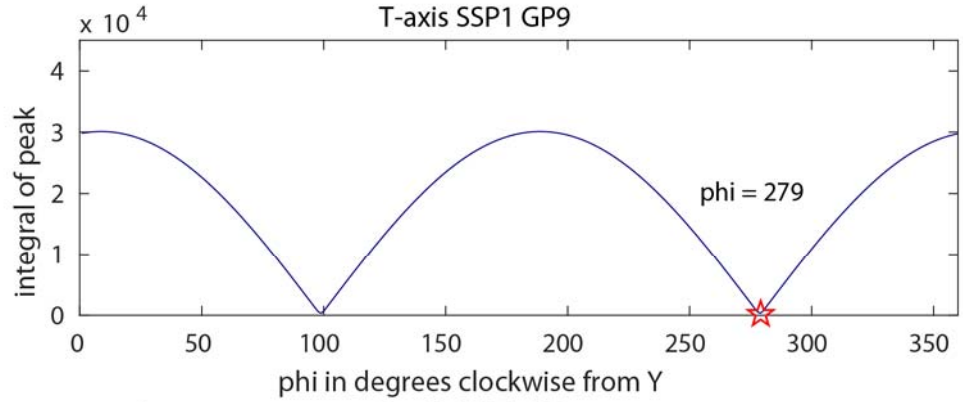
T-axis SSP1 GP9
x 10 4
integral of peak
phi = 279
phi in degrees clockwise from Y

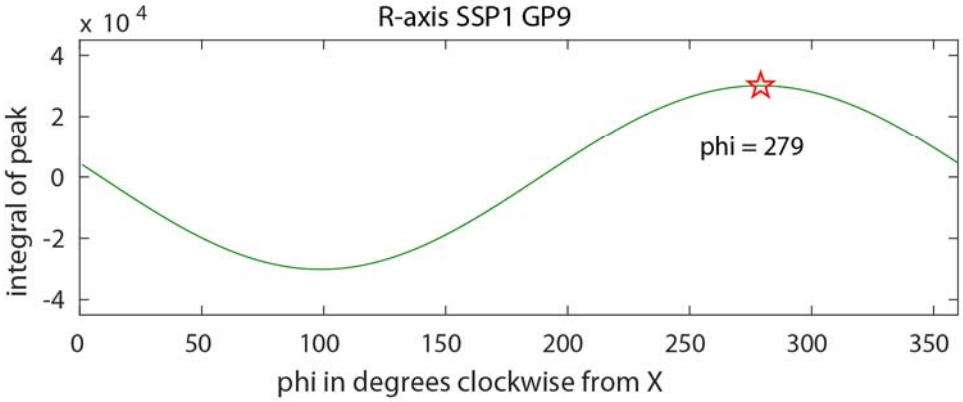
R-axis SSP1 GP9
x 10 4
integral of peak
phi = 279
phi in degrees clockwise from X

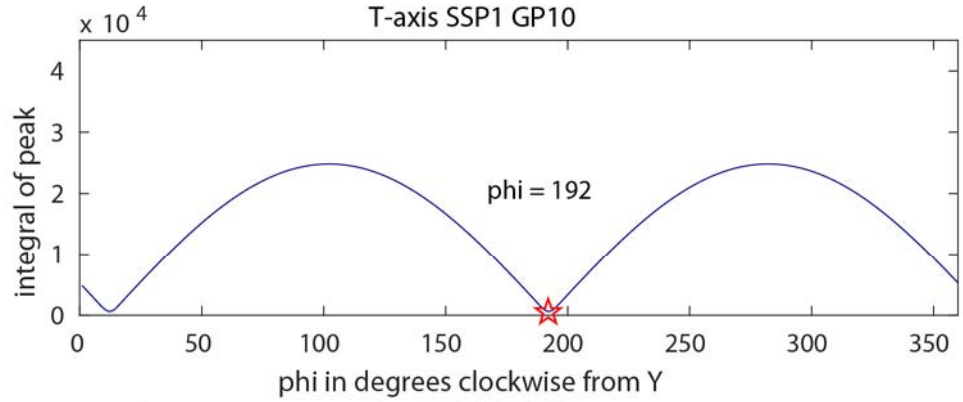
T-axis SSP1 GP10
x 10 4
integral of peak
phi = 192
phi in degrees clockwise from Y

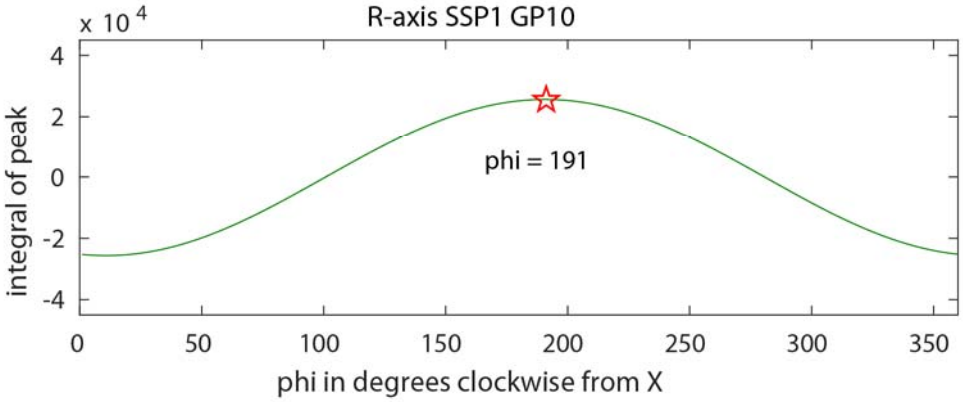
R-axis SSP1 GP10
x 10 4
integral of peak
phi = 191
phi in degrees clockwise from X

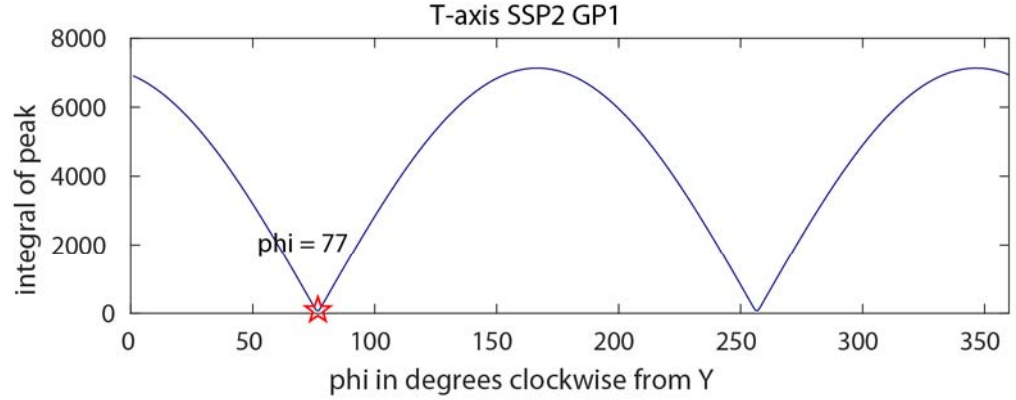
T-axis SSP2 GP1
integral of peak
8000
6000
4000
2000
0
phi = 77
0
50
100
150
200
250
300
350
phi in degrees clockwise from Y

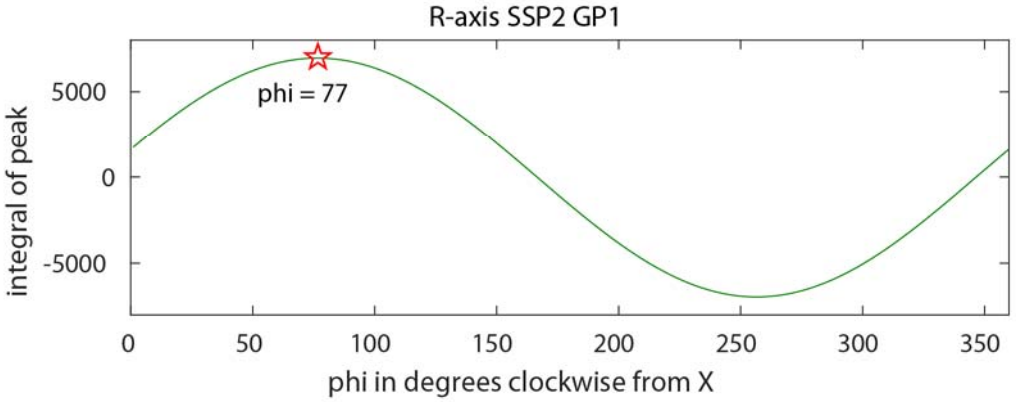
R-axis SSP2 GP1
integral of peak
5000
0
-5000
phi = 77
0
50
100
150
200
250
300
350
phi in degrees clockwise from X

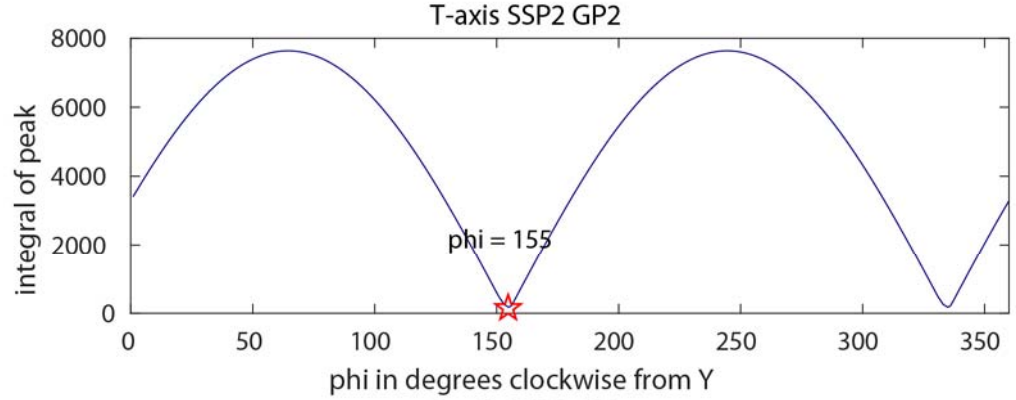
T-axis SSP2 GP2
integral of peak
8000
6000
4000
2000
0
phi = 155
0
50
100
150
200
250
300
350
phi in degrees clockwise from Y

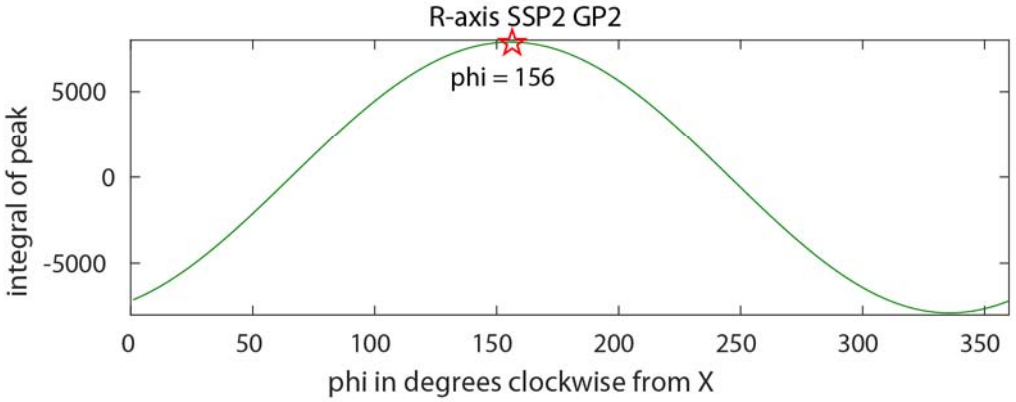
R-axis SSP2 GP2
integral of peak
5000
0
-5000
phi = 156
0
50
100
150
200
250
300
350
phi in degrees clockwise from X

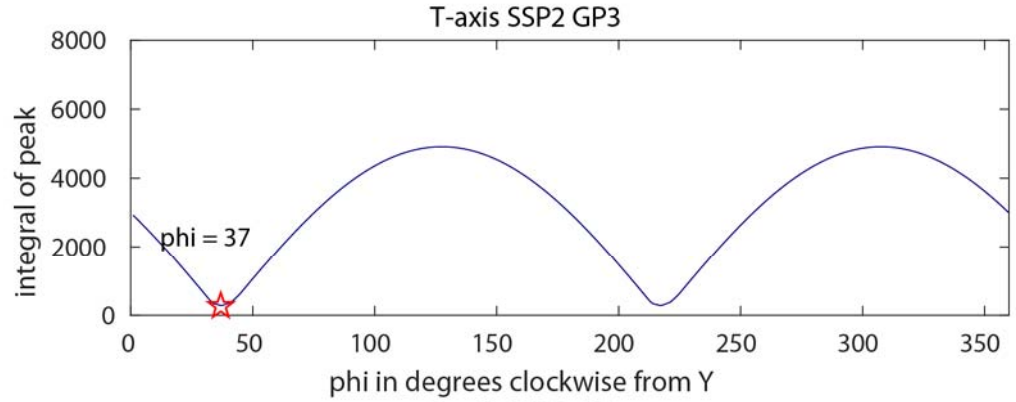
T-axis SSP2 GP3
integral of peak
phi = 37
phi in degrees clockwise from Y

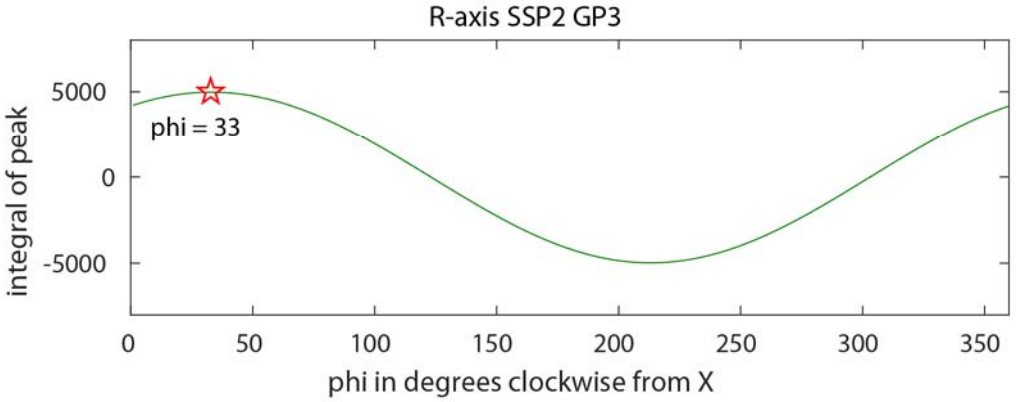
R-axis SSP2 GP3
integral of peak
phi = 33
phi in degrees clockwise from X

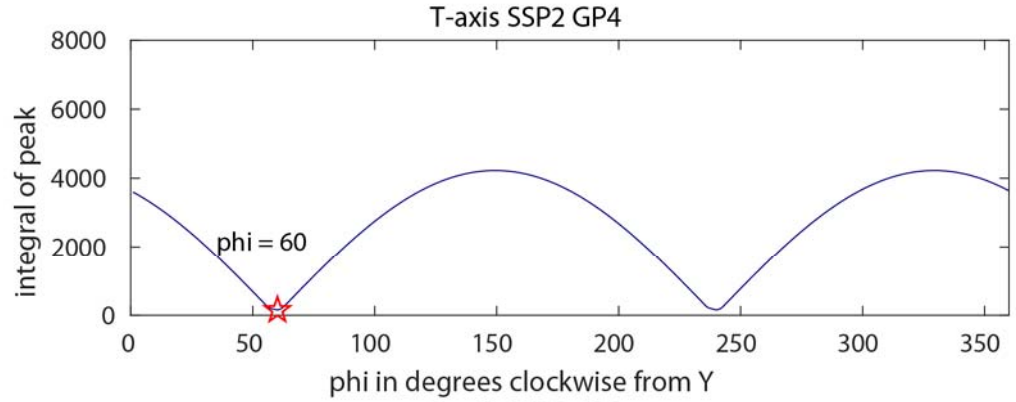
T-axis SSP2 GP4
integral of peak
phi = 60
phi in degrees clockwise from Y

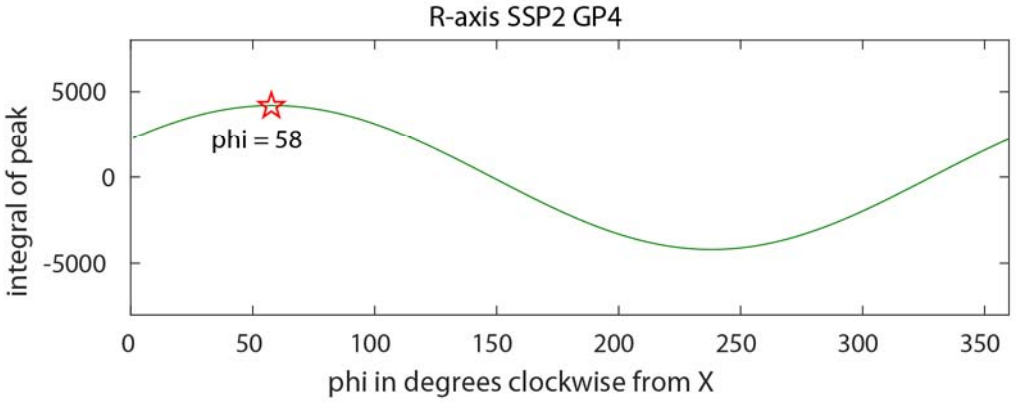
R-axis SSP2 GP4
integral of peak
phi = 58
phi in degrees clockwise from X

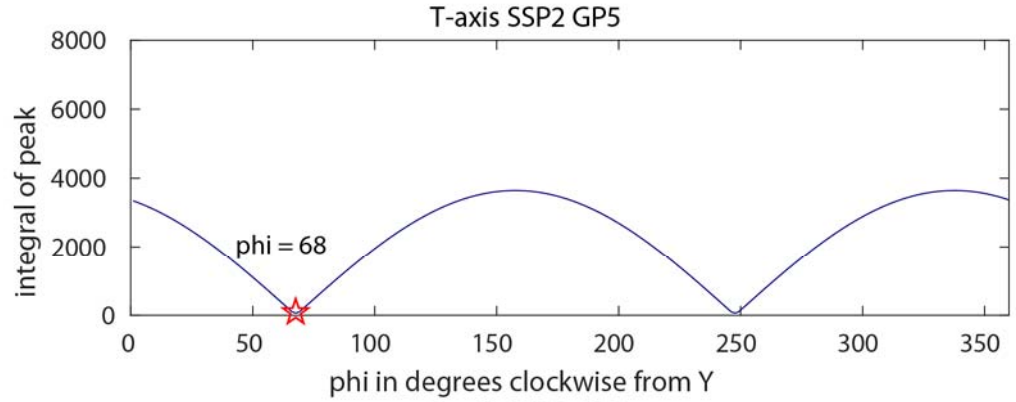
T-axis SSP2 GP5
integral of peak
8000
6000
4000
2000
0
phi = 68
0
50
100
150
200
250
300
350
phi in degrees clockwise from Y

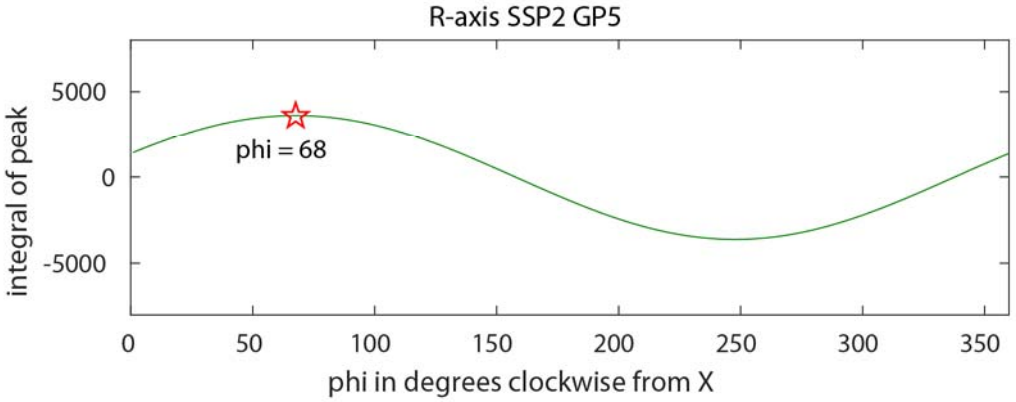
R-axis SSP2 GP5
integral of peak
5000
0
-5000
phi = 68
0
50
100
150
200
250
300
350
phi in degrees clockwise from X

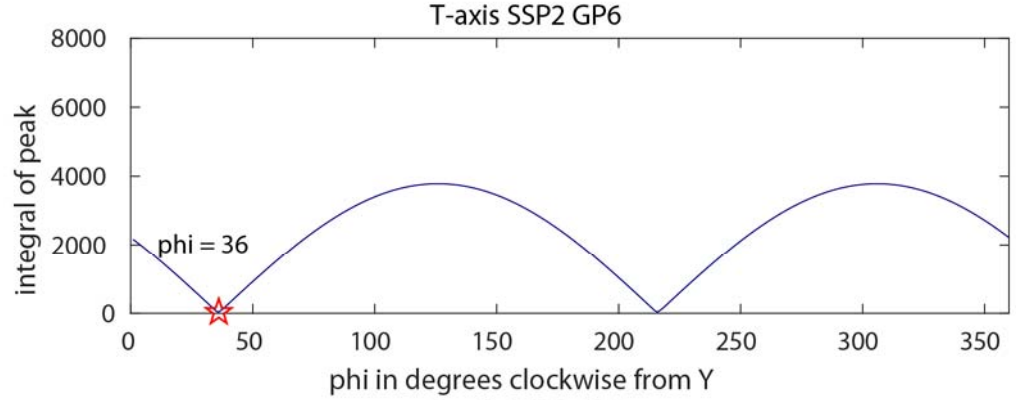
T-axis SSP2 GP6
integral of peak
8000
6000
4000
2000
0
phi = 36
0
50
100
150
200
250
300
350
phi in degrees clockwise from Y

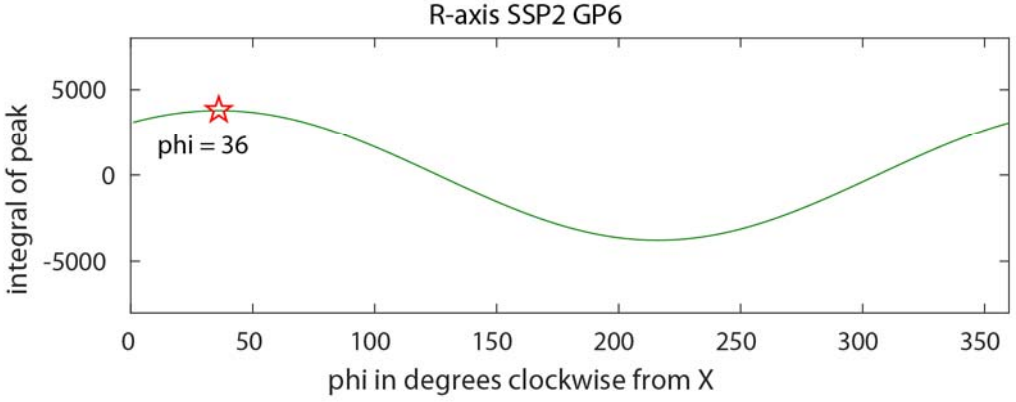
R-axis SSP2 GP6
integral of peak
5000
0
-5000
phi = 36
0
50
100
150
200
250
300
350
phi in degrees clockwise from X

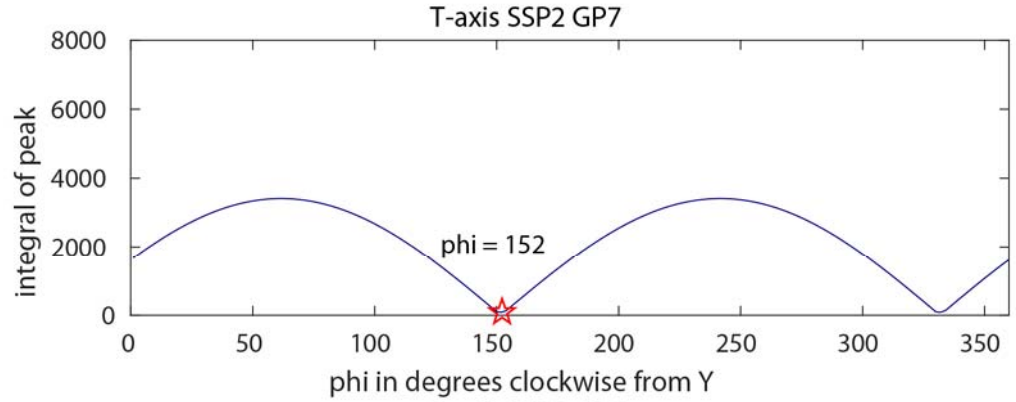
T-axis SSP2 GP7
integral of peak
8000
6000
4000
2000
0
phi = 152
0
50
100
150
200
250
300
350
phi in degrees clockwise from Y

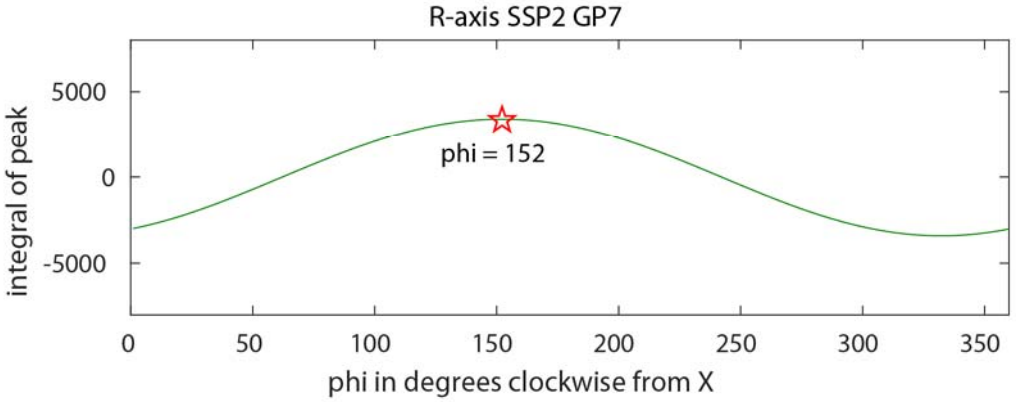
R-axis SSP2 GP7
integral of peak
5000
0
-5000
phi = 152
0
50
100
150
200
250
300
350
phi in degrees clockwise from X

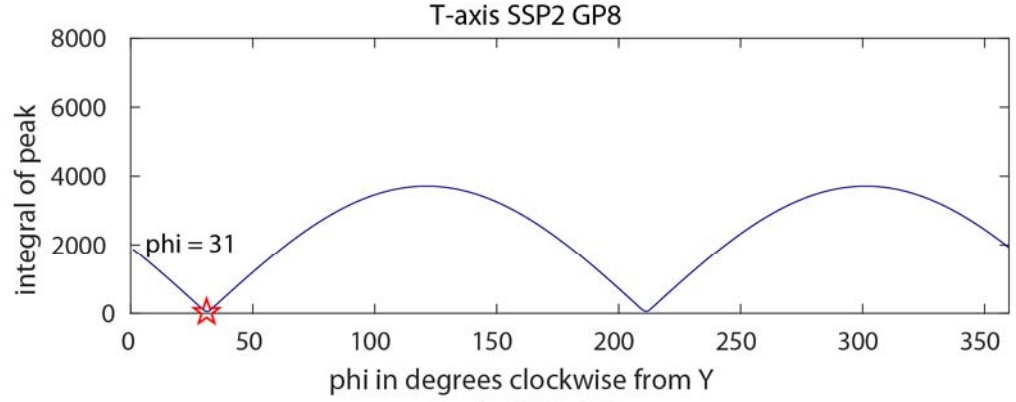
T-axis SSP2 GP8
integral of peak
8000
6000
4000
2000
0
phi = 31
0
50
100
150
200
250
300
350
phi in degrees clockwise from Y

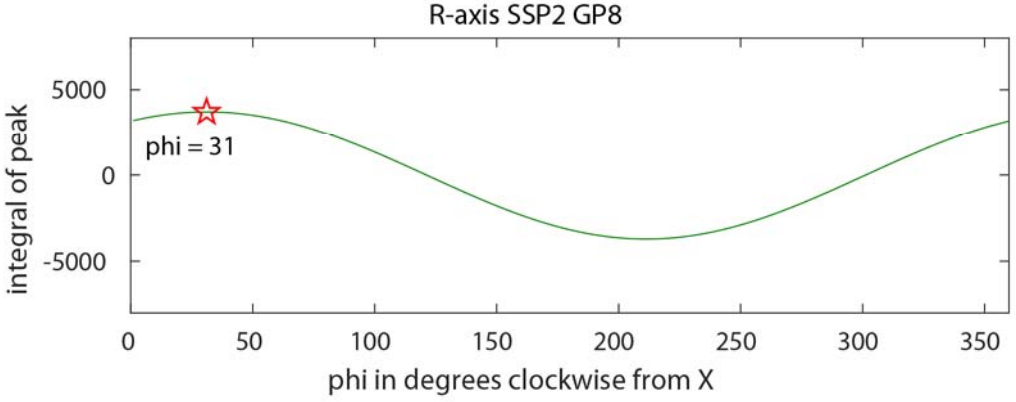
R-axis SSP2 GP8
integral of peak
5000
0
-5000
phi = 31
0
50
100
150
200
250
300
350
phi in degrees clockwise from X

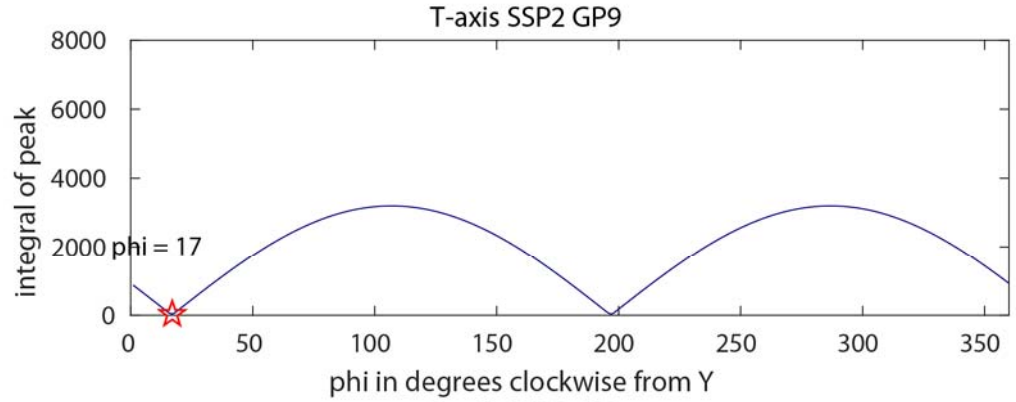
T-axis SSP2 GP9
integral of peak
8000
6000
4000
2000
0
phi = 17
0
50
100
150
200
250
300
350
phi in degrees clockwise from Y

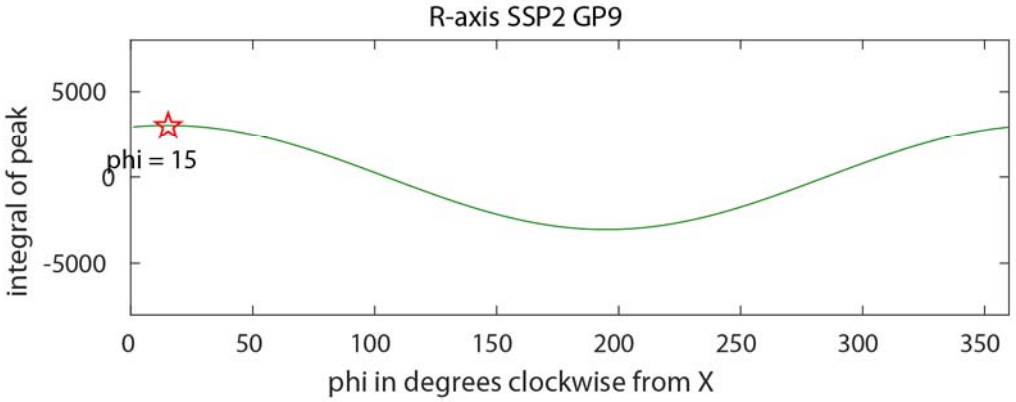
R-axis SSP2 GP9
integral of peak
5000
0
-5000
phi = 15
0
50
100
150
200
250
300
350
phi in degrees clockwise from X

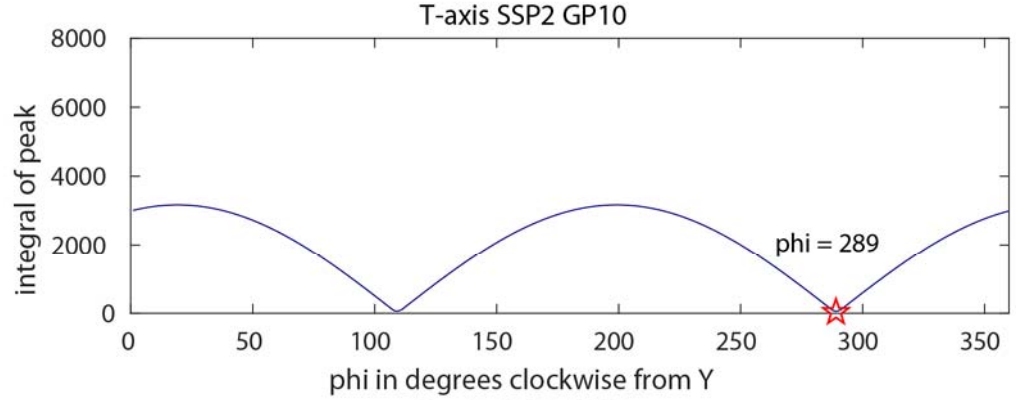
T-axis SSP2 GP10
integral of peak
8000
6000
4000
2000
0
phi = 289
0
50
100
150
200
250
300
350
phi in degrees clockwise from Y

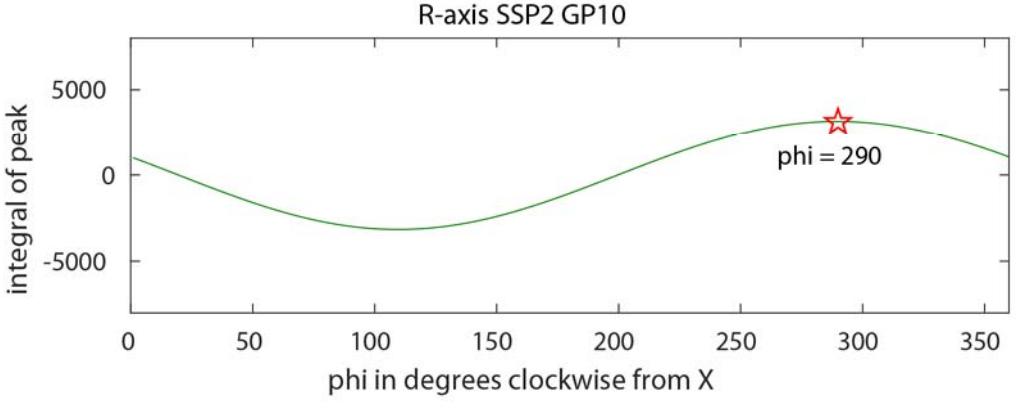
R-axis SSP2 GP10
integral of peak
5000
0
-5000
phi = 290
0
50
100
150
200
250
300
350
phi in degrees clockwise from X

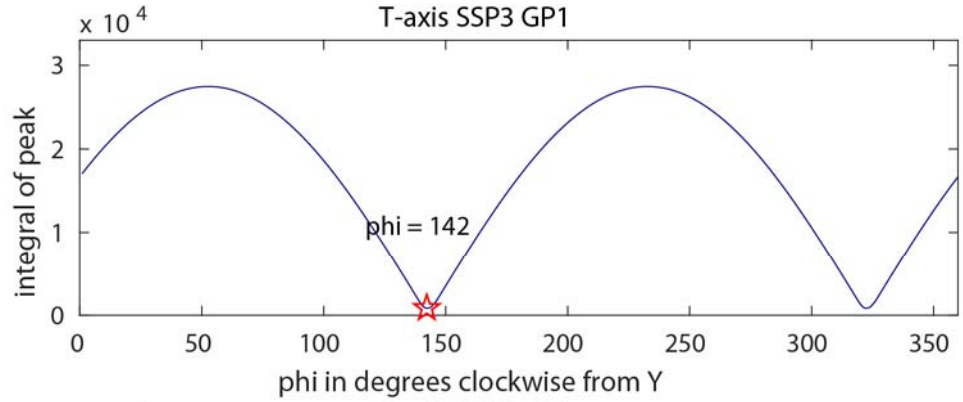
T-axis SSP3 GP1
x 10 4
integral of peak
phi = 142
phi in degrees clockwise from Y

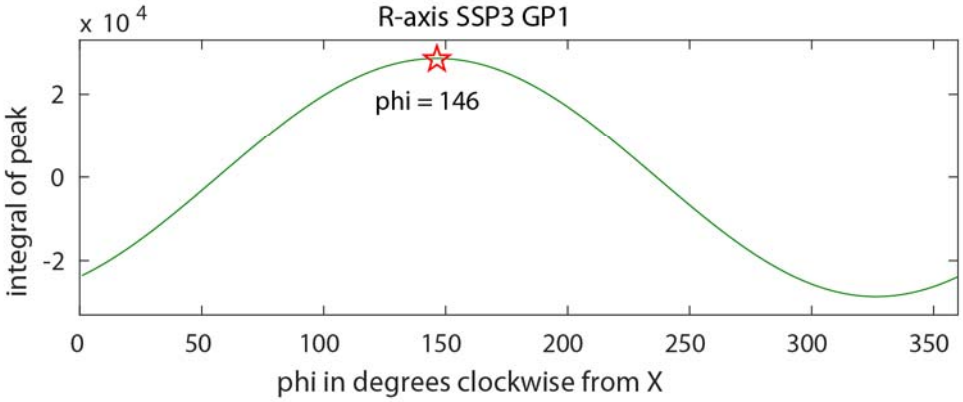
R-axis SSP3 GP1
x 10 4
integral of peak
phi = 146
phi in degrees clockwise from X

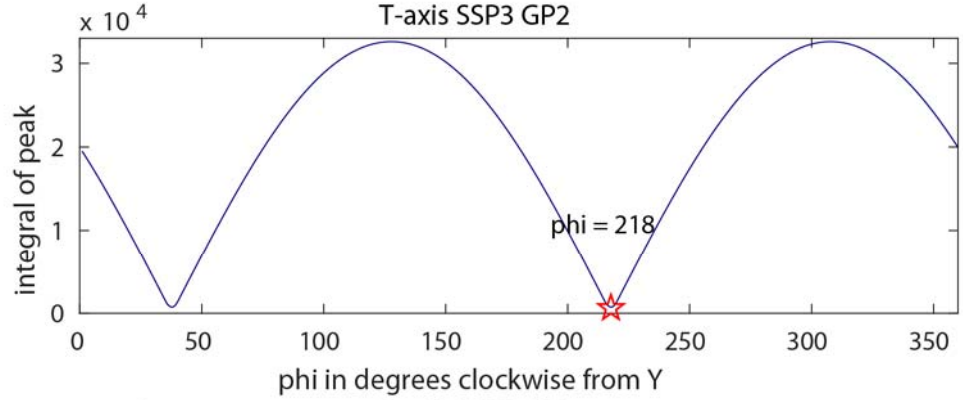
T-axis SSP3 GP2
x 10 4
integral of peak
phi = 218
phi in degrees clockwise from Y

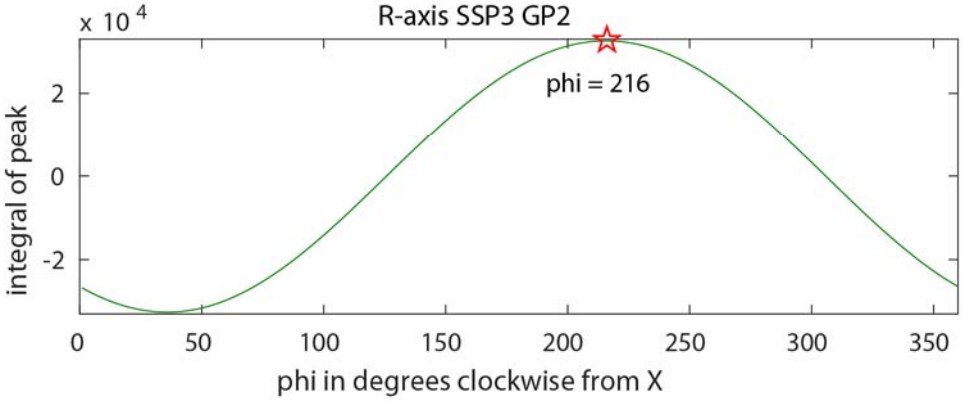
R-axis SSP3 GP2
x 10 4
integral of peak
phi = 216
phi in degrees clockwise from X

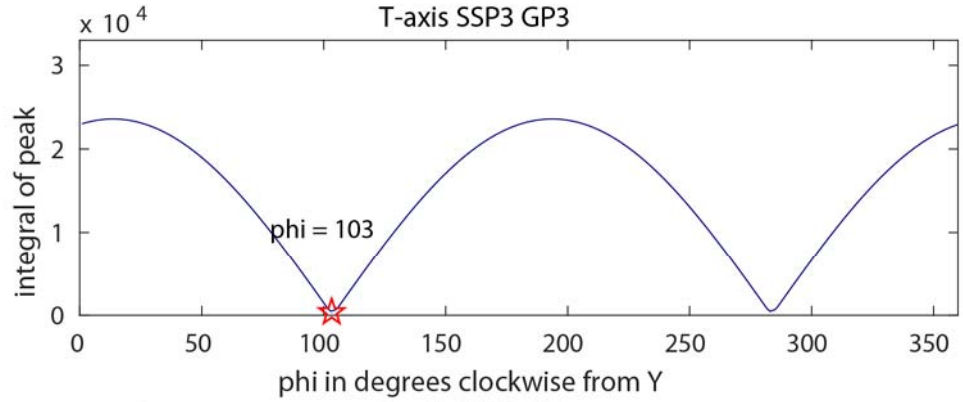
T-axis SSP3 GP3
x 10 4
integral of peak
phi = 103
phi in degrees clockwise from Y

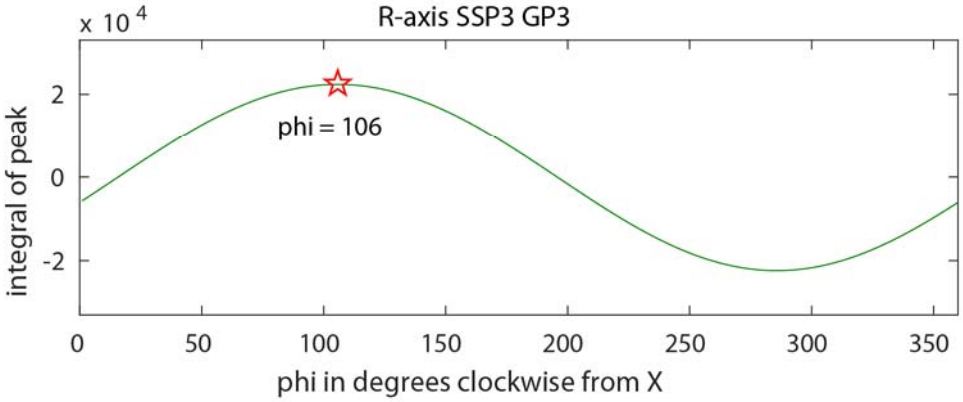
R-axis SSP3 GP3
x 10 4
integral of peak
phi = 106
phi in degrees clockwise from X

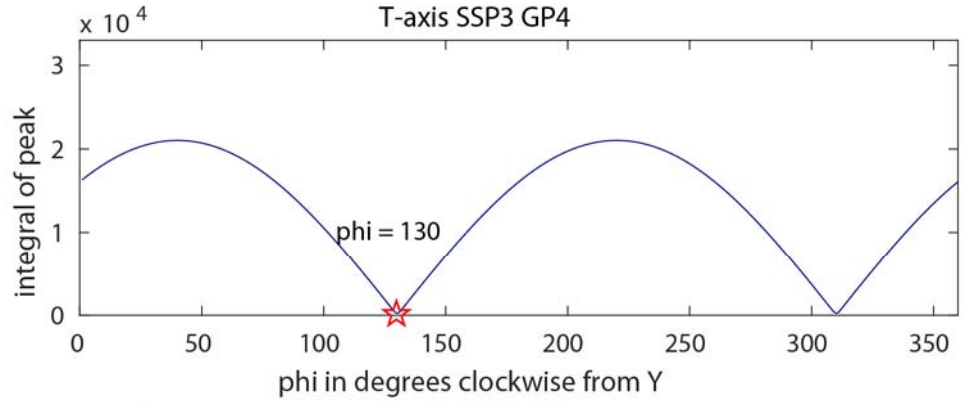
T-axis SSP3 GP4
x 10 4
integral of peak
phi = 130
phi in degrees clockwise from Y

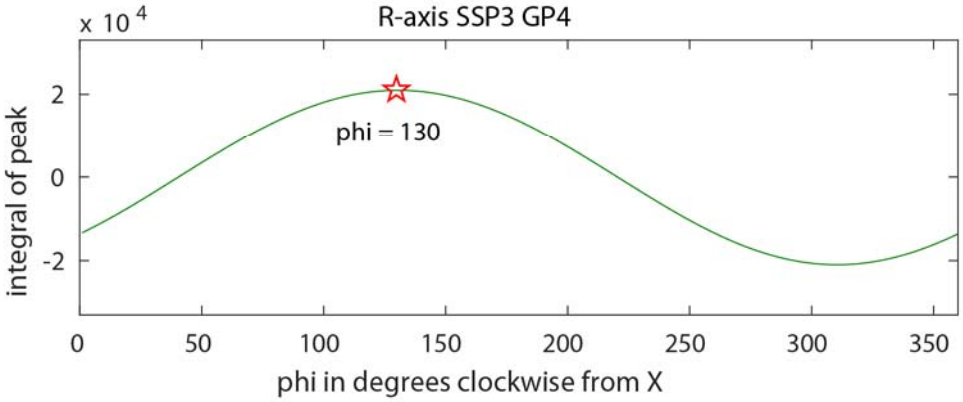
R-axis SSP3 GP4
x 10 4
integral of peak
phi = 130
phi in degrees clockwise from X

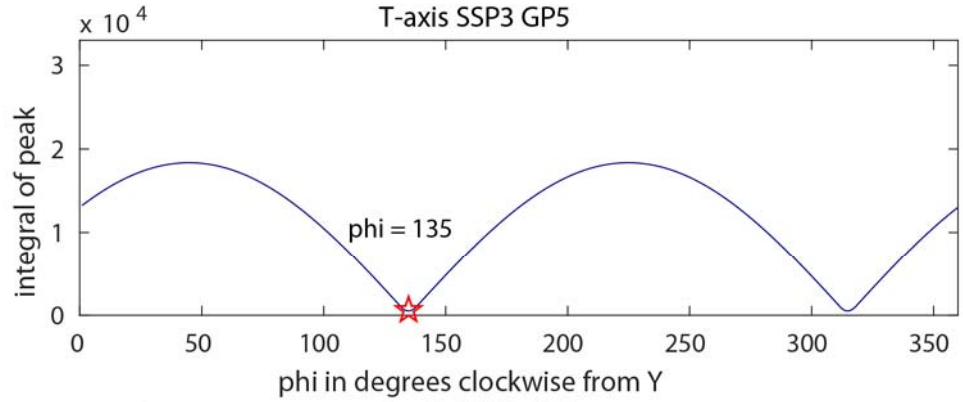
T-axis SSP3 GP5
x 10 4
integral of peak
phi = 135
phi in degrees clockwise from Y

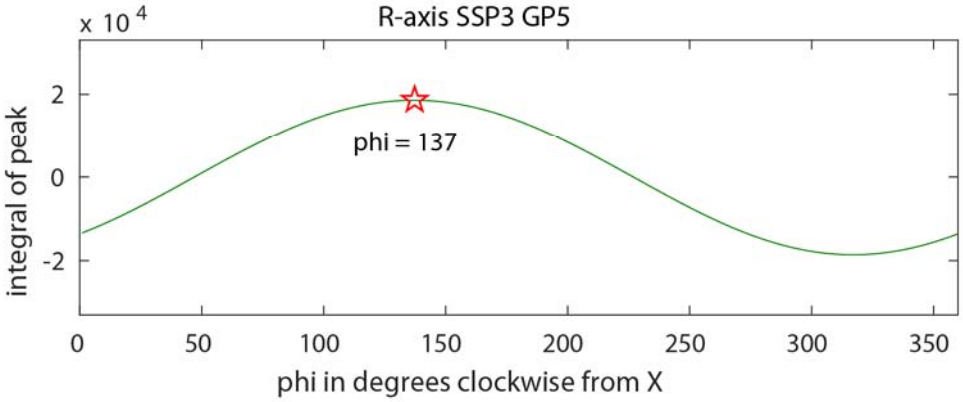
R-axis SSP3 GP5
x 10 4
integral of peak
phi = 137
phi in degrees clockwise from X

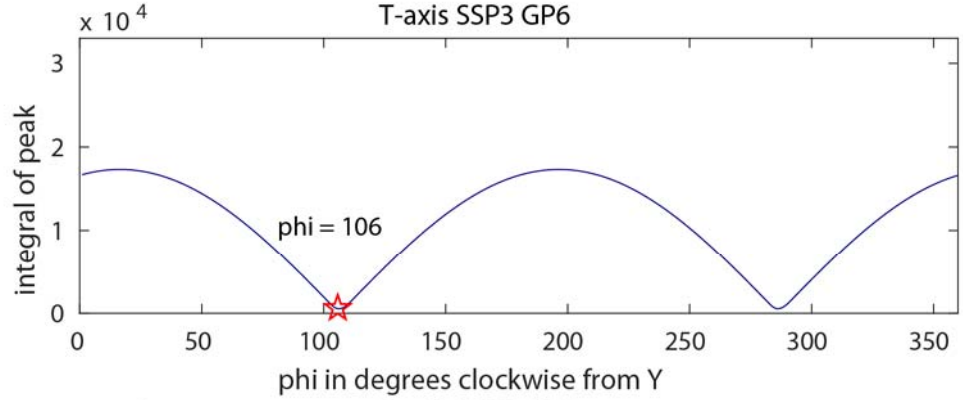
T-axis SSP3 GP6
x 10 4
integral of peak
phi = 106
phi in degrees clockwise from Y

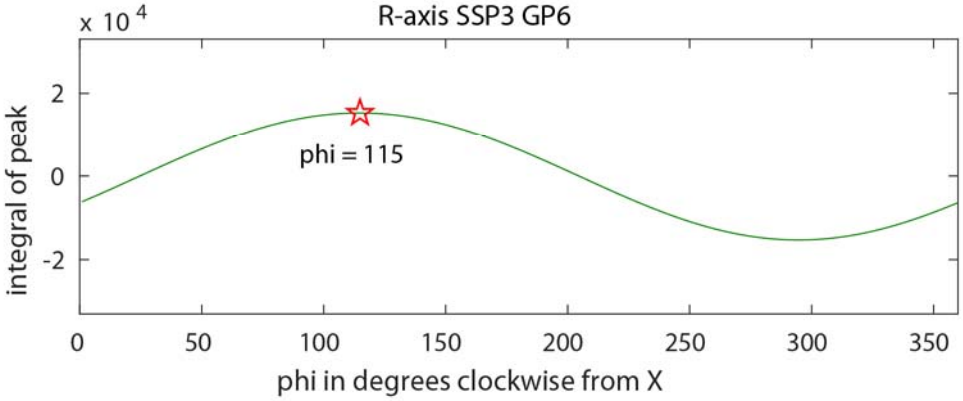
R-axis SSP3 GP6
x 10 4
integral of peak
phi = 115
phi in degrees clockwise from X

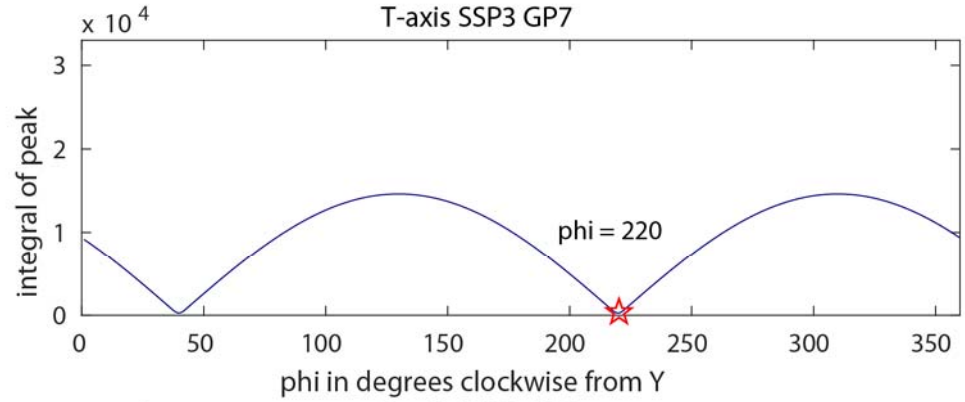
T-axis SSP3 GP7
x 10 4
integral of peak
phi = 220
phi in degrees clockwise from Y

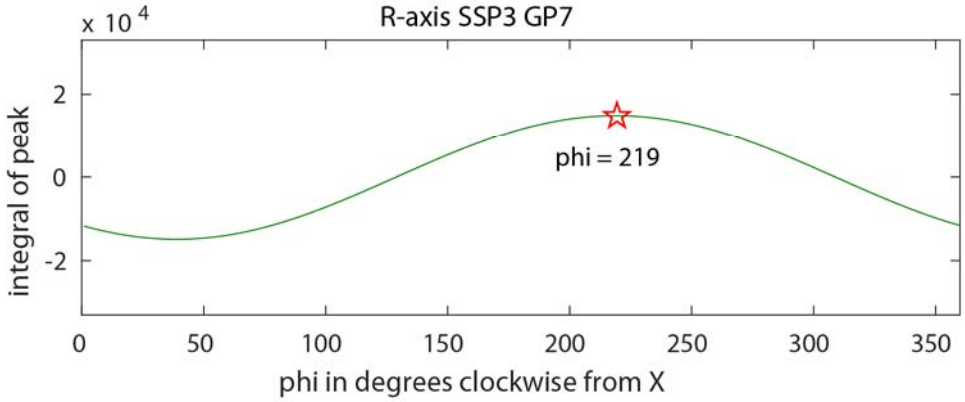
R-axis SSP3 GP7
x 10 4
integral of peak
phi = 219
phi in degrees clockwise from X

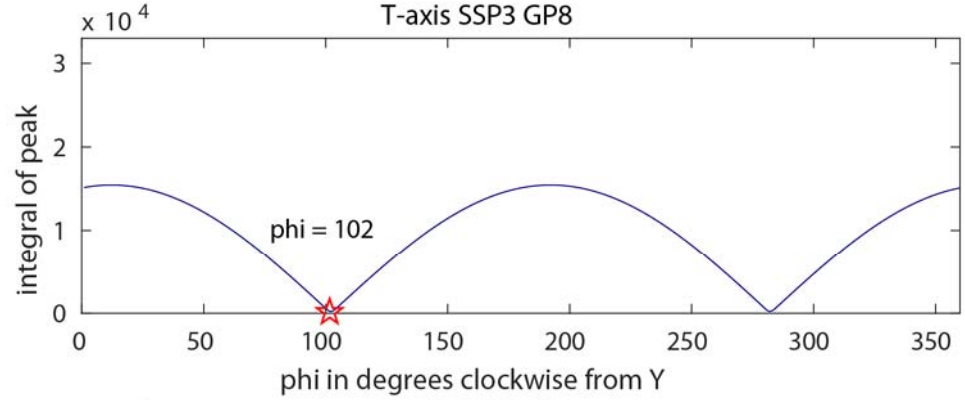
T-axis SSP3 GP8
x 10 4
integral of peak
phi = 102
phi in degrees clockwise from Y

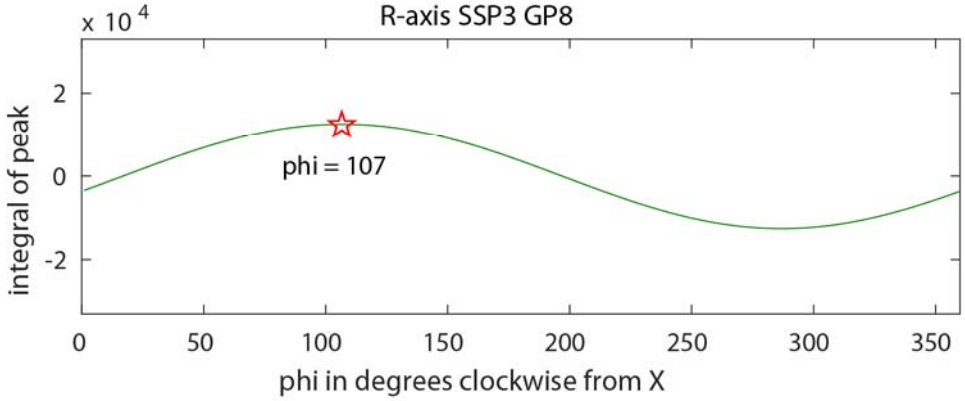
R-axis SSP3 GP8
x 10 4
integral of peak
phi = 107
phi in degrees clockwise from X

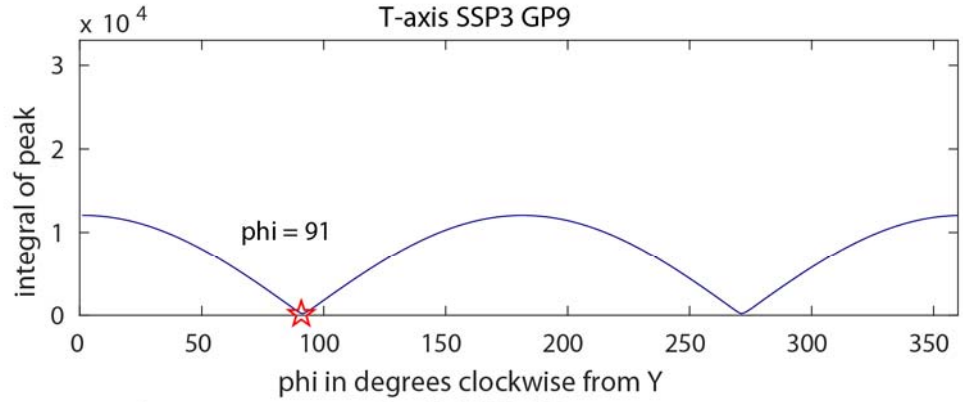
T-axis SSP3 GP9
x 10 4
integral of peak
phi = 91
phi in degrees clockwise from Y

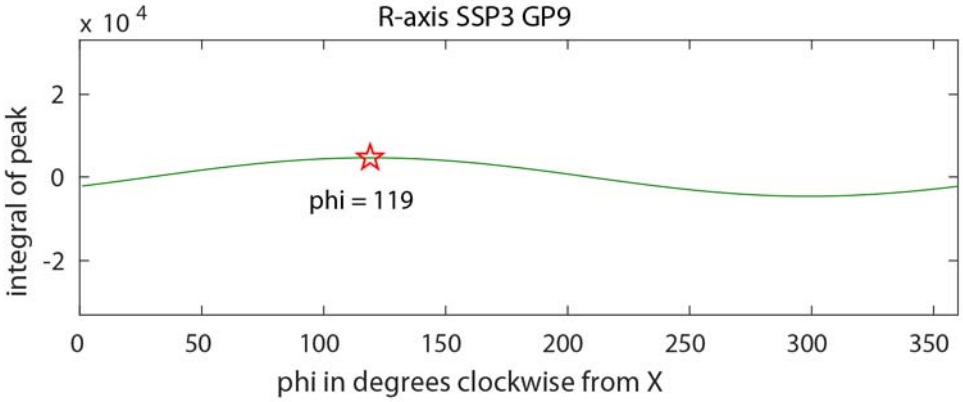
R-axis SSP3 GP9
x 10 4
integral of peak
phi = 119
phi in degrees clockwise from X

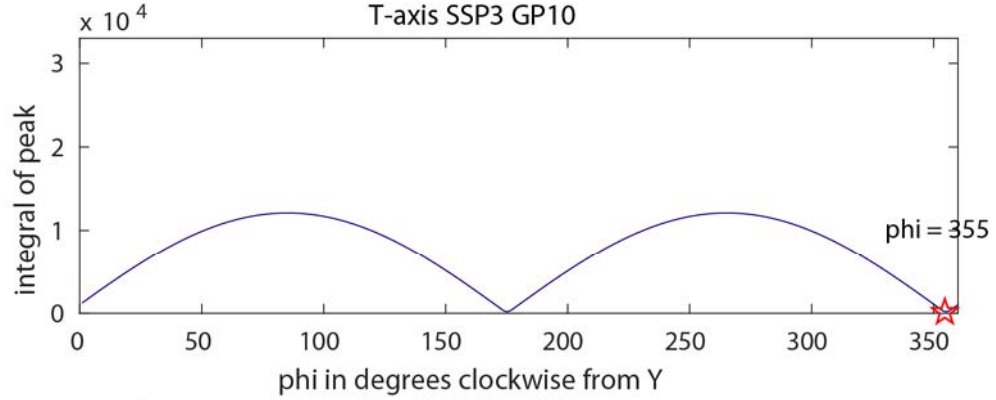
T-axis SSP3 GP10
x 10 4
integral of peak
phi = 355
phi in degrees clockwise from Y

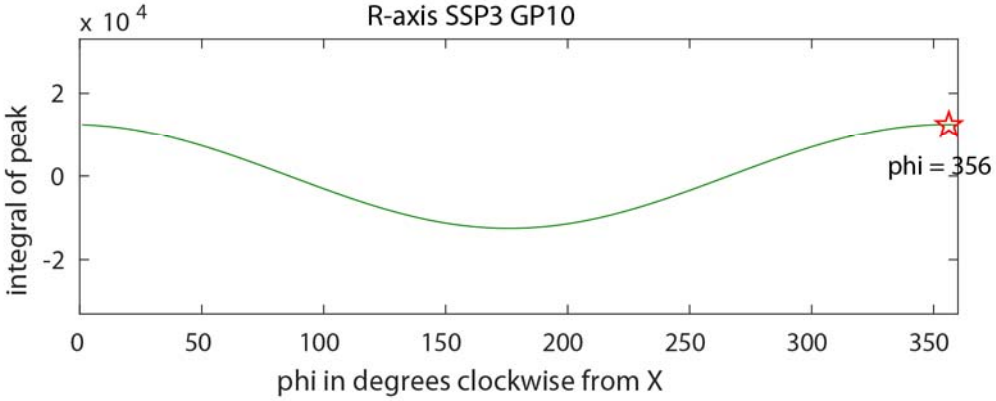
R-axis SSP3 GP10
x 10 4
integral of peak
phi = 356
phi in degrees clockwise from X

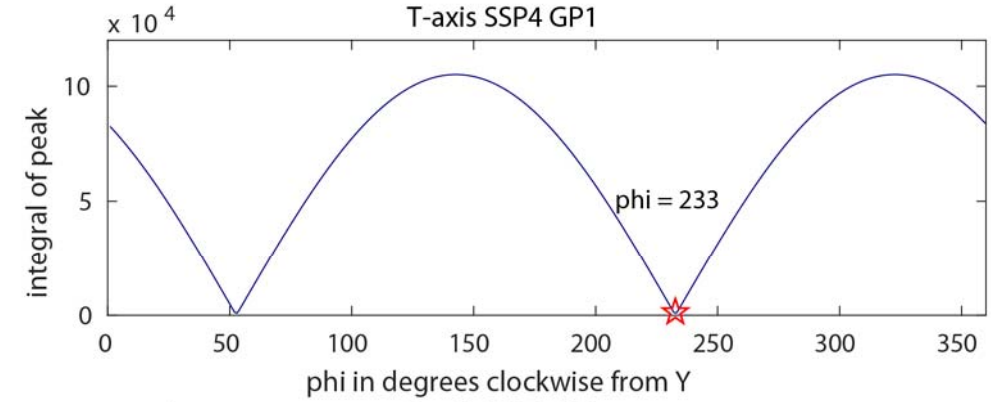
T-axis SSP4 GP1
x 10 4
integral of peak
phi = 233
phi in degrees clockwise from Y

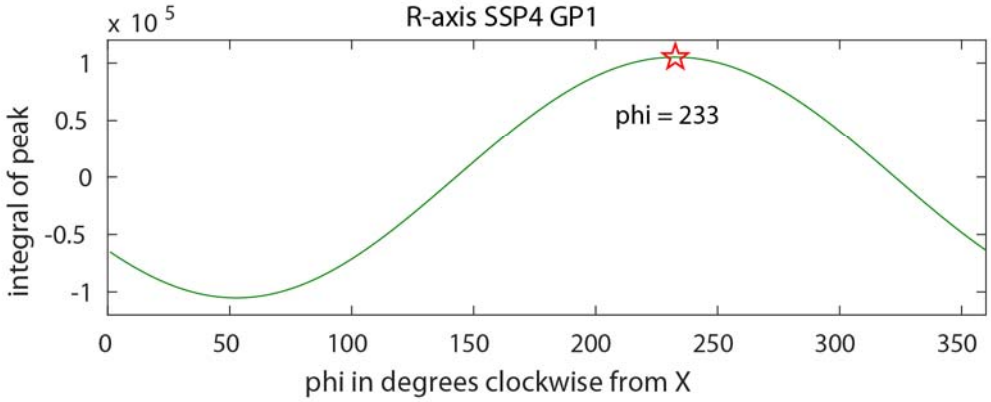
R-axis SSP4 GP1
x 10 5
integral of peak
phi = 233
phi in degrees clockwise from X

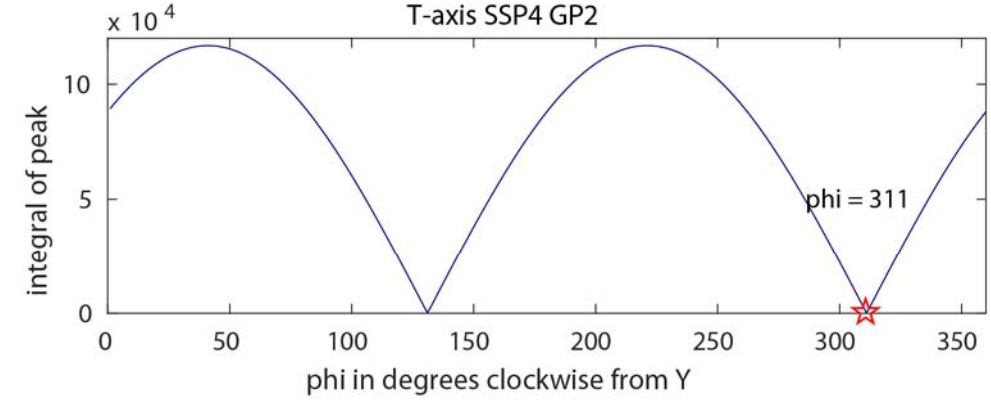
T-axis SSP4 GP2
x 10 4
integral of peak
phi = 311
phi in degrees clockwise from Y

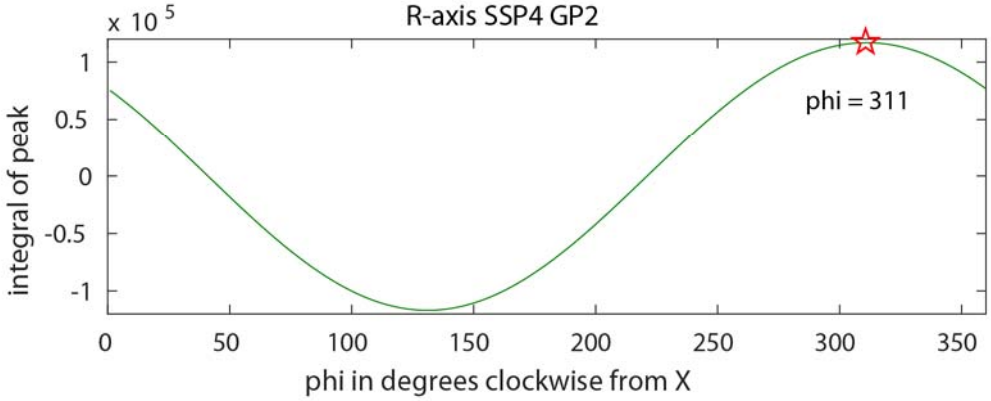
R-axis SSP4 GP2
x 10 5
integral of peak
phi = 311
phi in degrees clockwise from X

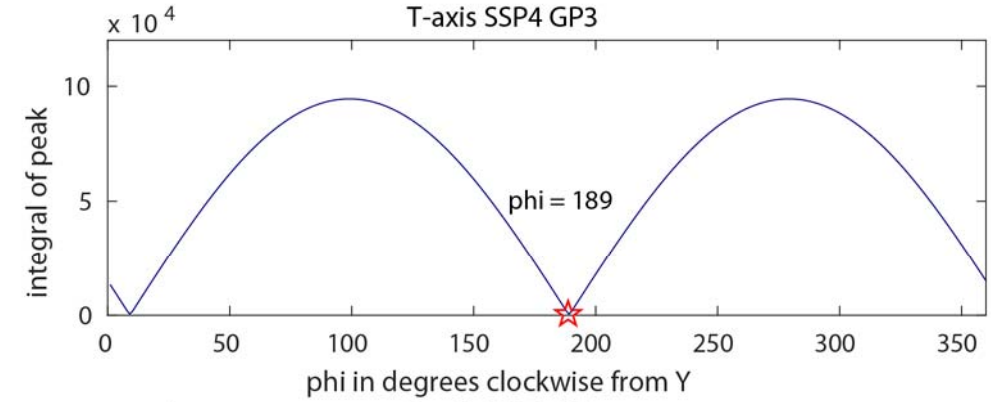
T-axis SSP4 GP3
x 10 4
integral of peak
phi = 189
phi in degrees clockwise from Y

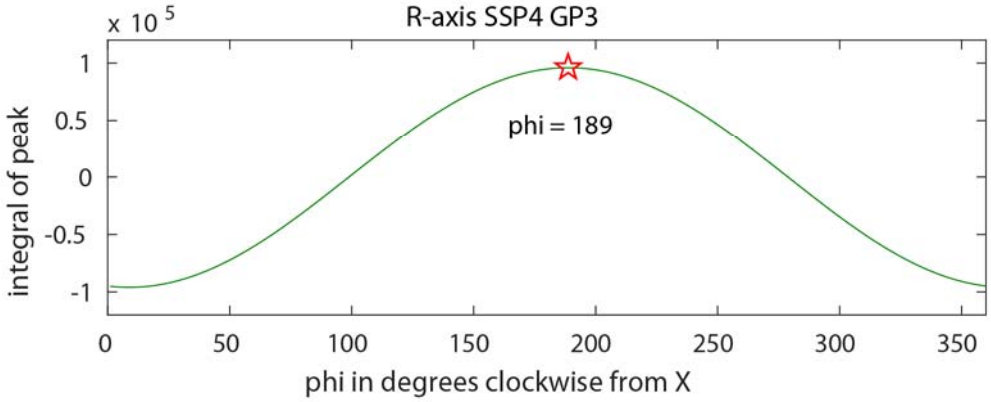
R-axis SSP4 GP3
x 10 5
integral of peak
phi = 189
phi in degrees clockwise from X

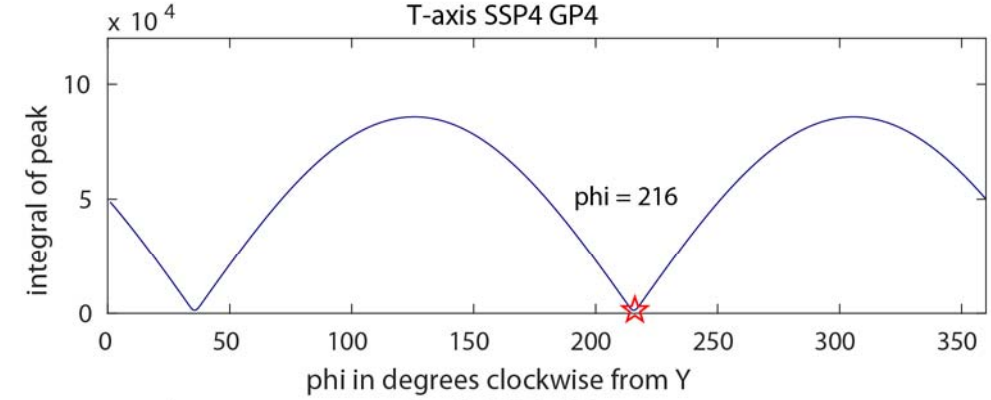
T-axis SSP4 GP4
x 10 4
integral of peak
phi = 216
phi in degrees clockwise from Y

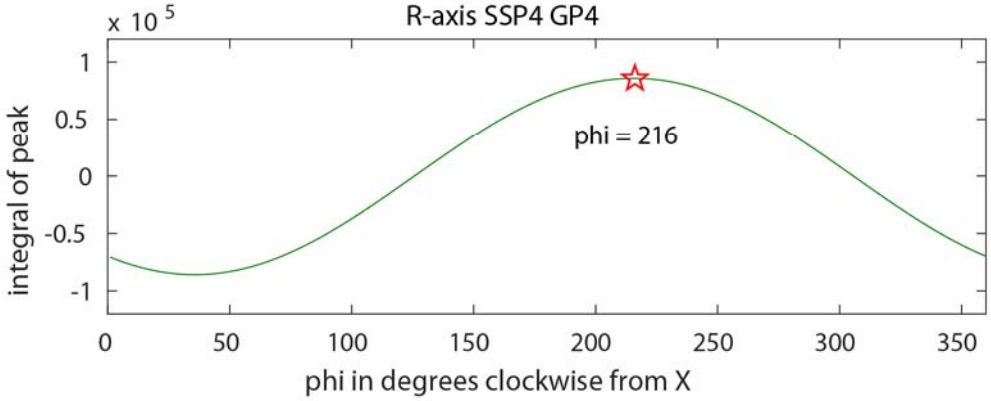
R-axis SSP4 GP4
x 10 5
integral of peak
phi = 216
phi in degrees clockwise from X

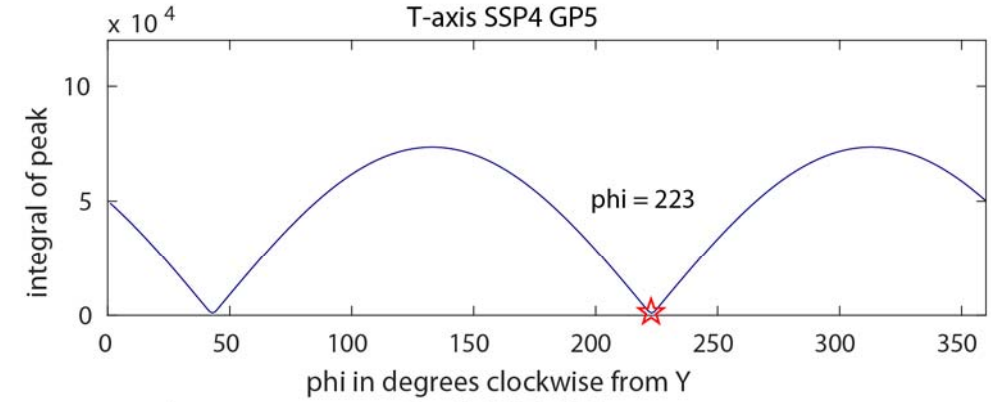
T-axis SSP4 GP5
x 10 4
integral of peak
phi = 223
phi in degrees clockwise from Y

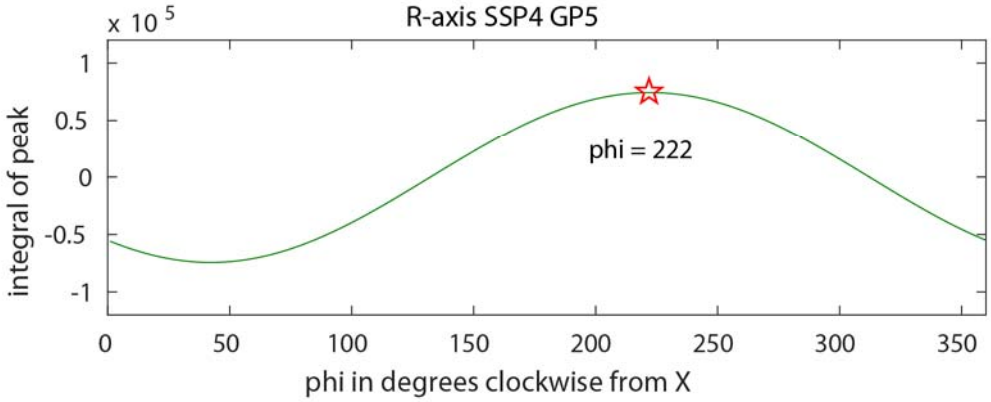
R-axis SSP4 GP5
x 10 5
integral of peak
phi = 222
phi in degrees clockwise from X

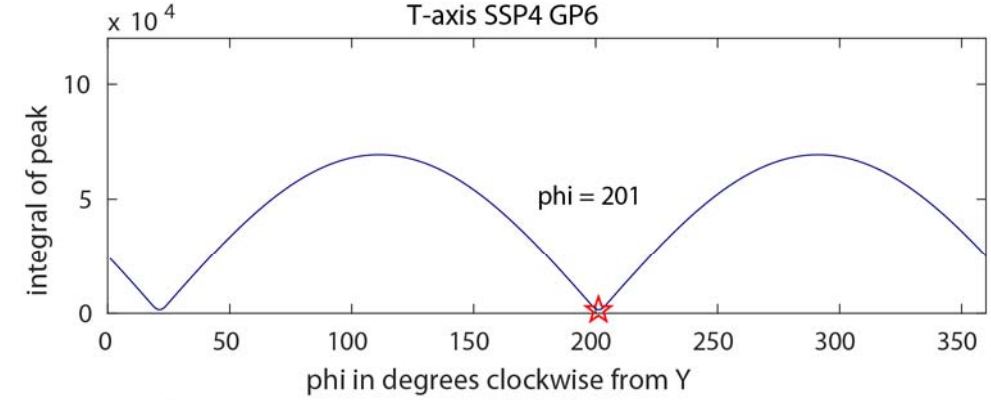
T-axis SSP4 GP6
x 10 4
integral of peak
phi = 201
phi in degrees clockwise from Y

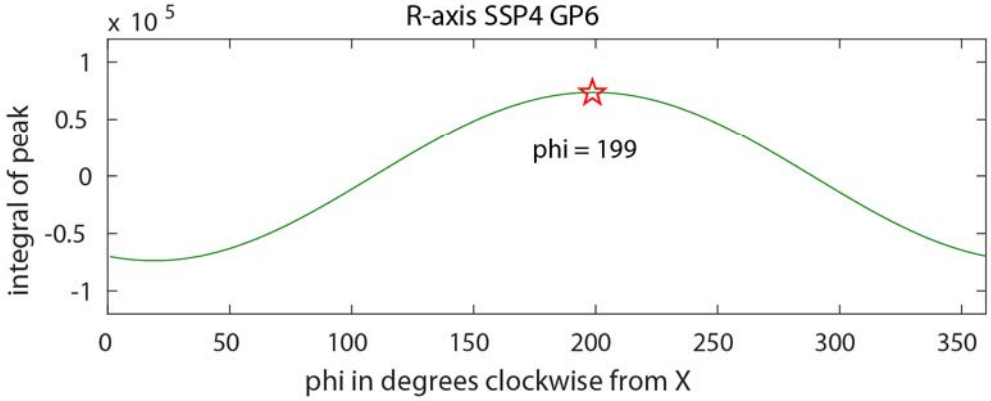
R-axis SSP4 GP6
x 10 5
integral of peak
phi = 199
phi in degrees clockwise from X

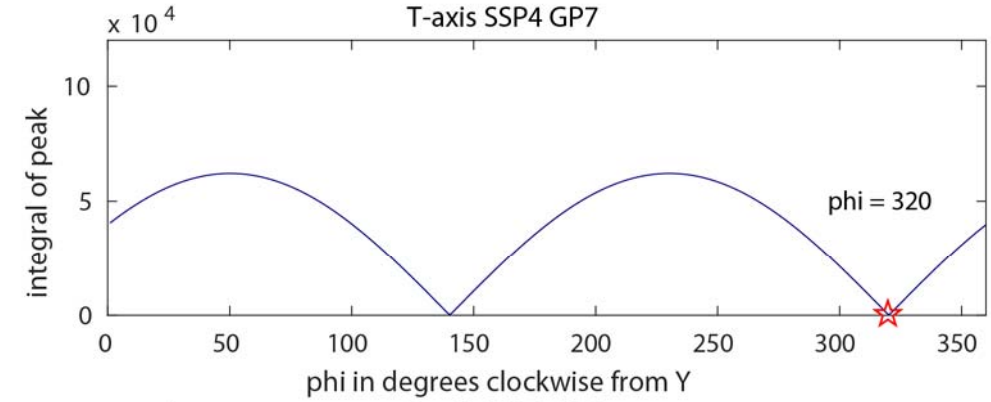
T-axis SSP4 GP7
x 10 4
integral of peak
phi = 320
phi in degrees clockwise from Y

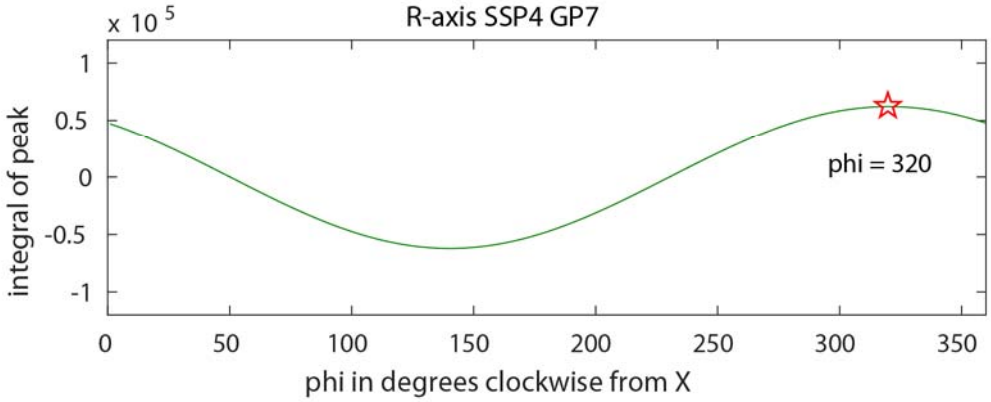
R-axis SSP4 GP7
x 10 5
integral of peak
phi = 320
phi in degrees clockwise from X

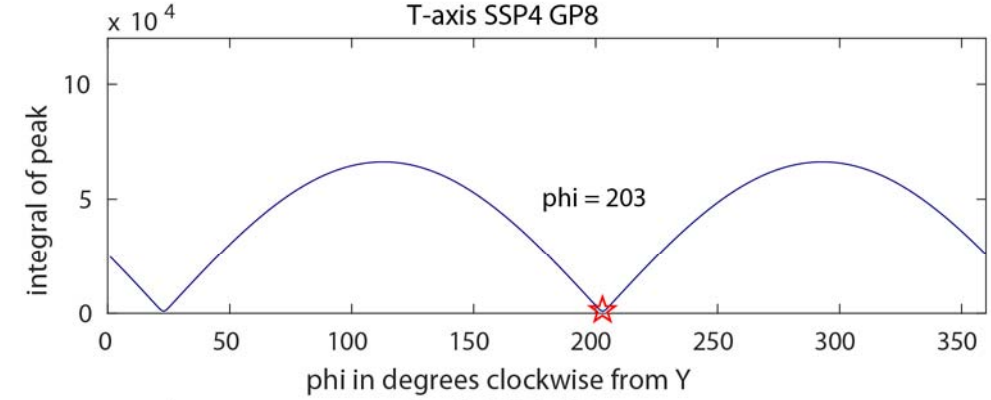
T-axis SSP4 GP8
x 10 4
integral of peak
phi = 203
phi in degrees clockwise from Y

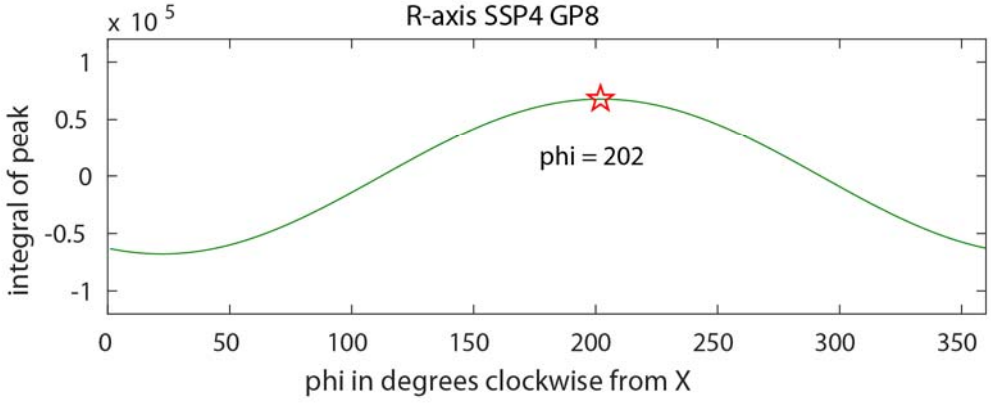
R-axis SSP4 GP8
x 10 5
integral of peak
phi = 202
phi in degrees clockwise from X

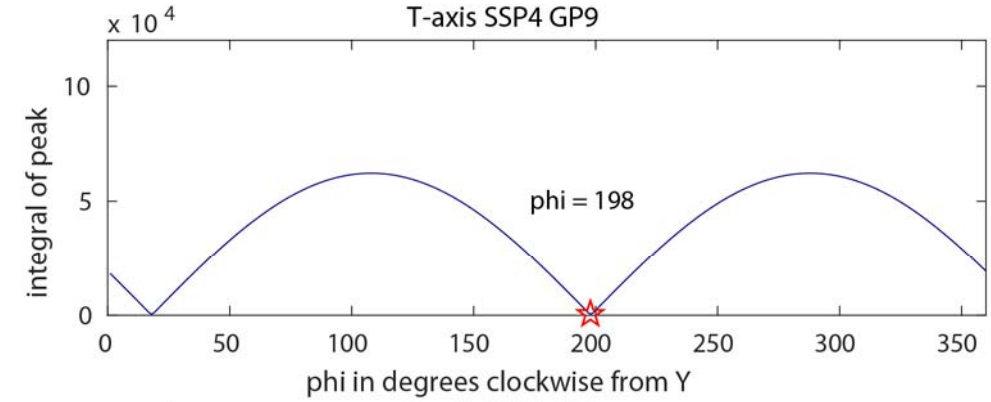
T-axis SSP4 GP9
x 10 4
integral of peak
phi = 198
phi in degrees clockwise from Y

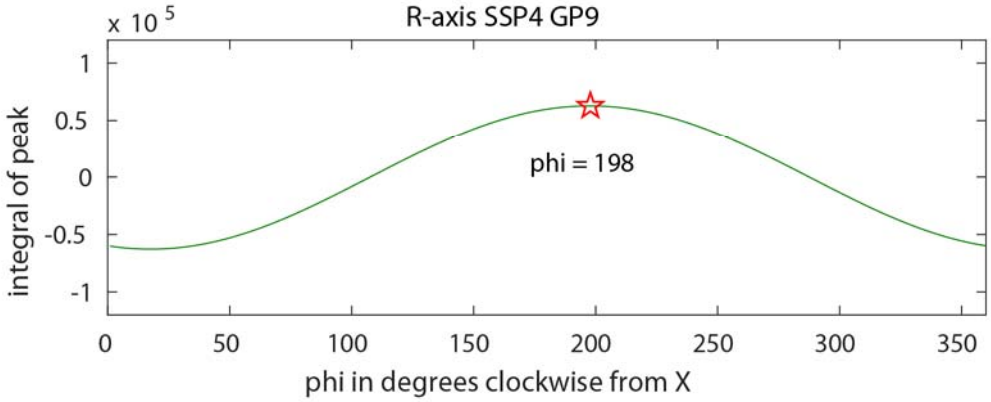
R-axis SSP4 GP9
x 10 5
integral of peak
phi = 198
phi in degrees clockwise from X

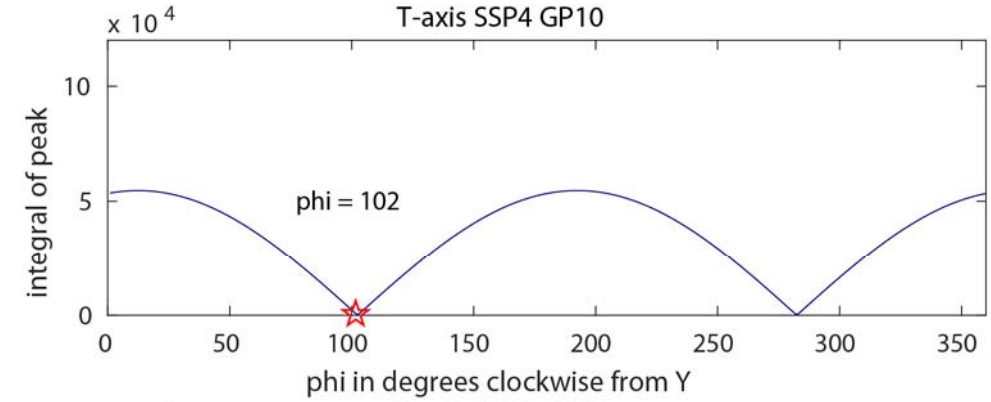
T-axis SSP4 GP10
x 10 4
integral of peak
phi = 102
phi in degrees clockwise from Y

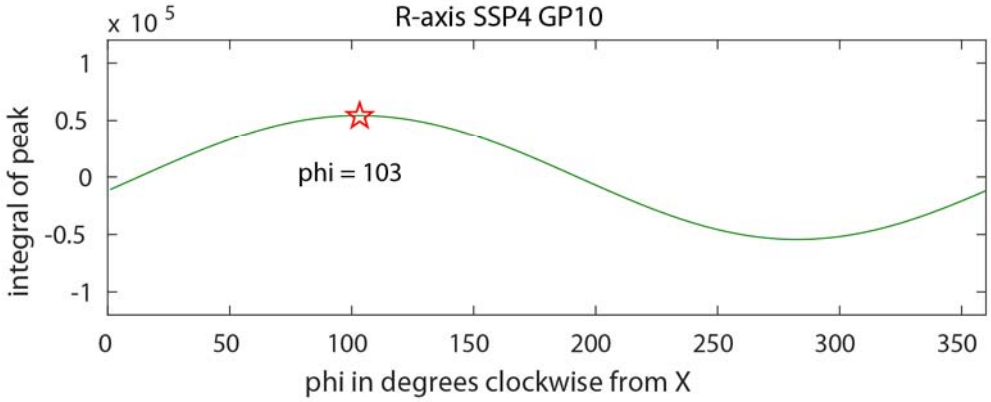
R-axis SSP4 GP10
x 10 5
integral of peak
phi = 103
phi in degrees clockwise from X

Appendix 3: First peaks

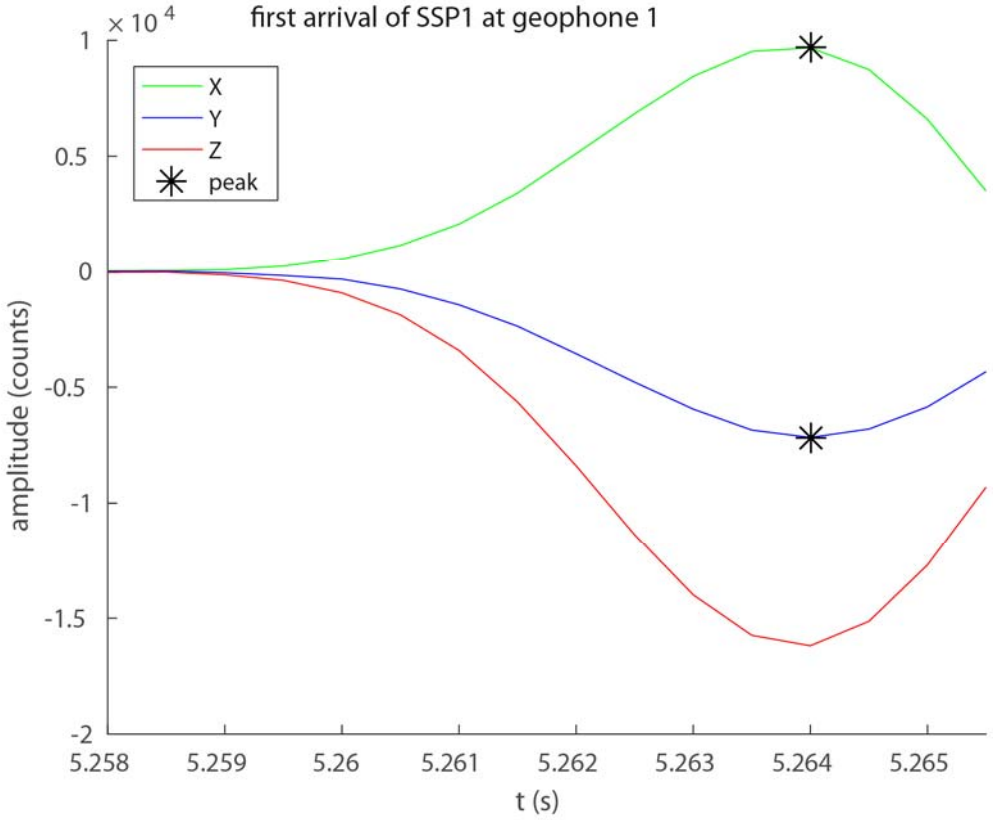
first arrival of SSP1 at geophone 1
× 10 4
X
Y
Z
peak
amplitude (counts)
t (s)
1
0.5
0
-0.5
-1
-1.5
-2
5.258
5.259
5.26
5.261
5.262
5.263
5.264
5.265

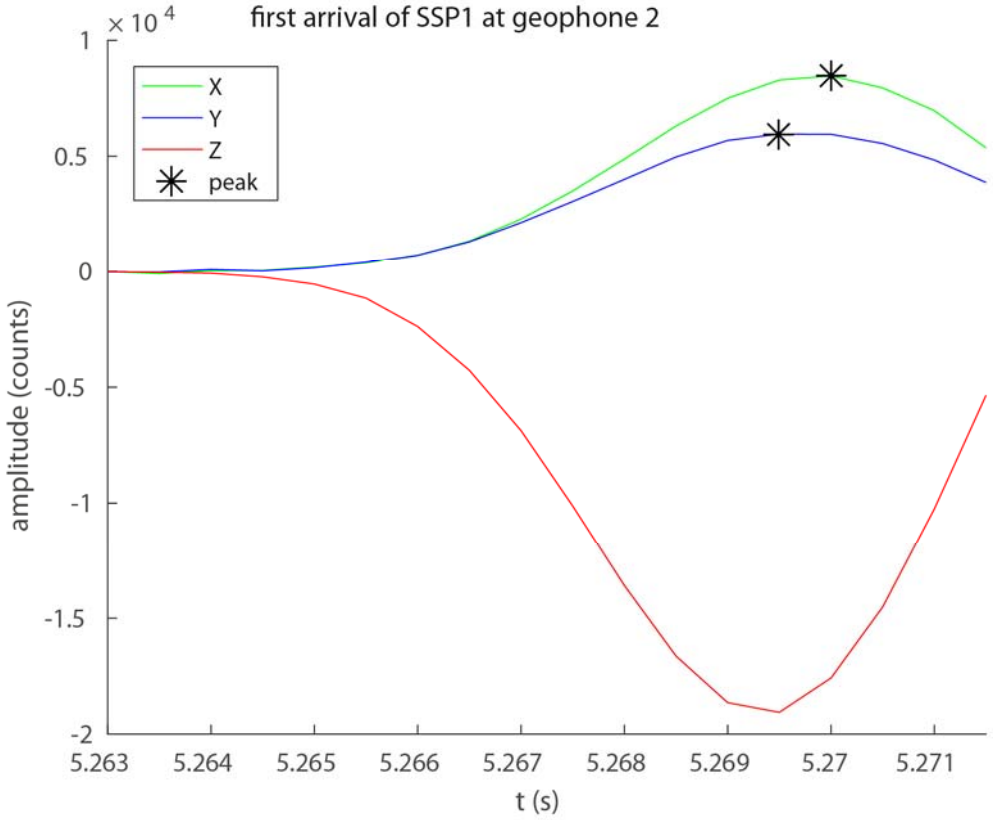
first arrival of SSP1 at geophone 2
× 10 4
X
Y
Z
peak
amplitude (counts)
t (s)
1
0.5
0
-0.5
-1
-1.5
-2
5.263
5.264
5.265
5.266
5.267
5.268
5.269
5.27
5.271

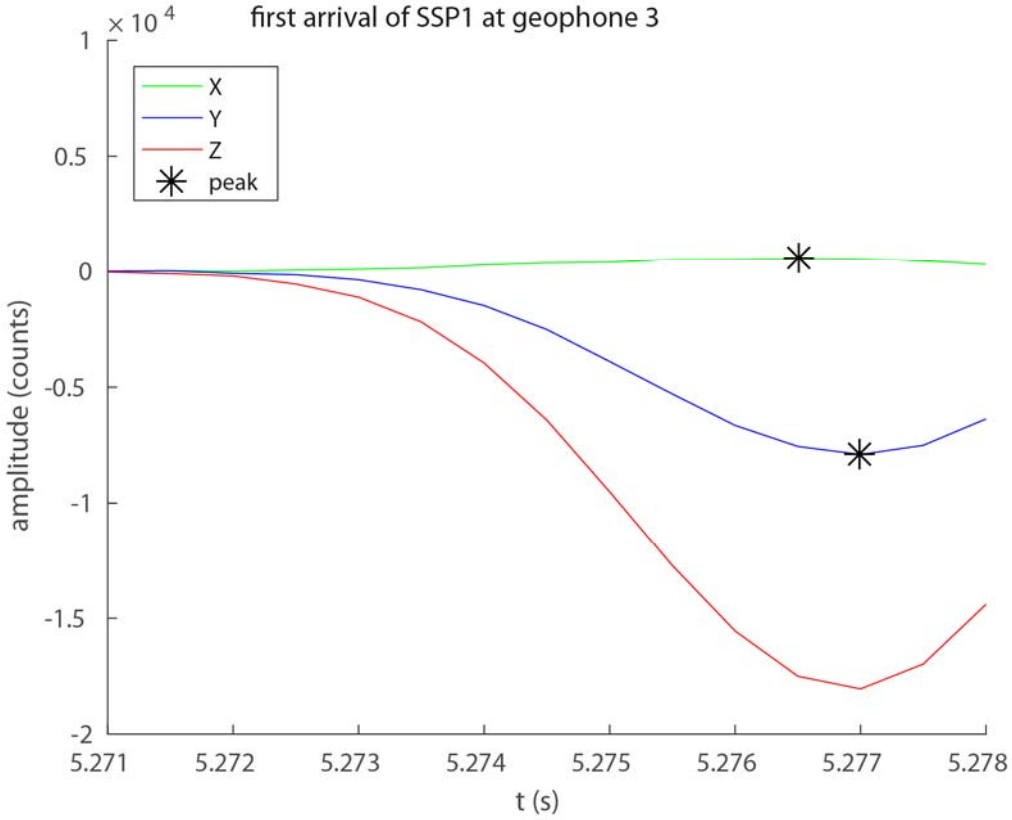
first arrival of SSP1 at geophone 3
× 10 4
X
Y
Z
peak
amplitude (counts)
t (s)
1
0.5
0
-0.5
-1
-1.5
-2
5.271
5.272
5.273
5.274
5.275
5.276
5.277
5.278

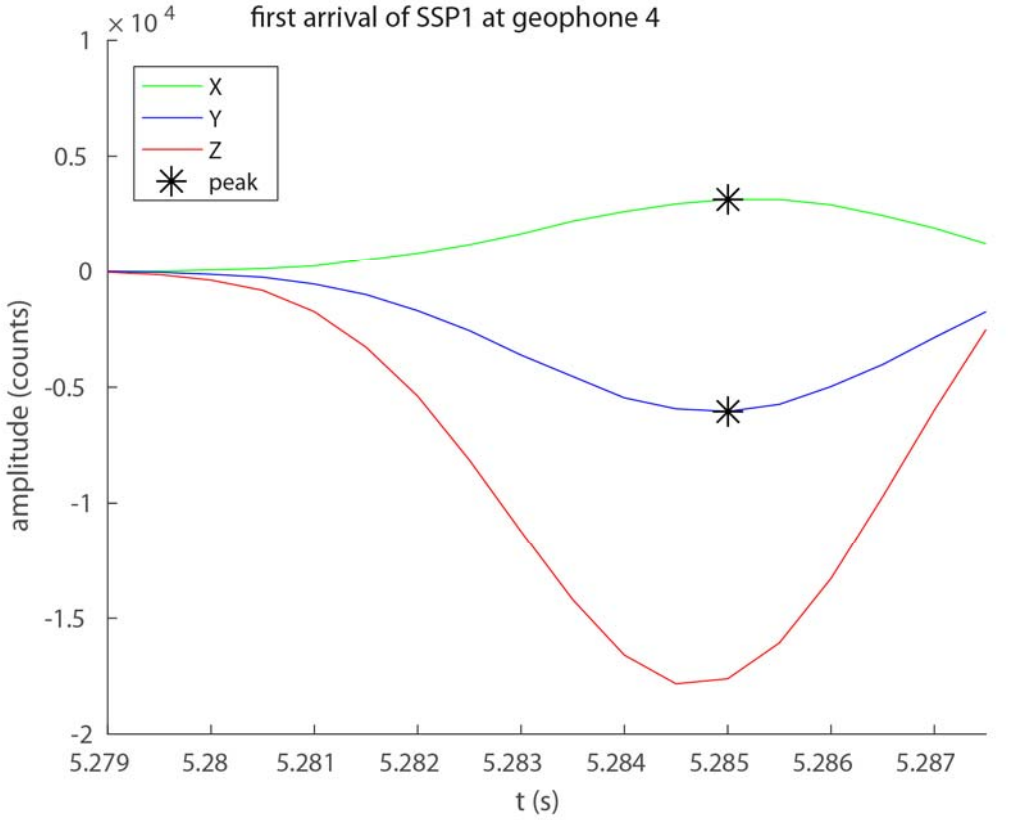
first arrival of SSP1 at geophone 4
× 10 4
X
Y
Z
peak
amplitude (counts)
t (s)
1
0.5
0
-0.5
-1
-1.5
-2
5.279
5.28
5.281
5.282
5.283
5.284
5.285
5.286
5.287

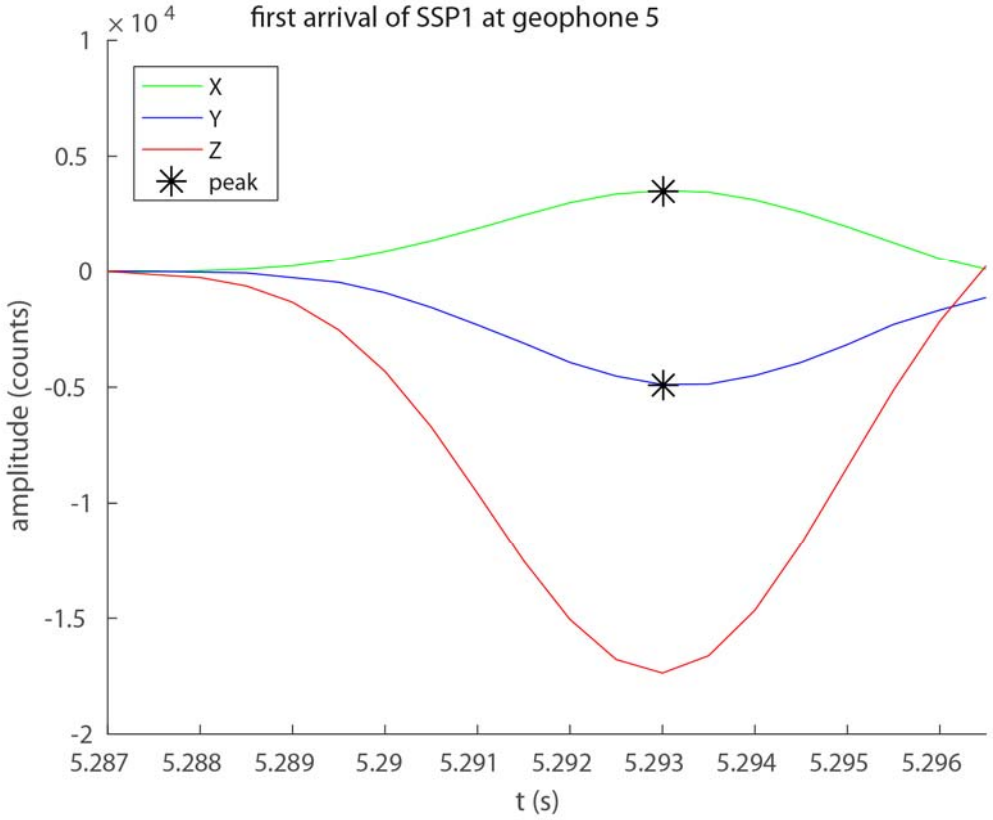
first arrival of SSP1 at geophone 5
× 10 4
X
Y
Z
peak
amplitude (counts)
t (s)
1
0.5
0
-0.5
-1
-1.5
-2
5.287
5.288
5.289
5.29
5.291
5.292
5.293
5.294
5.295
5.296

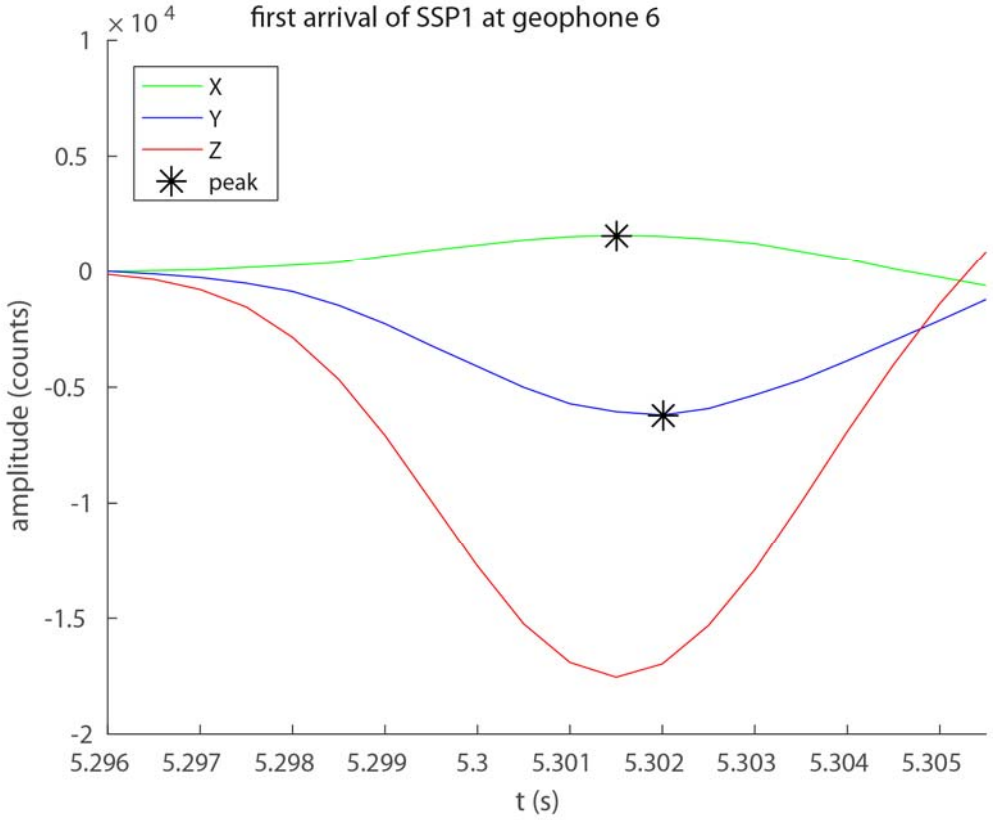
first arrival of SSP1 at geophone 6
× 10 4
X
Y
Z
peak
amplitude (counts)
t (s)
1
0.5
0
-0.5
-1
-1.5
-2
5.296
5.297
5.298
5.299
5.3
5.301
5.302
5.303
5.304
5.305

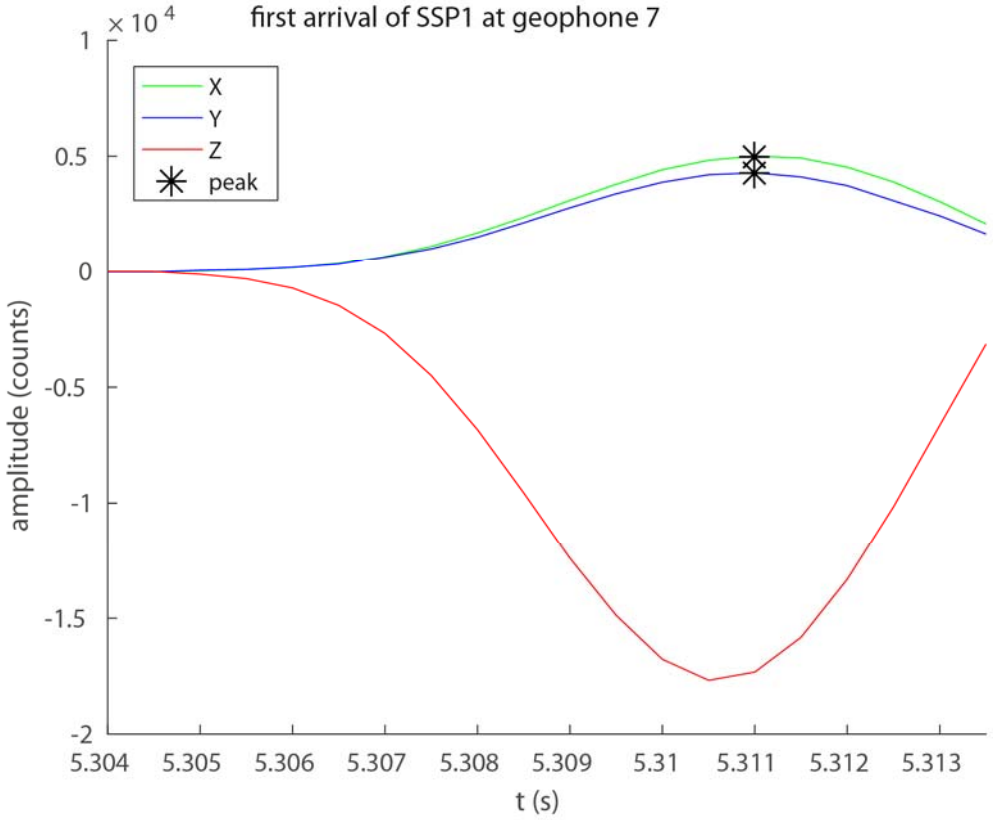
first arrival of SSP1 at geophone 7
× 10 4
X
Y
Z
peak
amplitude (counts)
t (s)
1
0.5
0
-0.5
-1
-1.5
-2
5.304
5.305
5.306
5.307
5.308
5.309
5.31
5.311
5.312
5.313

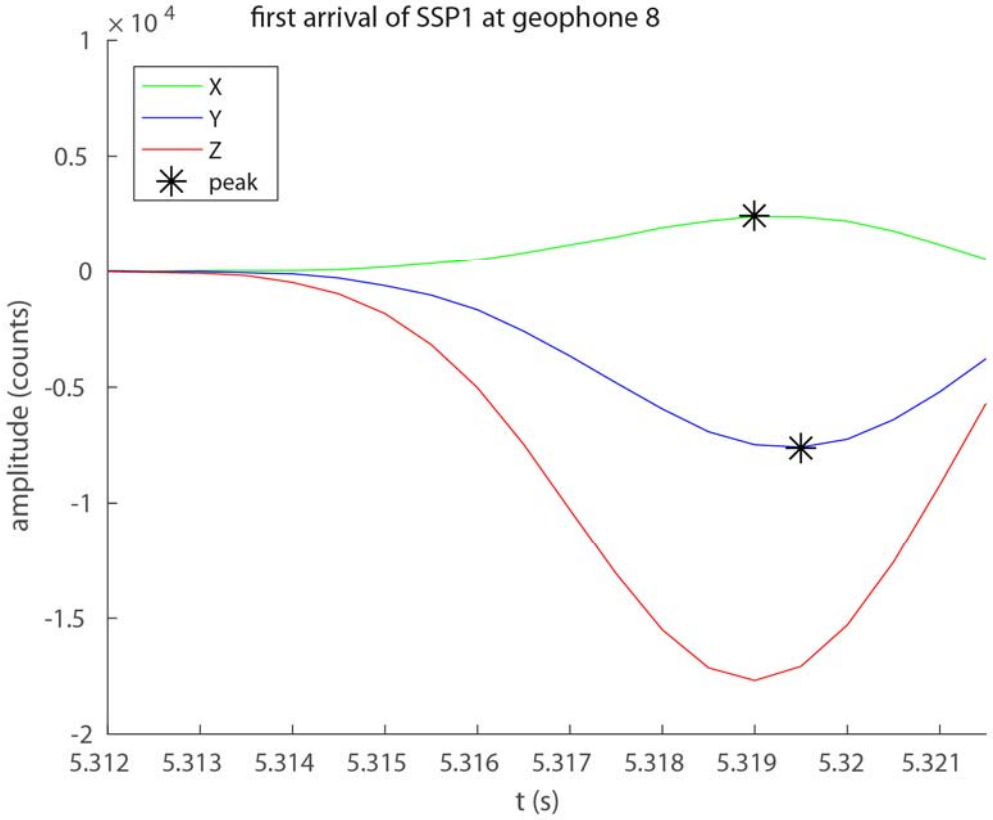
first arrival of SSP1 at geophone 8
× 10 4
X
Y
Z
peak
amplitude (counts)
t (s)
1
0.5
0
-0.5
-1
-1.5
-2
5.312
5.313
5.314
5.315
5.316
5.317
5.318
5.319
5.32
5.321

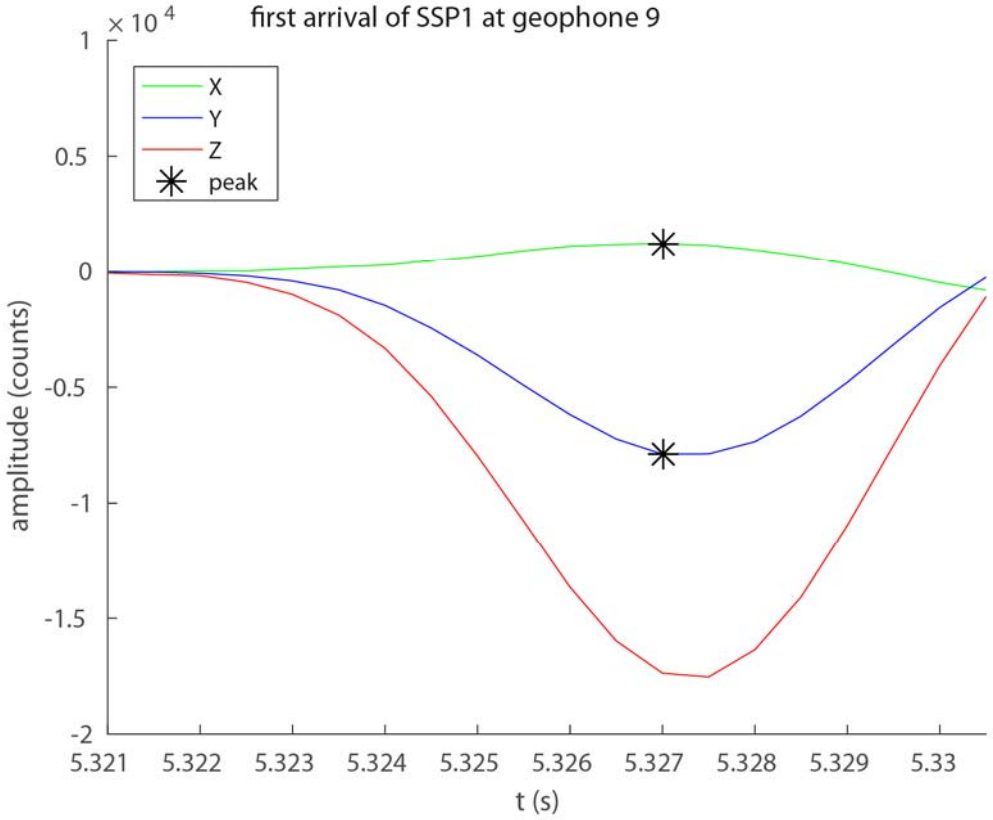
first arrival of SSP1 at geophone 9
× 10 4
X
Y
Z
peak
amplitude (counts)
t (s)

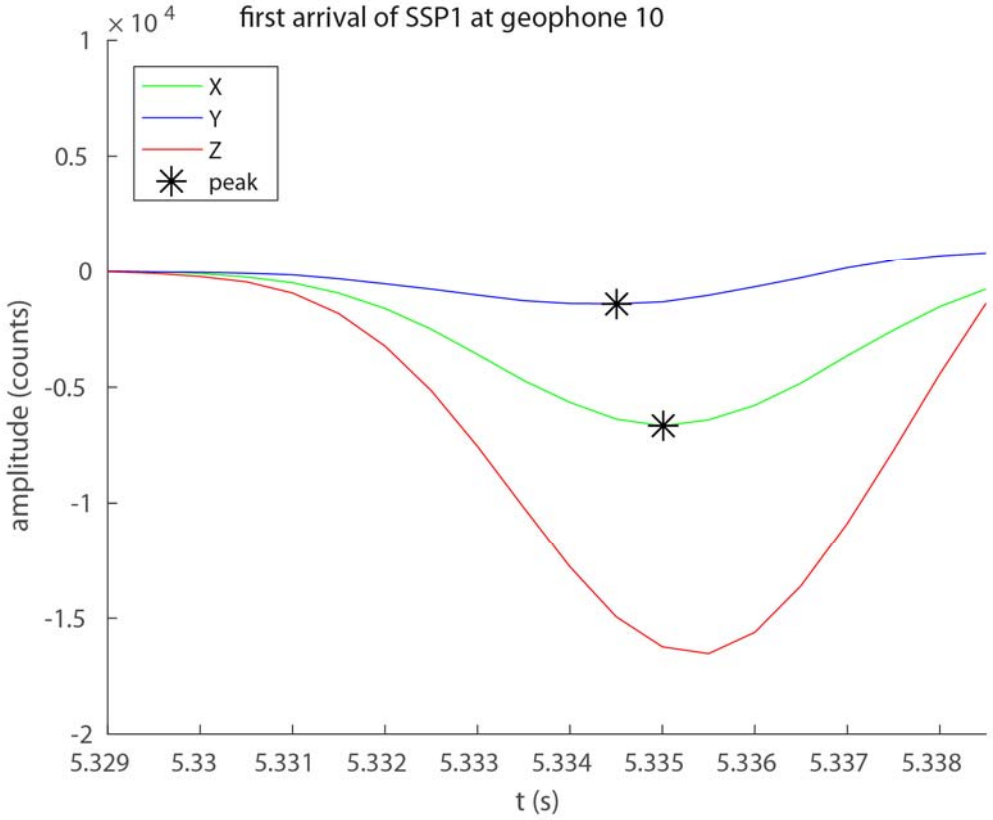
first arrival of SSP1 at geophone 10
× 10 4
X
Y
Z
peak
amplitude (counts)
t (s)

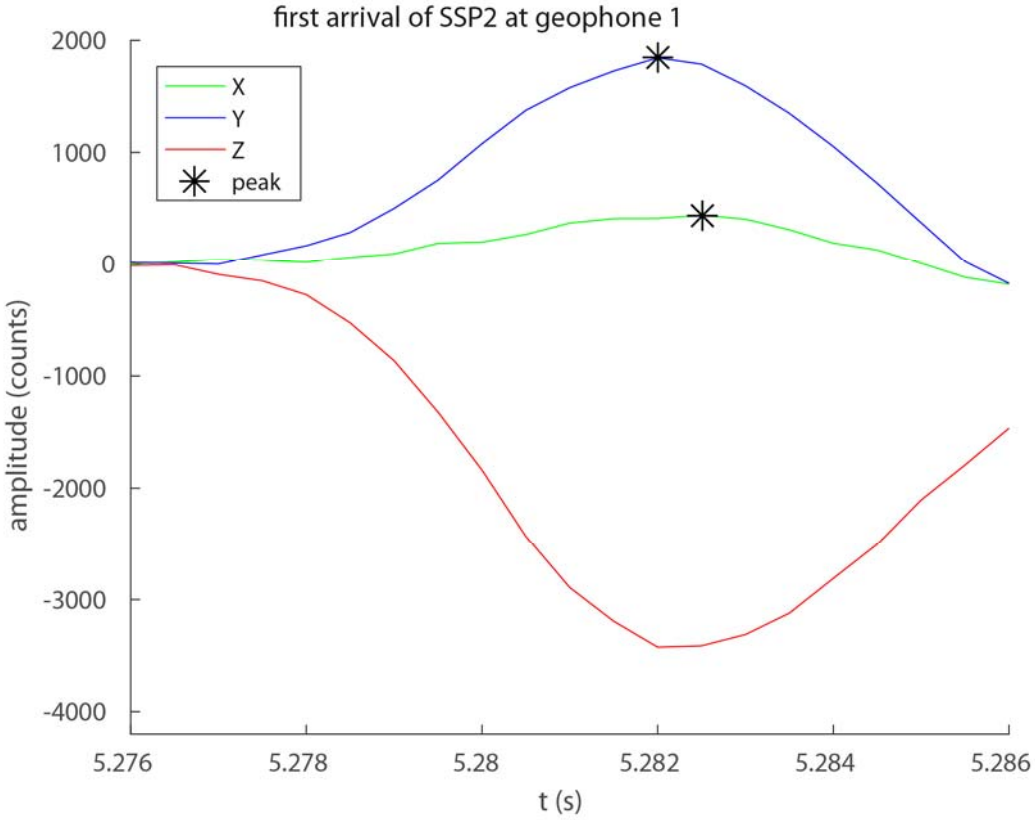
first arrival of SSP2 at geophone 1
X
Y
Z
peak
amplitude (counts)
t (s)
2000
1000
0
-1000
-2000
-3000
-4000
5.276
5.278
5.28
5.282
5.284
5.286

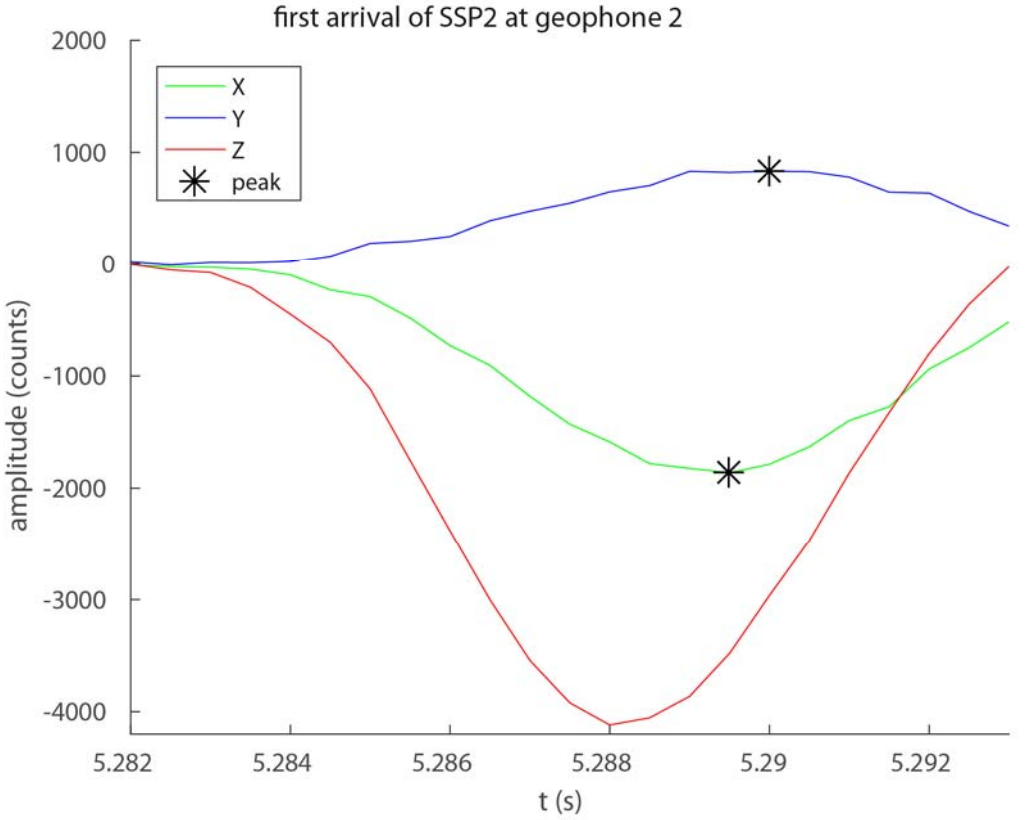
first arrival of SSP2 at geophone 2
X
Y
Z
peak
amplitude (counts)
t (s)
2000
1000
0
-1000
-2000
-3000
-4000
5.282
5.284
5.286
5.288
5.29
5.292

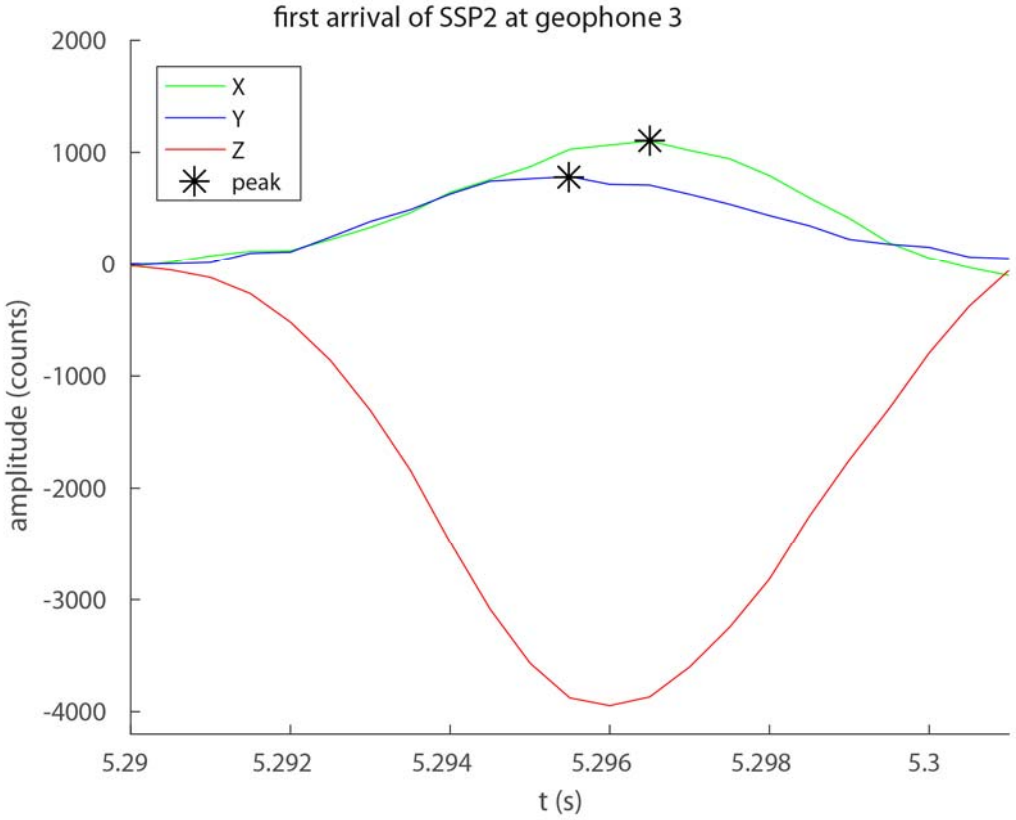
first arrival of SSP2 at geophone 3
X
Y
Z
peak
2000
1000
0
-1000
-2000
-3000
-4000
amplitude (counts)
5.29
5.292
5.294
5.296
5.298
5.3
t (s)

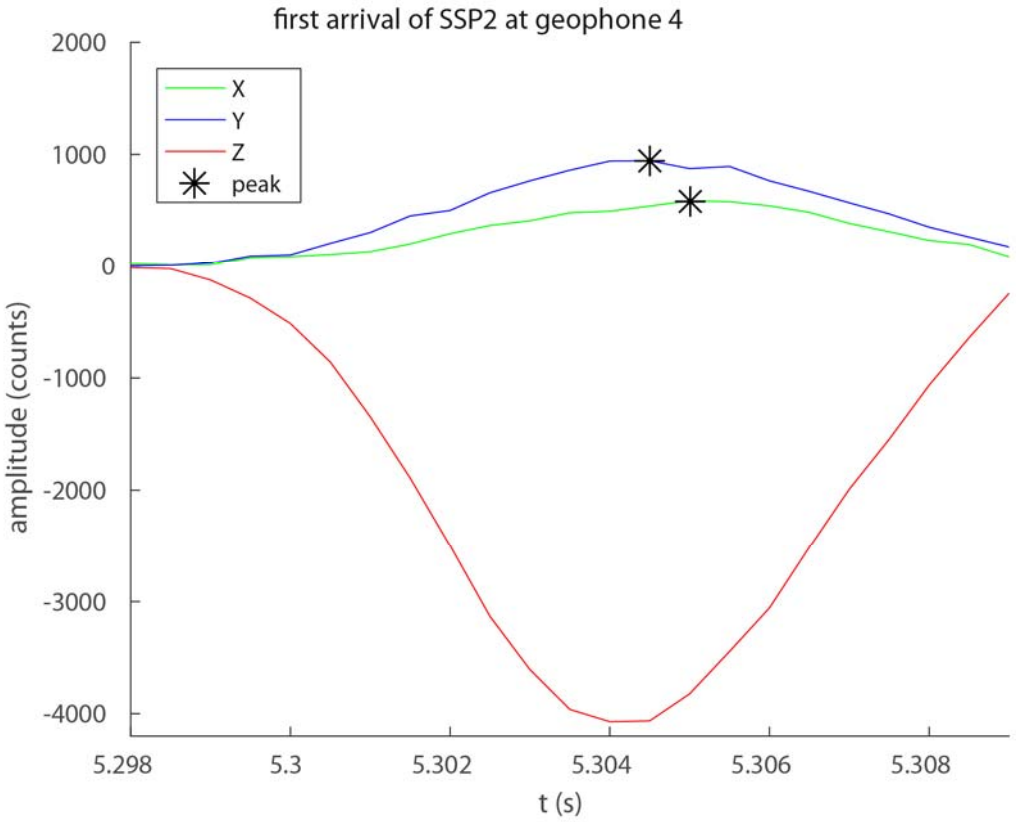
first arrival of SSP2 at geophone 4
X
Y
Z
peak
2000
1000
0
-1000
-2000
-3000
-4000
amplitude (counts)
5.298
5.3
5.302
5.304
5.306
5.308
t (s)

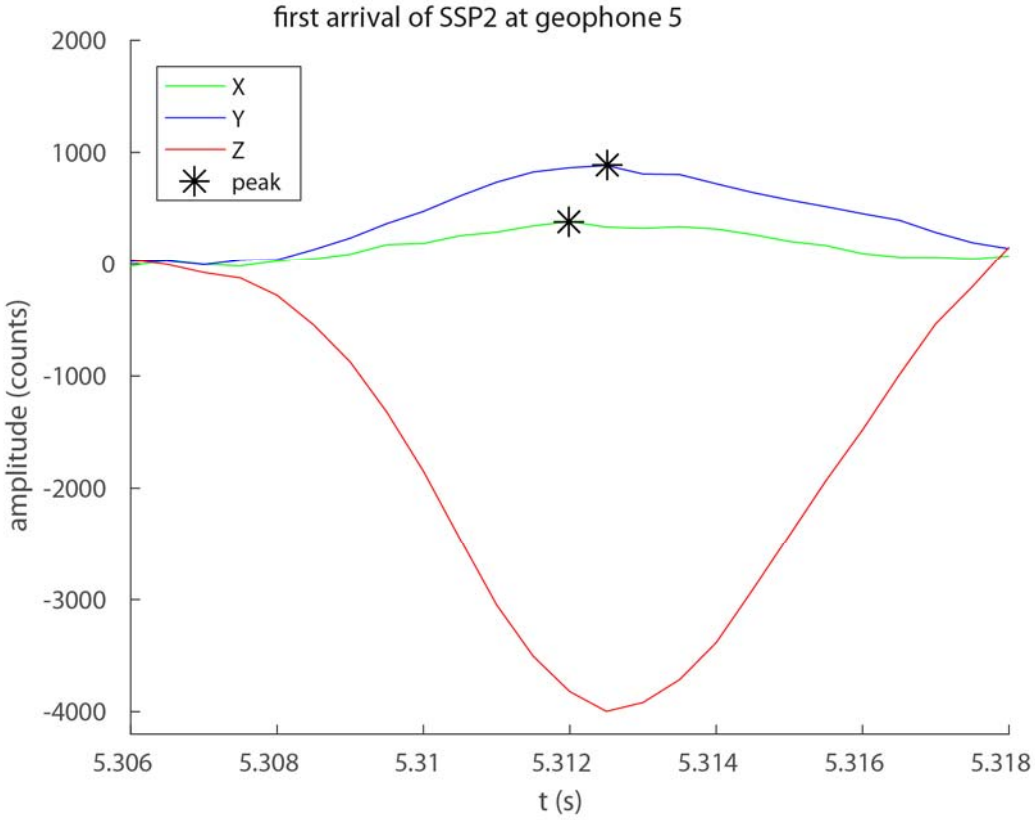
first arrival of SSP2 at geophone 5
X
Y
Z
peak
amplitude (counts)
t (s)
2000
1000
0
-1000
-2000
-3000
-4000
5.306
5.308
5.31
5.312
5.314
5.316
5.318

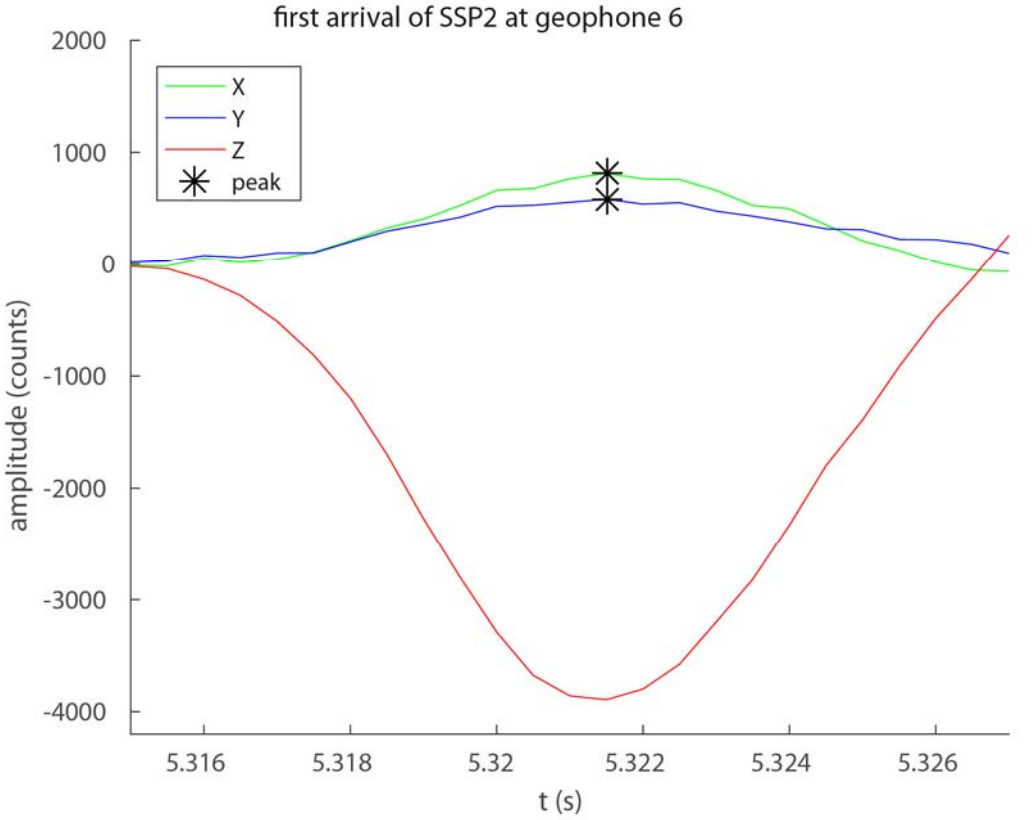
first arrival of SSP2 at geophone 6
X
Y
Z
peak
amplitude (counts)
t (s)
2000
1000
0
-1000
-2000
-3000
-4000
5.316
5.318
5.32
5.322
5.324
5.326

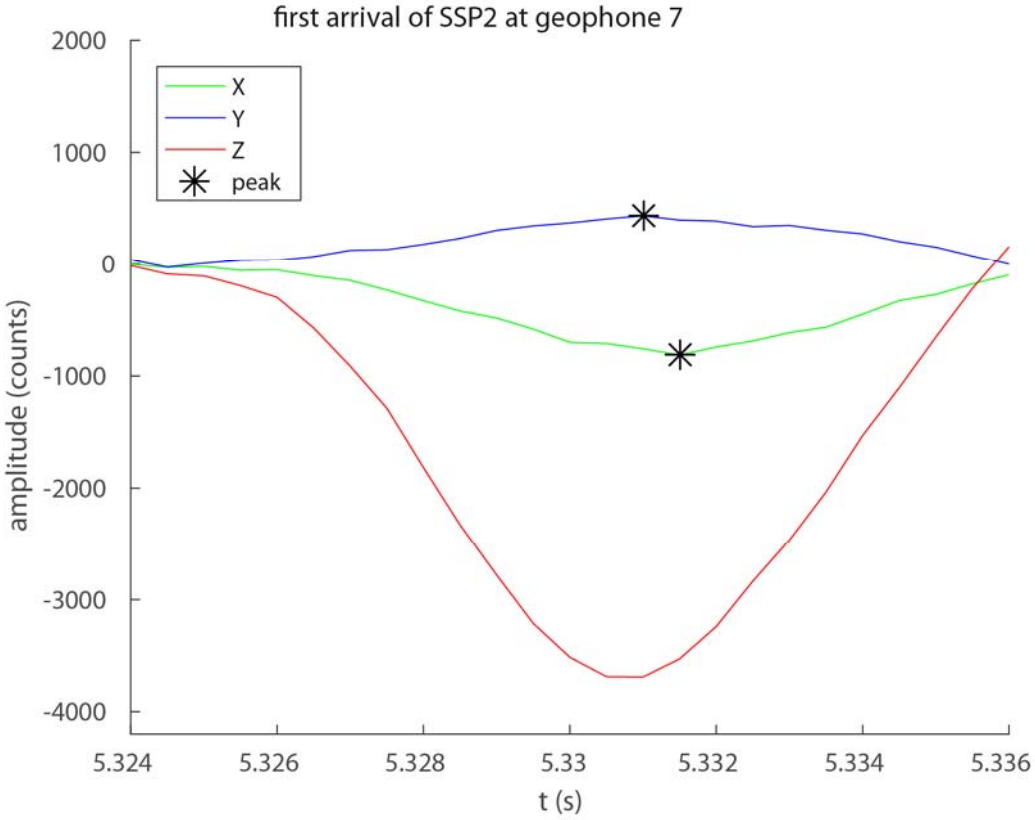
first arrival of SSP2 at geophone 7
X
Y
Z
peak
amplitude (counts)
t (s)
2000
1000
0
-1000
-2000
-3000
-4000
5.324
5.326
5.328
5.33
5.332
5.334
5.336

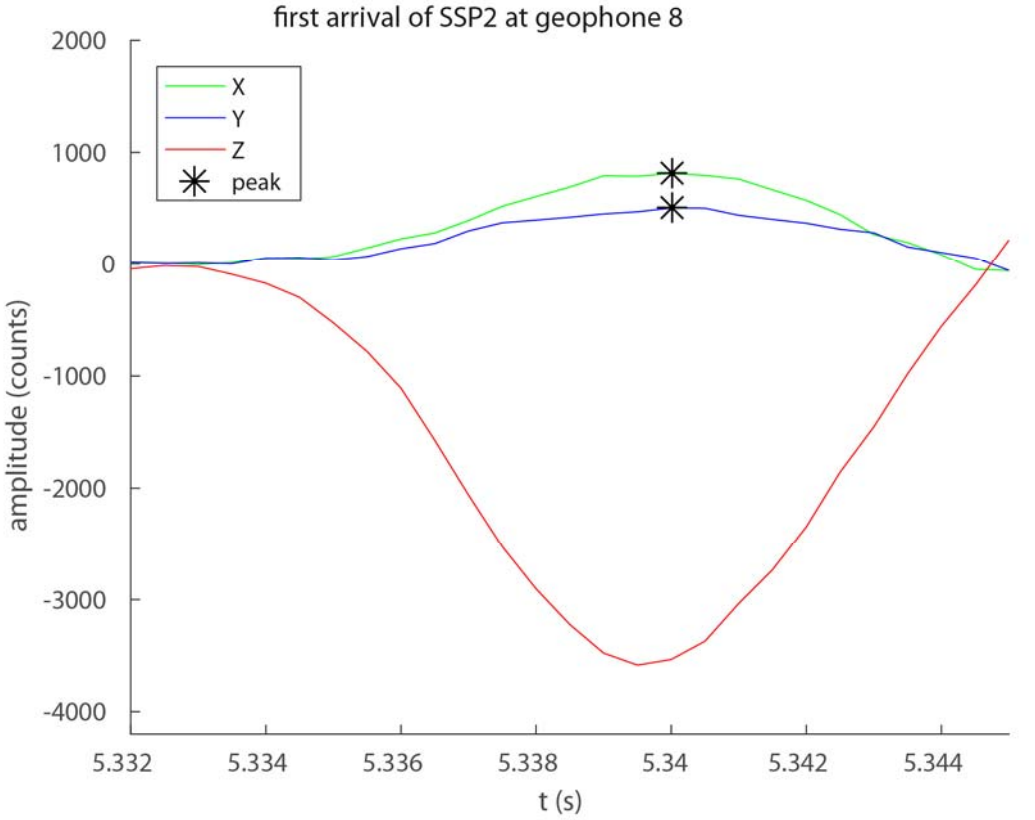
first arrival of SSP2 at geophone 8
X
Y
Z
peak
amplitude (counts)
t (s)
2000
1000
0
-1000
-2000
-3000
-4000
5.332
5.334
5.336
5.338
5.34
5.342
5.344

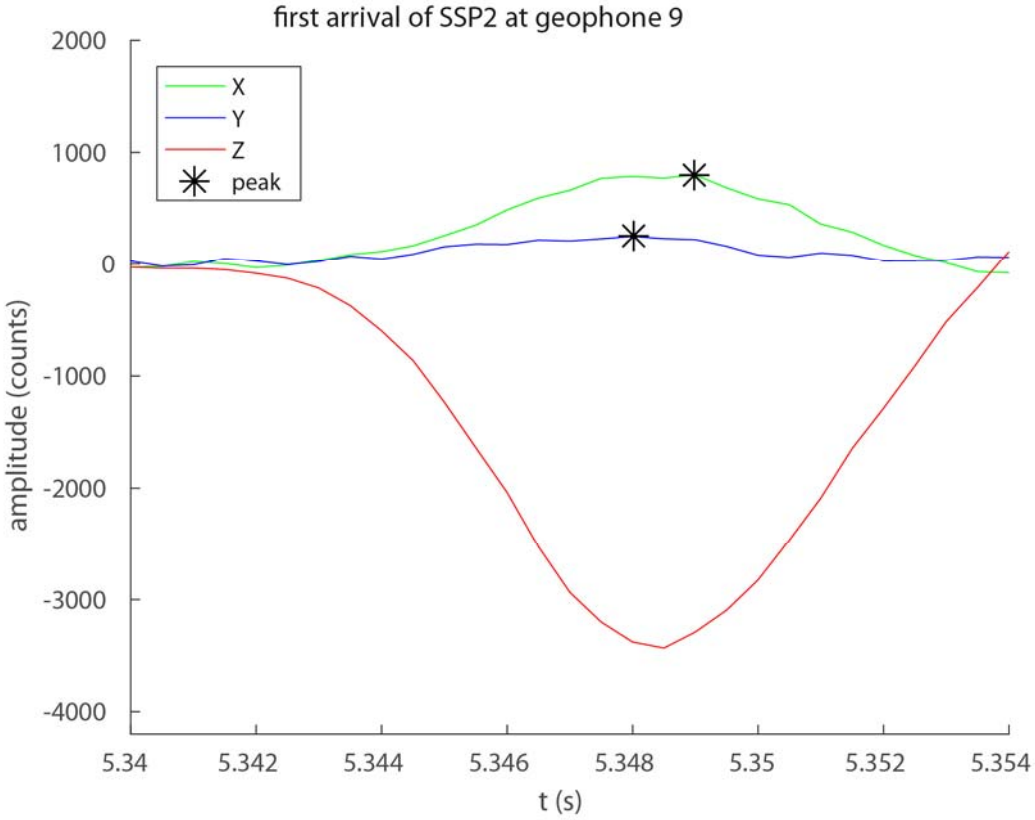
first arrival of SSP2 at geophone 9
X
Y
Z
peak
amplitude (counts)
t (s)
2000
1000
0
-1000
-2000
-3000
-4000
5.34
5.342
5.344
5.346
5.348
5.35
5.352
5.354

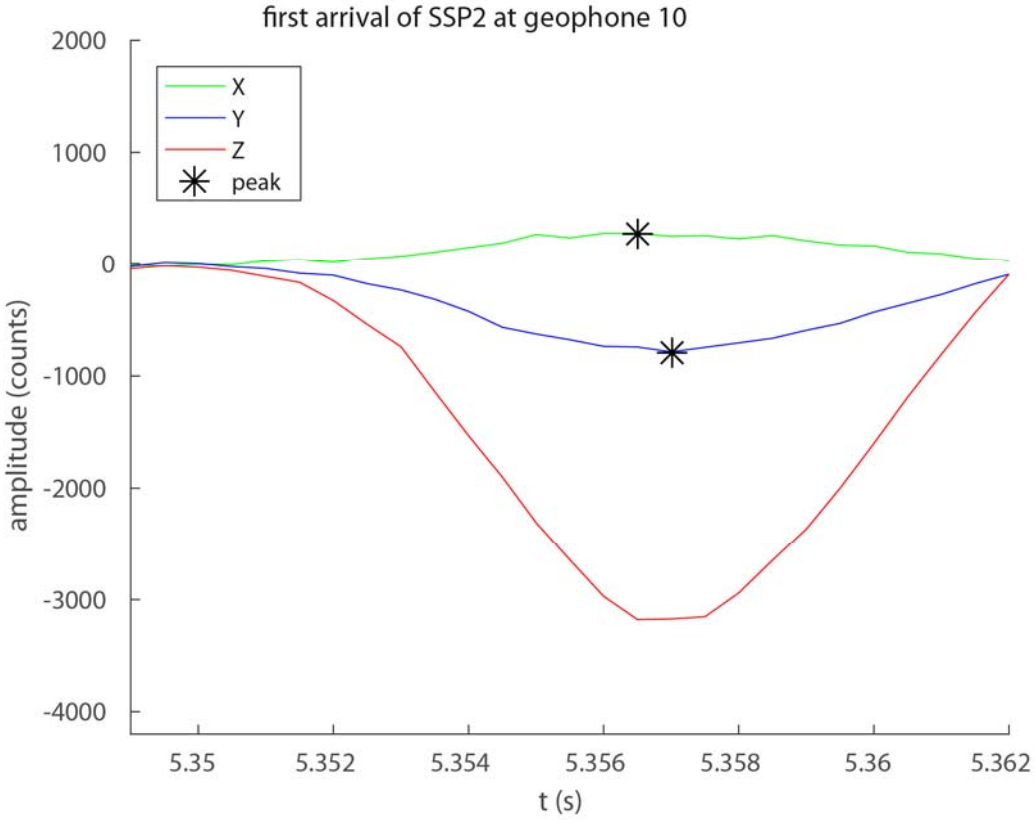
first arrival of SSP2 at geophone 10
X
Y
Z
peak
amplitude (counts)
t (s)
2000
1000
0
-1000
-2000
-3000
-4000
5.35
5.352
5.354
5.356
5.358
5.36
5.362

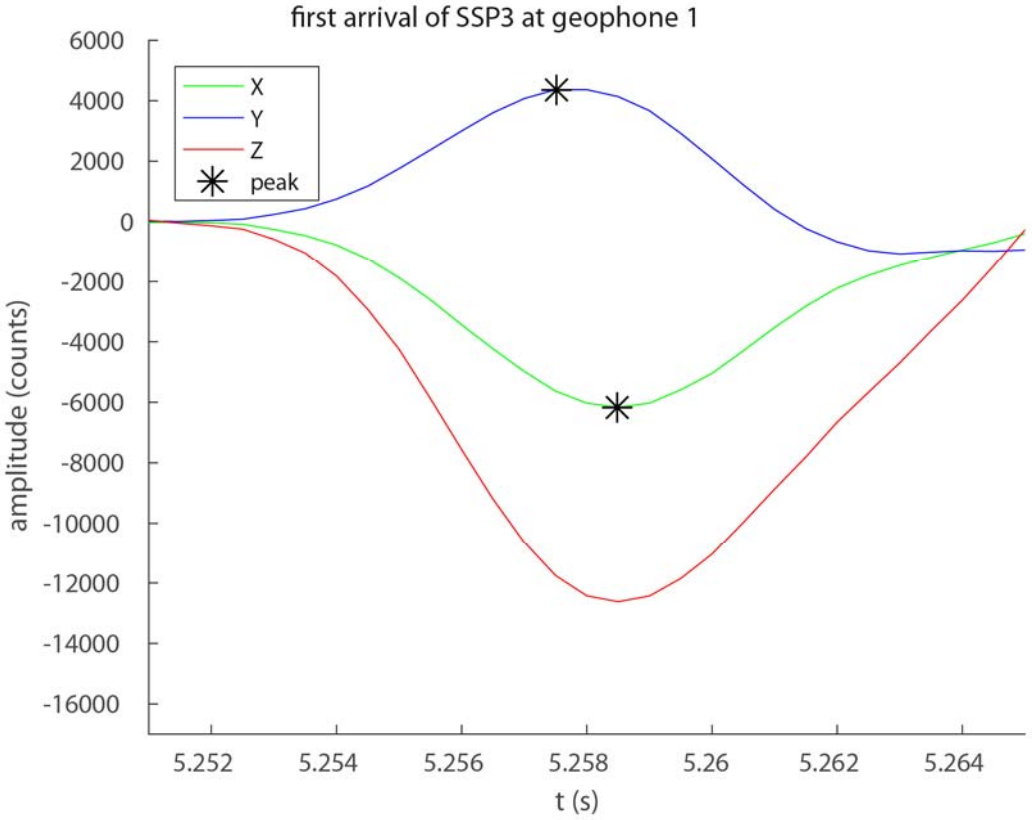
first arrival of SSP3 at geophone 1
X
Y
Z
peak
amplitude (counts)
t (s)
6000
4000
2000
0
-2000
-4000
-6000
-8000
-10000
-12000
-14000
-16000
5.252
5.254
5.256
5.258
5.26
5.262
5.264

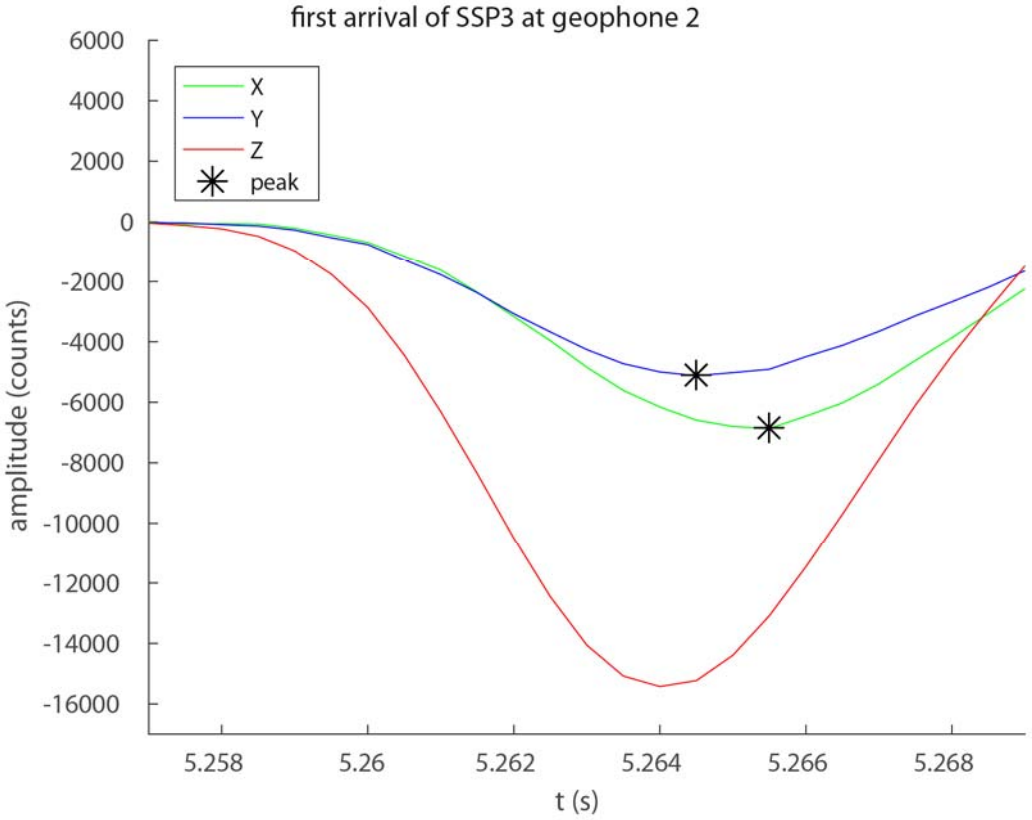
first arrival of SSP3 at geophone 2
X
Y
Z
peak
amplitude (counts)
t (s)
6000
4000
2000
0
-2000
-4000
-6000
-8000
-10000
-12000
-14000
-16000
5.258
5.26
5.262
5.264
5.266
5.268

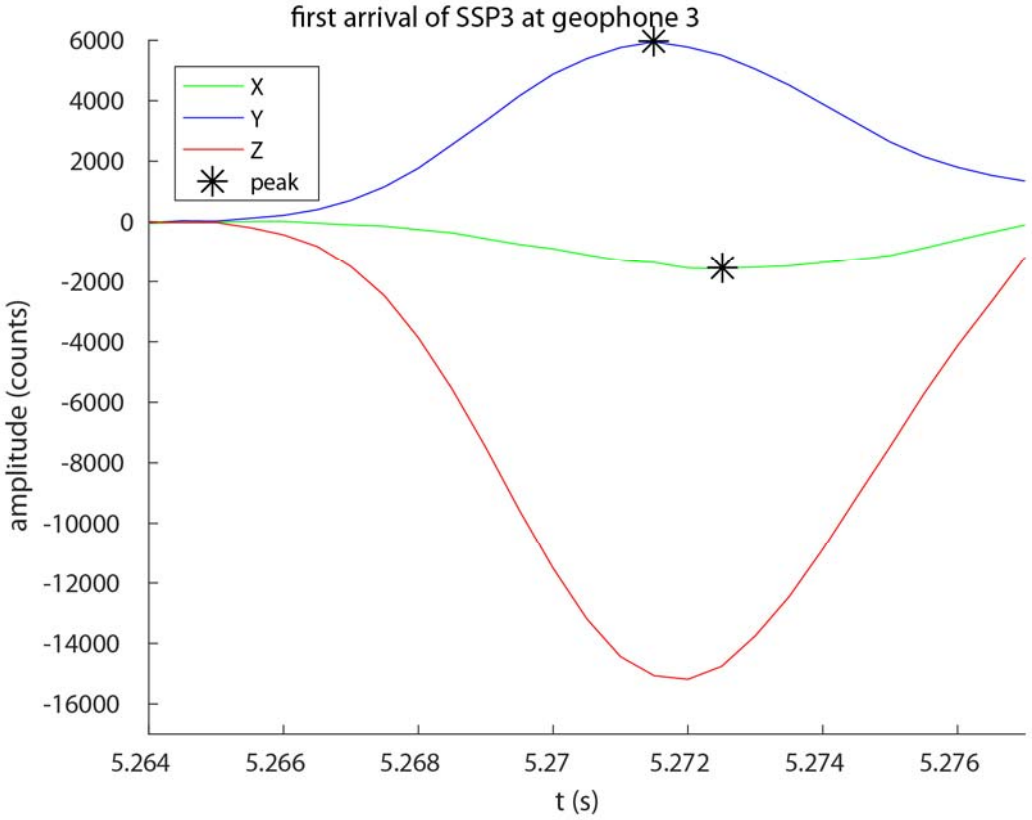
first arrival of SSP3 at geophone 3
X
Y
Z
peak
amplitude (counts)
t (s)
6000
4000
2000
0
-2000
-4000
-6000
-8000
-10000
-12000
-14000
-16000
5.264
5.266
5.268
5.27
5.272
5.274
5.276

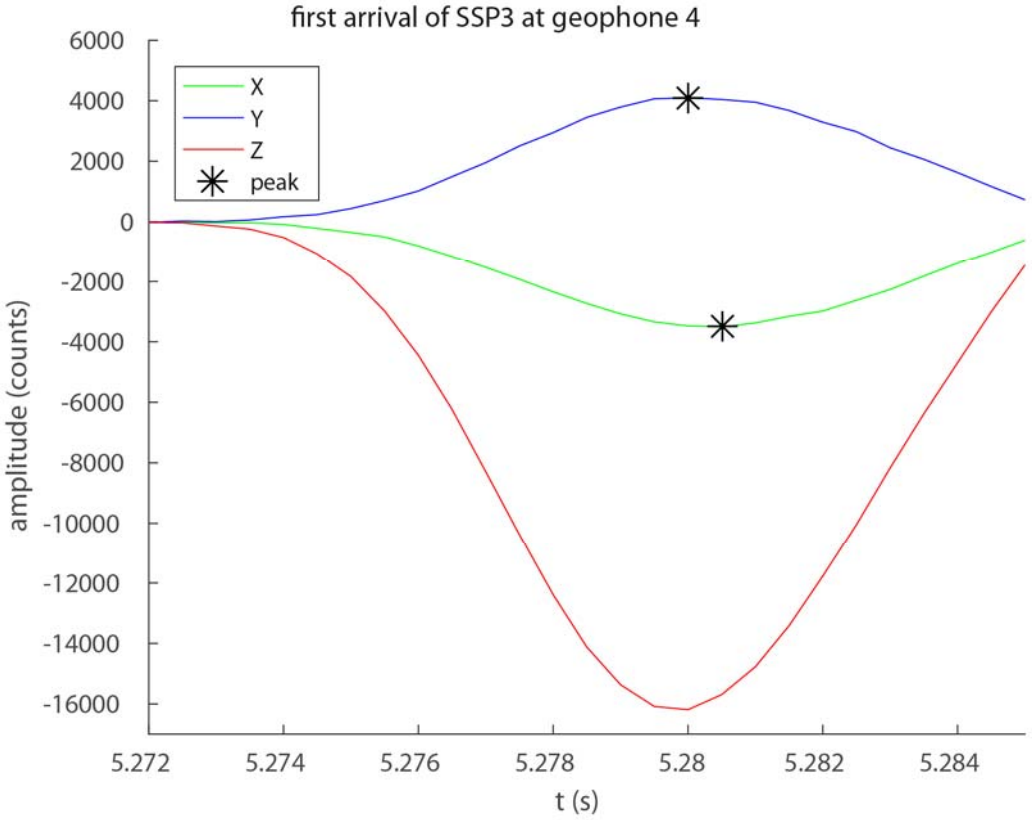
first arrival of SSP3 at geophone 4
X
Y
Z
peak
amplitude (counts)
t (s)
6000
4000
2000
0
-2000
-4000
-6000
-8000
-10000
-12000
-14000
-16000
5.272
5.274
5.276
5.278
5.28
5.282
5.284

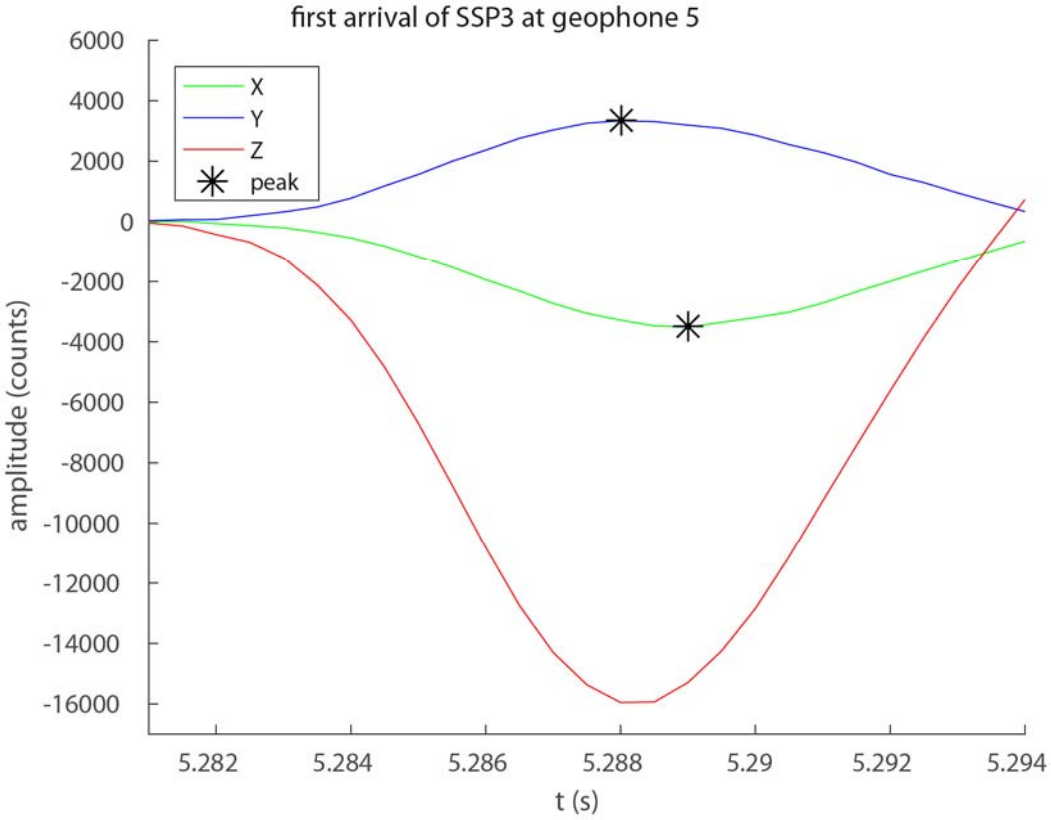
first arrival of SSP3 at geophone 5
X
Y
Z
peak
amplitude (counts)
t (s)
6000
4000
2000
0
-2000
-4000
-6000
-8000
-10000
-12000
-14000
-16000
5.282
5.284
5.286
5.288
5.29
5.292
5.294

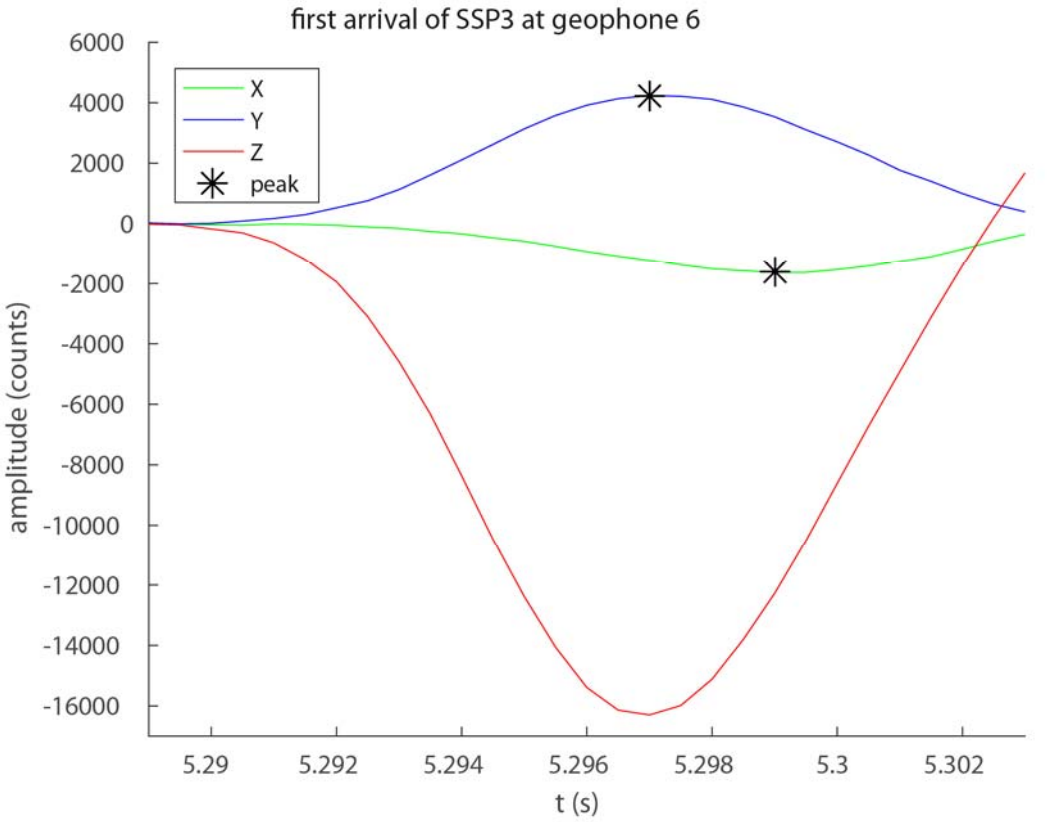
first arrival of SSP3 at geophone 6
X
Y
Z
peak
amplitude (counts)
t (s)
6000
4000
2000
0
-2000
-4000
-6000
-8000
-10000
-12000
-14000
-16000
5.29
5.292
5.294
5.296
5.298
5.3
5.302

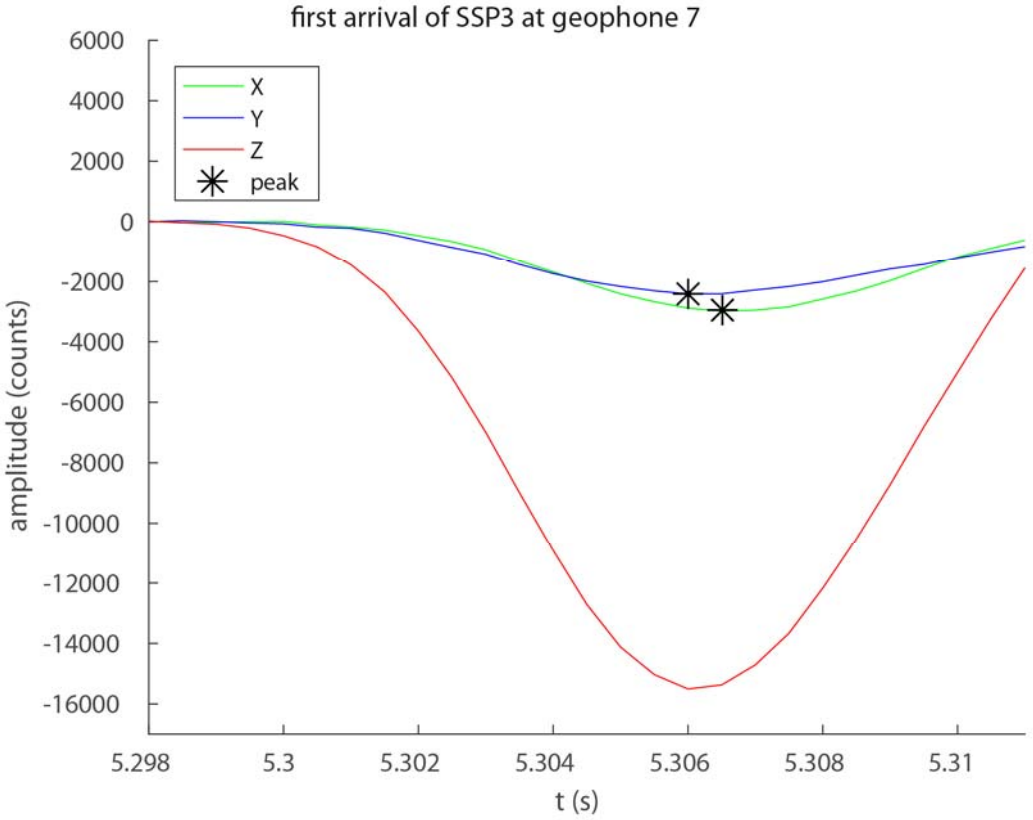
first arrival of SSP3 at geophone 7
X
Y
Z
peak
amplitude (counts)
t (s)
6000
4000
2000
0
-2000
-4000
-6000
-8000
-10000
-12000
-14000
-16000
5.298
5.3
5.302
5.304
5.306
5.308
5.31

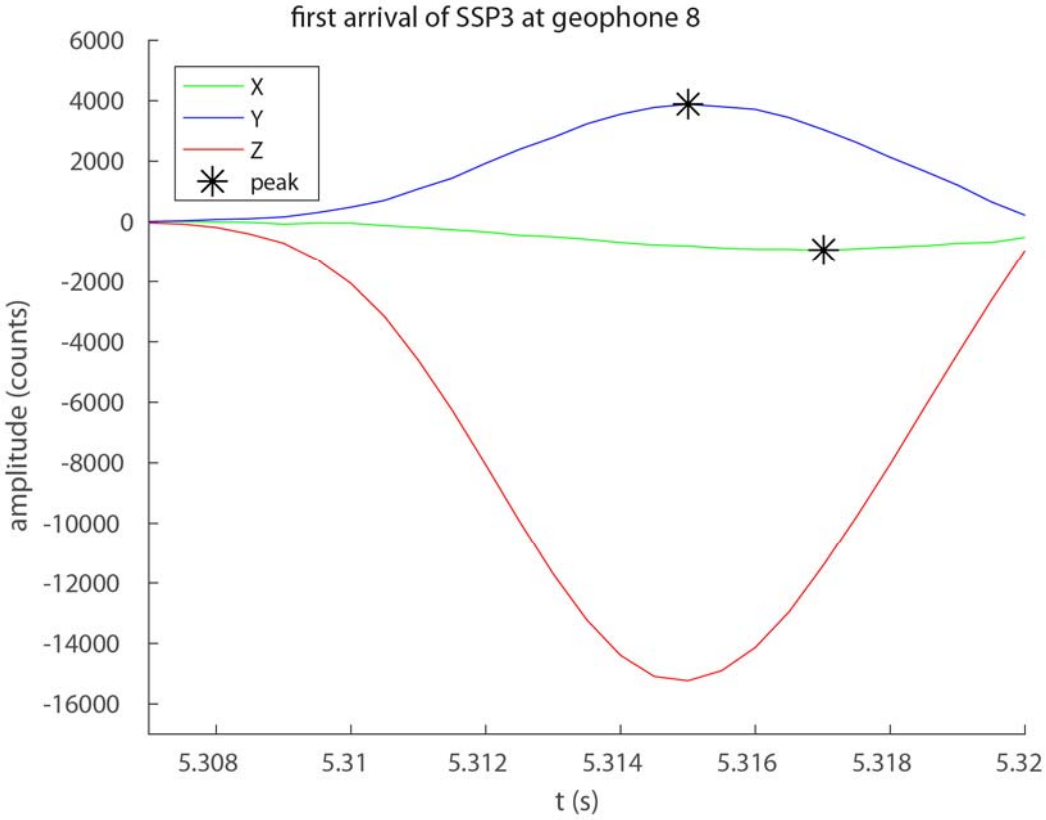
first arrival of SSP3 at geophone 8
X
Y
Z
peak
amplitude (counts)
t (s)
6000
4000
2000
0
-2000
-4000
-6000
-8000
-10000
-12000
-14000
-16000
5.308
5.31
5.312
5.314
5.316
5.318
5.32

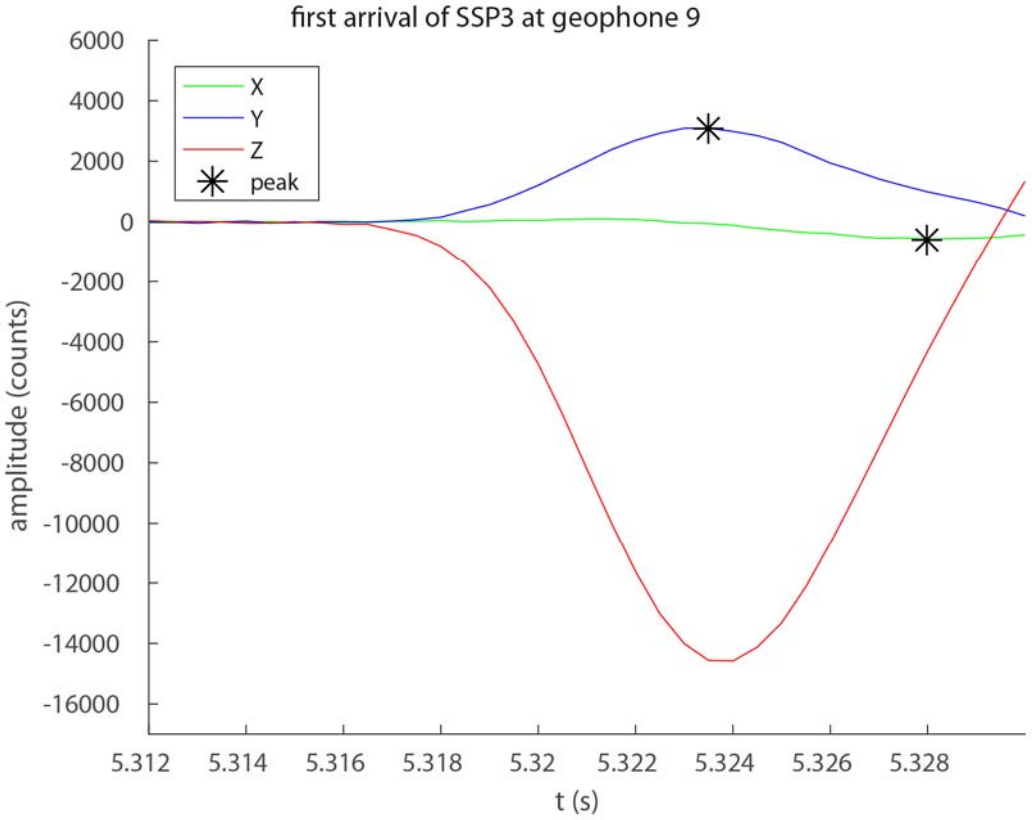
first arrival of SSP3 at geophone 9
X
Y
Z
peak
amplitude (counts)
t (s)
6000
4000
2000
0
-2000
-4000
-6000
-8000
-10000
-12000
-14000
-16000
5.312
5.314
5.316
5.318
5.32
5.322
5.324
5.326
5.328

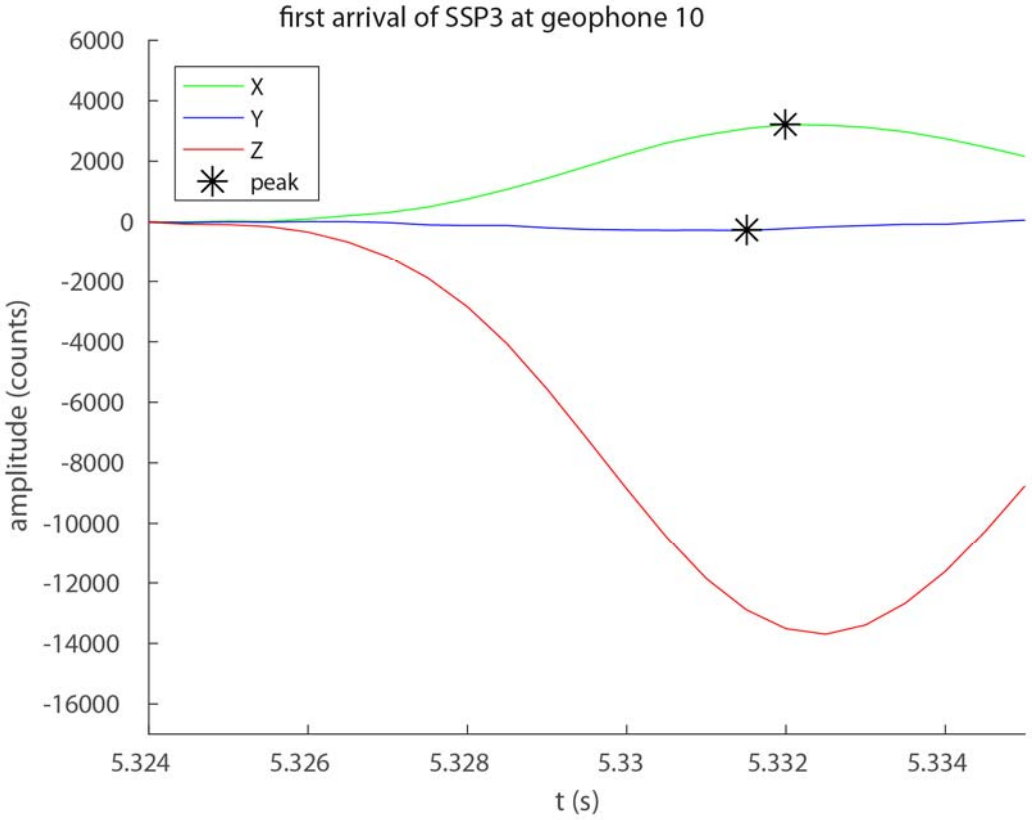
first arrival of SSP3 at geophone 10
X
Y
Z
peak
amplitude (counts)
t (s)
6000
4000
2000
0
-2000
-4000
-6000
-8000
-10000
-12000
-14000
-16000
5.324
5.326
5.328
5.33
5.332
5.334

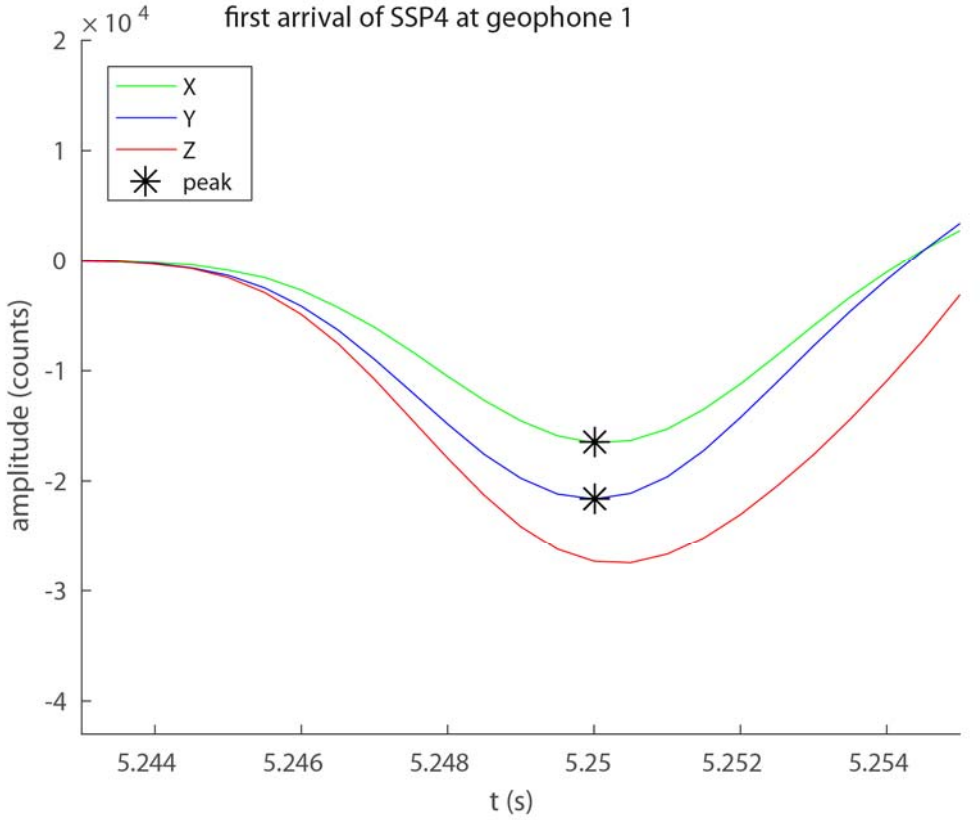
first arrival of SSP4 at geophone 1
× 10 4
X
Y
Z
peak
amplitude (counts)
t (s)

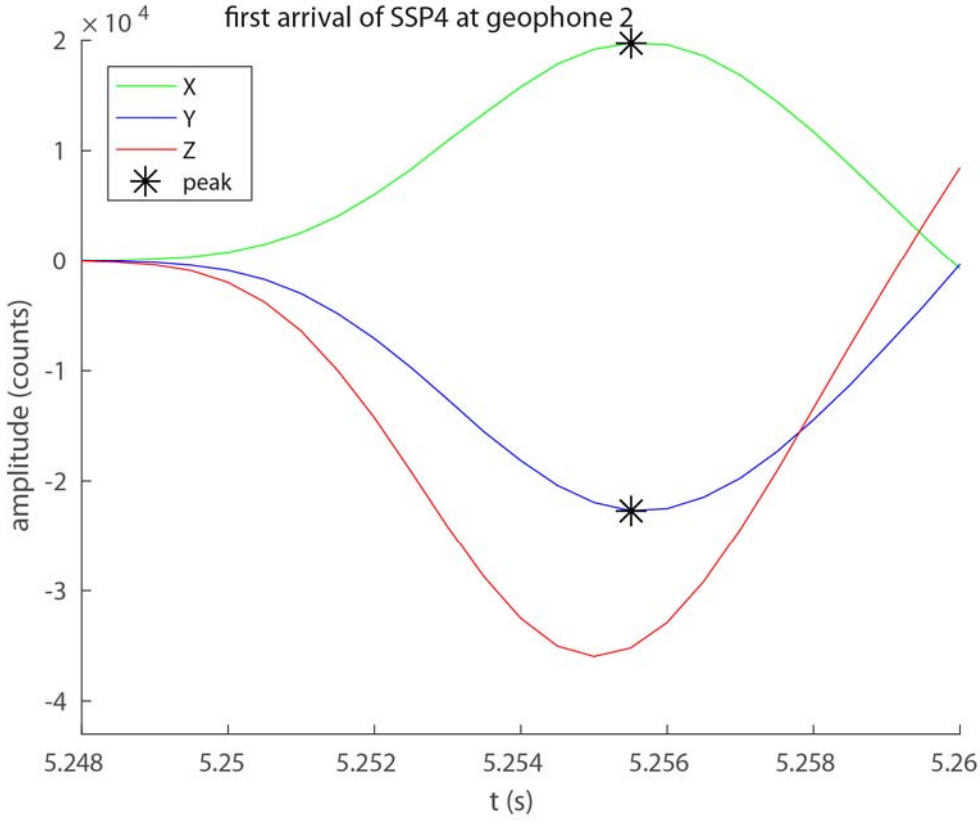
first arrival of SSP4 at geophone 2
× 10 4
X
Y
Z
peak
amplitude (counts)
t (s)

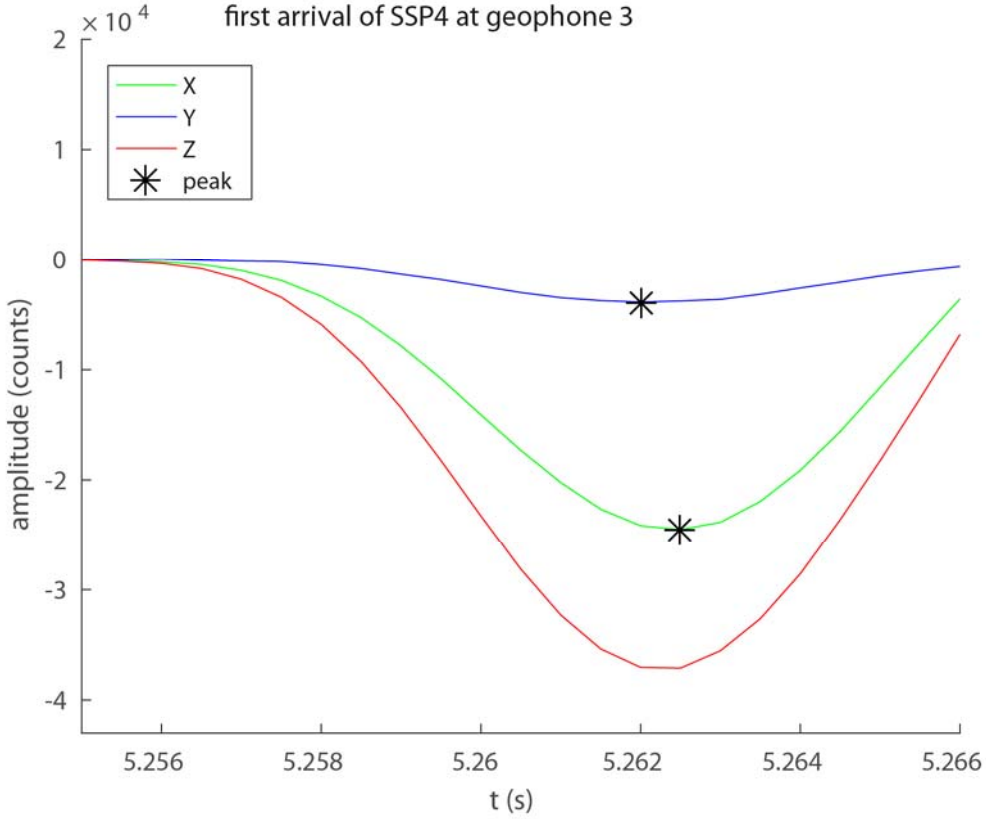
first arrival of SSP4 at geophone 3
× 10 4
X
Y
Z
peak
amplitude (counts)
t (s)
2
1
0
-1
-2
-3
-4
5.256
5.258
5.26
5.262
5.264
5.266

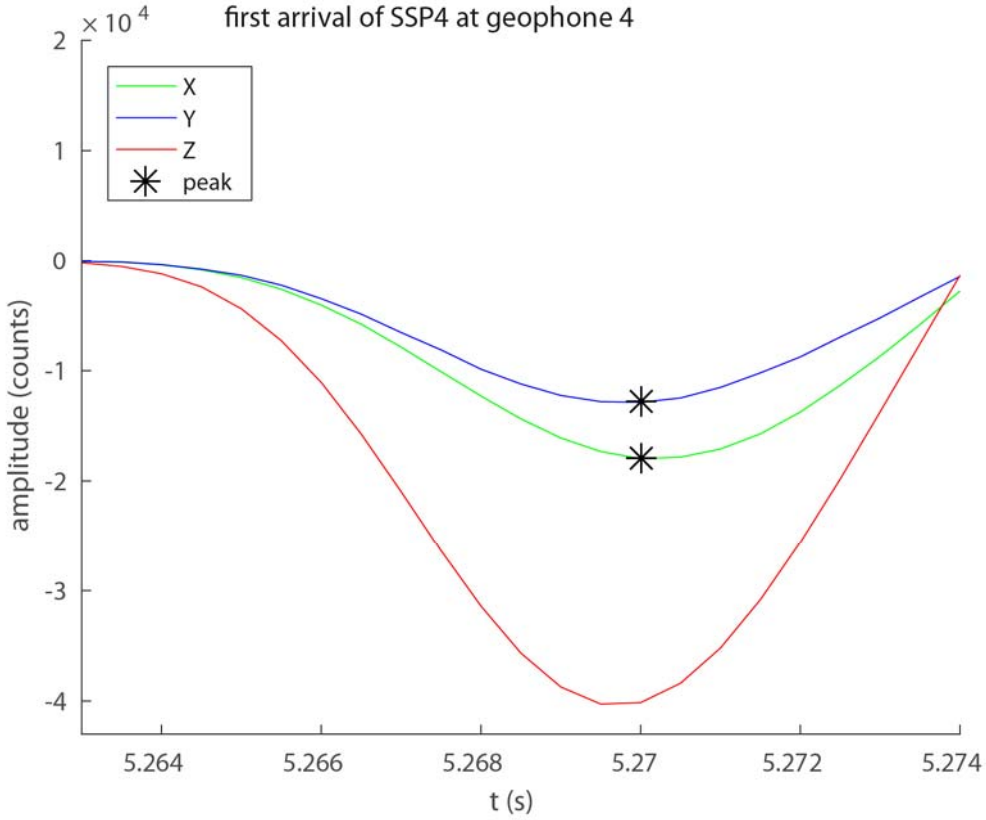
first arrival of SSP4 at geophone 4
× 10 4
X
Y
Z
peak
amplitude (counts)
t (s)
2
1
0
-1
-2
-3
-4
5.264
5.266
5.268
5.27
5.272
5.274

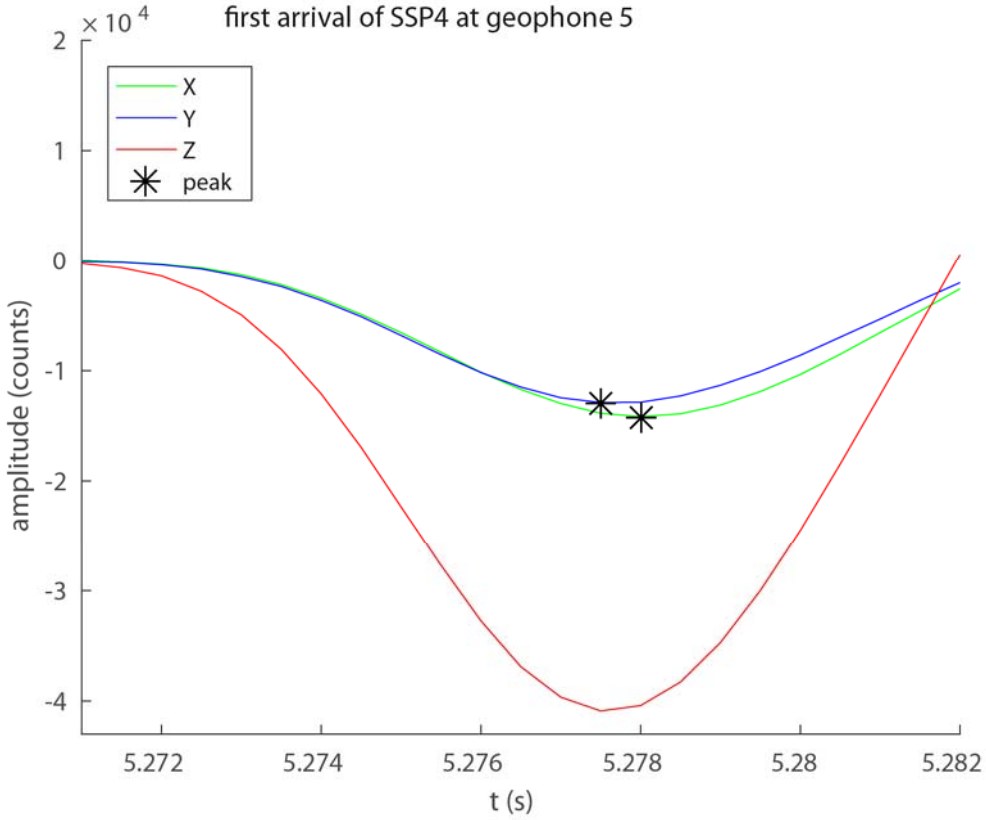
first arrival of SSP4 at geophone 5
× 10 4
X
Y
Z
peak
amplitude (counts)
t (s)
2
1
0
-1
-2
-3
-4
5.272
5.274
5.276
5.278
5.28
5.282

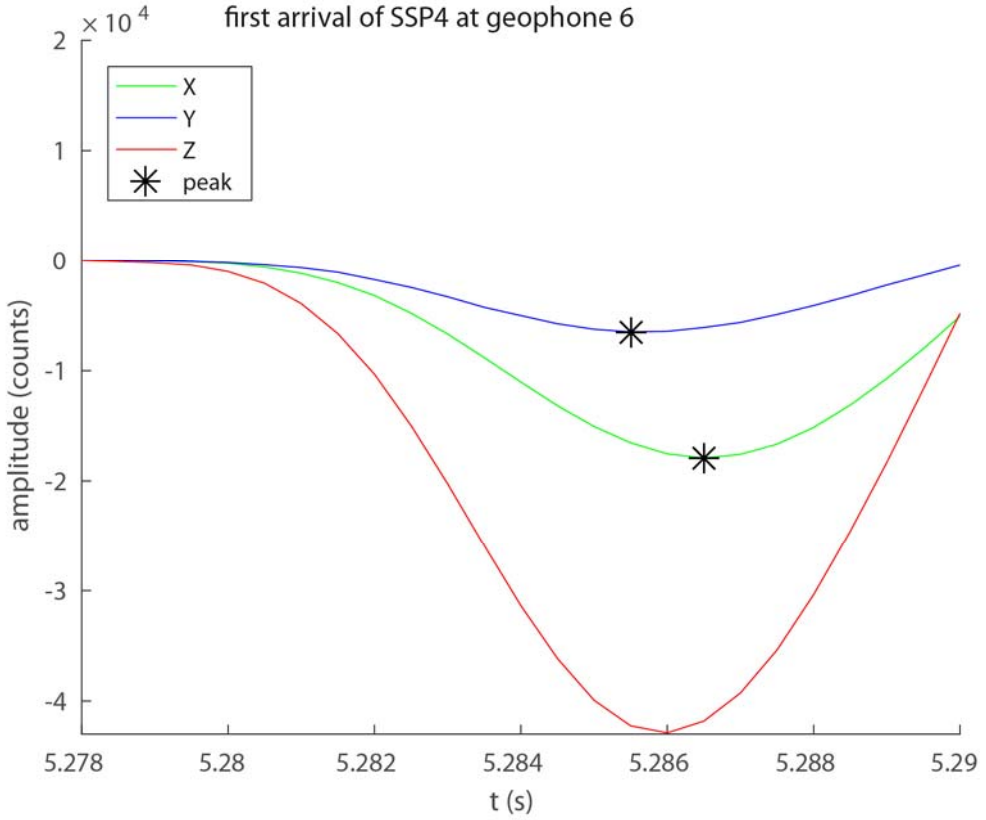
first arrival of SSP4 at geophone 6
× 10 4
X
Y
Z
peak
amplitude (counts)
t (s)
2
1
0
-1
-2
-3
-4
5.278
5.28
5.282
5.284
5.286
5.288
5.29

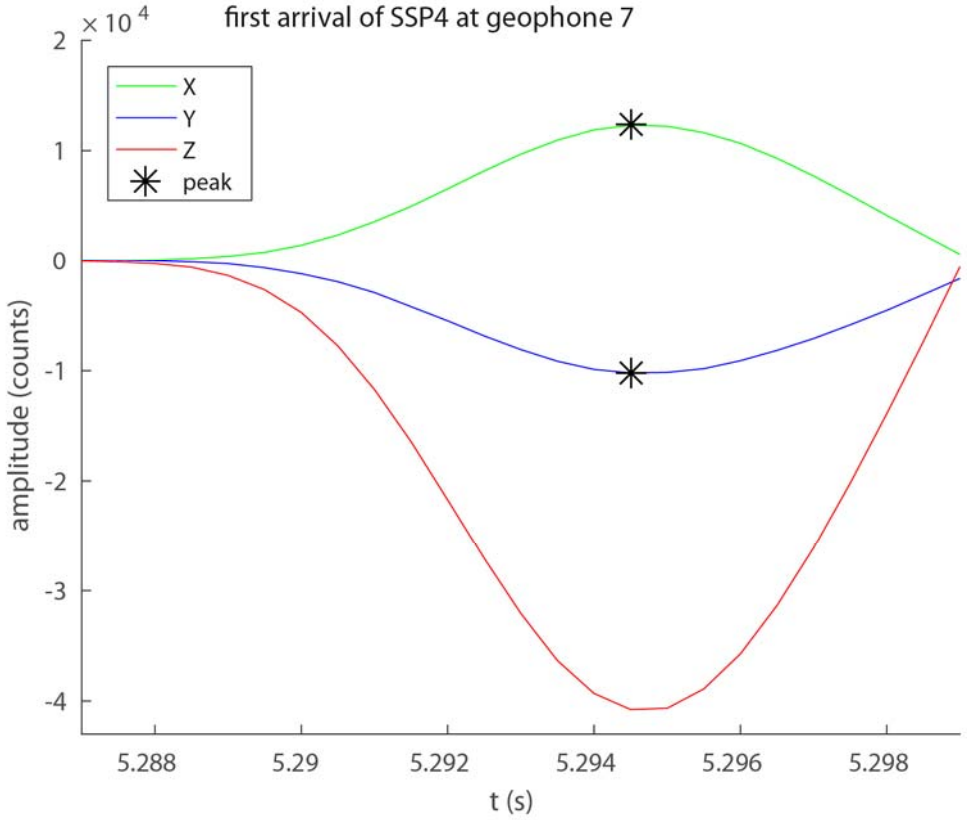
first arrival of SSP4 at geophone 7
× 10 4
X
Y
Z
peak
amplitude (counts)
t (s)
2
1
0
-1
-2
-3
-4
5.288
5.29
5.292
5.294
5.296
5.298

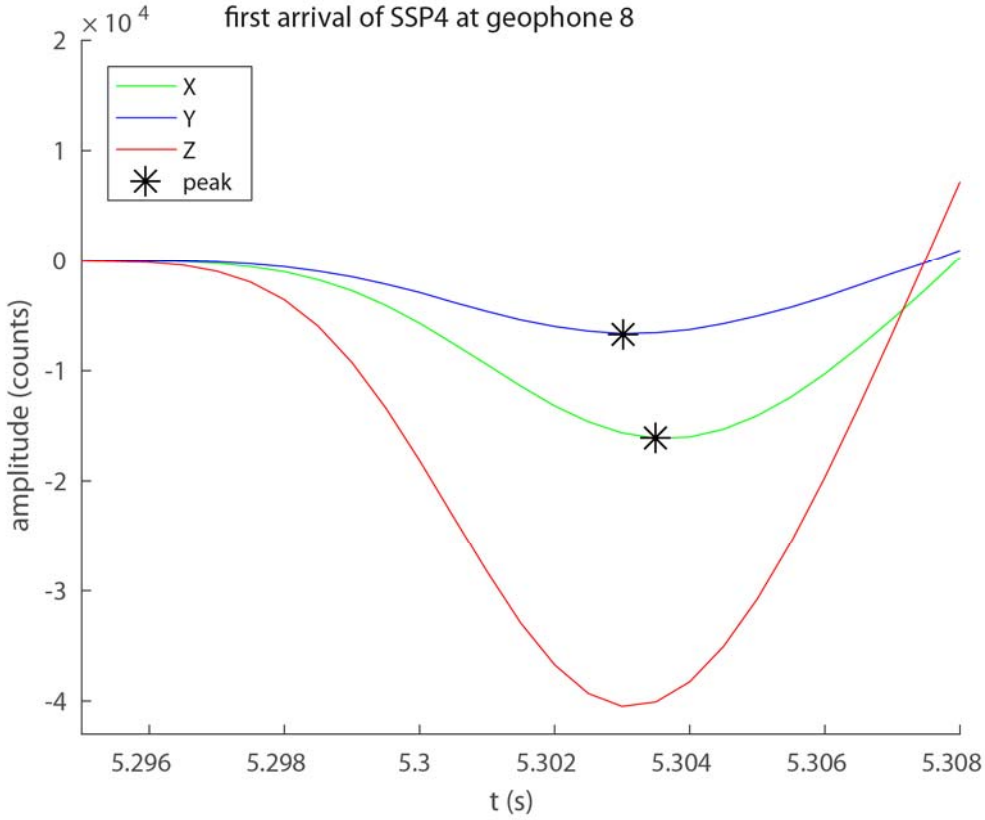
first arrival of SSP4 at geophone 8
× 10 4
X
Y
Z
peak
amplitude (counts)
t (s)
2
1
0
-1
-2
-3
-4
5.296
5.298
5.3
5.302
5.304
5.306
5.308

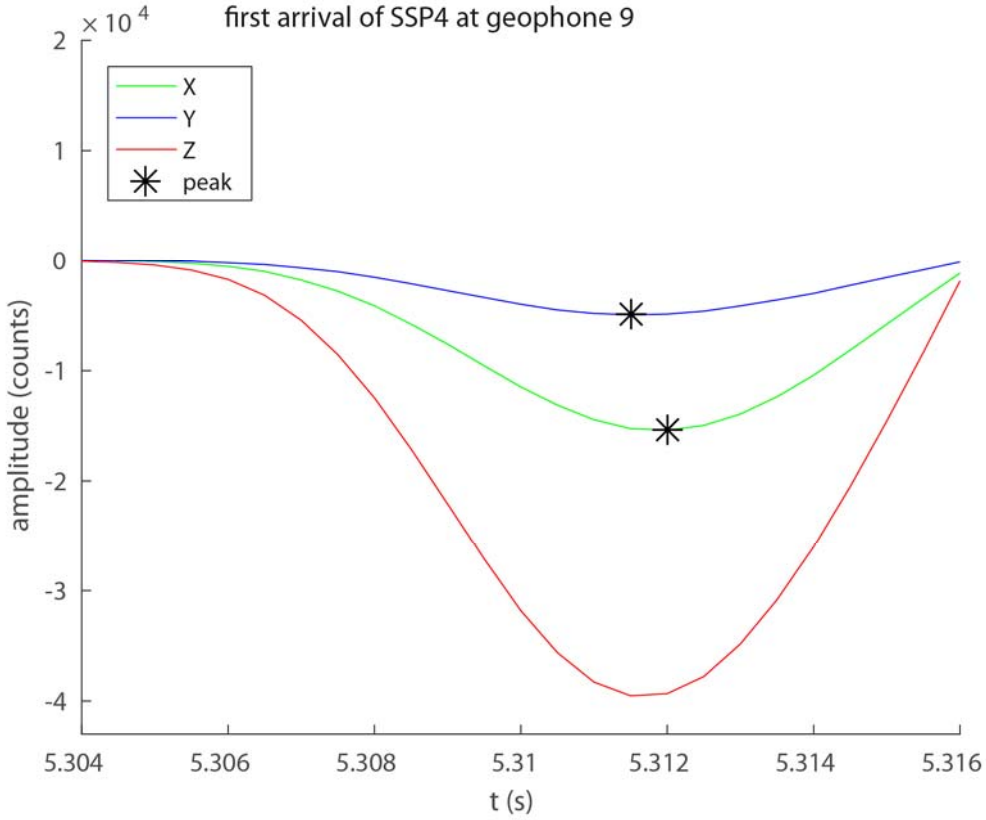
first arrival of SSP4 at geophone 9
× 10 4
X
Y
Z
peak
amplitude (counts)
t (s)
2
1
0
-1
-2
-3
-4
5.304
5.306
5.308
5.31
5.312
5.314
5.316

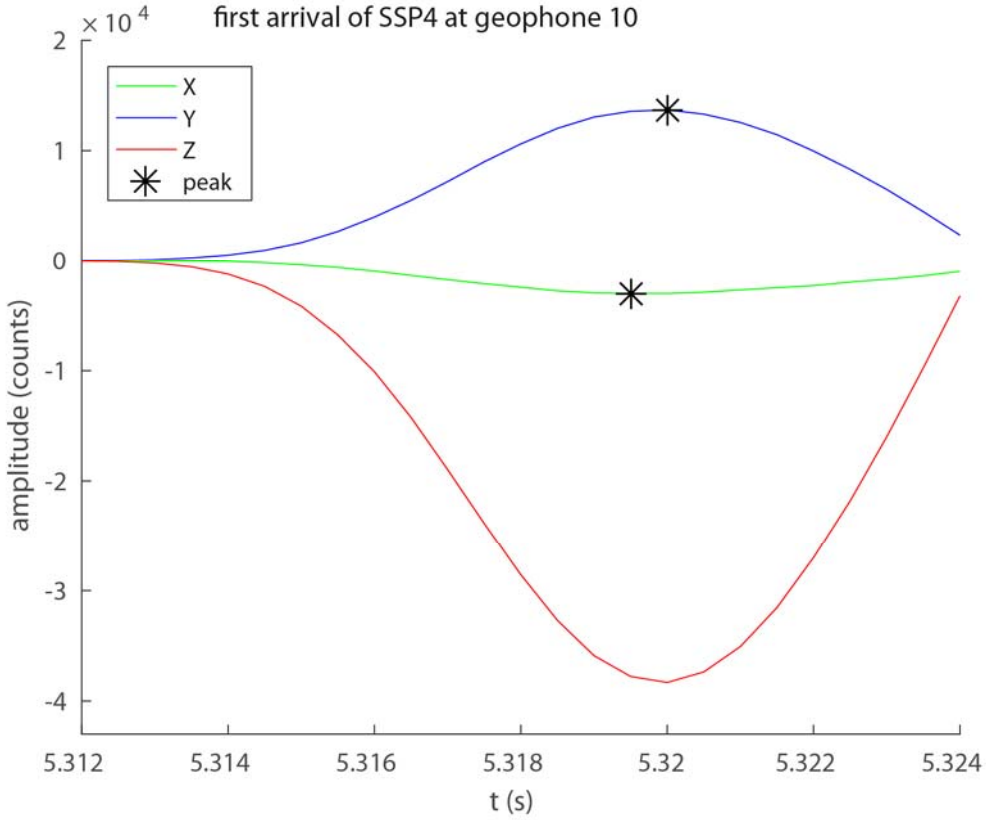
first arrival of SSP4 at geophone 10
× 10 4
X
Y
Z
peak
amplitude (counts)
t (s)
2
1
0
-1
-2
-3
-4
5.312
5.314
5.316
5.318
5.32
5.322
5.324

Appendix 4: Spectral-element method

To explain the spectral-element method, the classic 1D elastic wave equation is used, which is a second order differential equation:

$$\rho \frac{\partial^2 u}{\partial t^2} = \frac{\partial}{\partial x}\left(\mu \frac{\partial u}{\partial x}\right) + f$$

u = displacement, depends on x and t

f = external force, depends on x and t

ρ = mass density, depends on x

μ = shear modulus, depends on x

An important boundary property of wave propagation problems is a stress-free condition at the Earth's surface, expressed by the vanishing of the traction perpendicular to the free surface.

$$\sigma_{ij} n_j = 0$$

σ_{ij} = symmetric stress tensor

n_j = normal vector to the free surface

This stress-free surface condition is implicitly solved with the spectral-element method, which is a major advantage compared to other methods, such as the finite-difference method.

The spectral-element method is a method to create a numerical solution for partial differential equations. The solution is obtained by a series expansion, where the continuous solution field is replaced by a finite sum over basis functions. To make computation possible, the continuous solution has to be broken up into a finite number of elements with a finite size and in each element the exact solution is approximated by a finite number of basis functions.

In order to get to such an approximation, the weak form of the elastic wave equation is used. This is obtained by multiplying both sides of the elastic wave equation by a time-independent test function $v(x)$ and integrate by parts over the domain D [0,L], using the boundary condition $\frac{\partial u(0,t)}{\partial x} = \frac{\partial u(L,t)}{\partial x} = 0$:

$$\int_D v\rho \frac{\partial^2 u}{\partial t^2} dx + \int_D \mu \frac{\partial v}{\partial x}\frac{\partial u}{\partial x} dx = \int_D v f dx$$

For the approximation of the exact solution in a finite domain, the Galerkin method is used. Here, the exact solution $u(x,t)$ is approximated by a finite superposition of n basis functions $\varphi_i(x)$ weighted by time-dependent coefficients $u_i(t)$ with i = 1, … , N_p. The accuracy of the approximation will depend on the number N_p, which is the number of required basis functions for a specific polynomial order N. The approximate displacement field is denoted by $\overline{u}(x,t)$:

$$u(x,t) \approx \overline{u}(x,t) = \sum_{i=1}^{N_p} u_i(t)\varphi_i(x)$$

$u(x,t)$ = continuous solution field of the displacement

$\overline{u}(x,t)$ = approximate displacement field

$u_i(t)$ = time-dependent coefficients for weighting

$\varphi_i(x)$ = basis functions

To find a solution to the weak form of the elastic wave equation for the approximate displacement field $\overline{u}(x,t)$ instead of $u(x,t)$, and by using as test functions the same basis functions as for approximating the displacement field (Galerkin principle), the weak form of the elastic wave equation becomes:

$$\int_D \varphi_i \rho \frac{\partial^2 \overline{u}}{\partial t^2} dx + \int_D \mu \frac{\partial \varphi_i}{\partial x} \frac{\partial \overline{u}}{\partial x} dx = \int_D \varphi_i f dx$$

Combining this with the equation for the approximation of the displacement field, the well-known equation for finite-element problems is obtained for the global system:

$$\sum_{i=1}^{N_p} \left[\frac{\partial^2 u_i(t)}{\partial t^2} \int_D \rho(x)\varphi_j(x)\varphi_i(x)dx \right] + \sum_{i=1}^{N_p} \left[u_i(t) \int_D \mu(x) \frac{\partial \varphi_j(x)}{\partial x} \frac{\partial \varphi_i(x)}{\partial x} dx \right] = \int_D \varphi_i f(x,t) dx$$

When getting down to the element level, this equation becomes for the local system:

$$\sum_{i=1}^{N_p} \left[\frac{\partial^2 {u_i}^e(t)}{\partial t^2} \int_{D_e} \rho(x){\varphi_j}^e(x){\varphi_i}^e(x)dx \right] + \sum_{i=1}^{N_p} \left[{u_i}^e(t) \int_{D_e} \mu(x) \frac{\partial {\varphi_j}^e(x)}{\partial x} \frac{\partial {\varphi_i}^e(x)}{\partial x} dx \right] = \int_{D_e} {\varphi_i}^e f(x,t) dx$$

This can be written in matrix notation:

$$M^e \frac{\partial^2 u^e(t)}{\partial t^2} + K^e u^e(t) = f^e(t), \quad e = 1, \dots, n_e$$

u^e = coefficients of the unknown displacement inside the element

M^e = elemental mass matrix

K^e = elemental stiffness matrix

f^e = elemental vector containing the volumetric forces

n^e = number of elements

It is useful to apply a coordinate transformation from the global system with x belonging to domain D [0,L], to the local system with ξ belonging to domain D_e [-1,1], using the relations:

$$x(\xi) = h_e \frac{\xi + 1}{2} + x_e$$

$$\xi(x) = 2\frac{x - x_e}{h_e} - 1$$

x_e = coordinate of the left side of the element

h_e = element size

So far, the spectral-element method is similar to the finite-element method, but the difference comes with the choice of basis functions. Where the finite-element method leads to a system of linear equations, the spectral-element method leads to a system of polynomials, in this case Lagrange polynomials:

$$\varphi_i = l_i^{(N)}(\xi) := \prod_{j \neq i}^{N+1} \frac{\xi - \xi_j}{\xi_i - \xi_j}, \quad i, j = 1,2, \dots, N+1$$

At the maxima of each of these polynomials, the other polynomials are equal to zero, due to their orthogonality, which can be expressed as:

$$l_i^{(N)}(\xi_j) = \delta_{ij}$$

δ_{ij} = Kronecker delta, which is 1 if i=j and 0 otherwise

These extremal points are called collocation points, and at these points, the polynomials exactly interpolate an arbitrary discrete function. The collocation points are located at fixed points ξ_i in the interval [-1,1], where the density of collocation points increases towards the boundaries of the element. The number of collocation points is equal to N+1, so the higher order (N) polynomials is used, the more collocation points are present within an element, so the more accurate the interpolation will be. With the finite-element method, the order of polynomials used is N=1, so the number of collocation points is 2, located at the boundaries of the element.

Using an integration scheme for an arbitrary function defined in the interval x belonging to D_e [-1,1], with integration weights w_i decreasing towards the element boundaries, and using the expression for the orthogonality of the Langrange polynomials, the solution equation for the spectral-element system at the element level is obtained, in matrix notation:

$$\sum_{i=1}^{N+1} M_{ji}^e \frac{\partial^2 u_i^e(t)}{\partial t^2} + \sum_{i=1}^{N+1} K_{ji}^e u_i^e(t) = f_j^e(t), \quad e = 1, \dots, n_e$$

$$M_{ji}^e = w_j \rho(\xi) \frac{dx}{d\xi} \delta_{ij}|_{\xi=\xi_j}$$

$$K_{ji}^{e} = \sum_{k=1}^{N+1} w_k \mu(\xi) \frac{\partial l_j(\xi)}{\partial \xi} \frac{\partial l_i(\xi)}{\partial \xi} \left(\frac{d\xi}{dx}\right)^2 \frac{dx}{d\xi}|_{\xi=\xi_k}$$

$$f_j^e = w_j f(\xi, t) \frac{dx}{d\xi}|_{\xi=\xi_j}$$

These elemental matrices and vectors have the size $(N+1) \times (N+1)$ or $(N+1)$, which is the number of collocation points per element, with defined information on the density and elastic parameters at the collocation points. The global matrices and vectors, indicated with a subscript g, have the size $n_g \times n_g$ or n_g, which is the total number of collocation points of the entire domain D, given by $n_g = n_e N + 1$. These global matrices are obtained by combining the elemental matrices, which are overlapping and summed at the element boundaries.

This results in a system of equations for n_g coefficients for the displacement in the global system u_g. The time-dependent coefficients u_g are extrapolated with a simple centred finite-difference scheme to the next time step $t + dt$:

$$u_g(t + dt) = dt^2 \left[M_g^{-1}(f_g(t) - K_g u_g(t))\right] + 2u_g(t) - u_g(t - dt)$$

This way, the global displacement field is calculated for each time step. In Specfem2D, also the velocity field or the acceleration field can be chosen to calculate. These are simply obtained by the derivative and second derivative of the displacement field. For this study, the velocity field is calculated by Specfem2D, because the data of the geophones is also a measurement of the velocity. Specfem2D calculates the displacement field in 2D, making use of the 2D elastic wave equation. This causes u and f in de wave equation to become vectors, rather than scalars.

Appendix 5: Specfem2D parameters

Table 8: Input parameters for file defining the source

Parameter name	Parameter value	Description of parameter	Explanation of chosen value
source_surf	.false.	Source inside the medium (.false.) or automatically moved to the surface by the solver (.true.)	The source is not directly at the surface, to prevent loss of energy directly to the upper limit of the space
xs	0	Location of source in x-direction in meters	
zs	-20	Location of source in z-direction in meters	
source_type	2	Source type (1 = elastic force or acoustic pressure, 2 = moment tensor)	
time_function_type	1	Time function type (1 = second derivative of Gaussian a.k.a. Ricker, 2 = first derivative of Gaussian, 3 = Gaussian, 4 = Dirac, 5 = Heaviside)	
f0	15.0	Dominant source frequency in Herz	
Mxx	1	xx component of moment tensor	Positive, because the source is an explosion
Mzz	1	zz component of moment tensor	Positive, because the source is an explosion
Mxz	0	xz component of moment tensor	No shear component
Factor	5.d8	Amplification factor	

Table 9: Input parameters for parameter file

Parameter name	Parameter value	Description of parameter	Explanation of chosen value
title	“run6”	Title of the job	Multiple runs are done, so identifying each run clearly with a title is essential
NPROC	48	Number of processes	12 cores with 4 nodes are used
ngnod	9	Number of control nodes per element	4 corners of the element, 4 midpoints of the sides of the element, 1 center of the element
NSTEP	150000	Number of time steps	
DT	2d-5	Duration of time step in seconds	150000 time steps of 2d-5 seconds results in a time window of 3 seconds
P_SV	.true.	Occurrence of P-SV conversions	

NSOURCES	1	Number of sources	1 source and 5 receiver strings are used (incl. 1 reference receiver string), rather than 1 receiver and 4 sources (as is the case in reality), to minimize computation time
seismotype	2	Type of recording of the seismograms (1 = displacement, 2 = velocity, 3 = acceleration)	The real geophones also measure velocity
subsamp_seismos	25	Subsampling of the seismograms to create smaller files	For a subsampling value of 25, the DT becomes 5d-4, which is equal to the DT of the real seismograms
NSTEP_BETWEEN_OUTPUT_SEISMOS	50000	Number of time steps between output seismograms	
save_ASCII_seismograms	.false.		
SU_FORMAT	.true.		
nreceiversets	5	Number of receiver strings	4 receiver strings at the locations of the real check shot locations, 1 receiver string at the location of the source, for reference
nrec	426	Number of receivers per receiver string	To minimize the difference between the depth of the synthetic geophones and the depth of the real geophones, a distance of 7.4 meters between the receivers is chosen between 5.6 and 3150.6 meters depth. Real geophones 1 to 10 then correspond to synthetic geophones 372:4:408, with less than 1 meter difference
xdeb	1028 1232 947 858 0	Horizontal position of the first receiver per string in meters	Equal to the distance between the average location of the 10 real geophones and the four check shot locations, and 1 reference at a distance of 0 m
xfin	1028 1232 947 858 0	Horizontal position of the last receiver per string in meters	Equal to the position of the first receiver, so that the receiver string is a straight line
zdeb	-5.6	Vertical position of the first receiver per string in meters	
zfin	-3150.6	Vertical position of the last receiver per string in meters	

record_at_surface_same_vertical	.false.		
PERIODIC_HORIZ_DIST	16000.d0		
nbmodels	822	Number of blocks of models	The velocity model is built such that dz = 5 m for 0 < z < 2775 m, dz = 2.5 m for 2775 < z < 3040 m and dz = 20 m for z > 3040 m, resulting in 822 blocks of dz
Qmu	9999	Quality factor	Damping is ignored
Qkappa	9999	Quality factor	Damping is ignored
xmin	-1000.d0	The distance from the left side of the model to the vertical axis, measured parallel to the horizontal axis	
xmax	2000.d0	The distance from the right side of the model to the vertical axis, measured parallel to the horizontal axis	
nx	600	Number of elements in the x-direction	Dx = 5 m
nbregions	822	Number of different materials used in the model	Equal to the number of blocks of models, because each layer is different
NSTEP_BETWEEN_OUTPUT_IMAGES	2000	Number of time steps between images of wave propagation are created	

Appendix 6: Synthetic seismograms

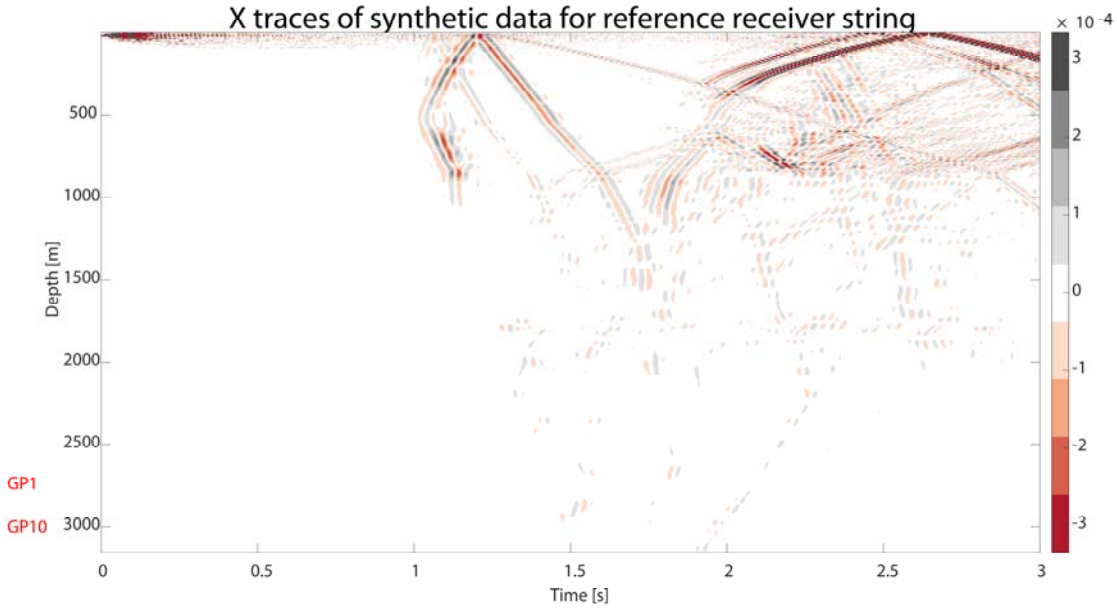
X traces of synthetic data for reference receiver string
Depth [m]
Time [s]
GP1
GP10
× 10 -4

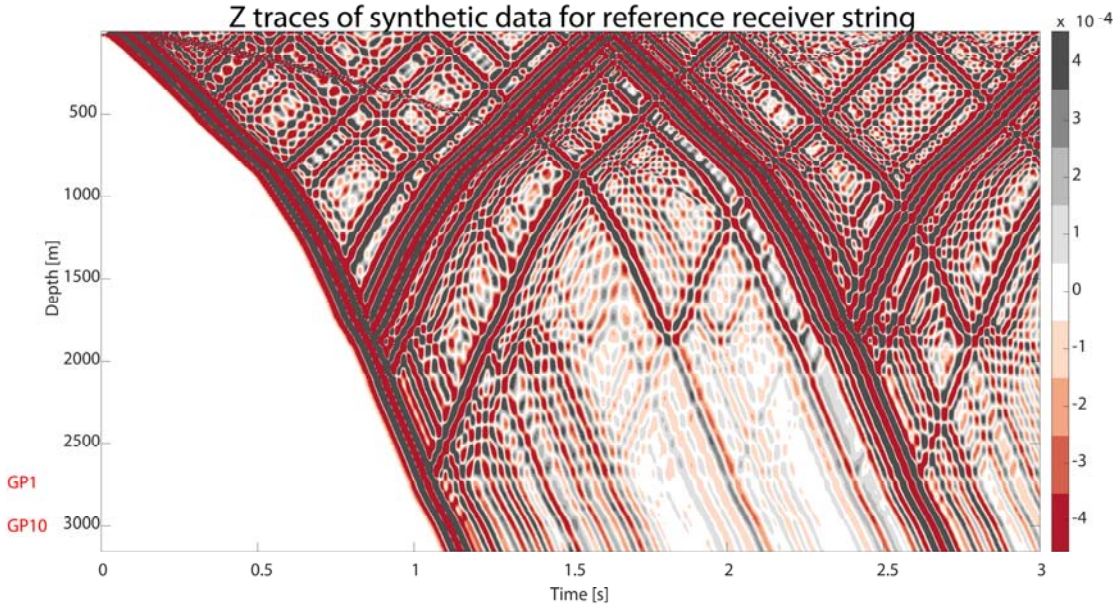
Z traces of synthetic data for reference receiver string
Depth [m]
Time [s]
GP1
GP10
x 10 -4

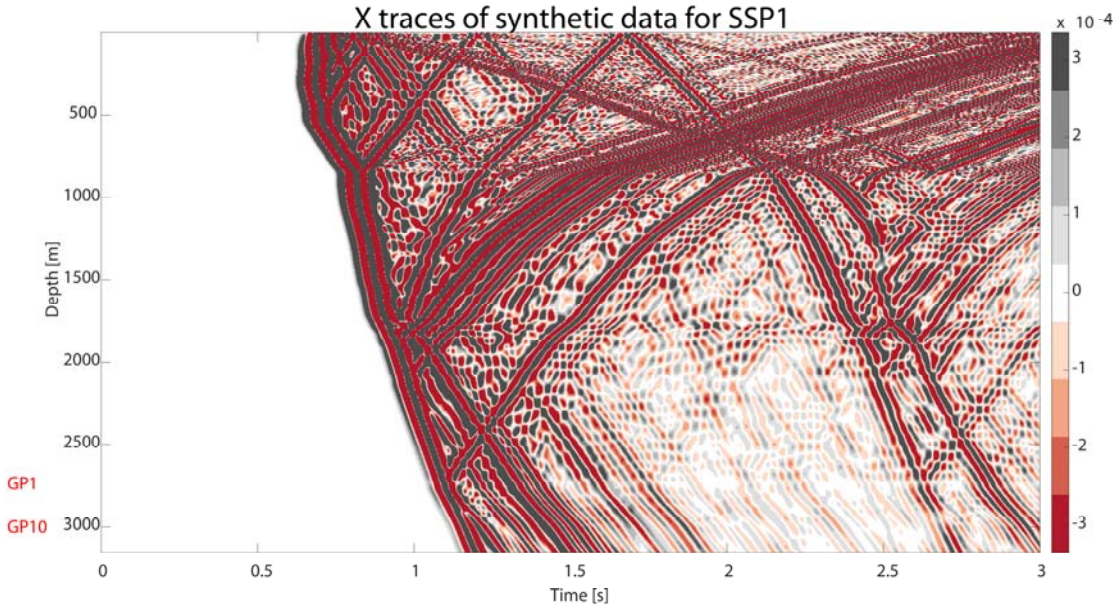
X traces of synthetic data for SSP1
x 10 -4
3
2
1
0
-1
-2
-3
Depth [m]
500
1000
1500
2000
2500
3000
GP1
GP10
0
0.5
1
1.5
2
2.5
3
Time [s]

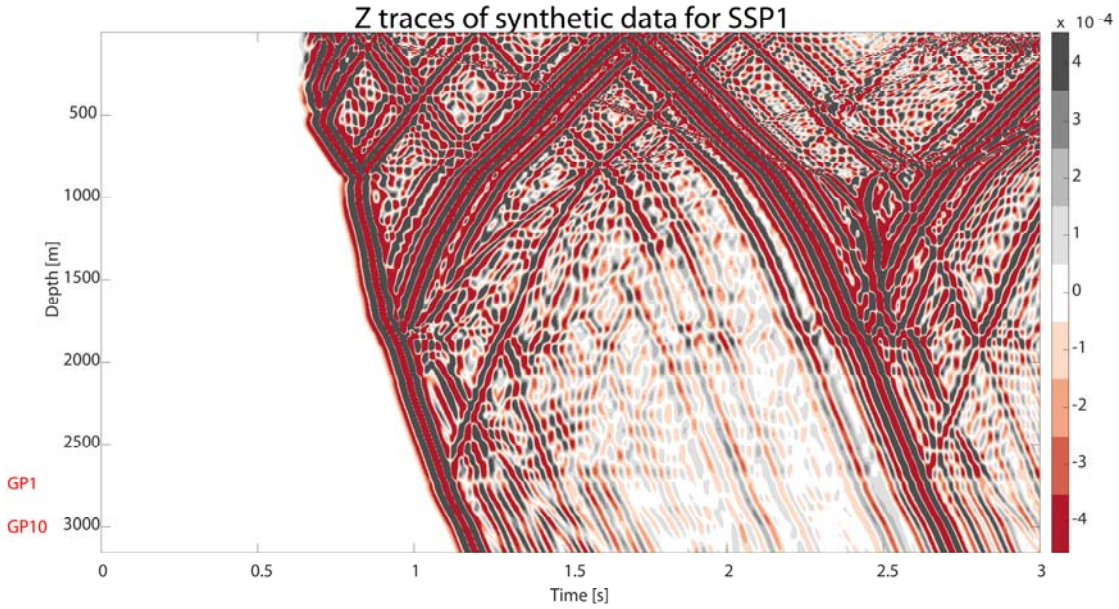
Z traces of synthetic data for SSP1
x 10 -4
4
3
2
1
0
-1
-2
-3
-4
Depth [m]
500
1000
1500
2000
2500
3000
GP1
GP10
0
0.5
1
1.5
2
2.5
3
Time [s]

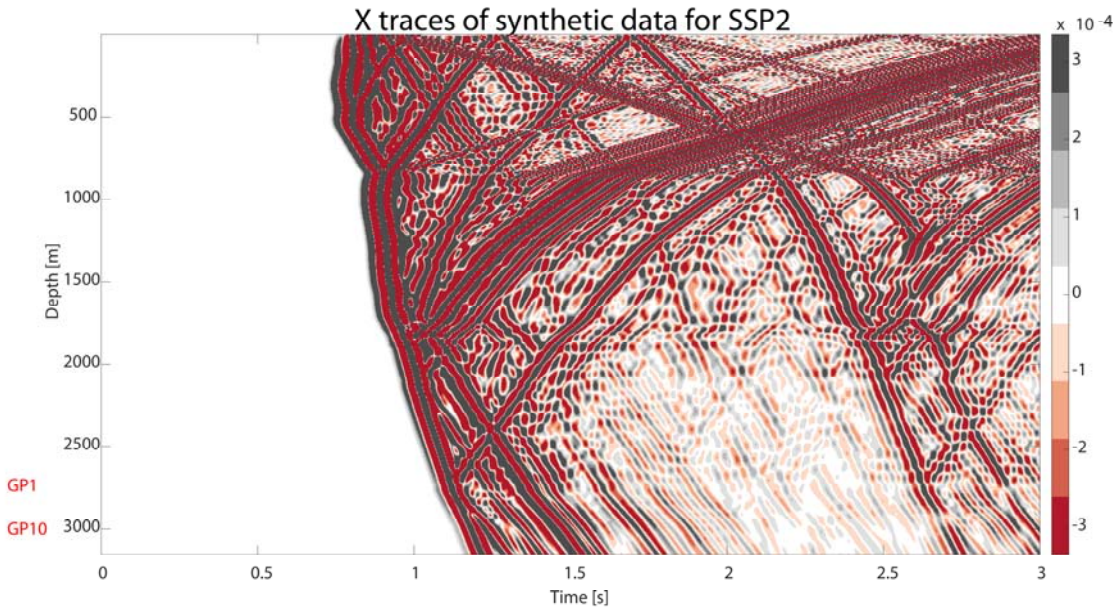
X traces of synthetic data for SSP2
x 10 -4
3
2
1
0
-1
-2
-3
Depth [m]
500
1000
1500
2000
2500
3000
GP1
GP10
0
0.5
1
1.5
2
2.5
3
Time [s]

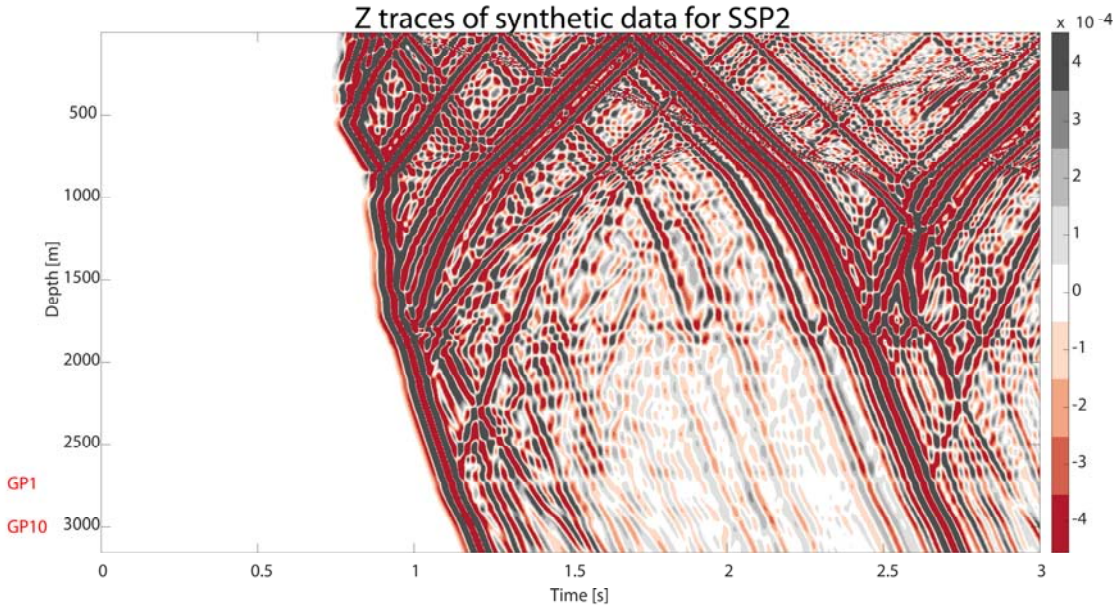
Z traces of synthetic data for SSP2
x 10 -4
4
3
2
1
0
-1
-2
-3
-4
Depth [m]
500
1000
1500
2000
2500
3000
GP1
GP10
0
0.5
1
1.5
2
2.5
3
Time [s]

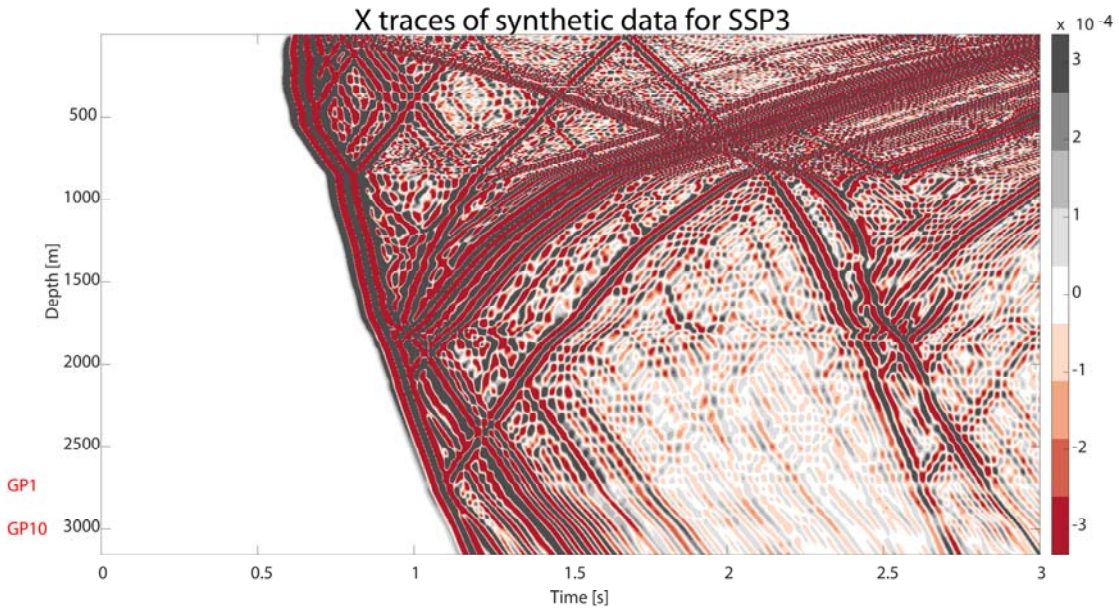
X traces of synthetic data for SSP3
x 10 -4
3
2
1
0
-1
-2
-3
Depth [m]
500
1000
1500
2000
2500
3000
GP1
GP10
0
0.5
1
1.5
2
2.5
3
Time [s]

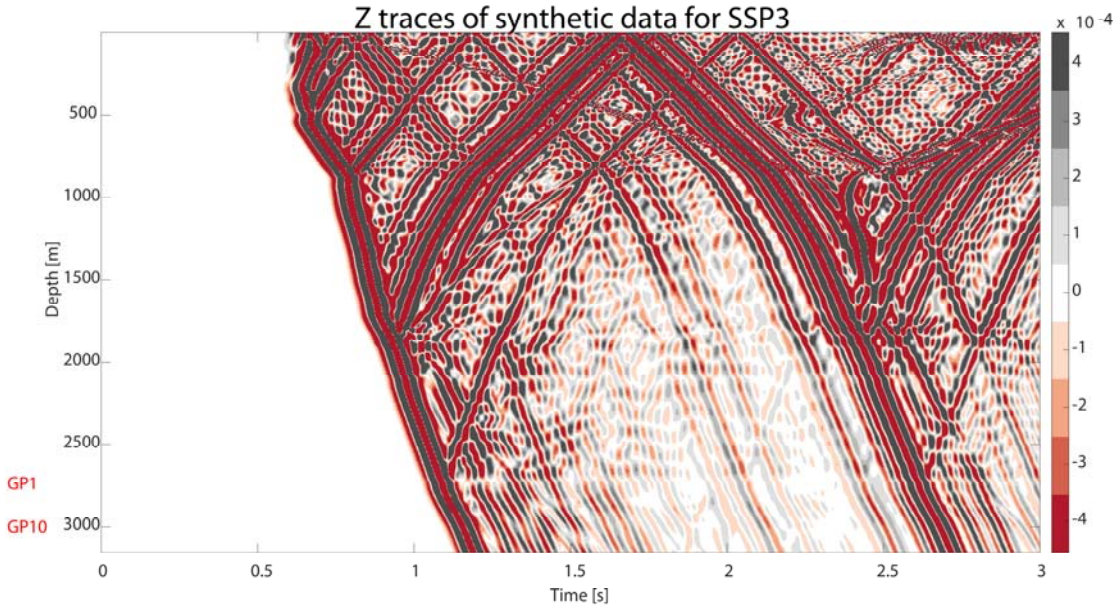
Z traces of synthetic data for SSP3
x 10 -4
4
3
2
1
0
-1
-2
-3
-4
Depth [m]
500
1000
1500
2000
2500
3000
GP1
GP10
0
0.5
1
1.5
2
2.5
3
Time [s]

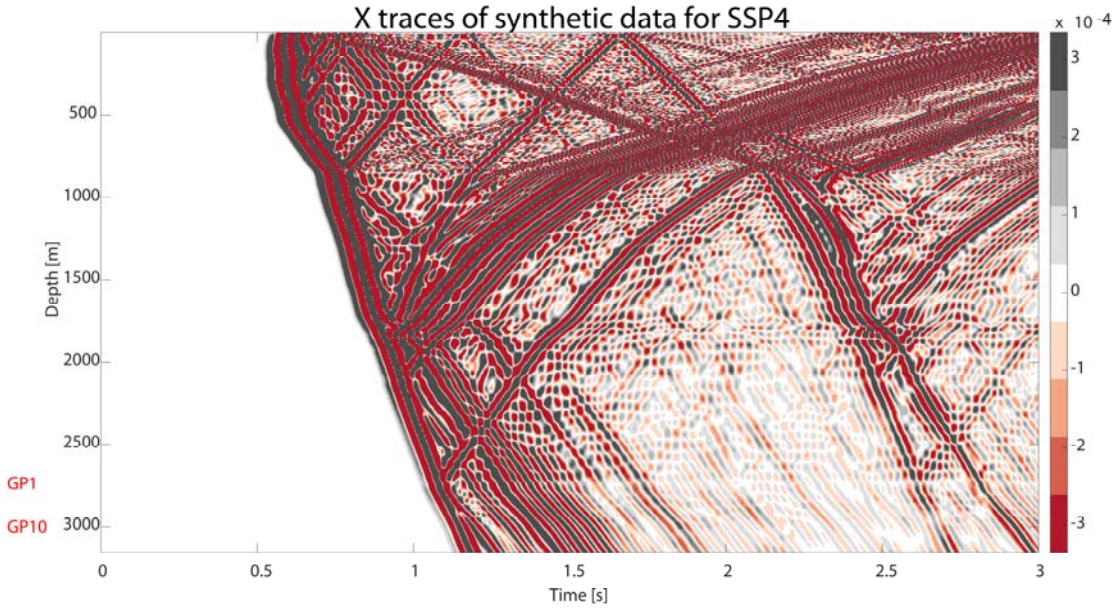
X traces of synthetic data for SSP4
x 10 -4
3
2
1
0
-1
-2
-3
Depth [m]
500
1000
1500
2000
2500
3000
GP1
GP10
0
0.5
1
1.5
2
2.5
3
Time [s]

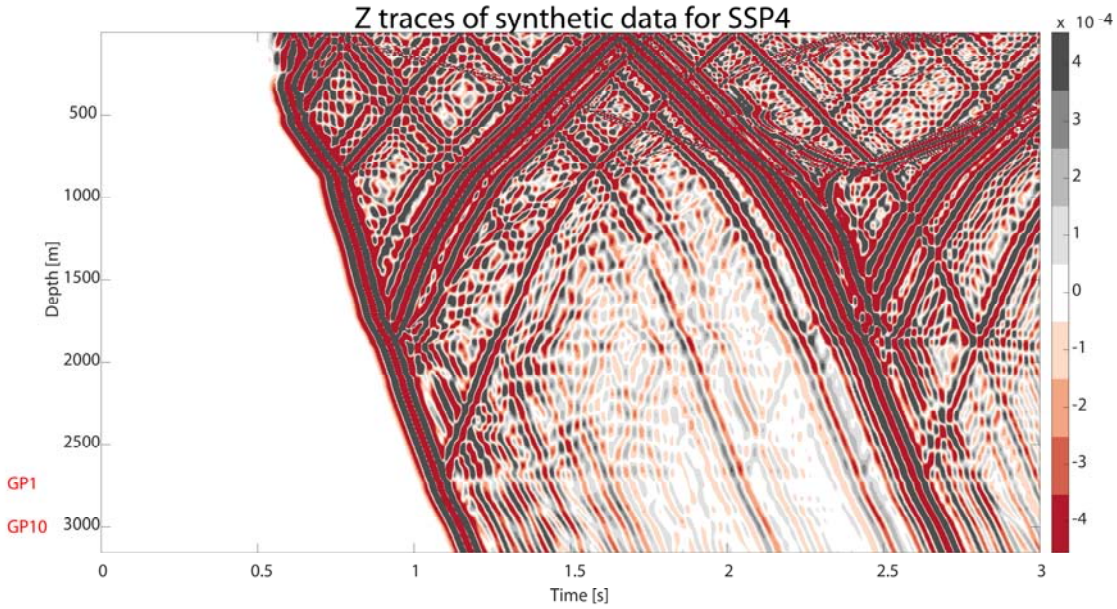
Z traces of synthetic data for SSP4
x 10 -4
4
3
2
1
0
-1
-2
-3
-4
Depth [m]
500
1000
1500
2000
2500
3000
GP1
GP10
0
0.5
1
1.5
2
2.5
3
Time [s]

Appendix 7: RZ-decon of synthetic data, all geophones

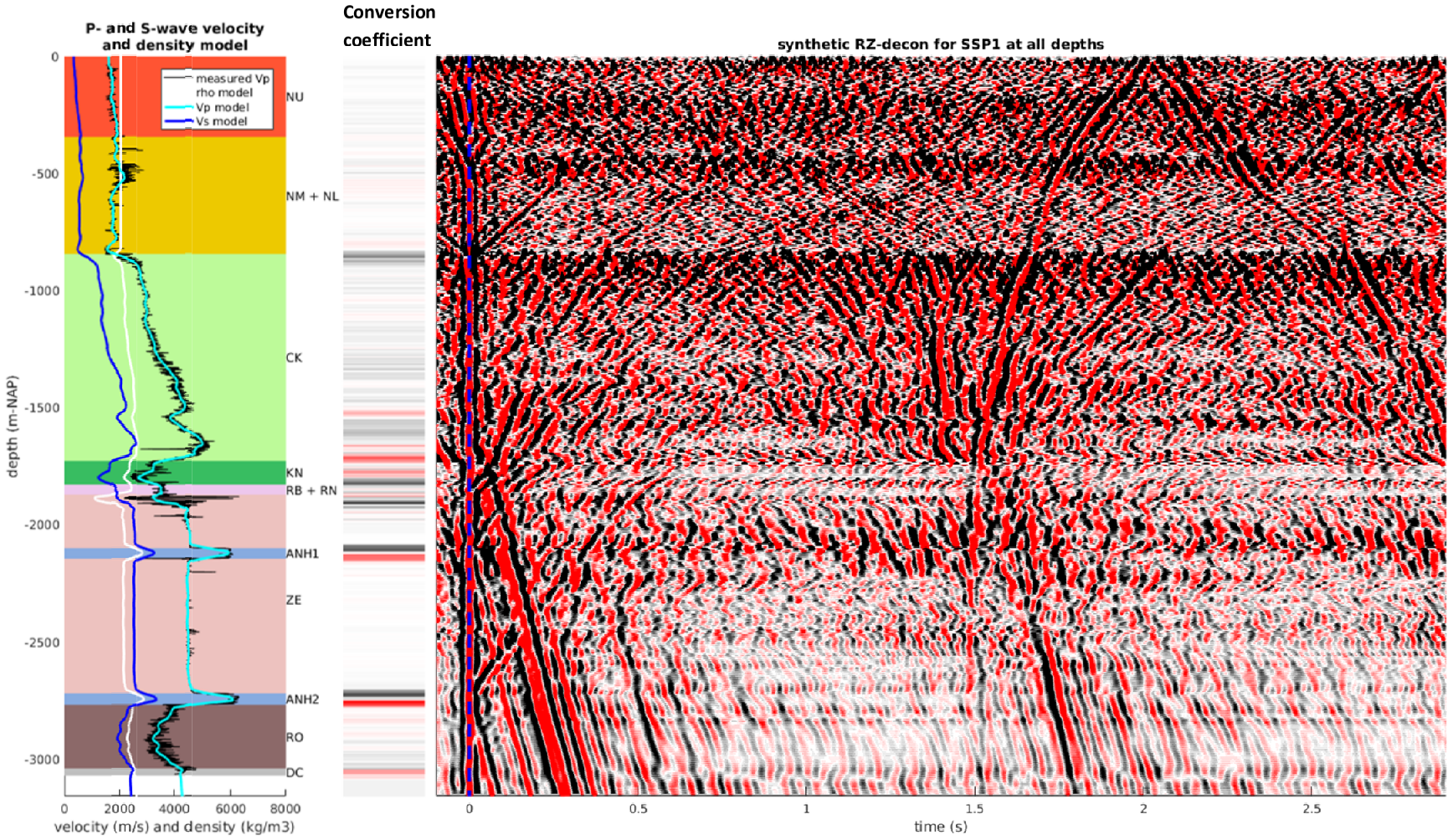
P- and S-wave velocity and density model
measured Vp
rho model
Vp model
Vs model
NU
NM + NL
CK
KN
RB + RN
ANH1
ZE
ANH2
RO
DC
depth (m-NAP)
0
-500
-1000
-1500
-2000
-2500
-3000
0
2000
4000
6000
8000
velocity (m/s) and density (kg/m3)
Conversion coefficient
synthetic RZ-decon for SSP1 at all depths
0
0.5
1
1.5
2
2.5
time (s)

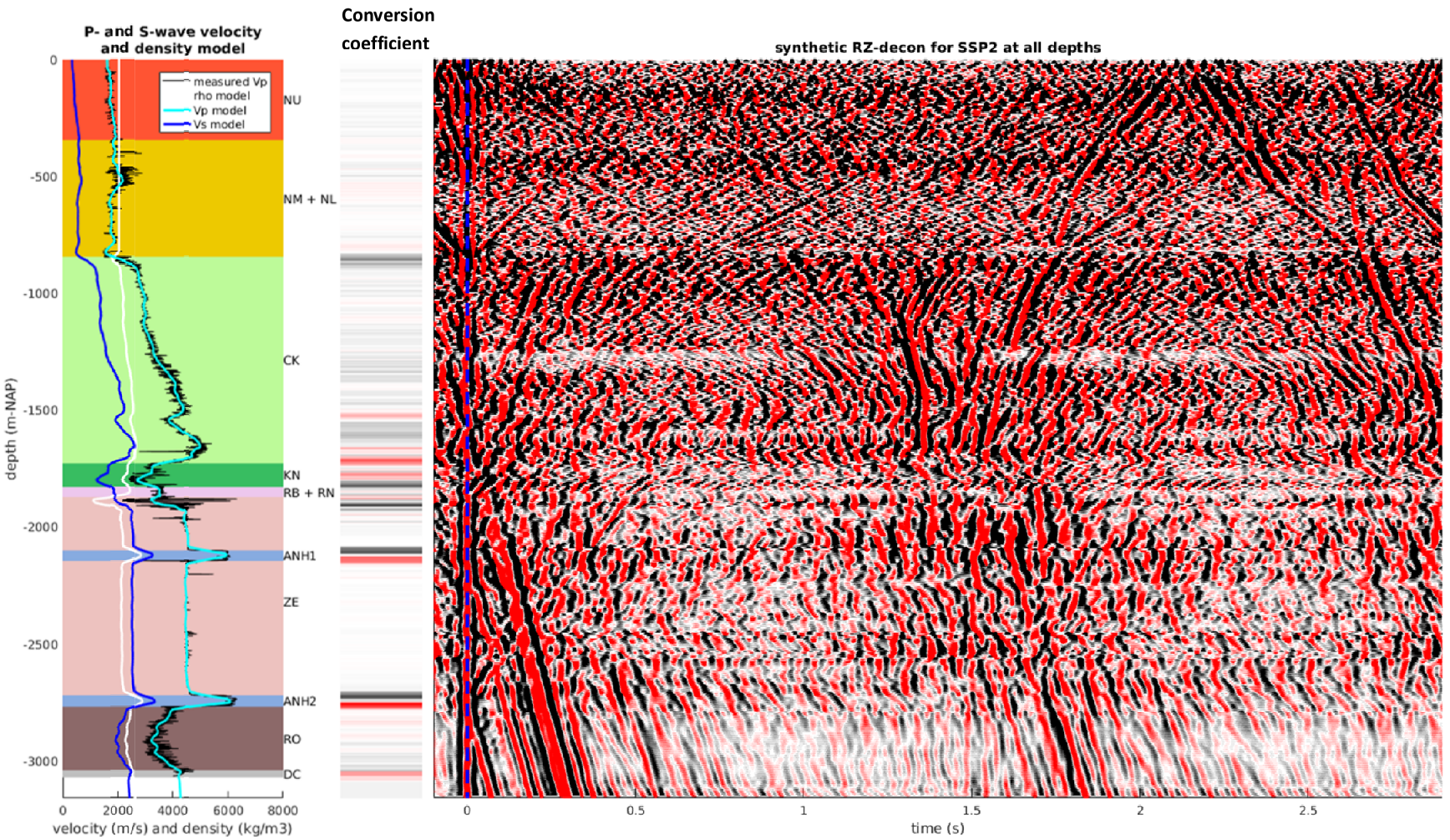
P- and S-wave velocity and density model
measured Vp
rho model
Vp model
Vs model
NU
NM + NL
CK
KN
RB + RN
ANH1
ZE
ANH2
RO
DC
depth (m-NAP)
velocity (m/s) and density (kg/m3)
Conversion coefficient
synthetic RZ-decon for SSP2 at all depths
time (s)

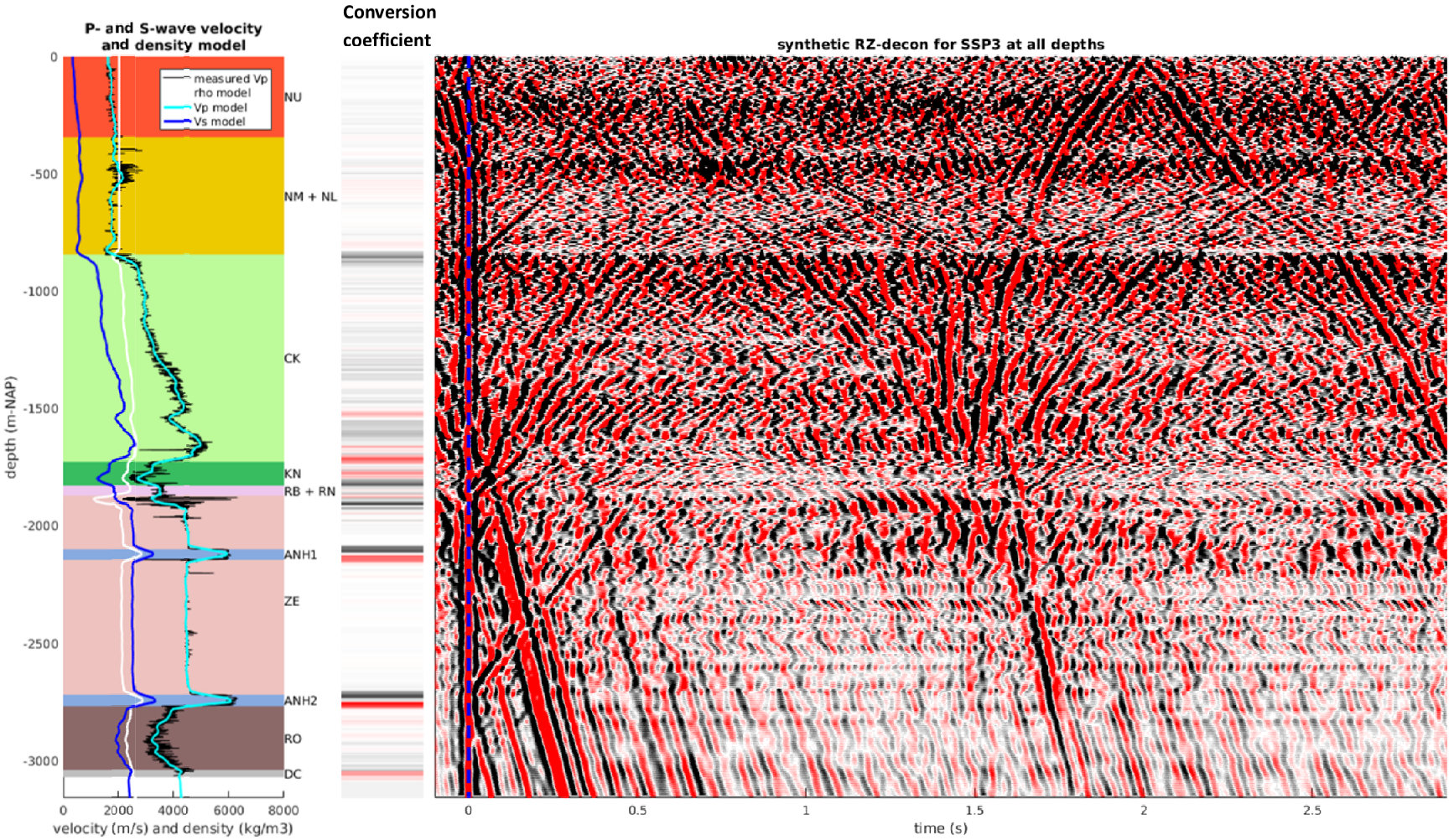
P- and S-wave velocity
and density model
measured Vp
rho model
Vp model
Vs model
NU
NM + NL
CK
KN
RB + RN
ANH1
ZE
ANH2
RO
DC
depth (m-NAP)
0
-500
-1000
-1500
-2000
-2500
-3000
0
2000
4000
6000
8000
velocity (m/s) and density (kg/m3)
Conversion
coefficient
synthetic RZ-decon for SSP3 at all depths
0
0.5
1
1.5
2
2.5
time (s)

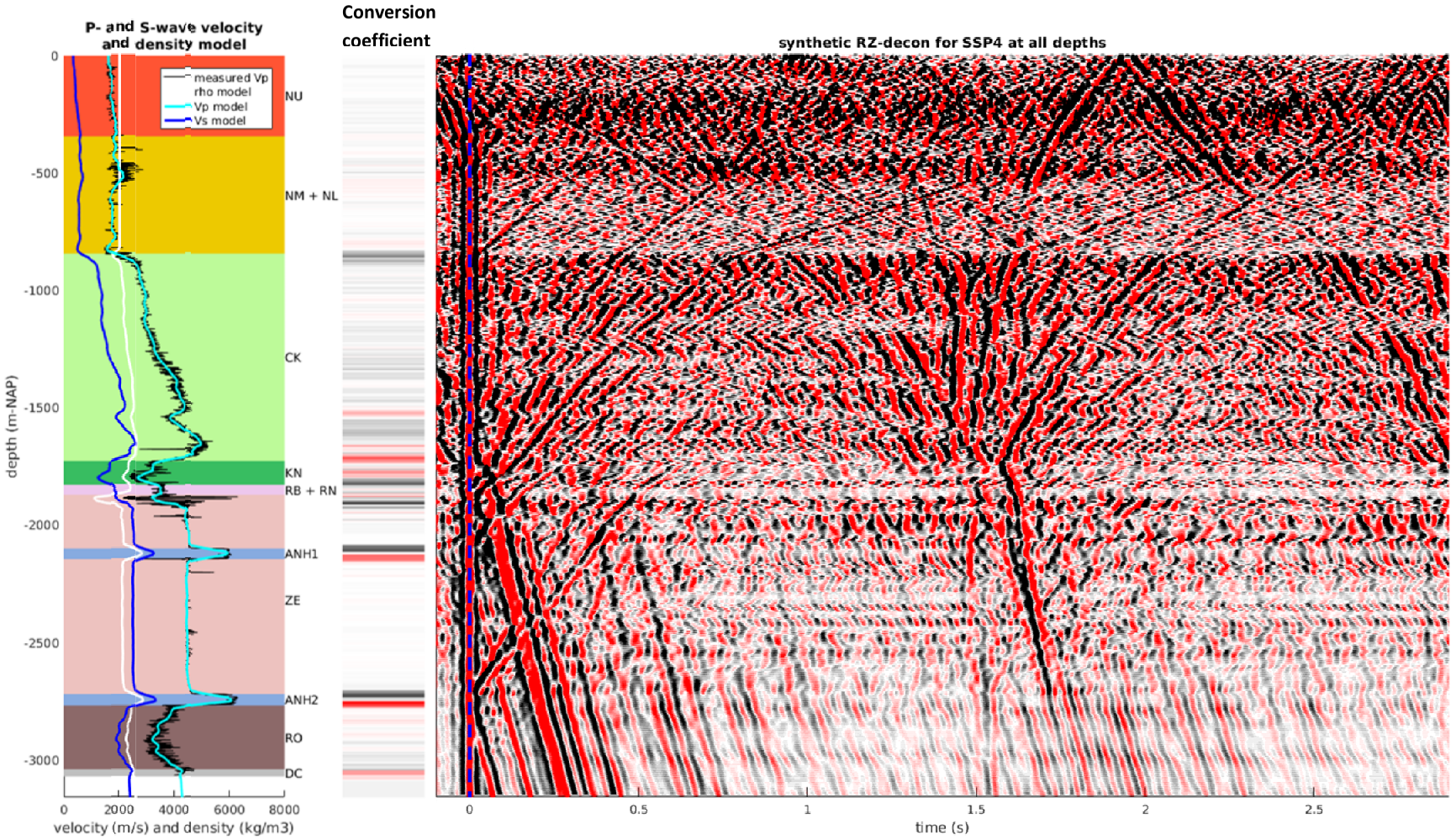
P- and S-wave velocity and density model
measured Vp
rho model
Vp model
Vs model
NU
NM + NL
CK
KN
RB + RN
ANH1
ZE
ANH2
RO
DC
depth (m-NAP)
velocity (m/s) and density (kg/m3)
Conversion coefficient
synthetic RZ-decon for SSP4 at all depths
time (s)

Appendix 8: RZ-decon of synthetic data, 10 geophones in reservoir

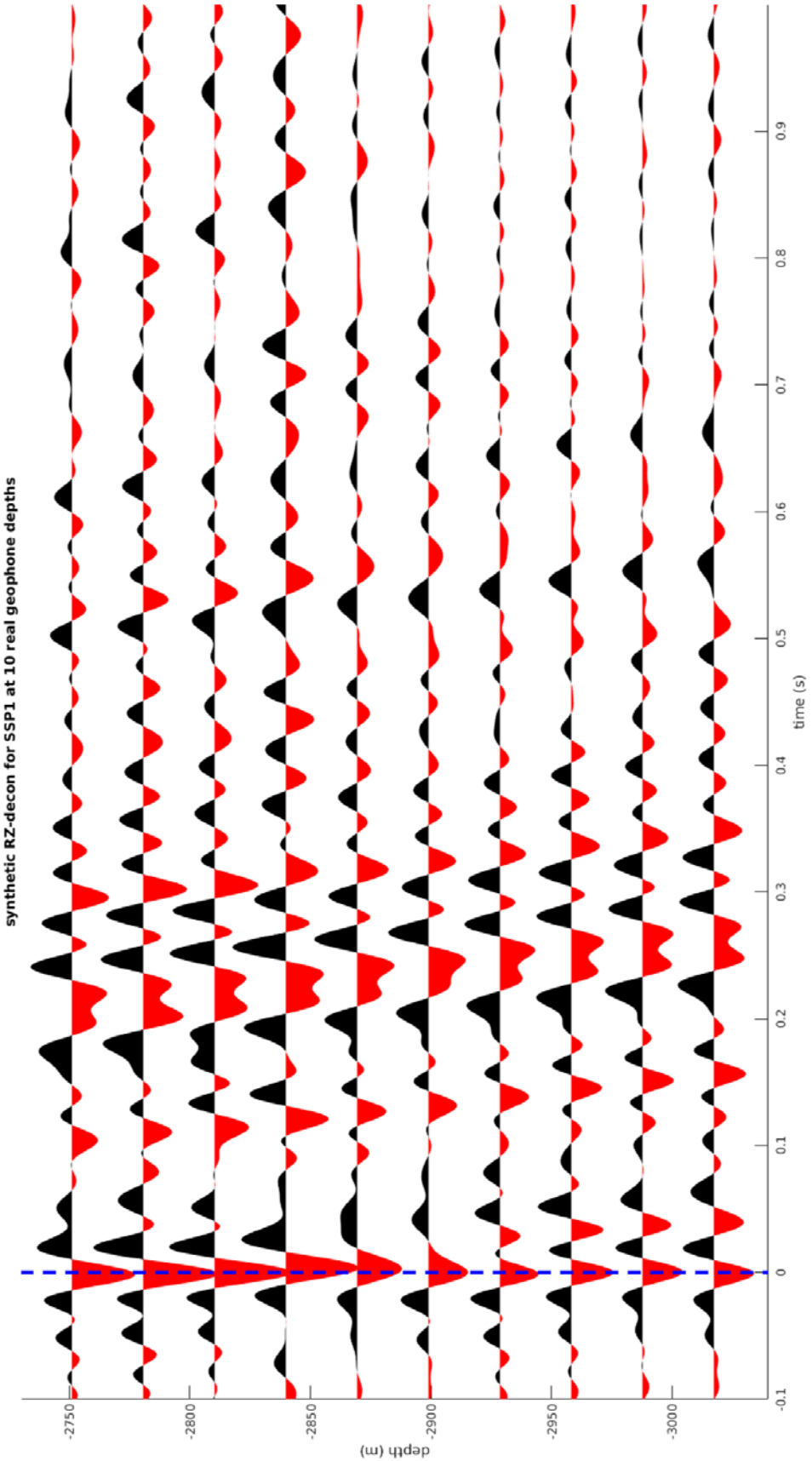
synthetic RZ-decon for SSP1 at 10 real geophone depths
depth (m)
-2750
-2800
-2850
-2900
-2950
-3000
time (s)
-0.1
0
0.1
0.2
0.3
0.4
0.5
0.6
0.7
0.8
0.9

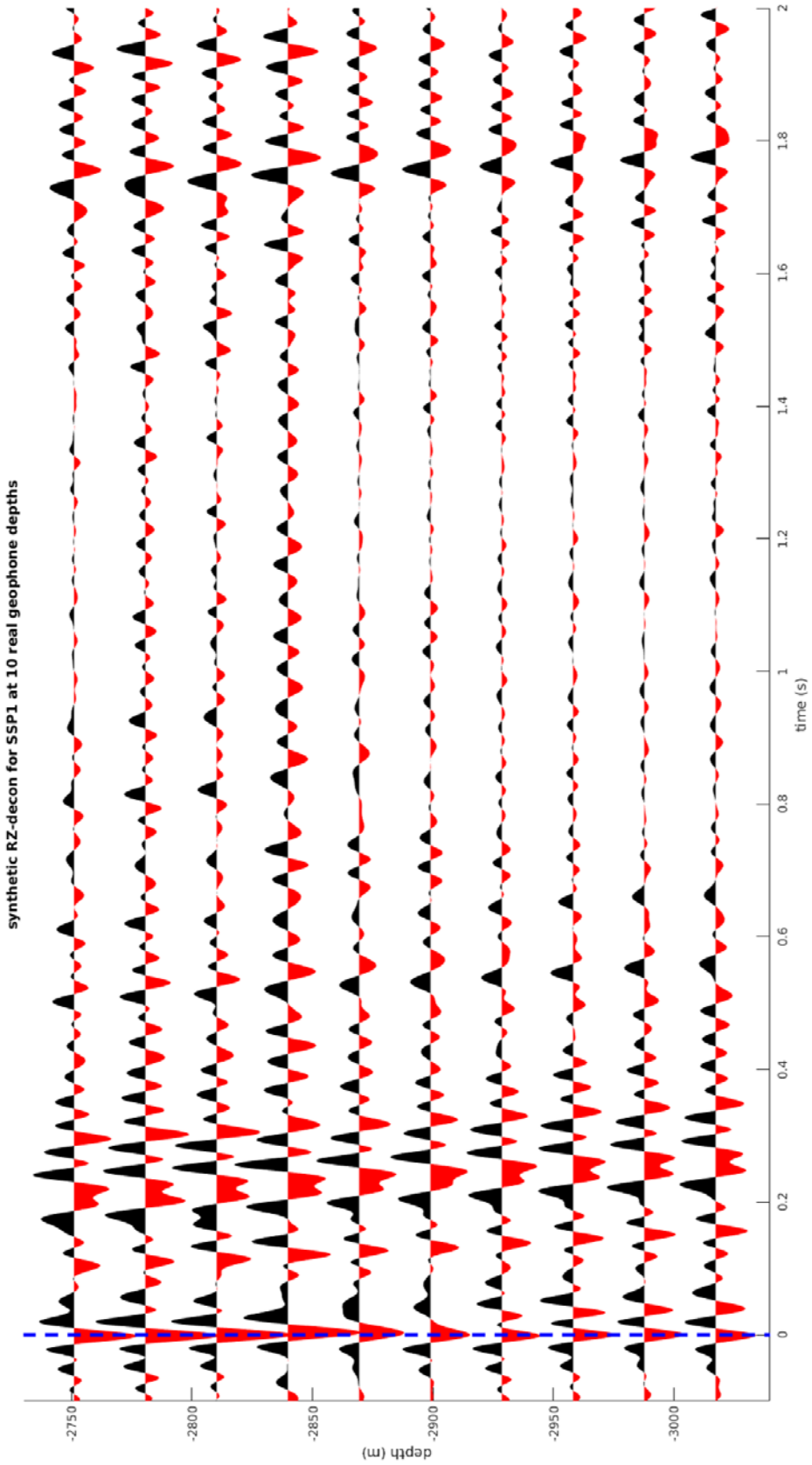
synthetic RZ-decon for SSP1 at 10 real geophone depths
depth (m)
-2750
-2800
-2850
-2900
-2950
-3000
0
0.2
0.4
0.6
0.8
1
1.2
1.4
1.6
1.8
2
time (s)

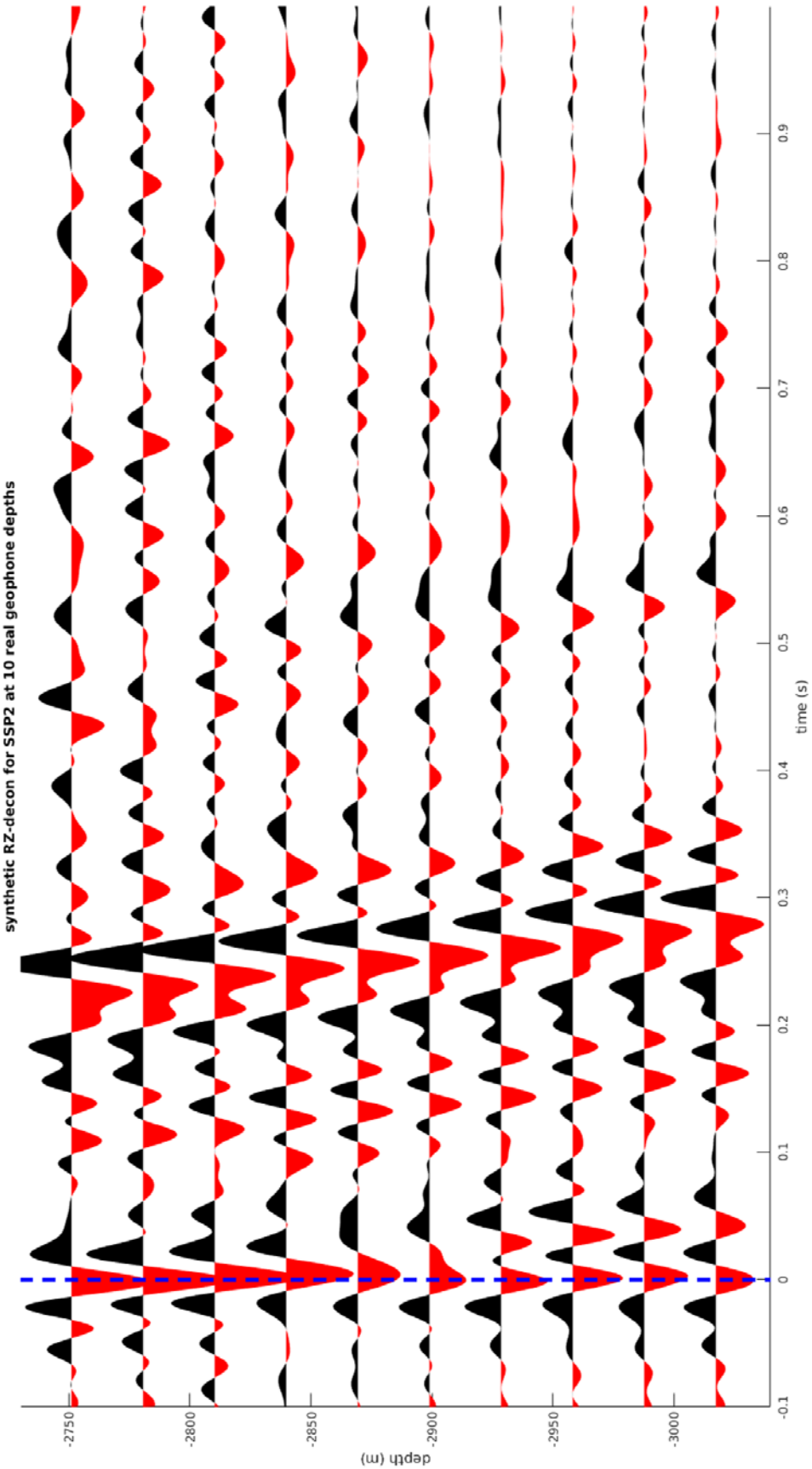
synthetic RZ-decon for SSP2 at 10 real geophone depths
depth (m)
-2750
-2800
-2850
-2900
-2950
-3000
time (s)
-0.1
0
0.1
0.2
0.3
0.4
0.5
0.6
0.7
0.8
0.9

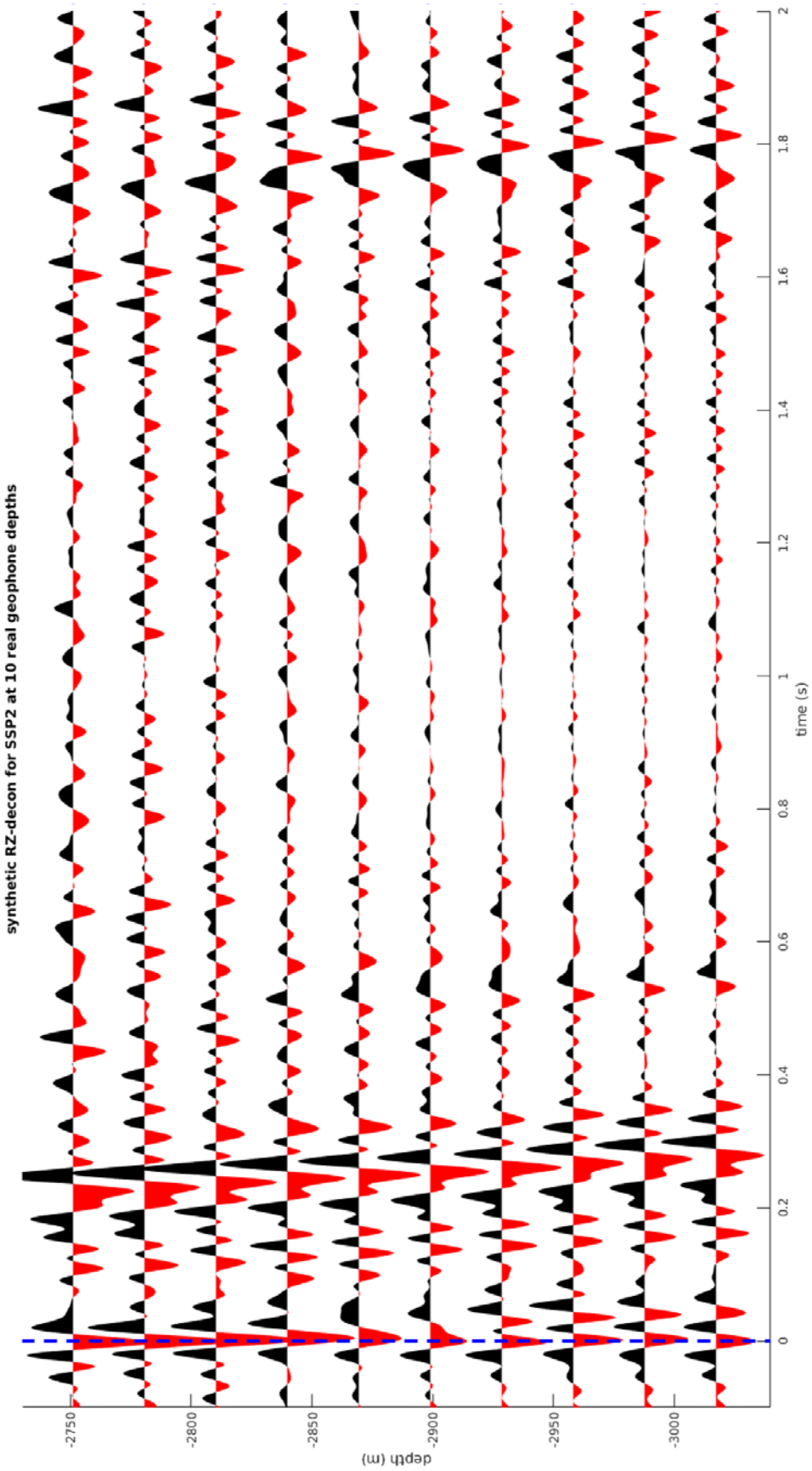
synthetic RZ-decon for SSP2 at 10 real geophone depths
depth (m)
-2750
-2800
-2850
-2900
-2950
-3000
0
0.2
0.4
0.6
0.8
1
1.2
1.4
1.6
1.8
2
time (s)

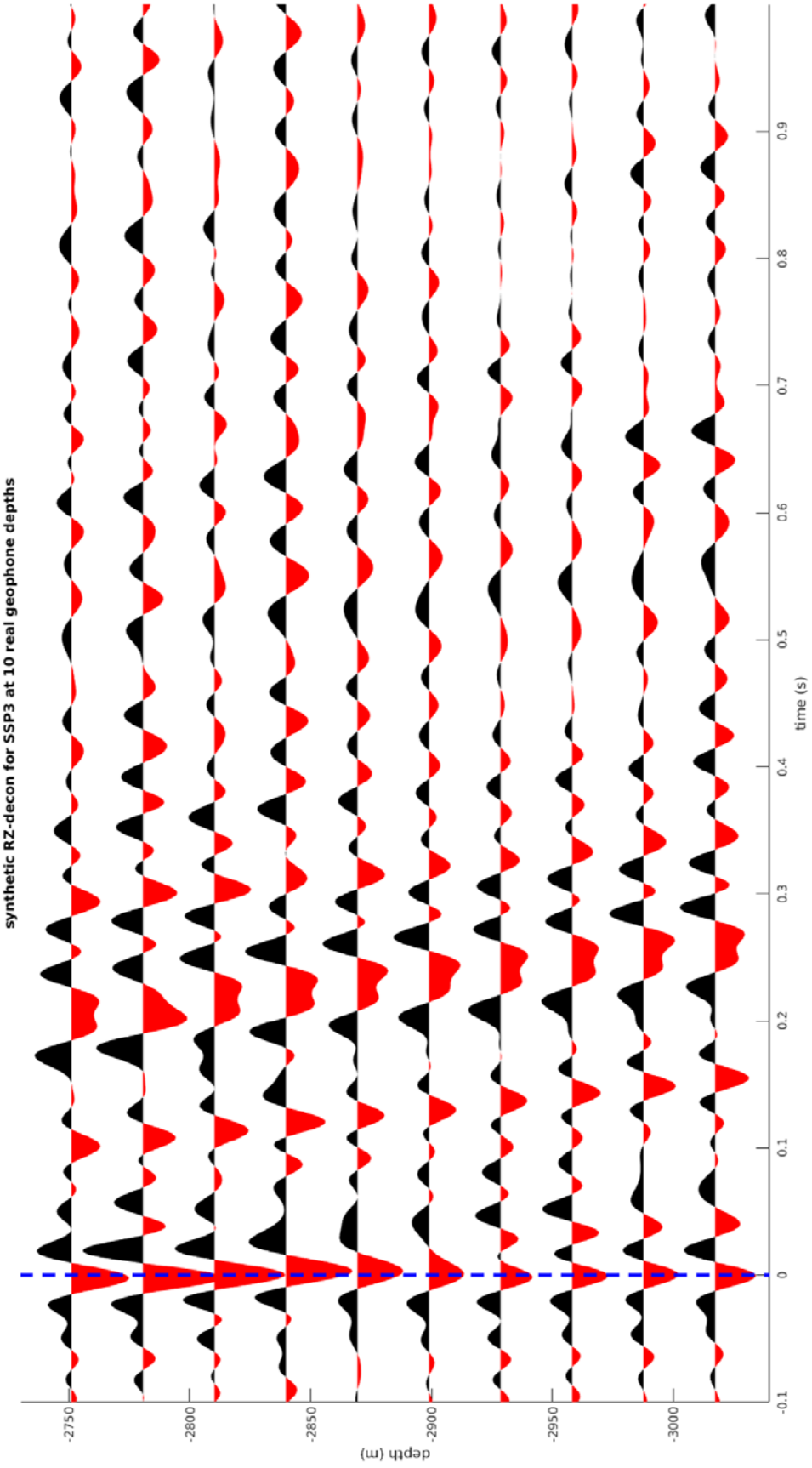
synthetic RZ-decon for SSP3 at 10 real geophone depths
depth (m)
-2750
-2800
-2850
-2900
-2950
-3000
time (s)
-0.1
0
0.1
0.2
0.3
0.4
0.5
0.6
0.7
0.8
0.9

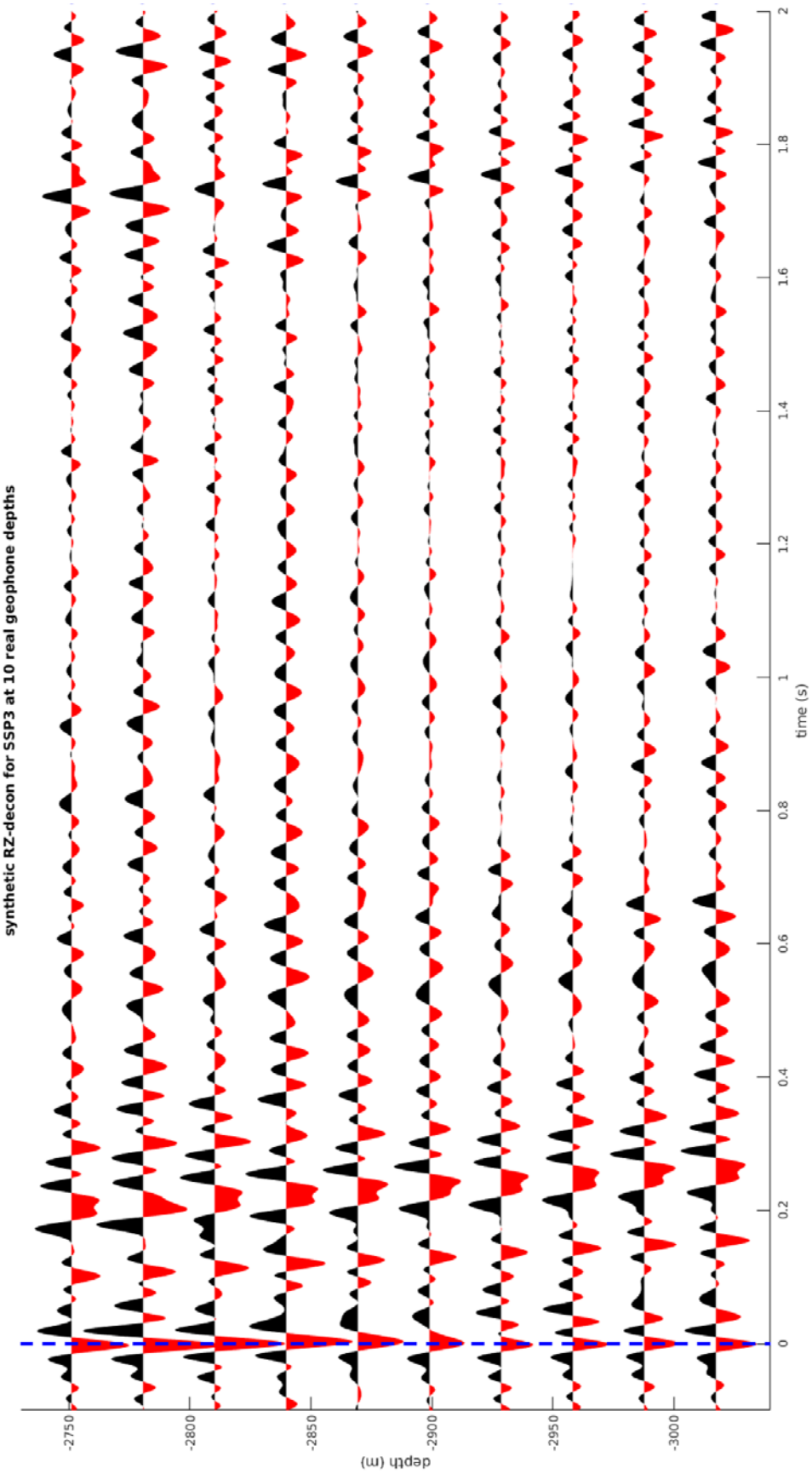
synthetic RZ-decon for SSP3 at 10 real geophone depths
depth (m)
-2750
-2800
-2850
-2900
-2950
-3000
time (s)
0
0.2
0.4
0.6
0.8
1
1.2
1.4
1.6
1.8
2

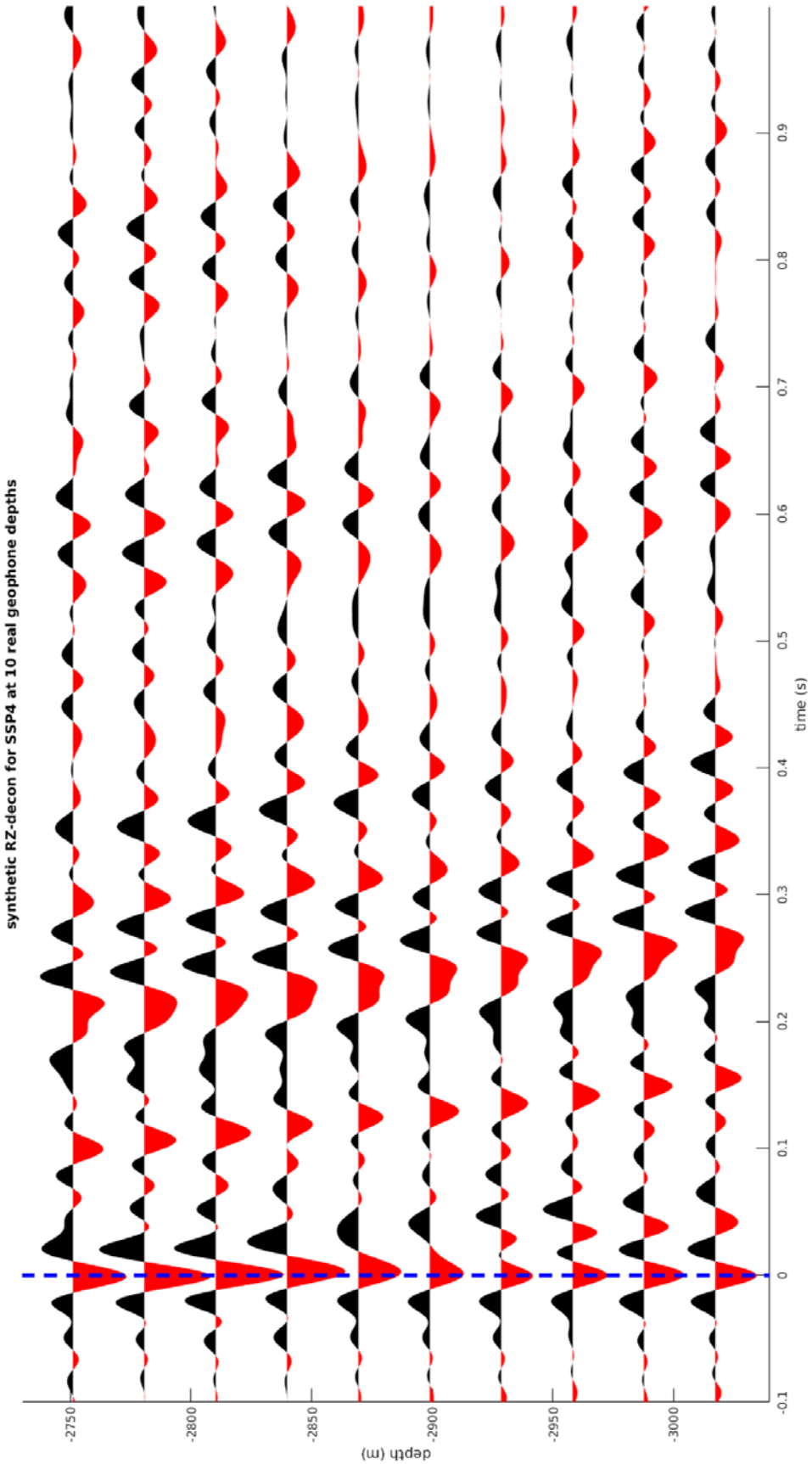
synthetic RZ-decon for SSP4 at 10 real geophone depths
depth (m)
-2750
-2800
-2850
-2900
-2950
-3000
time (s)
-0.1
0
0.1
0.2
0.3
0.4
0.5
0.6
0.7
0.8
0.9

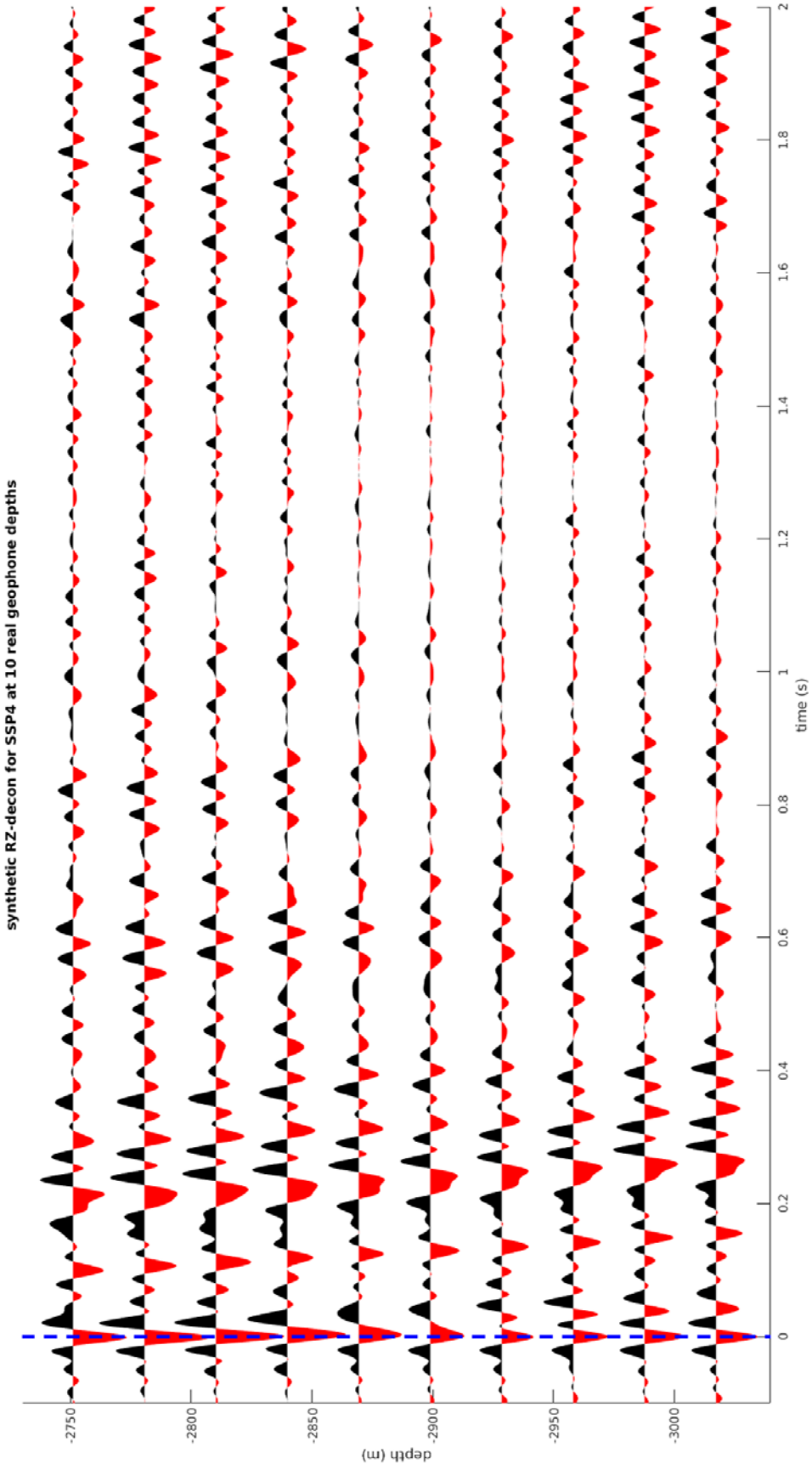
synthetic RZ-decon for SSP4 at 10 real geophone depths
depth (m)
-2750
-2800
-2850
-2900
-2950
-3000
time (s)
0
0.2
0.4
0.6
0.8
1
1.2
1.4
1.6
1.8
2

Appendix 9: RZ-decon of real data

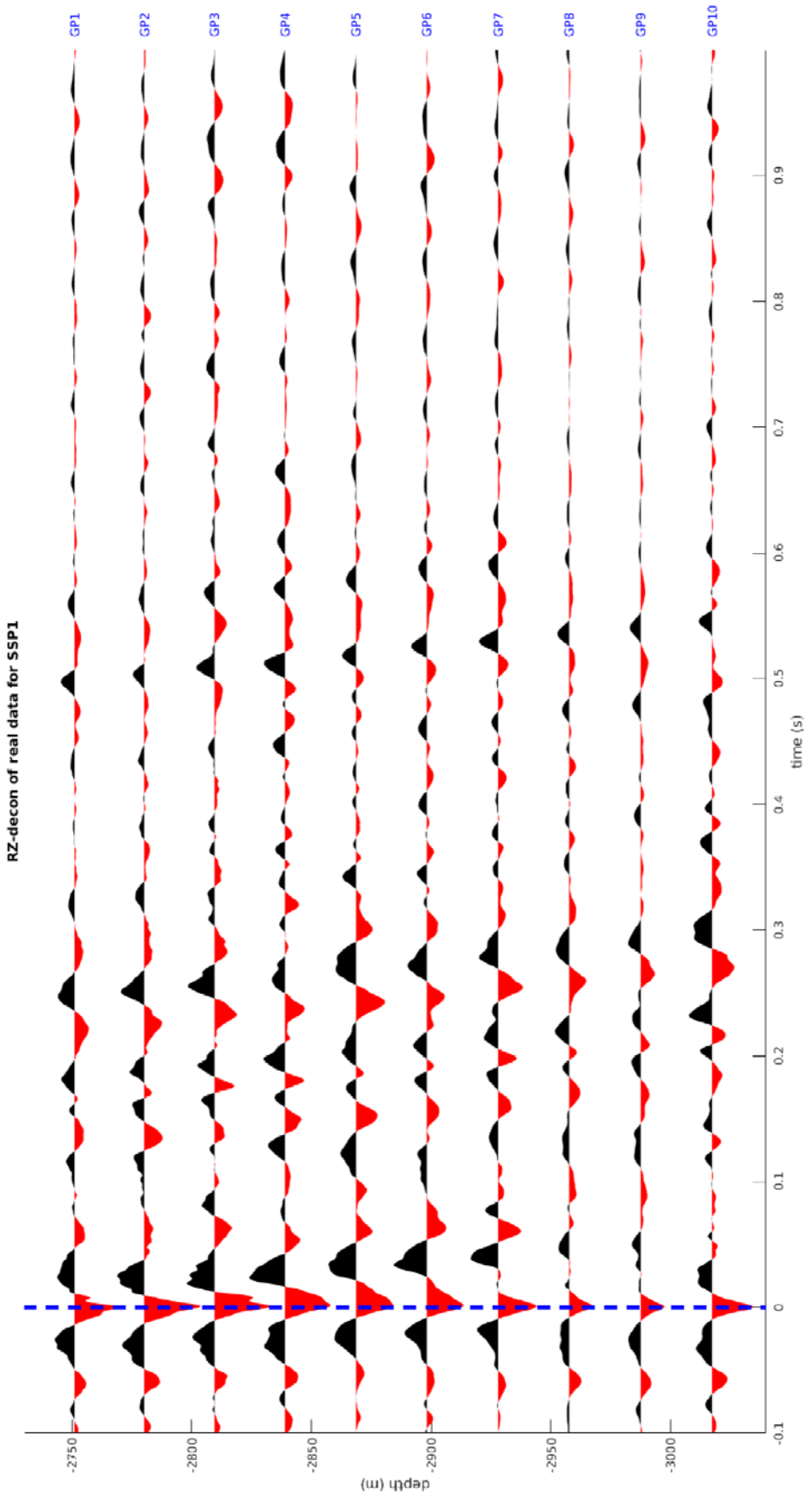
RZ-decon of real data for SSP1
GP1
GP2
GP3
GP4
GP5
GP6
GP7
GP8
GP9
GP10
depth (m)
-2750
-2800
-2850
-2900
-2950
-3000
time (s)
-0.1
0
0.1
0.2
0.3
0.4
0.5
0.6
0.7
0.8
0.9

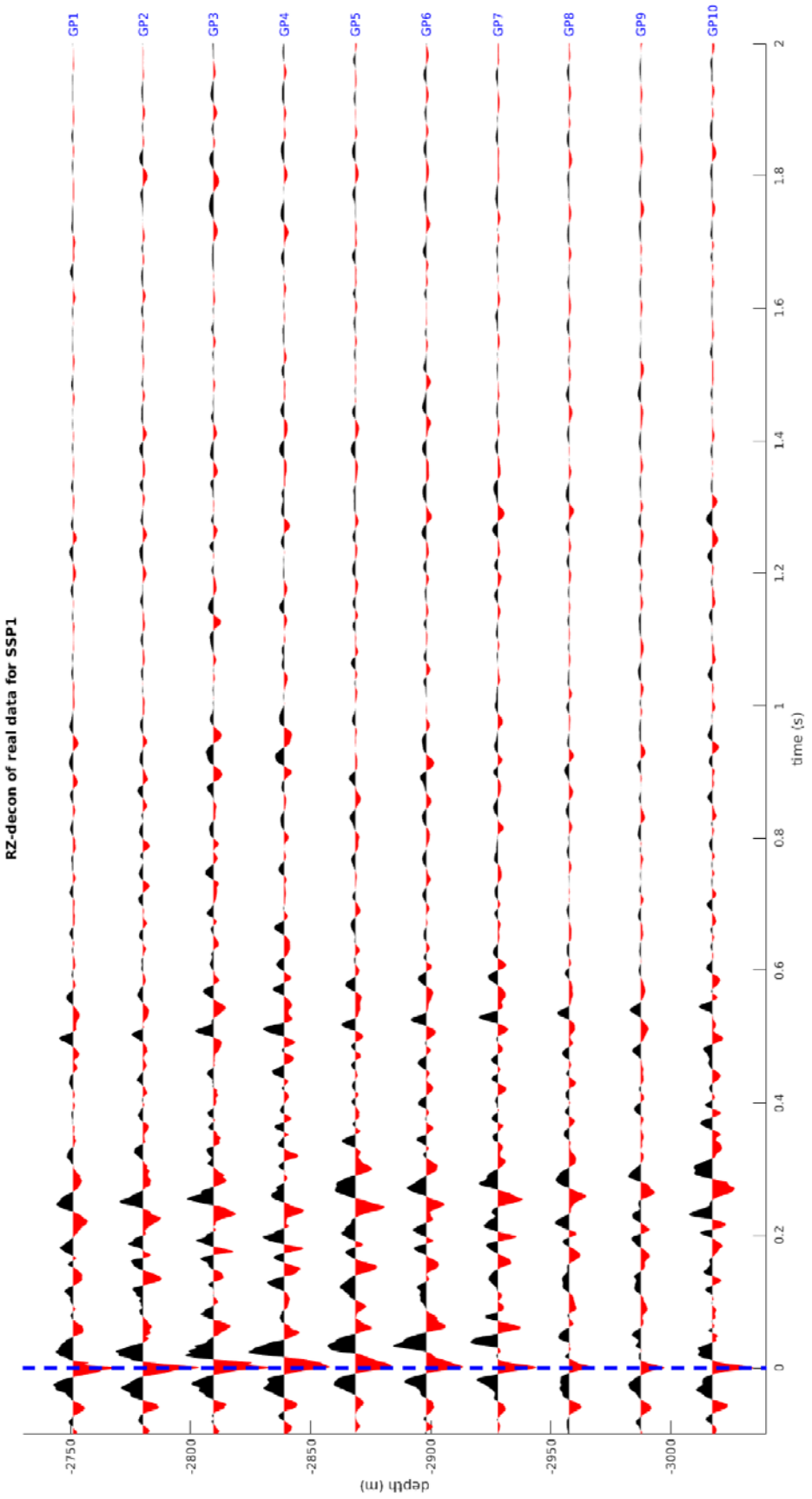
RZ-decon of real data for SSP1
GP1
GP2
GP3
GP4
GP5
GP6
GP7
GP8
GP9
GP10
depth (m)
-2750
-2800
-2850
-2900
-2950
-3000
time (s)
0
0.2
0.4
0.6
0.8
1
1.2
1.4
1.6
1.8
2

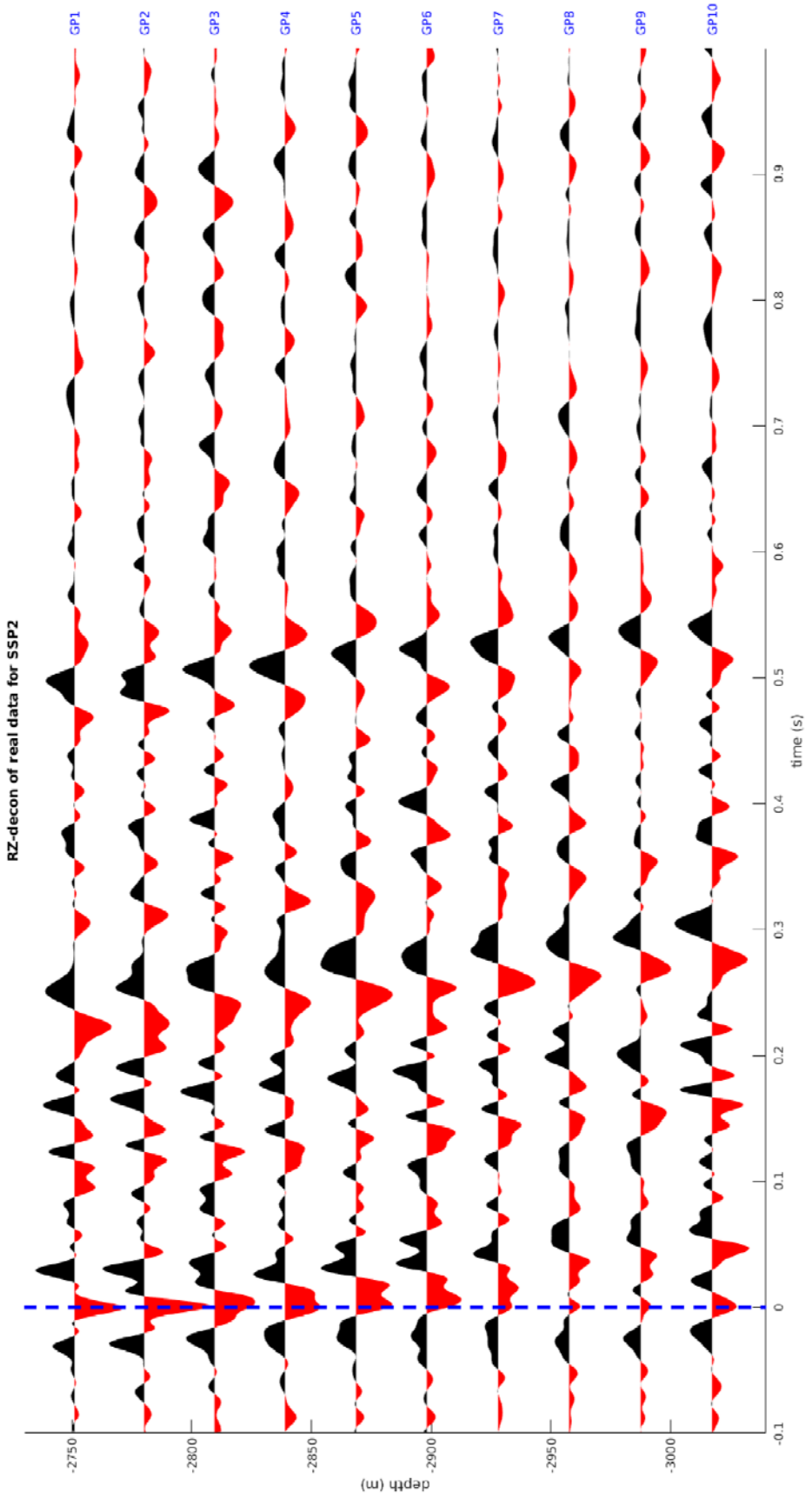
RZ-decon of real data for SSP2
GP1
GP2
GP3
GP4
GP5
GP6
GP7
GP8
GP9
GP10
depth (m)
-2750
-2800
-2850
-2900
-2950
-3000
time (s)
-0.1
0
0.1
0.2
0.3
0.4
0.5
0.6
0.7
0.8
0.9

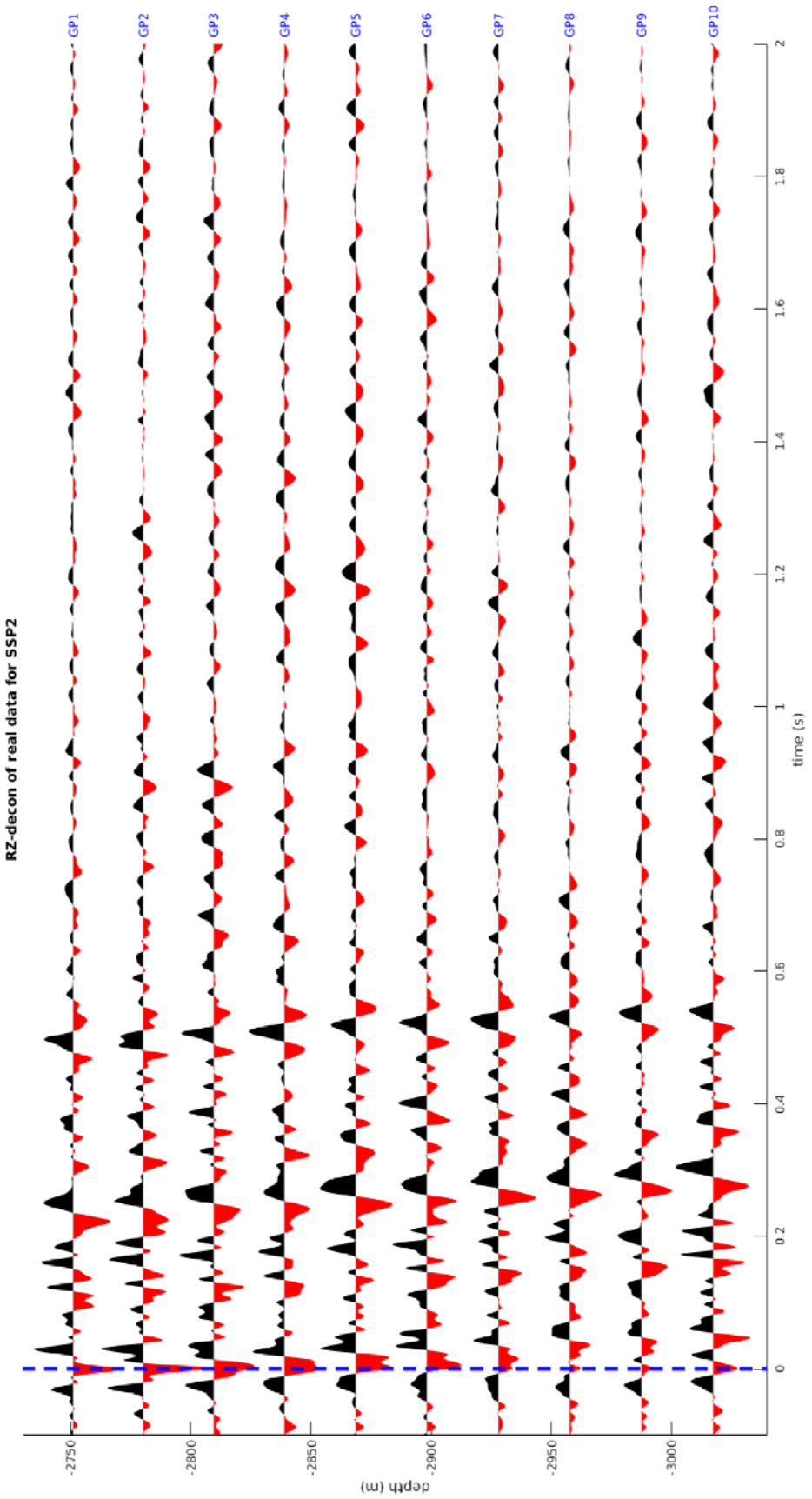
RZ-decon of real data for SSP2
GP1
GP2
GP3
GP4
GP5
GP6
GP7
GP8
GP9
GP10
depth (m)
-2750
-2800
-2850
-2900
-2950
-3000
time (s)
0
0.2
0.4
0.6
0.8
1
1.2
1.4
1.6
1.8
2

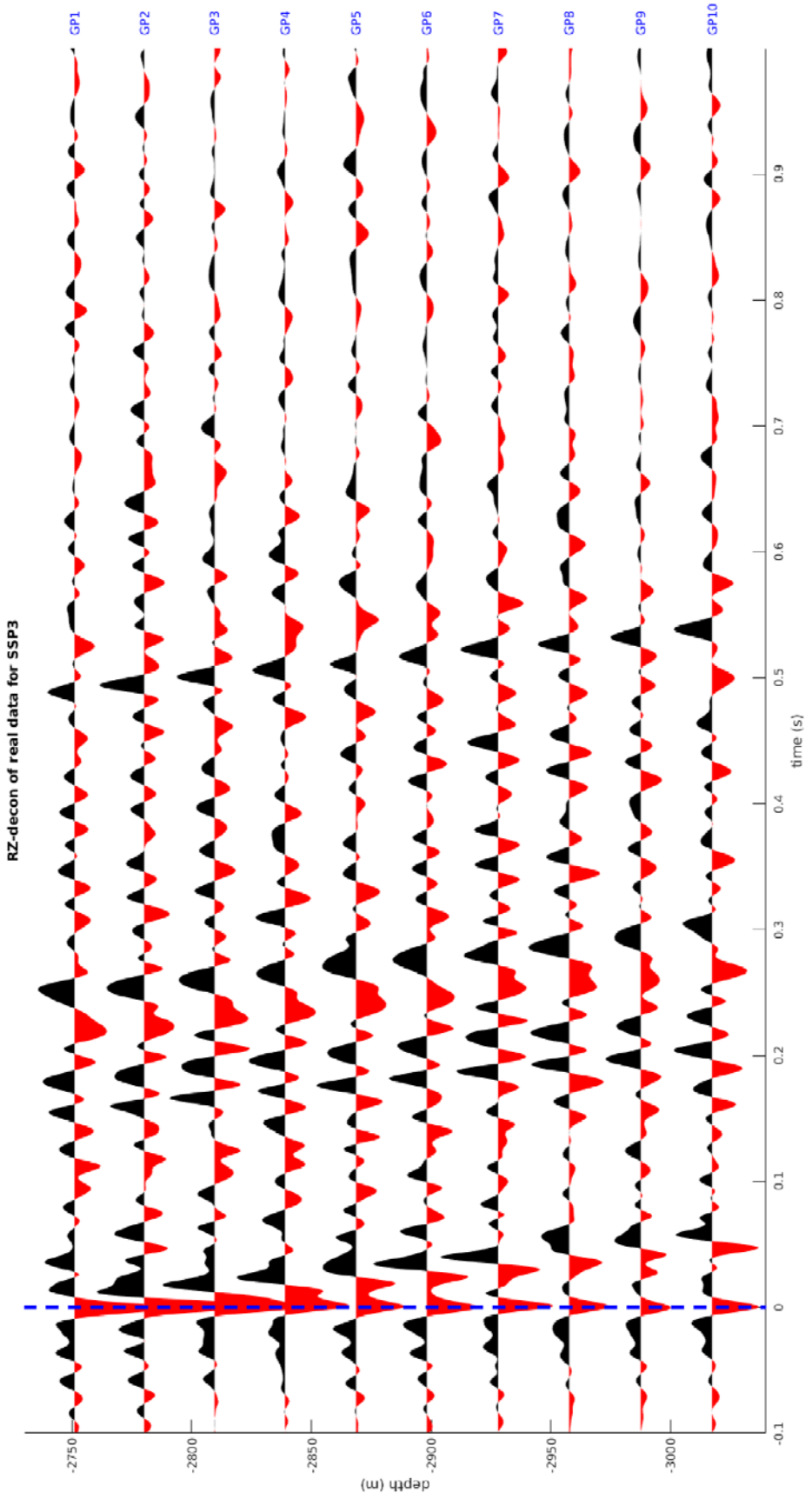
RZ-decon of real data for SSP3
GP1
GP2
GP3
GP4
GP5
GP6
GP7
GP8
GP9
GP10
depth (m)
-2750
-2800
-2850
-2900
-2950
-3000
time (s)
-0.1
0
0.1
0.2
0.3
0.4
0.5
0.6
0.7
0.8
0.9

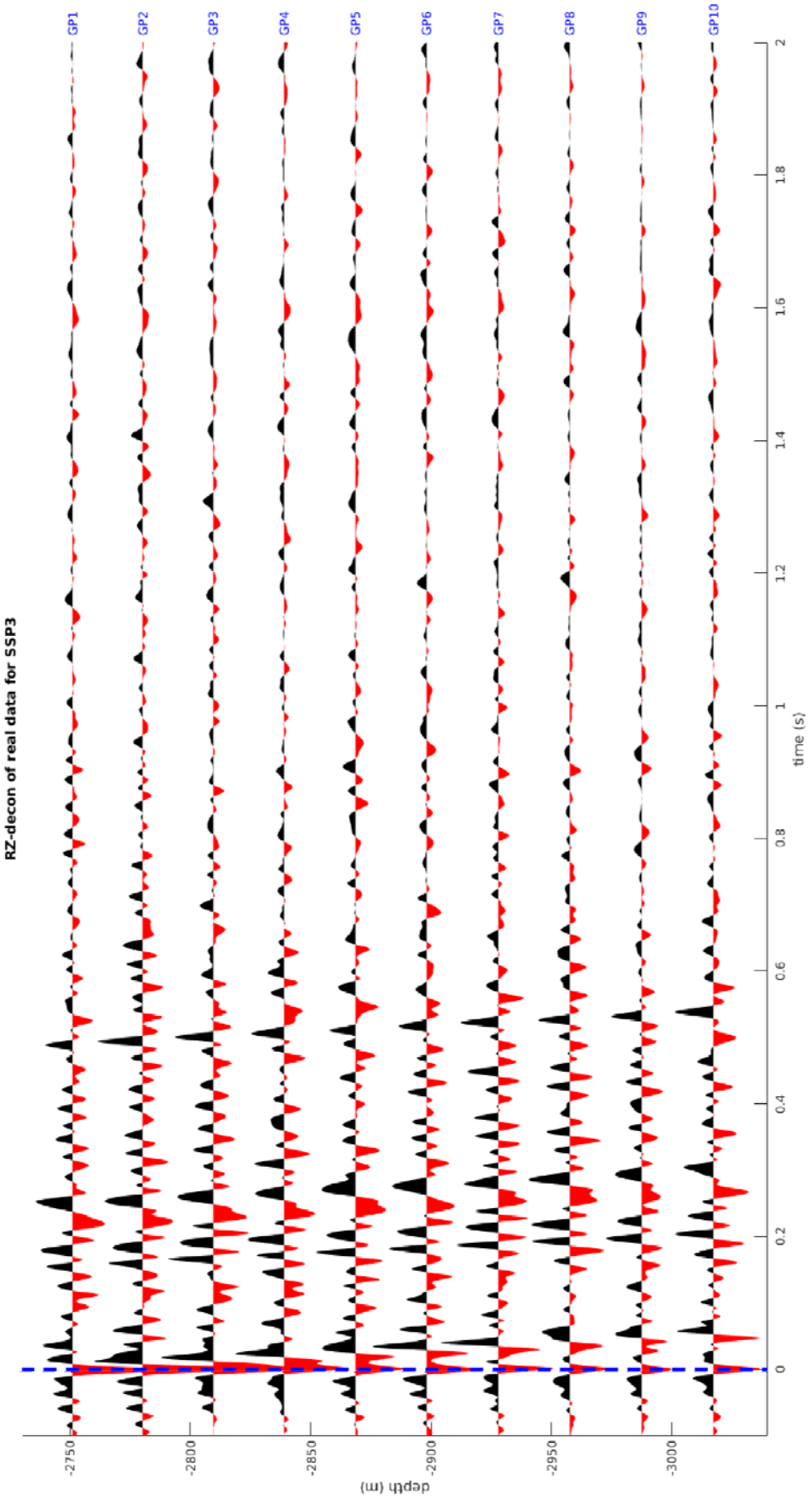
RZ-decon of real data for SSP3
GP1
GP2
GP3
GP4
GP5
GP6
GP7
GP8
GP9
GP10
depth (m)
-2750
-2800
-2850
-2900
-2950
-3000
time (s)
0
0.2
0.4
0.6
0.8
1
1.2
1.4
1.6
1.8
2

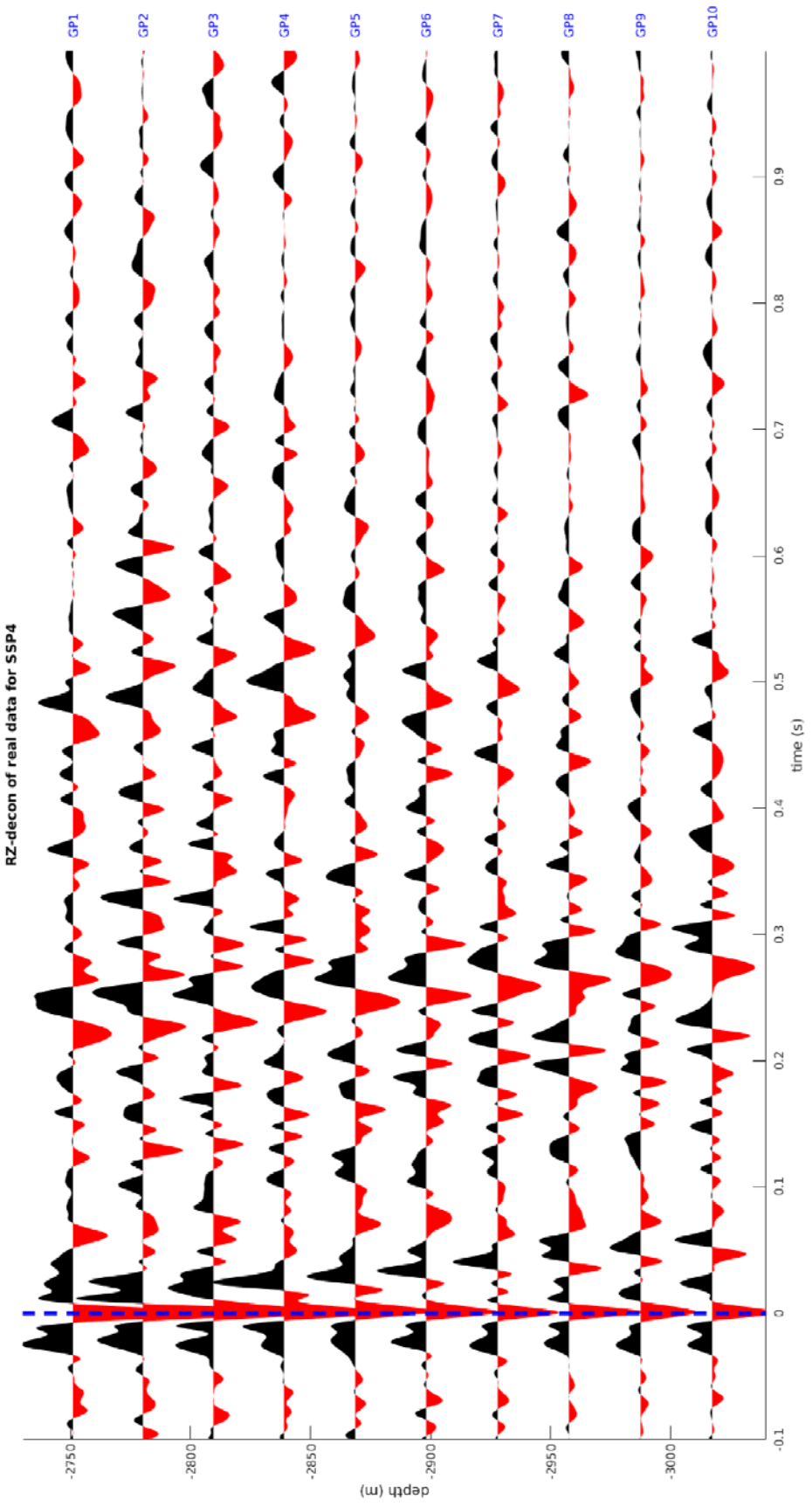
RZ-decon of real data for SSP4
GP1
GP2
GP3
GP4
GP5
GP6
GP7
GP8
GP9
GP10
depth (m)
-2750
-2800
-2850
-2900
-2950
-3000
time (s)
-0.1
0
0.1
0.2
0.3
0.4
0.5
0.6
0.7
0.8
0.9

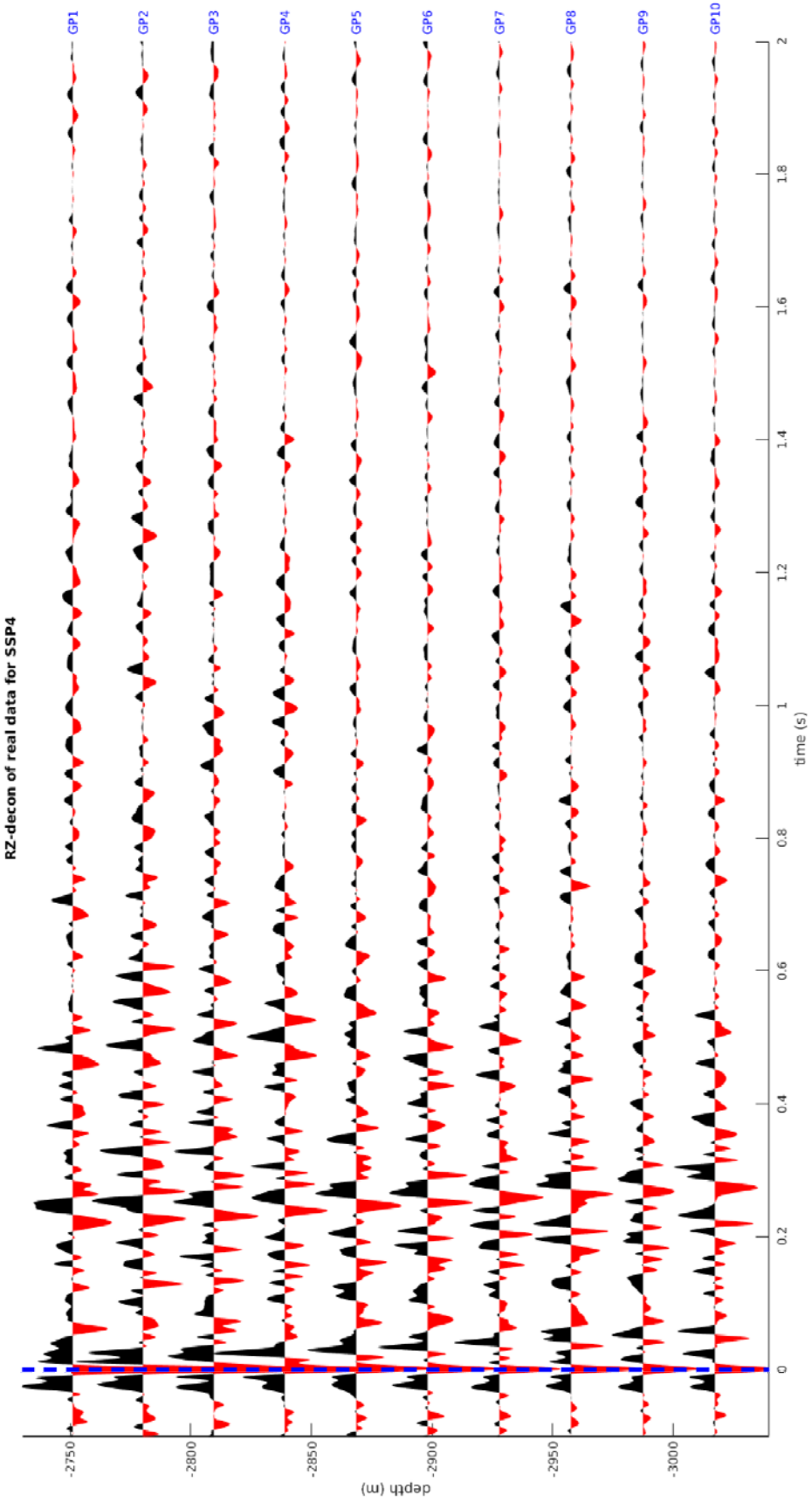
RZ-decon of real data for SSP4
GP1
GP2
GP3
GP4
GP5
GP6
GP7
GP8
GP9
GP10
depth (m)
-2750
-2800
-2850
-2900
-2950
-3000
time (s)
0
0.2
0.4
0.6
0.8
1
1.2
1.4
1.6
1.8
2